Measurement of the associated production of a vector boson (W, Z) and top quark pair in the opposite sign dilepton channel with pp collisions at $\sqrt{s} = 8$ TeV with the ATLAS detector

Dissertation

zur Erlangung des mathematisch-naturwissenschaftlichen Doktorgrades
“Doctor rerum naturalium”
der Georg-August-Universität Göttingen

im Promotionsprogramm ProPhys
der Georg-August University School of Science (GAUSS)

vorgelegt von

Tamara Vázquez Schröder

aus San Juan, Argentinien

Göttingen, 2014

Betreuungsausschuss

Prof. Dr. Kevin Kröninger
II. Physikalisches Institut, Georg-August-Universität Göttingen, now at
Experimentelle Physik IV, Technische Universität Dortmund

Prof. Dr. Arnulf Quadt
II. Physikalisches Institut, Georg-August-Universität Göttingen

Dr. Elizaveta Shabalina
II. Physikalisches Institut, Georg-August-Universität Göttingen

Mitglieder der Prüfungskommission:

Referent:	Prof. Dr. Arnulf Quadt II. Physikalisches Institut, Georg-August-Universität Göttingen
Koreferentin:	Prof. Dr. Ariane Frey II. Physikalisches Institut, Georg-August-Universität Göttingen

Weitere Mitglieder der Prüfungskommission:

PD Dr. Ralf Bernhard
II. Physikalisches Institut, Georg-August-Universität Göttingen

Prof. Dr. Wolfram Kollatschny
Institut für Astrophysik, Georg-August-Universität Göttingen

Prof. Dr. Kevin Kröninger
Experimentelle Physik IV, Technische Universität Dortmund

Jun.-Prof. Dr. Steffen Schumann
II. Physikalisches Institut, Georg-August-Universität Göttingen

Tag der mündlichen Prüfung: 17.12.2014

Referenz: II.Physik-UniGö-Diss-2014/06

“... esa grave ocupación que es jugar
cuando se buscan otras puertas.
Otros accesos a lo no cotidiano
simplemente para embellecer lo cotidiano
al iluminarlo bruscamente de otra manera,
sacarlo de sus casillas.
Definirlo de nuevo y mejor.”

- Julio Cortázar -

“... that serious pursuit which play becomes
when searching for other doors.
Other approaches to the unfamiliar
to simply enhance the familiar
by suddenly highlighting it in a different way,
thinking outside the box.
Defining it anew and better.”

- Julio Cortázar -

Contents

1. Introduction **1**

2. Physics **3**

2.1. Introduction . . . 3
2.2. The Standard Model of Particle Physics . . . 3
  2.2.1. Electroweak unification . . . 6
  2.2.2. The Higgs mechanism . . . 8
  2.2.3. Quantum Chromodynamics . . . 10
  2.2.4. The SM and beyond . . . 11
2.3. Top Quark Physics . . . 13
  2.3.1. Top Quark Production . . . 13
  2.3.2. Top Quark Decay . . . 16
  2.3.3. Top Couplings: Top & Co . . . 18
2.4. $t\bar{t}Z/W$ production at the LHC . . . 22
  2.4.1. Previous experimental measurements of $t\bar{t}Z/W$ . . . 24
2.5. Neutral current top coupling beyond the SM . . . 25

3. Experimental Setup **29**

3.1. The LHC . . . 29
3.2. The ATLAS detector . . . 31
  3.2.1. Detector coordinates and nomenclature . . . 31
  3.2.2. The Inner tracking detectors . . . 33
  3.2.3. The Calorimeters . . . 34
  3.2.4. The Muon System . . . 36
  3.2.5. The Trigger System and Data Acquisition . . . 38
3.3. ATLAS Performance in Run 1 . . . 39

4. Object definitions and preselection **43**

4.1. Introduction . . . 43
4.2. Electrons . . . 43
  4.2.1. Definition and Selection . . . 43
  4.2.2. Trigger . . . 45
  4.2.3. Performance . . . 45

4.3. Muons . . . 47
    4.3.1. Definition and Selection . . . 47
    4.3.2. Trigger . . . 48
    4.3.3. Performance . . . 48
4.4. Jets . . . 50
    4.4.1. Definition and Selection . . . 50
4.5. Missing Transverse Energy . . . 56
4.6. Event Preselection . . . 57

5. Modelling of Physics Processes **59**
5.1. Event Simulation . . . 59
5.2. Signal Processes . . . 61
5.3. Background Processes . . . 61
    5.3.1. $t\bar{t}$ corrections . . . 63
    5.3.2. Z+jets corrections . . . 64
    5.3.3. Misidentified lepton background . . . 68

6. Reconstruction of $t\bar{t}$ in the dilepton final state **71**
6.1. Challenges of the dileptonic $t\bar{t}$ system . . . 71
    6.1.1. The Kinematic Equations of the $t\bar{t}$ Dilepton System . . . 71
    6.1.2. The Neutrino Weighting Algorithm . . . 72
6.2. Kinematic Likelihood Fitter . . . 72
    6.2.1. The Dilepton Likelihood . . . 73
    6.2.2. Performance . . . 76
    6.2.3. Conclusions . . . 78

7. Analysis Strategy **81**
7.1. Introduction . . . 81
7.2. Event Selection . . . 81
    7.2.1. Classification of Event Categories . . . 82
    7.2.2. Tag Rate Function Method . . . 89
7.3. Multivariate Analysis . . . 90
    7.3.1. Introduction to the MVA . . . 91
    7.3.2. Neural Network . . . 92
    7.3.3. NeuroBayes package . . . 93

8. Statistical Analysis and Results **109**
8.1. The Fit . . . 109
8.2. Systematic Uncertainties . . . 114
    8.2.1. Detector Systematics . . . 116
    8.2.2. Background Modelling Systematics . . . 120
    8.2.3. Signal Modelling Systematics . . . 128
    8.2.4. Treatment of nuisance parameters . . . 130
8.3. Results . . . 132
    8.3.1. Introduction . . . 132
    8.3.2. Expected Fit Performance . . . 132
    8.3.3. Fit to Data . . . 133
8.4. Combined Results . . . 143

9. Conclusions $t\bar{t}V$ Results 147
9.1. Discussion of Results 147
9.1.1. Comparison with CMS $t\bar{t}V$ Measurements 147
9.2. Outlook 151

10. Precision Measurement of the $t\bar{t}$ Production Cross Section in the Single Lepton Channel 153
10.1. Introduction 153
10.2. The Analysed Dataset 153
10.3. The $t\bar{t}$ Signature 154
10.4. Signal and Main Background 154
10.5. Analysis Strategy 157
10.6. The Fit and Results 161
10.6.1. Systematic Uncertainties 161
10.6.2. Expected Fit Performance 163
10.6.3. Fit to Data 164
10.7. Conclusions 170

11. Conclusions 175

A. Validation of NN variables 177

B. Modelling Uncertainties on Z+jets and $t\bar{t}$ events 187
B.1. Alpgen Scales in Z+jets MC 187
B.2. Data/MC comparison for alternative MC models 189

C. Pruning 193

Bibliography 196

Acknowledgements 211

CHAPTER 1

Introduction

The progress in the understanding of Nature started with the attempt of answering a fundamental question: what constitutes the matter of our daily life? The answer to such a question lead to the discovery of the electron, proton and neutron in the late 19th and early 20th Century. Thus began the journey of modern day particle physics. Before the revolution of high energy particle accelerators in the early 1950s, cosmic rays were an excellent, free source of high energy particles produced in outer space. These particles would then eventually impact in the atmosphere, producing new particles that could be detected on Earth. This brought about the discovery of numerous hadrons. However, the detection of such particles is unfortunately quite inefficient. As a result of the ever-growing curiosity of mankind, the creation of an artificial version of the production of high energy particles was the next part of the journey: the design and construction of an accelerator, a collider, and a detector. With each new particle accelerator, the boundary of higher energies was continually surpassed. Each step along the way would lead to a more precise answer to the fundamental question, and would probe our understanding of Nature at its most primitive and fundamental level.

Seeking a theory which provides the underlying structure behind this apparently chaotic particle "zoo", the Standard Model of Particle Physics (SM) was developed. It provides, to date, the most precise description of the elementary particles constituting matter, and the forces between them, described by mediator particles. The heaviest known elementary particle predicted by the SM, the top quark, is the main focus of the work in this thesis. The large top quark mass translates into a coupling to the Higgs boson close to unity and, therefore, it is expected that the top quark may play a special role in electroweak symmetry breaking. Given its large mass, the energy of the collisions has to be enough to create this heavy particle. Therefore, it was only in 1995, when the top quark was discovered by the DØ and CDF experiments at the Tevatron collider, thus, completing the quark family predicted by the SM.

With the first collision data-taking in March 2010 with the Large Hadron Collider (LHC), a new era of high energy physics started. During the first run of the LHC, protons were collided under the surface of the Earth at an impressive centre-of-mass energy of $\sqrt{s} = 7$ TeV and 8 TeV, surpassing the previous collider by a factor of 4 in energy. The LHC provided the stage for the top quark to be studied in great detail; not only the rate of the production of top quark pairs could be studied, but also its properties and couplings to other particles. In particular, the coupling of the top quark to the Z-boson would provide the possibility to measure, for the first time, one of the defining quantum numbers of the top quark, the third component of the weak isospin. Furthermore, the measurement of such a coupling would allow to test the SM prediction, and search for any deviations caused by possible new physics signals. The first step towards the measurement of the coupling between the top quark and the Z-boson at hadron colliders, is the observation of the associated production of a Z-boson and a top quark pair, $t\bar{t}Z$. For the first time, such a measurement is possible at the LHC, due to the large amount of statistics and high enough energy needed to observe the $t\bar{t}Z$ process. The measurement of the $t\bar{t}Z$ production cross section, together with that of the associated production of a W-boson and a top quark pair, jointly denoted as $t\bar{t}V$, using the data collected by the ATLAS experiment at $\sqrt{s} = 8$ TeV in final states with two leptons, is the main topic of this thesis. This measurement, in combination with other channels, is the first evidence of such processes at ATLAS.

The work of this thesis is organised as follows: Chapter 2 introduces the Standard Model of Particle Physics and the current theoretical understanding of top quark physics, with particular emphasis on the $t\bar{t}Z$ and $t\bar{t}W$ processes. Afterwards, the LHC machine and the ATLAS detector, which collected the analysed data, is presented in Chapter 3. Chapters 4 and 5 describe the two key aspects crucial for a good experimental measurement of this kind: the understanding of the objects observed in the detector, and the modelling of the processes that occur in the collisions. In Chapter 6, a reconstruction algorithm developed for the dilepton $t\bar{t}$ final state is explained. This is followed by the actual "hunting" strategy for the $t\bar{t}Z$ and $t\bar{t}W$ processes in Chapter 7. The statistical analysis, together with the results in both the dilepton channel and the combination with other final states, are presented in Chapter 8. The discussion of these results, compared to other measurements, and the analysis prospects in the near future are summarised in Chapter 9. Additionally, a precision measurement of the production cross section of one of the main background processes to the $t\bar{t}V$ production, $t\bar{t}$, using early data at $\sqrt{s} = 7$ TeV, is presented in Chapter 10, and discussed from the perspective of the later $t\bar{t}V$ analysis. Finally, the thesis is concluded in Chapter 11.

Natural units are used in this thesis ($\hbar = c = 1$). Therefore, masses, energies and momenta are expressed in the unit of [eV].

CHAPTER 2

Physics

2.1. Introduction

In the first section of this chapter, an introduction to the SM will be presented, followed by a description of the gauge theories that provide the mathematical skeleton for our current understanding of Nature. More detailed descriptions of the SM can be found in References [1, 2]. In the second section, top quark physics is discussed in more detail. Finally, the production of $t\bar{t}Z$ and $t\bar{t}W$ and the connection to coupling measurements is presented, as well as a brief overview of the search for top couplings beyond the SM.

2.2. The Standard Model of Particle Physics

Particle physics is concerned with the fundamental constituents of the Universe, the elementary particles, and the interactions between them, the forces. The SM represents our current understanding of the building blocks of Nature and its interactions. It has successfully explained, to date, a large variety of phenomena in particle physics.

The SM provides a unified picture where the interactions among the constituents of matter (fermions) are described through the exchange of 'force carrier' particles (bosons). It also has an attractive aesthetic feature: all of the fundamental interactions derive from one general principle, the requirement of local gauge invariance (the invariance of the Lagrangian under a local gauge transformation of a given symmetry group). According to Noether's theorem [3], this combination of local gauge symmetries leads to conservation laws.

The SM combines the gauge group of the unification of electromagnetism, Quantum Electrodynamics or QED, and weak interactions in the so called electroweak force, with the one of Quantum Chromodynamics, QCD, the theory of strong interactions. The gravitational force is not described by the SM.

The building blocks of matter, the fermions, are spin-$\frac{1}{2}$ particles and come in two types: leptons and quarks. The leptons and quarks consist of six particles each, and are related in pairs, or 'generations'. The lightest and most stable particles make up the first generation and form all stable matter in the universe, whereas the heavier and less stable particles belong to the second and third generations. The dynamics of each of the twelve fundamental fermions is described by the Dirac equation of relativistic quantum mechanics. One important consequence of the Dirac equation is that for each of the twelve fermions, there exists an antiparticle state with the same properties as the particle, such as mass, but with opposite values of the additive quantum numbers. These quantum numbers include, for instance, the electric charge, Q, and the third component of the weak isospin, I_3.

The six quarks are paired in three generations as follows: the 'up quark' and the 'down quark' form the first generation, followed by the 'charm quark' and 'strange quark' from the second generation, and the 'top quark' and 'bottom, or beauty, quark' from the third generation. Each quark generation consists of an up-type quark with $I_3 = +\frac{1}{2}$ and $Q = +\frac{2}{3}e$ and its down-type quark partner with $I_3 = -\frac{1}{2}$ and $Q = -\frac{1}{3}e$ [1]. Each quark comes additionally in three *colours* (red, blue, green), the "charge" of the strong interaction. Table 2.1 shows an overview of the quarks classified in the three generations, along with their properties.

Generation	Quarks	Charge [e]	I_3	Mass
1	u	+2/3	+1/2	2.3 MeV
	d	−1/3	−1/2	4.8 MeV
2	c	+2/3	+1/2	1.275 GeV
	s	−1/3	−1/2	95 MeV
3	t	+2/3	+1/2	173.34 GeV
	b	−1/3	−1/2	4.18 GeV

Table 2.1.: Overview of the six quark flavours and their properties in the SM. The u-, d-, and s-quark masses are estimates of so called 'current-quark masses', in a mass independent subtraction scheme such as $\overline{MS}$ at a scale $\mu \approx 2$ GeV. The c- and b-quark masses are the 'running' masses in the $\overline{MS}$ scheme [4]. The top quark mass corresponds to the current measured world average [5].

The six leptons are similarly arranged in three generations - the 'electron' and the 'electron neutrino', the 'muon' and the 'muon neutrino', and the 'tau' and the 'tau neutrino'. The electron, muon, and tau have an electric charge $Q = -1e$, and a sizeable mass, whereas the neutrinos are electrically neutral and have very little mass. Nevertheless, the electron neutrino (ν_e), muon neutrino (ν_μ), and tau neutrino (ν_τ) are in fact quantum-mechanical mixtures of the three fundamental neutrino states with well-defined mass, labelled simply (ν_1), (ν_2) and (ν_3). This distinction is only relevant when discussing the behaviour of neutrinos that propagate over large distances. In contrast to quarks, leptons do not have colour charge. Table 2.2 shows an overview of the leptons classified in the three generations, along with their properties.

The interaction between fermions is mediated by the exchange of spin-1 gauge bosons:

- **Electromagnetic interaction**: carried by the photon (γ). Only affecting electrically charged particles.
- **Strong interaction**: carried by the gluons (g). Only affecting colour charged particles (quarks and gluons).
- **Weak interaction**: carried by the intermediate vector bosons, $W^\pm$, responsible for the charged weak interactions, and Z^0, responsible for the neutral weak interaction. All fermions may interact with the $W^\pm$ and Z^0-bosons [2].

---

[1] e is the absolute value of the charge of the electron.

[2] In the remainder, the Z^0-boson will be denoted as Z-boson.

Generation	Leptons	Charge [e]	I_3	Mass
1	ν_e	0	$+1/2$	< 2 eV
	e^-	-1	$-1/2$	511 KeV
2	ν_μ	0	$+1/2$	< 2 eV
	μ^-	-1	$-1/2$	105.7 MeV
3	ν_τ	0	$+1/2$	< 2 eV
	τ^-	-1	$-1/2$	1.78 GeV

Table 2.2.: Overview of the six lepton flavours and their properties in the SM. The e, μ, and τ masses are measured, and upper limits are set to the neutrino masses, from analysis of the low energy beta decay of tritium, combined with the neutrino oscillation results [4].

Figure 2.1 shows a summary of the interactions that affect each family of particles, organised in the corresponding generations. An overview of the properties of the aforementioned gauge bosons can be found in Table 2.3.

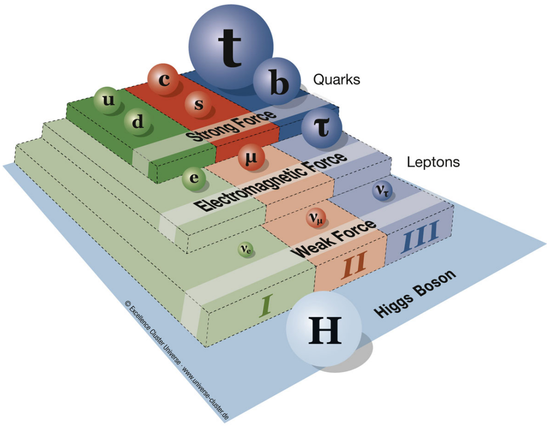

Figure 2.1.: Summary of the matter particles described by the SM and the interacting forces among them. For each hierarchy, the particles may interact via all forces from the lower levels [6].

Bosons	interaction	Charge [e]	Colour	Mass	tree-level self-interaction
γ	electromagnetic	0	-	$< 1 \text{ x } 10^{-18}$ eV	no
$W^\pm$	weak	±1	-	80.385 ± 0.015 GeV	yes
Z	weak	0	-	91.188 ± 0.0021 GeV	
g	strong	0	8 combinations	0	yes

Table 2.3.: Overview of the gauge bosons of the SM, given with their properties and associated interactions [4].

The gauge symmetry group in the SM is:

$$SU(3)_C \otimes SU(2)_L \otimes U(1)_Y, \tag{2.1}$$

where C and Y indices denote the colour quantum number for quarks in the strong interaction and the hypercharge, respectively. The suffix L indicates that the vector bosons described by this gauge group, only couple to the left handed chiral component of the fermions.

Table 2.4 summarises the characteristics of each of the individual gauge groups and relates them to the associated interaction.

	$SU(3)_C$	$SU(2)_L$	$U(1)_Y$
interaction	strong	electroweak	
Abelian group	no	no	yes
coupling	g_S	g	g'
conserved quantity	colour (C)	weak isospin ($\overrightarrow{I}$)	hypercharge (Y)
generator	8 vector bosons: gluons	3 vector bosons: W^1, W^2, W^3	1 vector boson: B

Table 2.4.: Description of the three gauge symmetry groups in the SM.

2.2.1. Electroweak unification

One of the main goals of particle physics is to provide a unified picture of fundamental particles and their interactions. In the 19th century, Maxwell presented electricity and magnetism as different aspects of a unified theory of electromagnetism. In the 1960s, Glashow, Salam and Weinberg [7, 8, 9] (GSW) developed a unified picture of electromagnetism and weak interaction, known as *electroweak theory*. The electroweak interaction is described by the $SU(2)_L \otimes U(1)_Y$ group, as can be seen in Table 2.4. To understand the implications of this unification, it is necessary to understand the characteristics of each symmetry group separately.

The electromagnetic theory (QED) is based on the unitary group $U(1)_Q$, where Q denotes the electric charge. The charged-current weak interaction is invariant under $SU(2)$ local phase transformations:

$$\varphi(x) \rightarrow \varphi'(x) = \exp[ig\alpha(\mathbf{x}) \cdot \mathbf{T}]\varphi(\mathbf{x}), \tag{2.2}$$

where $\mathbf{T}$ are the three generators of the $SU(2)$ group that can be written in terms of the Pauli spin matrices, σ, as $\mathbf{T} = \frac{\mathbf{1}}{\mathbf{2}}\sigma$, and $\alpha(\mathbf{x})$ are the three functions which specify the local phase at each point in space-time. The three gauge fields W^1, W^2, and W^3, are introduced to satisfy the required local gauge invariance. Since the generators of the $SU(2)$ gauge transformation are the 2×2 Pauli spin-matrices, the wavefunction $\varphi(x)$ in Equation 2.2 must be written in terms of two components, and therefore $\varphi(x)$ is denoted as the weak isospin doublet.

Fermion fields are described by spinors ($u(p)$) containing four components. The left-handed component is obtained by the projection of the operator $\frac{1-\gamma^5}{2}$ and the right-handed component is obtained by the projection of the operator $\frac{1+\gamma^5}{2}$, where γ^5 represents the product of the four Dirac matrices. While QED and QCD are vector interactions with a current of the form $j^\mu = \bar{u}(p')\gamma^\mu u(p)$, the weak-charged current is a vector minus axial vector (V - A) interaction, and the four-vector current is given by

$$j^\mu = \frac{g}{\sqrt{2}}\bar{u}(p')\frac{1}{2}\gamma^\mu(1-\gamma^5)u(p). \tag{2.3}$$

The weak-charged current already contains the left-handed chiral projection operator. Given the properties of the γ^5 matrix, the weak-charged current interaction only couples to left-handed

(LH) chiral particle states and right-handed (RH) chiral antiparticle states. Therefore, the weak isospin doublets are only composed of LH chiral particle states and RH chiral antiparticle states and, for this reason, the symmetry group of the weak interaction is referred as $SU(2)_L$.

The physical W-bosons can be identified as the linear combinations of W^1 and W^2:

$$W^{\pm}_{\mu} = \frac{1}{\sqrt{2}}(W^1_{\mu} \mp iW^2_{\mu}). \tag{2.4}$$

From the observed decay rates of muons and tau leptons, it can be shown that the strength of the weak-charged interaction is the same for all lepton flavours (*lepton universality*). According to the Cabibbo hypothesis, the weak interactions of quarks have the same strength as the leptons, but their weak eigenstates differ from the mass eigenstates. The unitary Cabibbo-Kobayashi-Maskawa [10, 11](CKM) matrix relates the weak and the mass eigenstates of quarks by:

$$\begin{pmatrix} d' \\ s' \\ b' \end{pmatrix} = \begin{pmatrix} V_{ud} & V_{us} & V_{ub} \\ V_{cd} & V_{cs} & V_{cb} \\ V_{td} & V_{ts} & V_{tb} \end{pmatrix} \begin{pmatrix} d \\ s \\ b \end{pmatrix}. \tag{2.5}$$

The CKM matrix elements can be most precisely determined by a global fit that uses all available measurements and imposes the SM constraints (i.e. three generation unitarity). The fit results for the magnitudes of all nine quark mixing parameters are [4]:

$$\begin{pmatrix} d' \\ s' \\ b' \end{pmatrix} = \begin{pmatrix} 0.97427 \pm 0.00015 & 0.22534 \pm 0.00065 & 0.00351^{+0.00015}_{-0.00014} \\ 0.22520 \pm 0.00065 & 0.97344 \pm 0.00016 & 0.0412^{+0.0011}_{-0.0005} \\ 0.00867^{+0.00029}_{-0.00031} & 0.0404^{+0.0011}_{-0.0005} & 0.999146^{+0.000021}_{-0.000046} \end{pmatrix} \begin{pmatrix} d \\ s \\ b \end{pmatrix}. \tag{2.6}$$

The $SU(2)_L$ symmetry of the weak interaction implies the existence of a weak-neutral current, the one corresponding to the W^3. Nevertheless, that neutral current cannot be identified simply as the one due to the exchange of the Z-boson, since it was shown experimentally that the physical Z-boson couples to both left- and right-handed chiral states.

Since both the photon and Z-boson, with the corresponding fields A_{μ} and Z_{μ}, are neutral, it is reasonable that they can be expressed in terms of quantum states formed from two neutral bosons (W^3_{μ} associated with the $SU(2)_L$ local gauge symmetry, and B_{μ} associated with the $U(1)_Y$ local gauge symmetry) as follows:

$$A_{\mu} = +B_{\mu} \cos\theta_W + W^3_{\mu} \sin\theta_W, \tag{2.7}$$

$$Z_{\mu} = -B_{\mu} \sin\theta_W + W^3_{\mu} \cos\theta_W, \tag{2.8}$$

where θ_W is the weak mixing angle.

By imposing invariance under $SU(2)_L$ and $U(1)_Y$ local gauge transformations and respecting the electric charge and the third component of the weak isospin of the LH and RH chiral particle states, the following relationship between couplings is derived:

$$e = g \sin\theta_W = g' \cos\theta_W, \tag{2.9}$$

and the weak hypercharge is given by:

$$Y = 2(Q - I_3). \tag{2.10}$$

Defining the coupling to the physical Z-boson as:

$$g_Z = \frac{g}{\cos\theta_W} \equiv \frac{e}{\sin\theta_W \cos\theta_W}, \tag{2.11}$$

the Z-boson interaction vertex factor can be expressed as:

$$-i\frac{1}{2}g_Z\gamma^\mu[c_V - c_A\gamma^5], \tag{2.12}$$

where the vector and axial-vector couplings of the Z-boson are:

$$c_V = I_3 - 2Q\sin^2\theta_W \quad \text{and} \quad c_A = I_3. \tag{2.13}$$

2.2.2. The Higgs mechanism

The local gauge principle provides an elegant description of the interactions in the SM. However, the required local gauge invariance is broken by terms in the Lagrangian corresponding to the particle masses. This is not a problem for QED and QCD, where the gauge bosons are massless, but it is not supported by the observation of the large masses of the W- and Z-bosons. Nevertheless, as shown by 't Hooft [12, 13, 14], only theories with local gauge invariance are renormalisable, such that the cancellation of all infinities takes place among only a finite number of interactions. The Higgs mechanism generates the masses of the electroweak gauge bosons in a way that it preserves the local gauge invariance of the SM. It also gives mass to the fundamental fermions. As a consequence, a new field, the Higgs field, is added to the SM Lagrangian [15, 16, 17, 18].

In the Salam-Weinberg model, the Higgs mechanism is embedded in the $U(1)_Y \otimes SU(2)_L$ local gauge symmetry of the electroweak sector of the SM. The simplest Higgs model consists of two complex scalar fields, placed in a weak isospin doublet:

$$\phi = \begin{pmatrix} \phi^+ \\ \phi^0 \end{pmatrix} = \frac{1}{\sqrt{2}} \begin{pmatrix} \phi_1 + i\phi_2 \\ \phi_3 + i\phi_4 \end{pmatrix}, \tag{2.14}$$

where ϕ^0 is a neutral scalar field and ϕ^+ is a charged scalar field, such that ϕ^+ and $(\phi^+)^* = \phi^-$ give the longitudinal degrees of freedom of the W^+ and W^-. The Lagrangian of this doublet of the complex scalar is:

$$\mathcal{L} = (\partial_\mu\phi)^\dagger(\partial^\mu\phi) - V(\phi), \tag{2.15}$$

with the Higgs potential expressed as:

$$V(\phi) = \mu^2\phi^\dagger\phi + \lambda(\phi^\dagger\phi)^2. \tag{2.16}$$

The shape of the potential depends on the sign of μ^2 (it is required that $\lambda > 0$ for the potential to have a finite minimum), as can be seen in a simplified example in Figure 2.2. For $\mu^2 < 0$, the potential has an infinite set of degenerate minima satisfying:

$$\phi^\dagger\phi = -\frac{\mu^2}{2\lambda} = \frac{v^2}{2}, \tag{2.17}$$

where v is the non-zero vacuum expectation value of the Higgs field. The choice of the vacuum state breaks the symmetry of the Lagrangian, a process known as *spontaneous symmetry breaking.*

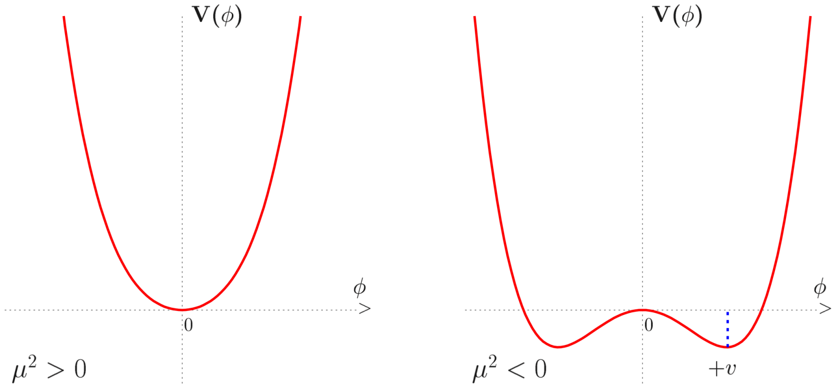

Figure 2.2.: Graphic representation of the potential $V(\phi) = \frac{1}{2}\mu^2\phi^2 + \frac{1}{4}\lambda\phi^4$ of a scalar real field ϕ for (left): $\mu^2 > 0$ and (right): $\mu^2 < 0$ [19].

In order to keep the neutral photon massless, the minimum of the potential must correspond to a non-zero expectation value only for the neutral scalar field ϕ^0. The fields can be expanded about this minimum in the form:

$$\phi(x) = \frac{1}{\sqrt{2}} \begin{pmatrix} \phi_1 + i\phi_2 \\ v + \eta(x) + i\phi_4 \end{pmatrix}. \tag{2.18}$$

From this spontaneous symmetry breaking, the creation of a massive scalar and three massless Goldstone bosons arises, which give the longitudinal degrees of freedom of the $W^\pm$ and Z bosons. The Higgs doublet can be written in a unitary gauge [3] as:

$$\phi(x) = \frac{1}{\sqrt{2}} \begin{pmatrix} 0 \\ v + h(x) \end{pmatrix}, \tag{2.19}$$

where $h(x)$ is the Higgs field.

The mass terms can be identified by writing the Lagrangian of Equation 2.15 such that it respects the $SU(2)_L \otimes U(1)_Y$ local gauge symmetry of the electroweak model and are expressed in terms of the vacuum expectation value as:

$$m_W = \frac{1}{2} g v, \tag{2.20}$$

$$m_Z = \frac{1}{2} v \sqrt{g^2 + g'^2}, \tag{2.21}$$

and

$$m_\gamma = 0. \tag{2.22}$$

Using the relationship between couplings from Equation 2.9, the masses of the Z- and the W-boson are related to one another as:

$$\frac{m_W}{m_Z} = \cos\theta_W. \tag{2.23}$$

---

[3] The gauge in which the Goldstone fields are eliminated from the Lagrangian.

The experimental verification of this relation provides a strong argument in favour of the validity of the Higgs mechanism.

In summary, the GSW model is described by four parameters: the gauge couplings g and g' and the two free parameters of the Higgs potential μ and λ, which are related to the vacuum expectation value of the Higgs field, v, and the mass of the Higgs boson, m_H, by:

$$v^2 = \frac{-\mu^2}{\lambda} \text{ and } m_H^2 = 2\lambda v^2. \tag{2.24}$$

The vacuum expectation value of the Higgs field can be calculated using Equation 2.20 and the measured values for m_W and g_W, resulting in $v = 246$ GeV. The remaining parameter, λ, can be obtained from the measured Higgs mass at the LHC.

The spontaneous symmetry breaking of the $SU(2)_L \otimes U(1)_Y$ gauge group of the SM can also be used to generate the masses of the fermions. The Yukawa couplings of the fermions to the Higgs field are given by:

$$g_f = \sqrt{2}\frac{m_f}{v}. \tag{2.25}$$

It is interesting to see that for the top quark, with measured mass given in Table 2.1 and $v = 246$ GeV, the Yukawa coupling is close to unity. This indicates that the top quark is closely connected to the electroweak symmetry breaking.

2.2.3. Quantum Chromodynamics

Quantum Chromodynamics (QCD) is the Quantum Field Theory of the strong interaction. The associated underlying symmetry is invariant under SU(3) local phase transformations,

$$\psi(x) \to \psi'(x) = \exp\left[ig_s\alpha(x) \cdot \hat{\mathbf{T}}\right]\psi(x), \tag{2.26}$$

where $\hat{\mathbf{T}} = T^a$ are the eight generators of the SU(3) symmetry group, which are related to the Gell-Mann matrices by $T^a = \frac{1}{2}\lambda^a$, and $\alpha^a(x)$ are eight functions of the space-time coordinate x. The required local gauge invariance can be fulfilled by introducing eight new fields $G^a_\mu(x)$, where the index $a = 1, \ldots, 8$, each corresponding to one of the eight generators of the SU(3) symmetry group. These eight new fields are the massless gluons of QCD.

The Dirac equation, including the interactions with the new gauge fields, is invariant under local SU(3) phase transformations, provided the new fields transform as:

$$G^k_\mu \to G^{k'}_\mu = G^k_\mu - \partial_\mu\alpha_k - g_S f_{ijk}\alpha_i G^j_\mu. \tag{2.27}$$

The last term in Equation 2.27 arises because the generators of the SU(3) group do not commute [4], thus allowing gluon self-interactions. f_{ijk} are the *structure constants* of the SU(3) group, defined by the commutation relations $[\lambda_i, \lambda_j] = 2if_{ijk}\lambda_k$, and g_S is the coupling constant of the strong interaction.

The quantum number of the strong interaction is called *colour*, and comes in three types: *red*, *green*, and *blue*. Only particles that have non-zero colour charge couple to gluons. The quarks, unlike the leptons, carry colour charge and exist in three orthogonal colour states. Also the gluons, unlike the photon, which are electrically neutral, carry colour charge[5] and can therefore interact among themselves. The SU(3) colour symmetry is exact and QCD is invariant

---

[4] Therefore, QCD is known as a non-Abelian gauge theory.

[5] To be more precise, gluons carry simultaneously both colour charge and anticolour charge.

under unitary transformations in colour space. Therefore, the strength of QCD interactions is independent of the colour charge of the quark.

Free quarks have never been observed directly. This is explained by the hypothesis of *colour confinement*, which states that coloured objects are always confined to colour singlet states and that no objects with non-zero colour charge can propagate as free particles. Colour confinement is believed to originate from the gluon-gluon self-interactions that arise because the gluons carry colour charge. Because the energy stored in the colour field between two quarks increases linearly with distance, it would require an infinite amount of energy to separate two quarks. As a result, it becomes energetically preferable to break the colour string and create another pair of quarks with opposite-colour charge from the vacuum. Consequently, coloured objects arrange themselves into colourless bound hadronic states with no confining colour field between them. To date, all confirmed observed hadronic states correspond to colour singlets either in the form of *mesons* ($q\bar{q}$), *baryons* (qqq) or *antibaryons* ($\bar{q}\bar{q}\bar{q}$). Also as a consequence of colour confinement, the high-energy quarks produced in processes such as $e^+e^- \to q\bar{q}$ do not propagate freely but are observed as *jets* of colourless particles. The process by which high-energy quarks (and gluons) produce jets is known as *hadronisation*.

The coupling constant g_S is related to α_S as:

$$\alpha_S = \frac{g_S^2}{4\pi}. \tag{2.28}$$

It is important to note that the coupling constant (or α_S) is not constant and its value depends on the energy scale of each interaction. The evolution of $\alpha_S(q^2)$ is given to lowest order by:

$$\alpha_S(q^2) = \frac{\alpha_S(\mu^2)}{1 + B\alpha_S(\mu^2)\ln\left(\frac{q^2}{\mu^2}\right)}, \tag{2.29}$$

with

$$B = \frac{11N_C - 2N_f}{12\pi}, \tag{2.30}$$

and μ being a chosen scale at which the coupling constant is known [6].

For $N_C = 3$ colours and $N_f \leq 6$ quarks, B is greater than zero and α_S decreases with increasing q^2. This behaviour of the coupling constant has important implications. At low energies ($|q| \sim 1$ GeV), α_S is of $\mathcal{O}(1)$ and perturbation theory cannot be used [7]. At high energies ($|q| > 100$ GeV), $\alpha_S \sim 0.1$, which is sufficiently small so that perturbation theory can be used. This property of QCD is known as *asymptotic freedom* [20, 21, 22], meaning that at high energies quarks can be treated as quasi-free particles. Nevertheless, $\alpha_S \sim 0.1$ is not small. As a result, higher-order corrections cannot be neglected. For this reason, QCD calculations for processes at the LHC are usually calculated beyond lowest order.

2.2.4. The SM and beyond

Despite the profound and elegant theoretical ideas that sustain the pillars of the SM, and the numerous experimental results confirming its unquestionable success in explaining a wide-range of phenomenas at energies up to the electroweak scale, the SM is still an *ad hoc* compilation of theories, put together in such a way that it reproduces the experimental data.

---

[6] A common scale is Λ_{QCD}, which effectively controls the hadron masses ($\Lambda_{QCD} \approx 200$ MeV).

[7] This non-perturbative regime applies to the latter stages in the hadronisation process.

If neutrinos are assumed to be Dirac fermions, the SM has 25 free parameters[8] that are not predicted, and must be measured in experiments. These parameters can be classified as [1]:

- Associated with the Higgs field
  - 12 masses of fermions (or 12 Yukawa couplings to the Higgs field)
  - 2 parameters describing the Higgs potential: v and m_H
- 3 coupling constants describing the strengths of the gauge interactions: g', g and g_S
- 8 mixing angles of the PMNS [9] and CKM matrices.

Besides the large number of free parameters of the SM, there are a handful of outstanding issues that the SM is not able to explain. Some of the open questions include:

- Observational facts unexplained by the SM:
  - What is dark matter?
  - What explains the matter-antimatter asymmetry of the Universe?
- Fine-tuning problems:
  - The hierarchy problem associated with the Higgs: Why is the EW scale (m_W) so small, in units of the (assumed) cutoff (M_{Planck})? What prevents quantities at the EW scale, such as the Higgs boson mass, from getting quantum corrections on the order of the Planck scale?
  - The flavour problem: Why are the fermion masses, mixing angles and CP (charge-parity) violating phases undetermined?
  - The strong CP problem: Why is there so little strong CP violation?
- Why are there three generations of fermions?
- Why is there such a fermion mass hierarchy?
- Are neutrinos Majorana [10] or Dirac particles?
- Is there gauge coupling unification at higher energies?

Because of these various open issues, the SM could be a *low-energy* approximation of the ultimate theory of particle physics. Other alternative theories beyond the SM, such as a supersymmetry [23] or large-scale extra dimensions [24, 25], provide solutions to some of these questions, as well as reproduce the complete range of current phenomena that the SM has successfully explained.

---

[8] It would be 26 parameters if the Lagrangian of QCD would contain a phase, denoted by θ_{CP}, different from zero that would lead to CP (charge-parity) violation in the strong interaction.

[9] Unitary matrix that relates the three neutrino weak eigenstates (ν_e, ν_μ and ν_τ) to the neutrino mass eigenstates (ν_1, ν_2 and ν_3)

[10] Contrary to the Dirac neutrinos, Majorana neutrinos would be their own antiparticles.

2.3. Top Quark Physics

The top quark is the charge $Q = +\frac{2}{3}$ and weak isospin $T_3 = +\frac{1}{2}$ partner of the b-quark in the third generation weak isospin doublet. Once the b-quark was discovered in 1977, there were many reasons to expect the existence of the top quark. Indirect evidence of its existence was obtained from limits on FCNC decays of the b-quark [26, 27] as well as from the absence of tree-level (lowest order) mixing in the $B_d^0 - \bar{B}_d^0$ system [28, 29, 30, 31], discarding the possibility of an isosinglet b-quark. Before it was discovered by the CDF and D0 Collaborations in 1995 [32, 33], the top quark mass was predicted by the electroweak precision data with very large uncertainty [34].

The top quark has two main properties that make it a particularly interesting and unique quark in the elementary-particle zoo:

- *The Heaviest* : the top quark is by far the heaviest known quark. The recently released first combination of the top quark mass measurements from the two experiments, CDF and D0, at the Tevatron, and from the two experiments, ATLAS and CMS, at the LHC, measures $m_{top} = 173.34 \pm 0.27(\text{stat.}) \pm 0.71(\text{syst.})$ GeV, with a total uncertainty of 0.76 GeV, corresponding to a precision of 0.4% [5].

  This large top quark mass translates into a large Yukawa coupling close to unity. Therefore, it is expected that the top quark may play a special role in electroweak symmetry breaking (EWSB) and might open a window to new physics. Due to its large mass, the top quark also gives a significant contribution to the Higgs self-energy. Before the Higgs boson discovery [35, 36], the top quark mass, together with the W-boson mass, gave indirect constraints on the possible Higgs boson mass.

- *The Quickest to Decay* : as a consequence of its large mass, the top quark has a very short lifetime ($\approx 0.5 \times 10^{-24}$ s [4]), and on average it decays before it can hadronise and before its spin is depolarised by the strong interaction. This “bare” quark transfers its properties to its decay products. This allows the study of its properties, such as the top quark polarisation or spin via the angular distribution of its decay products. Top quark physics is therefore described by perturbative QCD.

In the remainder of this section, the production mechanisms and decay modes of the top quark are described. Reviews of top quark physics at hadron colliders can be found in References [4, 37, 38, 39].

2.3.1. Top Quark Production

At hadron colliders, top quarks are dominantly produced in pairs via the strong interaction, or, with smaller cross section, as single top quarks via the electroweak interaction.

Top Quark Pair Production

Top quark pair production can be described by perturbative QCD. According to this approach, a hard scattering between two incoming hadrons (proton or anti-proton) is effectively the interaction between its constituents (quarks or gluons), denoted as *partons*, each carrying a certain fraction x of the initial momenta of the incoming hadrons. Using the factorisation theorem, the inclusive production cross section of the process $pp \to t\bar{t}$ at the LHC can be expressed as the convolution of parton distribution functions (PDF) and a partonic cross section $\hat{\sigma}$ [38, 40]:

$$\sigma_{pp\to t\bar{t}}(s, m_t, \mu_f, \mu_r) = \sum_{i,j=q,\bar{q},g} \int dx_i dx_j f_i(x_i, \mu_f^2) f_j(x_j, \mu_f^2) \times \hat{\sigma}_{ij\to t\bar{t}}(\hat{s}, m_t, \mu_f, \mu_r, \alpha_s(\mu_r^2)), \tag{2.31}$$

where:

- *parton distribution functions (PDF)* $f_i(x_i, \mu_f^2)$: probability density to observe a parton flavour i with longitudinal momentum fraction x_i in the incoming hadron, when probed at a factorisation scale μ_f [37]. Figure 2.3 shows the momentum densities in the proton of the quarks, antiquarks and gluons for the CT10 PDF set [41, 42] at $Q^2 = \mu_f^2 = 100$ GeV^2.
- *factorisation scale* μ_f: scale that separates the hard scattering regime from the PDF associated with the incoming hadrons.
- *renormalisation scale* μ_r: artificial scale introduced by a renormalisation procedure, that redefines fields and parameters in order to eliminate ultra-violet divergences from the QCD Lagrangian. It is common to use the same scale for both μ_r and μ_f.
- $\hat{s}$: effective centre-of-mass energy squared of the parton-parton process, related to the centre-of-mass energy squared of the pp process, s, by $\hat{s} = x_i x_j s$.

In order to produce $t\bar{t}$ pairs, it is required that $\hat{s} \geq 4m_t^2$. Given the available high centre-of-mass energy, the large gluon density at small x, as can be seen in Figure 2.3, and the presence of antiquarks in protons only as sea quarks, the $t\bar{t}$ production at the LHC is dominated by gluon-gluon fusion ($\approx 80\%$ at $\sqrt{s} = 7$ TeV) (Figure 2.4(a)), with a minor remaining contribution from quark-antiquark annihilation (Figure 2.4(b)). For opposite reasons, the main $t\bar{t}$ production at the Tevatron ($p\bar{p}$ collisions) is quark-antiquark annihilation ($\approx 85\%$ at $\sqrt{s} = 1.96$ TeV). Furthermore, given the high centre-of-mass energy at the LHC, top pairs are typically produced above the mass threshold, whereas at Tevatron energies (1.8 / 1.96 TeV at Run I / Run II), top pairs are typically produced at rest.

The theoretical calculation of the $t\bar{t}$ production cross section in pp collision at $\sqrt{s} = 8$ TeV used in the main analysis of this thesis is performed at full next-to-next-to-leading-order (NNLO) in QCD, including resummation of next-to-next-to-leading logarithmic (NNLL) soft gluon terms [11] with TOP++2.0 [44, 45, 46, 47, 48, 49]. It is computed for a renormalisation and factorisation scale of $\mu = m_t$, with $m_t = 172.5$ GeV, using the CT10 PDF set, and yields a $t\bar{t}$ cross section of:

$$\sigma_{pp\to t\bar{t}} = 252.89^{+6.39}_{-8.64}\ (\text{scale})^{+7.58}_{-7.33}\ (m_t) \pm 11.67\ (\text{PDF} + \alpha_S)\ \text{pb}. \tag{2.32}$$

The uncertainty on the calculation includes the scale uncertainty, the choice of PDF set, the uncertainties provided with the PDF sets, and the uncertainties on α_S and the top quark mass. The quoted scale uncertainty is derived from the independent variation of the renormalisation and factorisation scales by a factor of 2 and 0.5, excluding those variations for which the two scales differ from each other by a factor of 4. The PDF and α_S uncertainties are calculated using the PDF4LHC prescription [50] with the MSTW2008 68% CL NNLO [51, 52], CT10 NNLO and NNPDF2.3 5f FFN [53] PDF sets. The additional uncertainty from the top quark mass is calculated by varying m_t by ±1 GeV.

---

[11] Resummation primarily improves the stability of predictions with respect to changes of μ_f or μ_r [37].

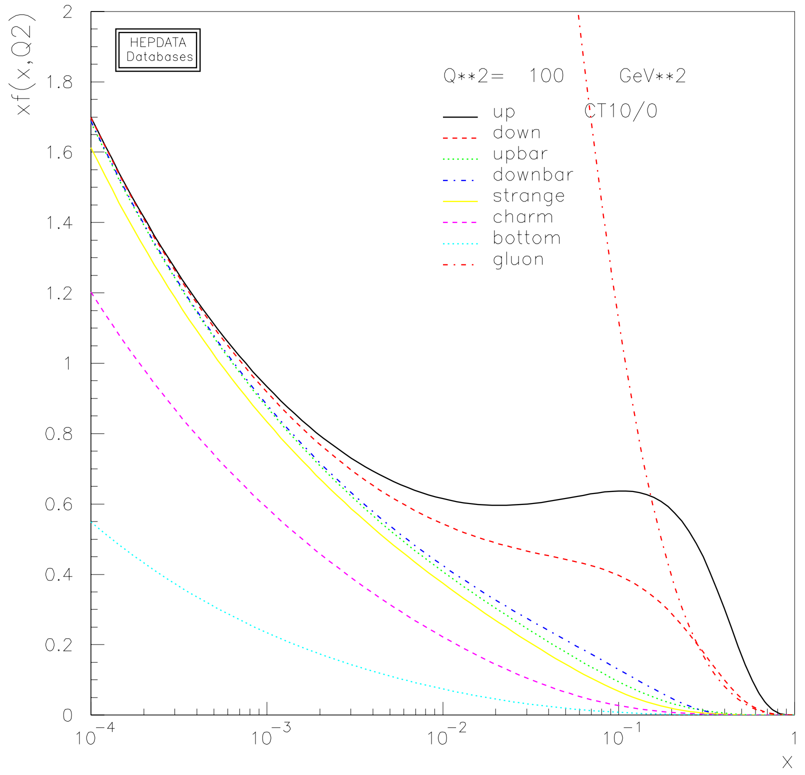

Figure 2.3.: Momentum densities in the proton of quark, antiquark and gluons for the CT10 PDF set [41, 42] at $Q^2 = \mu_f^2 = 100$ GeV^2. Figure generated with [43].

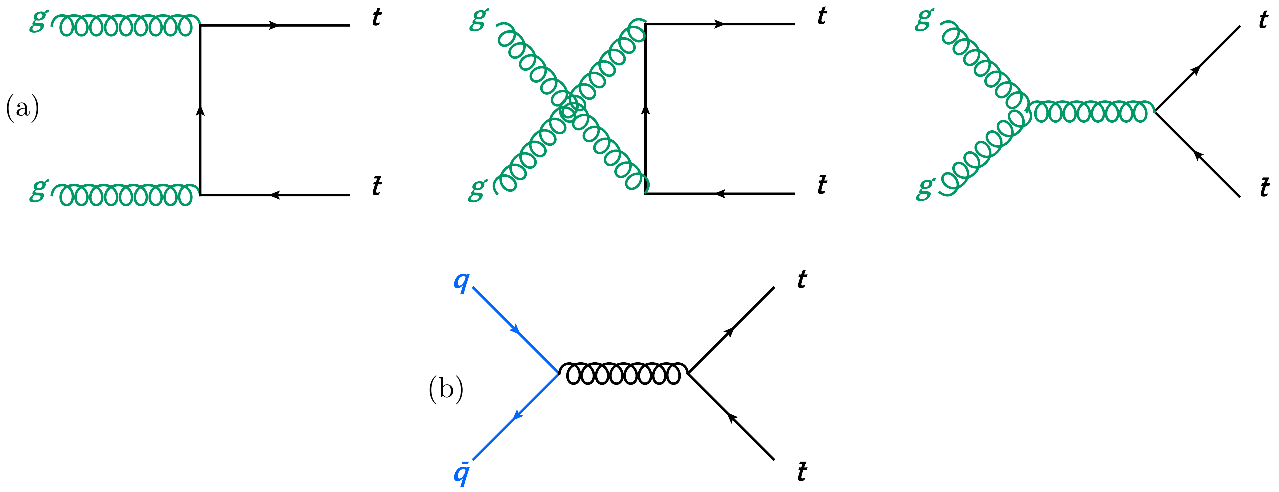

Figure 2.4.: Leading order diagrams contributing to the top quark pair production at hadron colliders. The production mechanisms can be **(a)** gg fusion or **(b)** $q\bar{q}$ annihilation.

An early measurement of the $t\bar{t}$ cross section at $\sqrt{s} = 7$ TeV with the ATLAS experiment is described in Section 10.

Single Top Quark Production

Single top quarks can be produced via three different electroweak mechanisms as shown in Figure 2.5:

- *t-channel* exchange of a W-boson: a space-like W-boson scatters off a b quark, which can be included in the initial state [12] (*massless* or *5-flavour scheme*) or produced via gluon splitting $g \to b\bar{b}$ (*massive* or *4-flavour scheme*) [54, 38].
- *s-channel* production and decay of a W-boson.
- *Wt-channel* or associated production of a top quark and a W-boson.

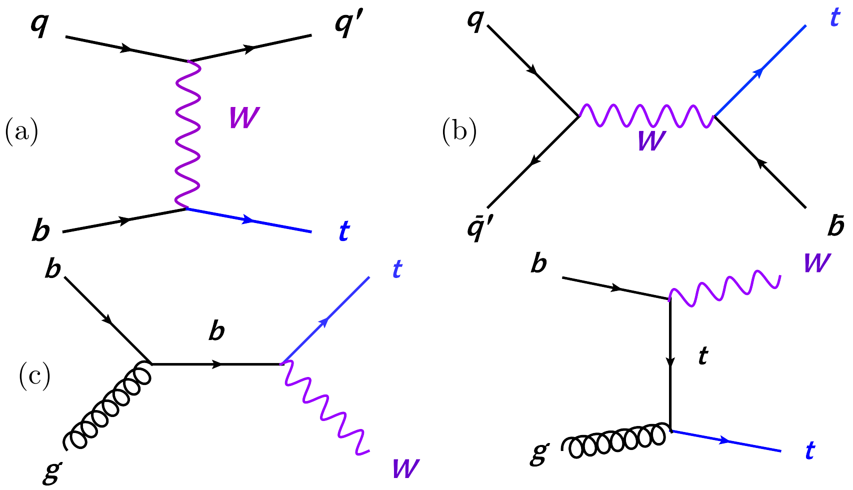

Figure 2.5.: Leading order diagrams contributing to the single top production at hadron colliders. The three production mechanisms are **(a)** *t-channel*, **(b)** *s-channel* and **(c)** *Wt-channel*.

The *t-channel* is the dominant single top production mode at the LHC, followed by the *Wt-channel* and the *s-channel*. Figure 2.6 shows the cross section values for the three single top production mechanisms as a function of the centre-of-mass energy at the LHC using MCFM [55], compared to the corresponding top pair production cross section.

Assuming the SM charged-weak coupling for a doublet pair of quarks, the single top production cross section provides direct sensitivity to the CKM matrix element V_{tb}.

2.3.2. Top Quark Decay

The top quark decays into lighter particles via the electroweak interaction. The probability of decaying into a W-boson and a certain down-type quark (d, s or b) is proportional to the corresponding CKM matrix element squared. In the SM (see Equation 2.6), $|V_{tb}| \gg |V_{td}|, |V_{ts}|$, and given that the top quark mass is above the Wb threshold, it decays almost exclusively as $t \to W^{+}b$ (and equivalently $\bar{t} \to W^{-}\bar{b}$).

The top quark pair decay final states can be classified according to the decay modes of the W-boson. W-bosons can decay *leptonically*, where the W-boson decays into a charged lepton

---

[12] It allows the resummation of possibly large initial state logarithms into the b-PDF.

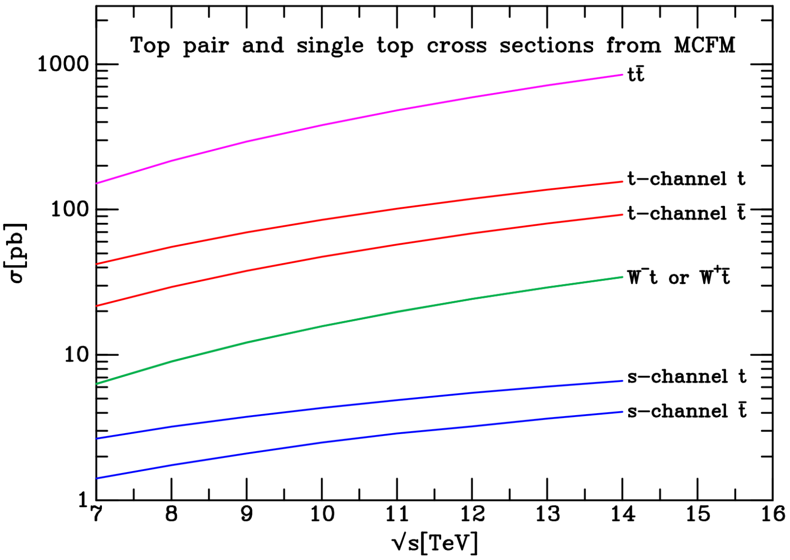

Figure 2.6.: Cross section values for the top pair and single top production calculated at NLO QCD using MCFM. The cross sections are evaluated at $\mu = \mu_r = \mu_f = m_t$, where $m_t = 173.2$ GeV, using the CTEQ6M PDFs [56].

(antilepton) and the same flavour antineutrino (neutrino), or *hadronically*, where the W-boson decays into an up-type quark (antiquark) and a down-type antiquark (quark), as shown in Figure 2.7.

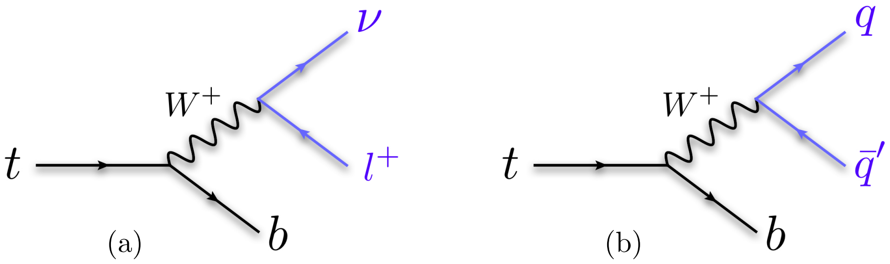

Figure 2.7.: Two possible decay modes of the W-boson: **(a)** leptonically or **(b)** hadronically.

The W-boson mass is sufficiently large for it to decay into any quark except the top quark, so that the possible quark pairs in the final state not suppressed by the CKM matrix elements are $(u\bar{d})$ and $(c\bar{s})$. Since the quark pairs have to be colour neutral, there are three possibilities for each of them, given the three colour charges, *red (r), blue (b),* and *green (g)*: $r\bar{r}$, $b\bar{b}$ and $g\bar{g}$. Together with the three possible leptonic final states, there are in total nine different possible final states for the W-boson decay. Given lepton universality of the charged-weak interaction and the Cabibbo hypothesis for equal weak interaction strength for leptons and quarks (see Section 2.2.1), at Born level, the W-boson decays $\frac{1}{3}$ of the time into a $l\nu$ pair and $\frac{2}{3}$ of the time into a $q\bar{q}'$ pair.

Since quarks evolve into a jet of hadrons, and neutrinos do not leave any trace in their path through the detector, the experimental signatures of a top quark pair decay can be classified in three classes. They are divided in terms of the decay modes of the two W-bosons:

- **lepton+jets**: one W-boson decays leptonically, the other one decays hadronically. The final signature includes: four jets, two of which originate from the b-quarks, one charged lepton and a large imbalance of the momentum in the transverse plane from one neutrino.
- **allhadronic**: both W-bosons decay hadronically. The final signature includes: six jets, two of which originate from the b-quarks.
- **dileptonic**: both W-bosons decay leptonically. The final signature includes: two jets originating from the two b-quarks, two charged leptons and a large imbalance of the momentum in the transverse plane from two neutrinos.

The branching fractions of the different top quark pair decay modes can be seen in Figure 2.8. The dileptonic channel is the chosen channel in the main analysis of this thesis. Although it has a comparatively small branching ratio, the very clear signature of two charged leptons reduces the contribution of other physical processes (*backgrounds*) mimicking the $t\bar{t}$ signature. The presence of the two neutrinos in the final state, seen experimentally as an overall transverse momentum imbalance, prevents a full kinematic reconstruction of the $t\bar{t}$ system unless certain assumptions are made. A kinematic likelihood technique developed to reconstruct the $t\bar{t}$ dilepton channel will be explained in Section 6. Depending on the lepton flavour, three dilepton final states are considered: electron-electron ee, muon-muon $\mu\mu$, and electron-muon $e\mu$. Since the τ lepton decays rather quickly [13] into either leptonic or hadronic states, leptonic decays of the τ lepton ($\tau \rightarrow e\bar{\nu}_e\nu_\tau$ and $\tau \rightarrow \mu\bar{\nu}_\mu\nu_\tau$) are included as well in the corresponding three dilepton categories.

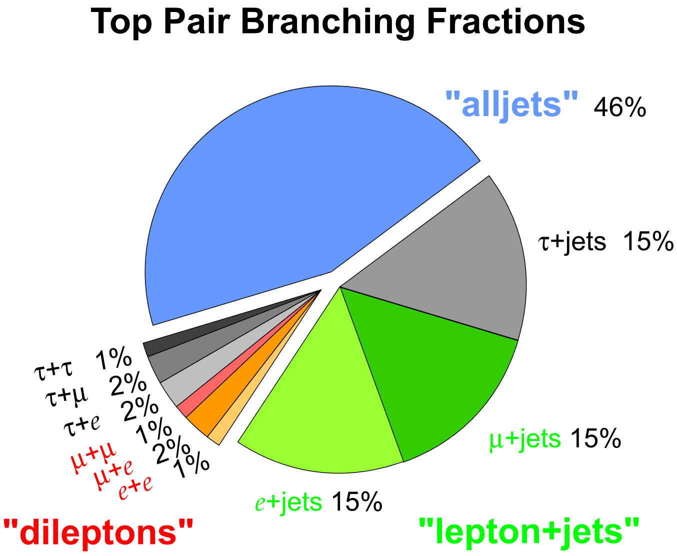

Figure 2.8.: Branching ratios of the different top quark pair decay channels at Born level [57].

2.3.3. Top Couplings: Top & Co

The top quark couples to the SM fields through its gauge and Yukawa interactions. Some of these couplings have been investigated at the Tevatron, through studies of the Wtb vertex and the $t\bar{t}\gamma$ production, while others, such as the $t\bar{t}Z$ and $t\bar{t}H$ production, are becoming accessible

---

[13] The τ mean lifetime is of the order of 10^{-13} s [4].

only with the high statistics top quark sample at the LHC, also called for this reason a 'top quark factory'. At hadron colliders, the first evidence of the coupling of the top quark to the γ, Z, and H boson will come from the production rate, while constraints on the coupling of the top quark with the W-boson come from both the top quark decay and the single top production.

New physics related to EWSB may be found first in top quark precision measurements. Possible new physics signals would cause deviations of the top quark couplings tZ, $t\gamma$, and Wtb, from the SM prediction. Some examples include technicolor and other models with a strongly coupled Higgs sector [58].

Figure 2.9 shows a summary of the processes involving the top quark at hadron colliders that provide information of the coupling of the top quark with the corresponding bosons at the LHC.

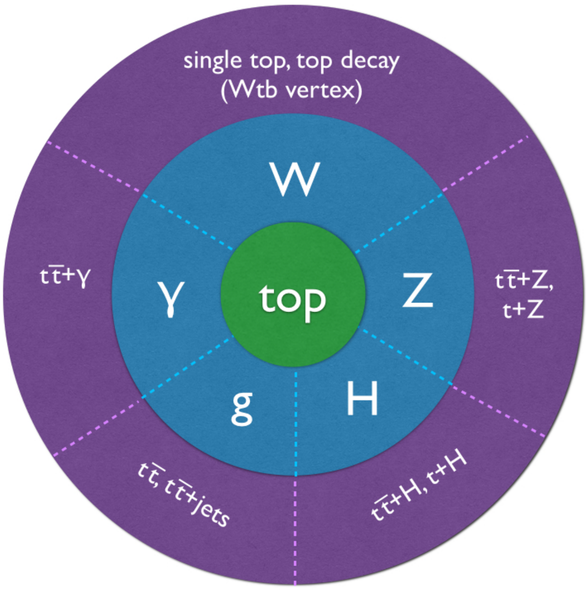

Figure 2.9.: Summary of the different processes involving the top quark coupling to the Z, W, γ, H and g bosons.

Top & W

Experimental information on the coupling of the top quark to the W-boson can be obtained from the top quark decay and from electroweak single top quark production.

- *Top Decay: W polarisation*
  Since the top quark decays almost exclusively to W^+b, the measurement of the W-boson helicity in top quark decays probes the structure of the Wtb vertex, which in the SM is V-A. Since the W-bosons are produced as real particles in top quark decays, their polarisation can be longitudinal, left-handed or right-handed. The fractions with a certain polarisation, F_0, F_L and F_R, can be extracted from measurements of the angular distribution of the decay products of the top quark, given by:
  $$\frac{1}{\sigma}\frac{d\sigma}{d\cos\theta^*} = \frac{3}{4}(1-\cos^2\theta^*)F_0 + \frac{3}{8}(1-\cos\theta^*)^2F_L + \frac{3}{8}(1+\cos\theta^*)^2F_R, \tag{2.33}$$
  where θ^* is defined as the angle between the W-boson momentum in the top quark rest frame and the momentum of the down-type decay fermion in the rest frame of the W-boson.

The next-to-next-to-leading-order (NNLO) QCD prediction for the helicity fractions in the SM, for a top quark mass $m_t = 172.8$ GeV and a b-quark mass $m_b = 4.8$ GeV, are $F_0 = 0.687 \pm 0.005$, $F_L = 0.311 \pm 0.005$ and $F_R = 0.0017 \pm 0.0001$ [59]. Recent measurements of the W-boson helicity fractions have been performed by both CDF and D0 experiments at the Tevatron [60, 61, 62] and by ATLAS and CMS experiments at the LHC [63, 64, 65, 66]. All measurements are in agreement with SM predictions.

- *Top Decay:* R_b
  Under the assumption of a unitary 3×3 CKM matrix, the top quark decays almost exclusively to Wb ($|V_{tb}| \approx 1$). A fourth generation of quarks would accommodate significantly smaller values of $|V_{tb}|$, affecting, for example, the decay rates in the $t\bar{t}$ production channel. Therefore, a measurement of the ratio of branching fractions of the form:

  $$R = \frac{B(t \to Wb)}{B(t \to Wq)} = \frac{|V_{tb}|^2}{|V_{tb}|^2 + |V_{ts}|^2 + |V_{td}|^2}, \tag{2.34}$$

  would test the three generations assumption. A measurement of $|V_{tb}|$ can also be extracted from R by assuming a unitary 3×3 CKM matrix, where $R = |V_{tb}|^2$. The most precise measurement to date of R has been performed by the CMS Collaboration at $\sqrt{s} = 8$ TeV, resulting in an unconstrained measured value of $R = 1.014 \pm 0.003\,(\text{stat.}) \pm 0.032\,(\text{syst.})$, which translates into $|V_{tb}| = 1.007 \pm 0.016\,(\text{stat.+syst.})$ under the three-generation CKM matrix assumption, and a lower limit of $|V_{tb}| > 0.975$ at 95% CL when requiring $|V_{tb}| \leq 1$, all consistent with SM predictions [67].

- *Single Top Production*
  As seen in Figure 2.5, all of the single top quark channels include an interaction between a top quark, a bottom quark, and a W-boson. The strength of this Wtb interaction is given by the CKM matrix element V_{tb}. Observations of single top quark events can thus provide direct measurements of V_{tb} without assuming unitarity, and, at the same time, test for additional structure in the CKM matrix. The most precise measurement to date of V_{tb} has been performed by the CMS experiment, combining the single top quark measurements in the t-channel at $\sqrt{s} = 7$ and 8 TeV. In the approximation $|V_{td}|, |V_{ts}| \ll |V_{tb}|$ and parametrisation of a possible anomalous form factor that could modify the coupling strength as f_{Lv}, the V_{tb} matrix element can be obtained as:

  $$|f_{Lv} V_{tb}| = \sqrt{\frac{\sigma_{t-ch.}}{\sigma_{t-ch.}^{theo.}}}. \tag{2.35}$$

  This relationship yields a combined measured value of: $|f_{Lv} V_{tb}| = 0.998 \pm 0.038\,(\text{exp.}) \pm 0.016\,(\text{theo.})$ [68].

Top & γ

At hadron colliders, a measurement of the $t\gamma$ coupling via $q\bar{q} \to \gamma^* \to t\bar{t}$ is unrealistic due to the overwhelming contribution from the QCD processes $q\bar{q} \to g^* \to t\bar{t}$ and $gg \to t\bar{t}$. Therefore, a more feasible approach to probe the $t\gamma$ coupling is via the measurement of the associated production of a photon with a top quark pair. The photon can be radiated from:

- the top quark: $pp \to t\bar{t}\gamma$, with the top quark decaying without photon radiation, or

- the top quark decay products: $pp \to t\bar{t}$, with a photon radiated from the decay of an on-shell top quark ($t \to Wb\gamma$).

Only events of the first type are sensitive to the $t\gamma$ coupling, and therefore, to the top quark electric charge. However, for a well-defined $t\bar{t}\gamma$ final state, all interferences between both types of processes have to be taken into account. First evidence of the associated production of photon radiation and a top quark pair was announced by the CDF Collaboration at $\sqrt{s} = 1.96$ TeV [69], followed by measurements by the ATLAS Collaboration and CMS Collaboration at $\sqrt{s} = 7$ TeV and 8 TeV, respectively [70, 71]. All measurements are in agreement with SM predictions.

Top & H

One of the important tests of the SM is the measurement of the top quark Yukawa coupling. The coupling of the top quark to the Higgs can be studied from the production rates of the Higgs boson in pp collisions at the LHC. Since gluon-gluon fusion production of the Higgs boson proceeds via loop contributions, the heaviest particles are expected to contribute the most. Therefore, indirect constraints on the top Yukawa coupling can be made from gluon-gluon fusion production of the Higgs boson, as well as from $H \to \gamma\gamma$ decays, where the same loop contributions occur. This, however, assumes no additional heavy particles which could couple to the Higgs boson. The only direct measurement of the top Yukawa coupling at the LHC can be performed in the $t\bar{t}H$ and tH channels, corresponding to the associated production of a top quark pair with a Higgs boson or the production of a single top quark and the Higgs boson, respectively.

The production of the Higgs boson in association with a single top quark, tH, is strongly suppressed with respect to $t\bar{t}H$ production, due to the substantial cancellation between the two diagrams where the Higgs boson is emitted from the top quark or from the W-boson exchanged in the t-channel. Since the resulting cross section is very small, any non-standard physics affecting the cancellation (e.g. change of the sign of the tH coupling) will lead to a much larger cross section, making this process an interesting window to search for new physics.

The measurements of the $t\bar{t}H$ final state are not trivial, since not only it is the Higgs production mechanism with the smallest cross section, but also its signature is quite complicated.

Searches have been performed by both ATLAS and CMS Collaborations in the following channels:

- $t\bar{t}H, H \to \gamma\gamma$, with very small branching ratio (0.2%), with QCD multi-photon/jet final states as main backgrounds. The Higgs boson can be reconstructed in this case as a narrow mass peak.

- $t\bar{t}H, H \to WW/ZZ$, with significant branching ratio (22% for $H \to WW$), with main background contribution from $t\bar{t}Z$ and $t\bar{t}W$ processes, as well as from processes with non-prompt leptons. Leptonic decays of the W- and Z-bosons can give a distinct signature with multiple leptons, which challenges the reconstruction of the Higgs boson.

- $t\bar{t}H, H \to b\bar{b}$, which gives the largest branching ratio of all $t\bar{t}H$ channels (58%), but needs a good understanding of its large main irreducible background, $t\bar{t}$ production in association with extra jets (typically heavy flavour jets). Since the final state involves multiple b-quarks, the reconstruction of the Higgs boson as a peak in the invariant mass spectrum of two b-jets becomes challenging.

Neither experiment observes a significant $t\bar{t}H$ signal so far. The latest limits that have been set by the ATLAS experiment are: in the $t\bar{t}H, H \to b\bar{b}$ final state at $\sqrt{s} = 8$ TeV, the observed (expected) limit for a Higgs boson mass of 125 GeV is 4.1 (2.6) times the SM cross section at 95% CL [72], and in the $t\bar{t}H, H \to \gamma\gamma$ final state at both $\sqrt{s} = 7$ and 8 TeV combined, the observed (expected) limit is 6.7 (4.9) times the SM cross section times the branching ratio BR($H \to \gamma\gamma$) at $m_H = 125.4$ GeV at 95% CL [73]. The CMS experiment combined their results in all three aforementioned $t\bar{t}H$ final states, yielding a combined best-fit signal strength, $\mu = \sigma_{t\bar{t}H}/\sigma^{SM}_{t\bar{t}H}$, assuming an $m_H = 125$ GeV, of $\mu = 2.9^{+1.1}_{-0.9}$. This result corresponds to a 3.5 standard deviation excess over the background-only hypothesis, and represents a 2.1 standard deviation upward fluctuation with respect to the SM $t\bar{t}H$ expectation. This excess is driven by the $t\bar{t}H, H \to WW/ZZ$ channel with two leptons with same-sign charge in the final state, with a best-fit value of $\mu = 5.3^{+2.1}_{-1.8}$ [74].

Further information and references to theoretical calculations of this process can be found in [56].

Top & Z

Similarly to the $t\gamma$ coupling measurement, a measurement of the tZ coupling via $q\bar{q} \to Z^* \to t\bar{t}$ at hadron colliders is hard given the dominance of QCD processes. Instead, the neutral current coupling of the top quark can be directly measured via the associated production of a Z-boson and a top quark pair, $t\bar{t}Z$. This process, together with $t\bar{t}W$, constitute the main topics of this thesis and will be explained in more detail in the following section.

2.4. $t\bar{t}Z/W$ production at the LHC

The first step towards the measurement of the tZ coupling at hadron colliders is the observation of the associated production of a Z-boson and a top quark pair. The representative lowest order diagrams of this process can be seen in Figure 2.10. In the upper part, the $t\bar{t}Z$ process includes the Z-boson as initial state radiation (ISR), i.e. radiated from the incoming quarks, and therefore it does not provide any information about the tZ coupling. In the lower part, the $t\bar{t}Z$ processes include the Z-boson as final state radiation (FSR), i.e. radiated from the top quark, thus being sensitive to the weak neutral current top coupling (the $t\bar{t}Z$ vertex is marked with a red dot).

In analogy with the $t\bar{t}\gamma$ processes, an off-shell Z can also be radiated from the top quark decay products, although this contribution is expected to be negligible.

Several calculations of the inclusive cross section of $t\bar{t}Z$ in pp collisions at $\sqrt{s} = 7$ and 8 TeV in next-to-leading order (NLO) QCD are available. In contrast to the $t\bar{t}Z$ production at leading order QCD, which can only occur through gluon fusion (gg) and quark-antiquark annihilation ($q\bar{q}$), at NLO QCD, real emission corrections allow for production modes via qg and $\bar{q}g$ [75]. The latest calculations at NLO accuracy in QCD use PowHel, an event generator relying on the POWHEG-BOX [76, 77, 78] computer framework. The input matrix elements are computed with the HELAC-NLO [79] package. Both renormalisation and factorisation scales are fixed to $\mu_0 = m_t + m_Z/2$. The NLO QCD prediction at $\sqrt{s} = 8$ TeV is:

$$\sigma^{t\bar{t}Z}_{NLO} = 205.7\ ^{+9\%}_{-13\%}(\text{scale})\ \text{fb}, \tag{2.36}$$

where the scale dependence uncertainty is calculated in the range $[\mu_0/2, 2\mu_0]$, with μ_0 as the central value [80].

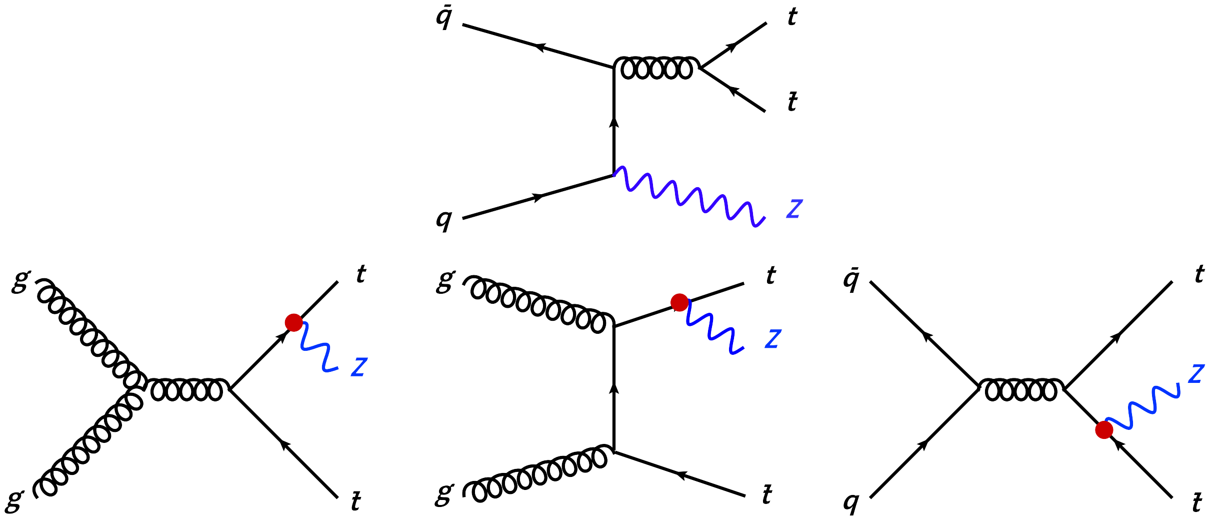

Figure 2.10.: Examples of leading order diagrams of the $t\bar{t}Z$ process at hadron colliders, where the Z-boson is radiated either from (bottom): the top quark, or from (top): the incoming quarks. Similar diagrams can be obtained when radiating the Z-boson from the other fermions in each diagram. The red dot indicates the $t\bar{t}Z$ vertex.

The $t\bar{t}W^+$ and $t\bar{t}W^-$ processes (denoted in the remainder as $t\bar{t}W$) are also the subject of study in this thesis. In contrast to $t\bar{t}Z$, the associated W-boson in $t\bar{t}W$ does not couple to the top quark, but is radiated from the incoming quarks (ISR process), as can be seen in Figure 2.11. The ISR processes are similar for $t\bar{t}Z$ and $t\bar{t}W$, and therefore, the understanding of the $t\bar{t}W$ production could be useful to disentangle the ISR from the FSR contribution in the $t\bar{t}Z$ processes. Moreover, the $t\bar{t}W$ process is an important (and sometimes irreducible) background for other searches, such as $t\bar{t}H$ in the same-sign dilepton channel. Therefore, the understanding and measurement of this process has high priority in order to be able to distinguish it from other signatures.

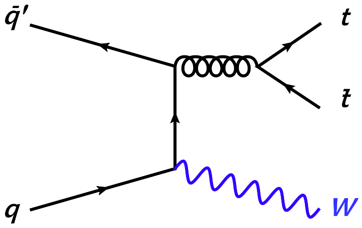

Figure 2.11.: Leading order diagram of the $t\bar{t}W$ process at hadron colliders. A similar diagram can be obtained when radiating the W-boson from the incoming antiquark.

The rates for $t\bar{t}W^+$ and $t\bar{t}W^-$ are not equal at a pp collider, as can be seen in Figure 2.12. The cross section of $t\bar{t}W^+$ is larger than $t\bar{t}W^-$ due to the different PDFs of the “up” and “down” quarks within the incoming protons at the LHC (more details on the charge asymmetry of the W-boson production in pp collisions are given in Section 10.4). Another interesting feature is the smaller increase in cross section with higher centre-of-mass energy of $t\bar{t}W$, compared to $t\bar{t}Z$ or $t\bar{t}H$. This can be understood with the relative decrease of quark-antiquark annihilation initiated $t\bar{t}$ processes with respect to the gluon fusion initiated ones towards higher centre-of-mass energies and the fact that $t\bar{t}W$ production occurs via quark-antiquark annihilation at lowest order QCD.

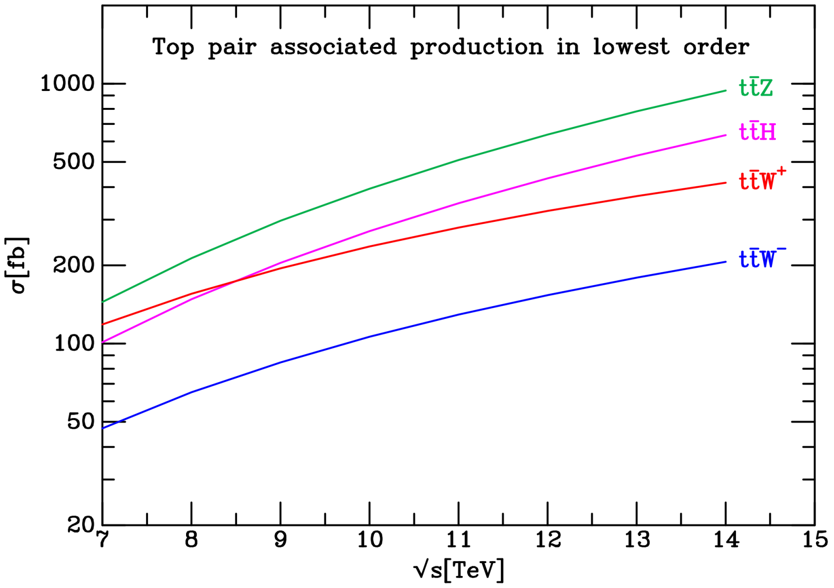

Figure 2.12.: Lowest order cross sections for the $t\bar{t}Z$, $t\bar{t}W^{\pm}$ and $t\bar{t}H$ at pp collider, as a function of the centre-of-mass energy, with $\mu_r = \mu_f = m_t$ and $m_H = 125$ GeV for $t\bar{t}H$ [81].

The NLO QCD calculation of $t\bar{t}W$ used in the main result of this thesis is derived using the MCFM [55] parton-level Monte Carlo program. Both renormalisation and factorisation scales are fixed to $\mu_0 = m_t$. The NLO QCD predictions for $t\bar{t}W^{\pm}$ at $\sqrt{s} = 8$ TeV are [81]:

$$\sigma_{NLO}^{t\bar{t}W^+} = 161 \; {}^{+12\%}_{-20\%}(\text{scale}) \; {}^{+7\%}_{-8\%}(\text{PDF} + \alpha_S) \text{ fb}, \text{ and} \tag{2.37}$$

$$\sigma_{NLO}^{t\bar{t}W^-} = 71 \; {}^{+16\%}_{-21\%}(\text{scale}) \; {}^{+6\%}_{-8\%}(\text{PDF} + \alpha_S) \text{ fb}, \tag{2.38}$$

where the scale dependence uncertainty is calculated in the range $[\mu_0/4, 4\mu_0]$, with μ_0 as the central value, and the PDF uncertainty originates from the PDF fitting procedure [14], including also the 90% confidence-level uncertainty on $\alpha_S(M_Z)$.

Although in Reference [80], a NLO QCD calculation for $t\bar{t}W$ is also provided, PDF variations are not quoted and the scale variation range is less conservative than in Reference [81]. The reference value for the $t\bar{t}W$ cross section is taken to be 232 fb from Reference [81]. Since the relative scale uncertainties are of the same size for $t\bar{t}W$ and $t\bar{t}Z$ in Reference [80], the same relative uncertainties are used for both processes. Taking the largest uncertainty symmetrised per variation from Reference [81], a total theoretical uncertainty of 22% [15] is assigned to both $t\bar{t}W$ and $t\bar{t}Z$ cross sections in the main result of this thesis.

2.4.1. Previous experimental measurements of $t\bar{t}Z/W$

The first measurements of the $t\bar{t}Z/W$ processes were performed by the ATLAS and CMS Collaborations at $\sqrt{s} = 7$ TeV using the full data set, corresponding to an integrated luminosity of 4.7 fb^{-1} and 5.0 fb^{-1}, respectively. The ATLAS measurement searched for the $t\bar{t}Z$ process in final states with three leptons, setting an upper limit on the $t\bar{t}Z$ cross section of $\sigma_{t\bar{t}Z} <$

---

[14] For NLO QCD calculations the corresponding NLO PDF fit is used.

[15] Adding in quadrature the largest uncertainty for scale dependence and for PDF+α_S.

0.71 pb at 95% CL [82]. The CMS Collaboration measured the $t\bar{t}Z$ and $t\bar{t}V$, combined $t\bar{t}Z$ and $t\bar{t}W$, cross sections in final states with three leptons and with two leptons of same-sign electric charge, respectively, resulting in: $\sigma_{t\bar{t}Z} = 0.28^{+0.14}_{-0.11}\,(\text{stat.})^{+0.06}_{-0.03}\,(\text{syst.})$ pb, and $\sigma_{t\bar{t}V} = 0.43^{+0.17}_{-0.15}\,(\text{stat.})^{+0.09}_{-0.07}\,(\text{syst.})$ pb. These measurements have an observed significance of 3.3 and 3.0 standard deviations from the background-only hypothesis, respectively, providing first evidence of the $t\bar{t}Z$ process. The measured cross sections are compatible within uncertainties with the corresponding NLO QCD predictions of $\sigma_{t\bar{t}Z} = 0.137^{+0.012}_{-0.016}$ pb and $\sigma_{t\bar{t}V} = 0.306^{+0.031}_{-0.053}$ pb [83].

The CMS collaboration also performed a measurement of $t\bar{t}Z$, $t\bar{t}W$ and $t\bar{t}V$ at $\sqrt{s} = 8$ TeV using the full data set corresponding to an integrated luminosity of 19.5 fb^{-1}. A combination of channels with final states with three leptons and four leptons is performed for the $t\bar{t}Z$ cross section measurement, resulting in: $\sigma_{t\bar{t}Z} = 200^{+80}_{-70}\,(\text{stat.})^{+40}_{-30}\,(\text{syst.})$ fb. Final states with two leptons of same-sign electric charge are used for the $t\bar{t}W$ cross section measurement, obtaining: $\sigma_{t\bar{t}W} = 170^{+90}_{-80}\,(\text{stat.}) \pm 70\,(\text{syst.})$ fb. These measurements have an observed significance of 3.1 and 1.6 standard deviations from the background-only hypothesis, respectively. Combining all channels, the inclusive $t\bar{t}V$ process is measured with an observed significance of 3.7 standard deviations from the background-only hypothesis. Besides the measurements of each process individually, a simultaneous measurement of $t\bar{t}Z$ and $t\bar{t}W$ is also performed [84]. The measured cross sections are compatible with the NLO QCD predictions within uncertainties.

The ATLAS measurement at $\sqrt{s} = 8$ TeV is the core of this thesis, in particular the measurement of $t\bar{t}Z$, $t\bar{t}W$ and $t\bar{t}V$ in the final states with two oppositely-charged leptons, and will be covered in the following chapters.

2.5. Neutral current top coupling beyond the SM

As was previously mentioned in Section 2.4, the associated production of a top pair and a Z-boson is a direct probe of the tZ coupling. Indirect probes from LEP measurements of the ρ-parameter [16] [85], and the $Z \to b\bar{b}$ branching ratio [86], closely related to the parameters ϵ_1 and ϵ_b [17], set indirect constraints on the tZ vector and axial vector couplings [75].

Based on the Z-boson vertex factor in Equation 2.12, the $t\bar{t}Z$ interaction Lagrangian in the SM can be expressed as:

$$\mathcal{L}^{SM}_{t\bar{t}Z} = ie\bar{u}(p_t)[\gamma^\mu(c^{SM}_V + \gamma_5 c^{SM}_A)]v(p_{\bar{t}})Z_\mu, \tag{2.39}$$

with e being the electromagnetic coupling constant. c^{SM}_V and c^{SM}_A are the vector and axial vector couplings, respectively, and are defined as:

$$C^{SM}_V = \frac{I^3_t - 2Q_t \sin^2\theta_W}{2\sin\theta_W\cos\theta_W} \quad \text{and} \quad C^{SM}_A = \frac{-I^3_t}{2\sin\theta_W\cos\theta_W}, \tag{2.40}$$

where I^3_t and Q_t are the third component of the weak isospin and the electric charge of the top quark, respectively.

The numerical values for the SM couplings are $C^{SM}_V \simeq 0.244$ and $C^{SM}_A \simeq -0.601$.

---

[16] The ρ-parameter describes the ratio of the electroweak neutral to charged current couplings in neutrino interactions at low momentum transfer.

[17] The parameters $\epsilon_1, \epsilon_2, \epsilon_3, \epsilon_b$ were introduced to allow for a fully model-independent analysis of the electroweak precision observables, in the absence of experimental information on the Higgs sector [87, 88, 89].

New physics affecting the tZ coupling can be represented by the following effective Lagrangian [90]:

$$\mathcal{L}_{t\bar{t}Z}^{SM} = ie\bar{u}(p_t)\left[\gamma^\mu(C_{1,V}+\gamma_5 C_{1,A}) + \frac{i\sigma_{\mu\nu}q_\nu}{m_Z(C_{2,V}+i\gamma_5 C_{2,A})}\right]v(p_{\bar{t}})Z_\mu, \tag{2.41}$$

with $\sigma_{\mu\nu} = \frac{i}{2}[\gamma_\mu, \gamma_\nu]$ and $q_\nu = (p_t - p_{\bar{t}})_\nu$. The four anomalous couplings, $C_{1,V/A}$ and $C_{2,V/A}$, correspond to the vector and axial vector couplings, and the weak magnetic and electric dipole moments of the top quark, respectively.

The couplings $C_{1,V/A}$ can be expressed as the SM terms plus contributions due to higher dimensional operators:

$$C_{1,V} = C_{1,V}^{SM} + (\frac{v^2}{\Lambda^2})\Re[C_{\phi q}^{(3,33)} - C_{\phi q}^{(1,33)} - C_{\phi u}^{33}], \text{ and} \tag{2.42}$$

$$C_{1,A} = C_{1,A}^{SM} + (\frac{v^2}{\Lambda^2})\Re[C_{\phi q}^{(3,33)} - C_{\phi q}^{(1,33)} + C_{\phi u}^{33}]. \tag{2.43}$$

Since any new fermion which couples to the third generation quarks might induce deviations from the tZ SM couplings, the associated production of a top pair and Z-boson opens an avenue to search for new physics in the top quark sector. Studying the potential of the LHC experiments to constrain non-standard tZ couplings is therefore crucial. Previous studies have been performed at leading order in [58], [91] and [92], the limiting factor to stronger constraints on the tZ coupling being the large residual scale uncertainty on the $t\bar{t}Z$ cross section [58]. The latest study has been performed with NLO QCD calculations for $t\bar{t}Z$ production, accounting for NLO QCD spin correlation in the decay of the top quarks and hadronically decaying W-bosons, as well as in leptonically decaying Z-boson [75]. Including spin correlations is crucial since an observable sensitive to the vector and axial vector tZ couplings is the leptonic opening angle, $\Delta\Phi(ll)$, from $Z \to l^+l^-$, as already discussed in Reference [58]. The first direct constraints on possible effects of physics beyond the SM affecting the tZ couplings at the LHC were set using the $t\bar{t}Z$ cross section measurement at $\sqrt{s} = 7$ TeV by the CMS collaboration [83]. Furthermore, projected constraints were placed on the operators $C_{\phi q}^{(3,33)}$ and $C_{\phi u}^{33}$ [18] at the $\sqrt{s} = 13$ TeV LHC using the $\Delta\Phi(ll)$ distribution in $t\bar{t}Z$ production. Figure 2.13 shows the latter constraints for the integrated luminosities of 300 fb^{-1} and 3000 fb^{-1}, overlaid with the above mentioned indirect constraints from LEP measurements, updated to account for $m_H = 125.6$ GeV, as measured by the CMS collaboration [93]. It is clear from the figure that electroweak precision observables put much stronger constraints on the tZ coupling than the ones expected from future measurements of the process $pp \to t\bar{t}Z$ at the LHC, but only the latter will allow to set direct limits for the first time.

The tZ coupling can also be directly probed through the associated production of a single top and a Z-boson. Furthermore, the cross section of the $t\bar{t}Z$ production is comparable to that of the sum of tZ and $\bar{t}Z$ production at the LHC [94], as can be seen in Figure 2.14, offering an additional path to constrain the tZ coupling in the second run of the LHC.

Additionally, a precise measurement of the tZ coupling would provide the possibility to measure for the first time, assuming the SM weak neutral current vertex, the third component of the weak isospin of the top quark, I_t^3, thus experimentally confirming that the top quark is indeed the weak isospin partner of the bottom quark. The third component of the weak isospin

---

[18] Given the excellent agreement between experiment and prediction for the $Zb_L\bar{b}_L$ couplings and the $SU(2)_L$ symmetry of the SM, it can be shown that $C_{\phi q}^{(3,33)} \approx -C_{\phi q}^{(1,33)}$, and the operator $C_{\phi q}^{(1,33)}$ is thus eliminated from the study in [75].

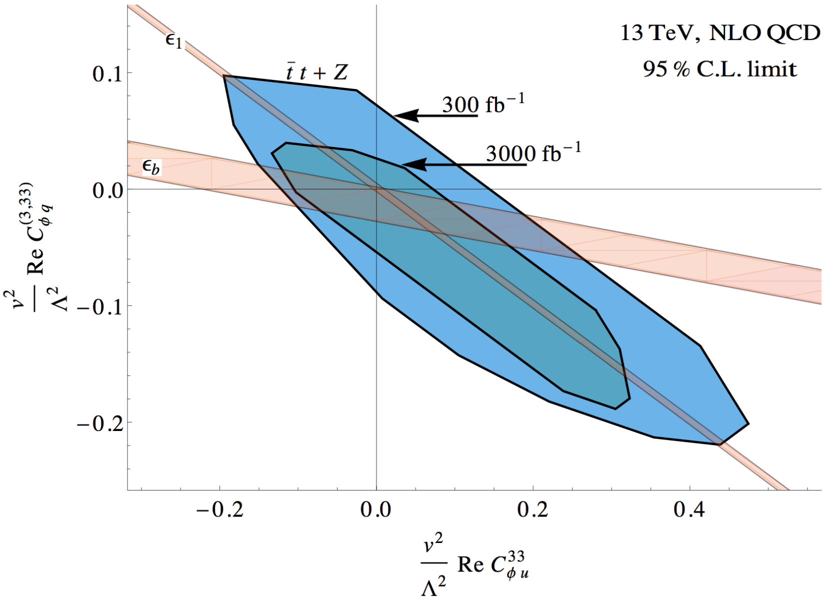

Figure 2.13.: Constraints on the operators $C_{\phi q}^{(3,33)}$ and $C_{\phi u}^{33}$ at the future $\sqrt{s} = 13$ TeV LHC. The parameter space outside the blue coloured area can be excluded at 95% C.L. The overlaid thin bands are indirect constraints from the electroweak precision observables, ϵ_1 and ϵ_b [75].

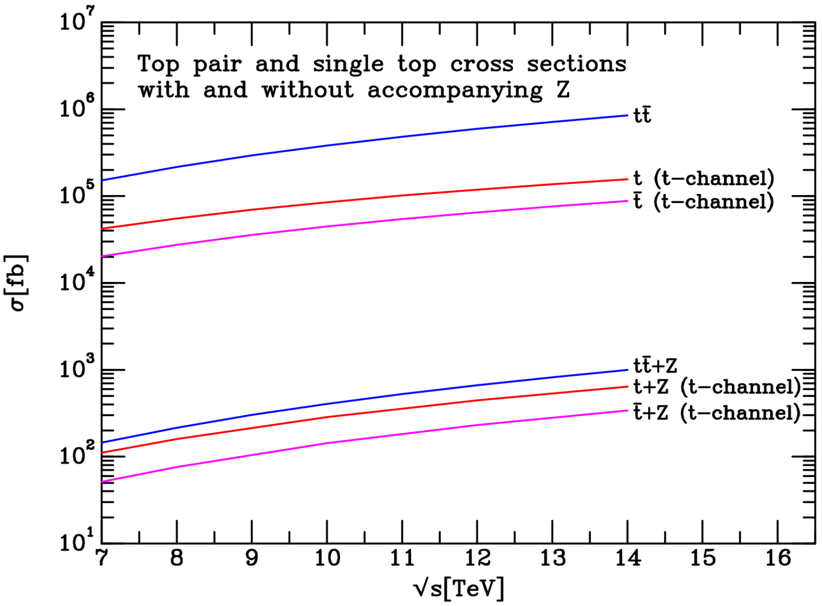

Figure 2.14.: NLO inclusive cross sections for single top quark and top quark pair production, with and without an associated Z-boson, as a function of the centre-of-mass energy [94].

of the b-quark was already obtained from earlier measurements of the partial width $\Gamma_{b\bar{b}}$ and the forward-backward asymmetry A_{FB} at LEP, SLC and low energy experiments [37].

At a future high energy e^+e^- machine, the tZ coupling measurement will be possible via the process $e^+e^- \to \gamma^*/Z \to t\bar{t}$. However, this process is sensitive to both $t\gamma$ and tZ couplings, and significant cancellations between the various couplings have to be considered [58].

CHAPTER 3

Experimental Setup

3.1. The LHC

The Large Hadron Collider (LHC) [95, 96, 97] at CERN is the world's largest and most powerful particle accelerator to date and is the machine that made possible the measurements presented in this thesis. It is a circular *pp* collider located close to Geneva, Switzerland, in the same 27 km circumference tunnel originally built for its predecessor collider, the Large Electron-Positron (e^+e^-) collider (LEP) [98], which operated from the year 1989 to 2000. In addition to protons, the LHC can also collide heavy ions, hence the term "Hadron" in the name. The tunnel lies approximately 100 m underground [1]. The LHC is the last element of the accelerator complex chain at CERN, which is sketched in Figure 3.1. Each of the other pre-accelerators of the complex injects the particle beam into the next accelerator in the chain, which brings the beam to an even higher energy. In this way, the particles are increasingly accelerated at each stage of the accelerator complex before they reach the main accelerator ring, the LHC. The starting point is a bottle containing hydrogen gas, from where protons are obtained via ionisation of these atoms, and accelerated to 50 MeV in the first accelerator of the complex, the linear accelerator LINAC2. The protons are then injected into the PS Booster (PSB) and accelerated to 1.4 GeV. The next accelerator in the line, the Proton Synchrotron (PS), accelerates the protons to 25 GeV. The Super Proton Synchrotron (SPS) takes over and brings the protons to an energy of 450 GeV. With this energy, protons are injected into two transfer lines of the LHC, resulting in two proton beams travelling in opposite directions inside the LHC beam pipes. These two pipes are kept at ultrahigh vacuum. After accelerating up to the final energy, proton beams are brought to collision at four interaction points along the LHC ring. In the first run of the LHC, this final energy corresponded to 3.5 TeV during the year 2010-2011 (resulting in a centre-of-mass energy of $\sqrt{s} = 7$ TeV) and 4 TeV in 2012 (resulting in a centre-of-mass energy of $\sqrt{s} = 8$ TeV). During the second run, it is expected to reach the designed centre-of-mass energy of $\sqrt{s} = 14$ TeV. Each crossing point is surrounded by a particle detector, marked with a yellow dot in Figure 3.1. These four experiments are ATLAS [99], CMS [100], ALICE [101], and LHCb [102]. The data used for the results in this thesis were collected by the ATLAS experiment, which will be explained in more detail in Section 3.2. CMS

---

[1] Its depth varies between 175 m (under the Jura) and 50 m (towards lake Geneva).

(Compact Muon Solenoid), as well as ATLAS, is a general-purpose detector aiming to cover a wide range of physics, from precision measurements to searches for new physics. Although the scientific goals of CMS are similar to those of ATLAS, it has different technical solutions and design, providing complementary results, such as for the recent Higgs discovery announced on the 4th of July 2012 [35, 36]. LHCb (Large Hadron Collider beauty), on the other hand, concentrates on b-physics to investigate the differences between matter and antimatter. Finally, ALICE (A Large Ion Collider Experiment), studies the physics of strongly interacting matter at extreme energy densities, when matter is in a quark-gluon plasma phase, occurring in heavy ion collisions.

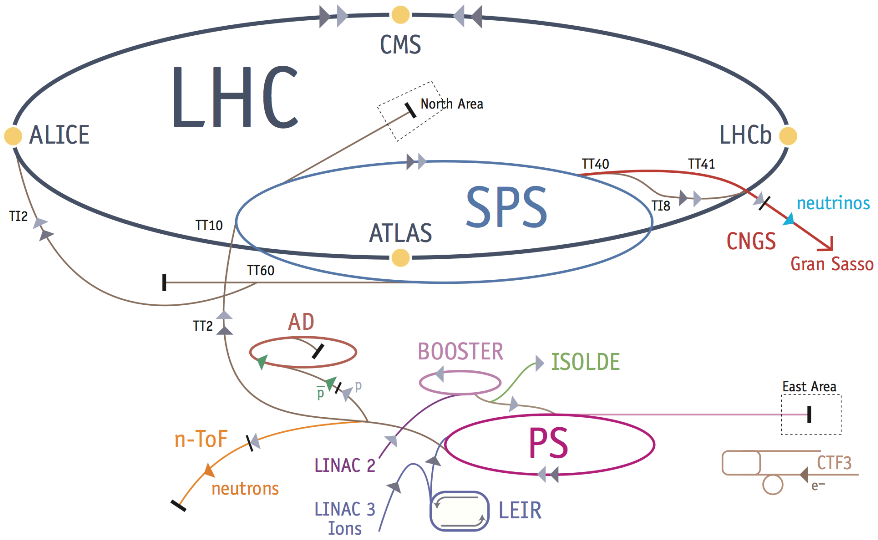

Figure 3.1.: The CERN accelerator complex [103].

For the acceleration of charged particles, radio-frequency (RF) cavities are used, supplied with an oscillating electromagnetic field. Therefore, depending on the timing of arrival of the particles, each of them will be accelerated or decelerated, resulting in a particle beam discretised in packages called *bunches*. Each proton bunch contains about 10^{11} particles. The LHC is designed to circulate up to 2808 bunches with a bunch spacing of 25 ns, being able to achieve an instantaneous luminosity [2] $\mathcal{L} = 10^{34}$ cm^{-2}s^{-1}. In 2011 and 2012, during the first LHC run, a bunch spacing of 50 ns was used for the largest part of data taking, reaching 1380 particle bunches circulating the LHC ring - the maximum number of bunches for such bunch spacing [104]. The 16 RF cavities of the LHC are located in four cylindrical refrigerators which keep the RF cavities working in a superconducting state, without losing energy to electrical resistance.

In order to guide the particles around the LHC accelerator ring, superconducting magnets are needed. Dipole magnets are used to bend the particles' trajectory, making them follow the circular ring. There are 1232 main dipoles at the LHC, each 15 m long and generating 8.4 T powerful magnetic fields. In order to increase the probability of the particles to collide when they reach the collision points, quadropole magnets help to keep the particles in a tight beam, by squeezing the beam either vertically or horizontally. Furthermore, sextupole, octupole and decapole magnets are also needed to correct for small imperfections in the magnetic field at the extremities of the dipoles, stabilising the beams.

---

[2] Number of interactions per second and unit area.

3.2. The ATLAS detector

The ATLAS (A Toroidal LHC ApparatuS) [99] detector is the largest-volume-collider-detector ever constructed (44 m in length and 25 m in height). It sits in a cavern underground near the main CERN site, located in one of the four interaction points in the LHC ring.

The unprecedented high energy and luminosity of the LHC, implying higher interaction rates, radiation doses, particle multiplicities and energies, have set new standards for the design of particle detectors. Requirements for the ATLAS detector have also been defined to cover a wide range of signatures from possible new physics phenomena which could appear at the TeV scale, and to allow precise measurements of SM parameters. For instance, the search for the SM Higgs boson in different production and decay mechanisms has been used as a benchmark to establish the performance of the various subsystems of the ATLAS detector.

Given the expected small cross-sections of interesting processes predicted by the SM or by new physics models, the large LHC luminosity, and hence the large interaction rate, is needed for a large number of candidate events from such processes. The number of collected events, N, from a certain physics process relates to the corresponding cross-section, σ, and to the integrated luminosity, $L = \int \mathcal{L} dt$, as: $N = \sigma \cdot L$. The integrated luminosity is usually expressed in inverse pico or femto-*barns*, corresponding, for instance, to $\mathrm{fb}^{-1} = 10^{39}$ cm^{-2}.

Furthermore, in *pp* collisions, QCD jet production cross-sections dominate over the interesting rare processes, requiring a good performance of the detector in identifying characteristic experimental signatures of these physics process, such as missing transverse energy [3] (E_T^{miss}), charged leptons with high transverse momentum, photons, and secondary vertices (for offline tagging of τ leptons and b-jets).

The anatomy of the ATLAS detector is sketched in Figure 3.2. Each subsystem of the ATLAS detector is disposed around the interaction point in a similar manner as the layer structure of an onion. The system of magnets includes a thin superconducting solenoid surrounding the inner detector, and three large superconducting toroids (one barrel and two end-caps) arranged around the calorimeters. The design of each subdetector is oriented to the identification of different types of particles, as can be seen in Figure 3.3. The only SM particle that travels through the detector without leaving a trace is the neutrino, whose presence can be inferred from the E_T^{miss} in the event.

In the following subsections, a more detailed description of each subdetector will be presented, as well as the trigger systems needed to handle the high interaction rate.

3.2.1. Detector coordinates and nomenclature

The origin of the coordinate system is located in the nominal interaction point. The beam direction defines the z-axis and the $x-y$ plane is transverse to the beam direction. The positive x-axis is defined as pointing from the interaction point to the centre of the LHC ring and the positive y-axis is defined as pointing upwards.

Given the symmetry of the ATLAS detector, a cylindrical coordinate system is more adequate than the cartesian one. The azimuthal angle ϕ is the angle in the xy-plane measured around the beam axis, counting positive clockwise and negative counterclockwise. Instead of the polar angle θ, defined as the opening angle to the z-axis, the pseudorapidity η is often used, defined

---

[3] Energy imbalance in the transverse plane of the detector.

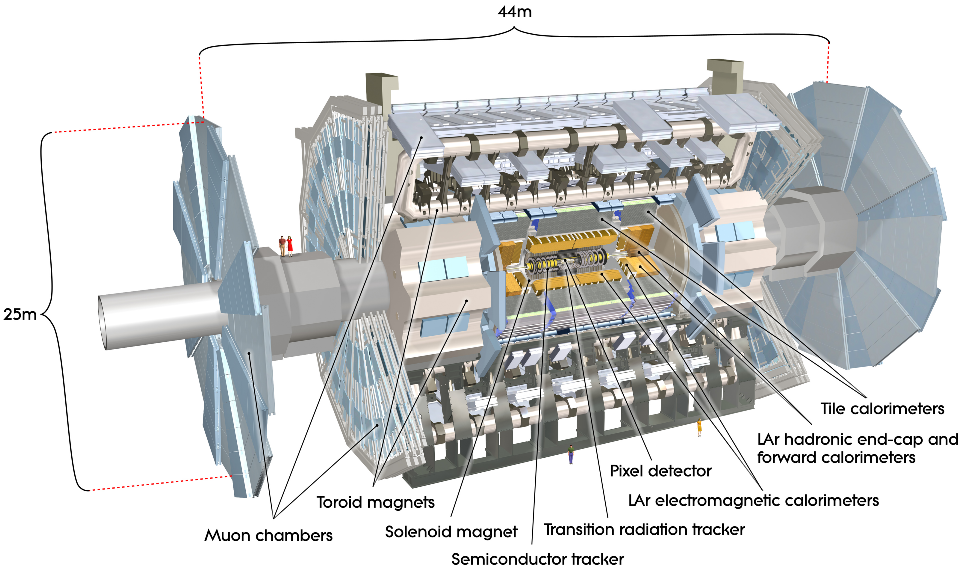

Figure 3.2.: Schematic view of the ATLAS detector and its subsystems [105].

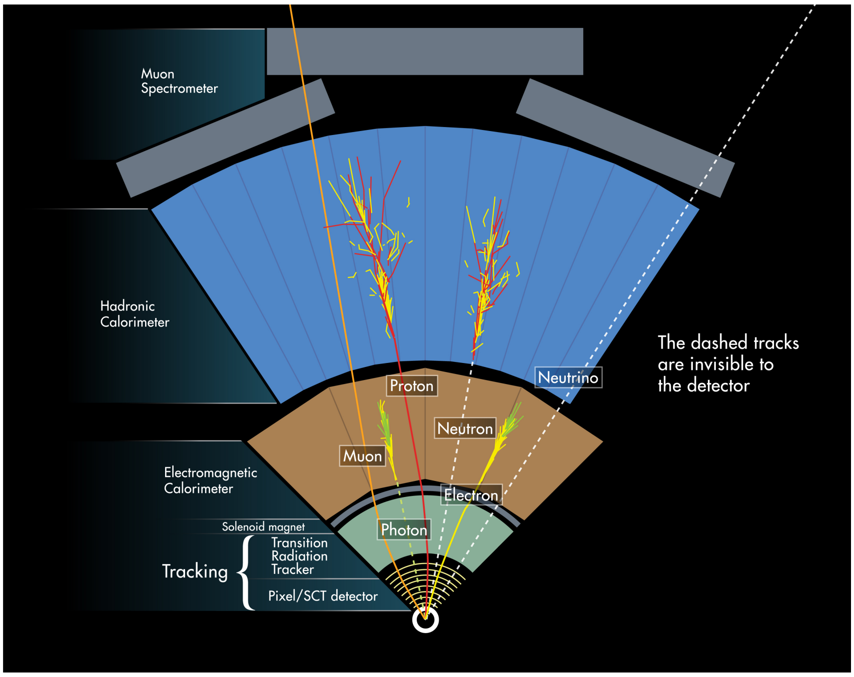

Figure 3.3.: Sketch of the transversal view of the ATLAS detector and its subsystems, showing how particles interact with each subdetector [105].

as:

$$\eta = -\ln \tan \frac{\theta}{2}. \tag{3.1}$$

It is an approximation of the rapidity $y = \frac{1}{2}\ln\left[\frac{E+p_z}{E-p_z}\right]$, valid for particles with very small masses. The pseudorapidity is very useful in the context of experimental particle physics, since the particle production is approximately constant as a function of η. Moreover, the distance $\Delta\eta$ is invariant under Lorentz boosts along the beam axis.

Therefore, the cylindrical coordinate system used is given by (ϕ, η, z). In this coordinate system, distances between two objects are given by $\Delta R = \sqrt{\Delta\eta^2 + \Delta\phi^2}$. The transverse momentum p_T, the transverse energy E_T and the missing transverse energy E_T^{miss} are defined in the $x - y$ plane.

3.2.2. The Inner tracking detectors

The ATLAS inner detector, the closest one to the interaction point, consists of three subsystems: the pixel detector, the semiconductor tracker (SCT), and the transition radiation tracker (TRT), as shown in Figure 3.4. It is contained within a cylindrical envelope of length 3.5 m and radius 1.15 m, within a solenoidal magnetic field of 2 T, which bends the trajectory of the charged particles passing through the inner detector. The goals of the inner detector are pattern recognition, track momentum and vertex measurements with high resolution, as well as electron identification. At the inner part of the tracking volume, high-resolution pattern recognition is possible using discrete space-points from silicon pixel layers and stereo pairs of silicon microstrip (SCT) layers. At the outermost part, straw-tube tracking detectors have the capability to generate and detect transition radiation. To prevent a decrease in efficiency due to energy loss of the tracks in the detector, the total detector material had to be as low as possible while keeping it robust and rigid.

Since the solenoid magnet deflects charged particles mostly in the xy-plane, the inner detector is designed to have the highest precision in the transverse plane, with a resolution goal on the transverse momentum of $\sigma_{p_T}/p_T = 0.05\% p_T[\text{GeV}] \oplus 1\%$.

Given the high-radiation environment, and in order to maintain an adequate noise performance after radiation damage, the silicon sensors must be kept at low temperatures (approximately -5 to -10°C) implying coolant temperatures of ≈ -25°C. In contrast, the TRT is designed to operate at room temperature.

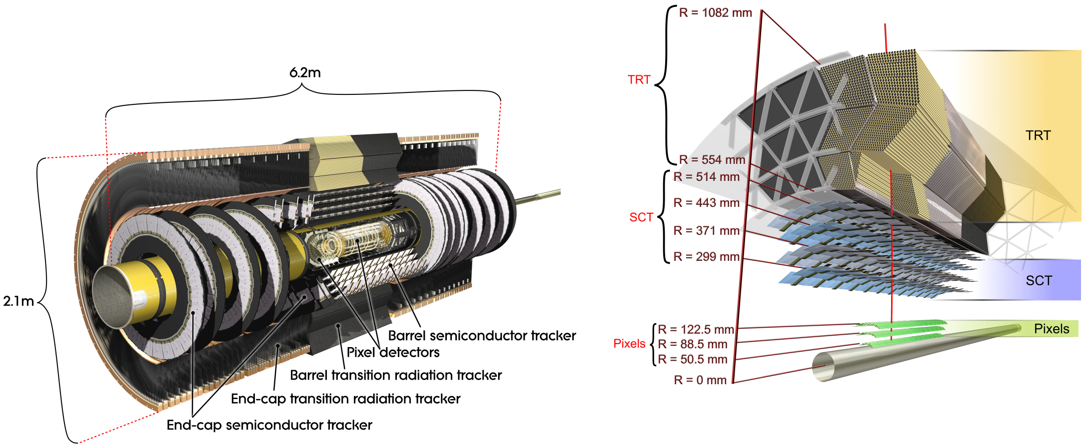

Figure 3.4.: Schematic view of the ATLAS inner detector [105].

The precision tracking detector (pixels and SCT) provides coverage up to $|\eta| = 2.5$, given the increasing radiation damage at higher values of $|\eta|$, while the TRT is able to cover up to $|\eta| = 2.0$.

The pixel detector is the innermost subsystem, and with its high granularity, it aims to provide a high precision measurement of the impact parameter of a track. It is made of three concentric cylinders (barrel layers) and three disks in each endcap, perpendicular to the beam axis. It contains 1744 identical sensors, each consisting of a segmented silicon wafer with pixels of minimum size $50 \times 400\ \mu\text{m}^2$ and 46080 readout channels. The pixel detector uses a charge depleted layer of silicon to measure the charge deposition caused by the ionisation of a charged particle transversing the pixel.

Before the energy and luminosity upgrade of the LHC in 2015, an upgrade of the ATLAS pixel detector is needed in order to avoid degradation of the ATLAS performance in tracking, vertex reconstruction and b-tagging due to the high number of interactions per bunch-crossing, the so called *pile-up*. Therefore, as part of the planned detector upgrades during the long shutdown of the LHC that started in 2013, a new layer closest to the beam pipe has been recently put in place, the so called *insertable B-layer* or IBL. It is located between the existing pixel detector and a new smaller radius beam pipe at a radius of only 3.3 cm. Faster read-out chips and two different silicon sensor technologies (thin planar sensors and 3D double sided sensors) were developed for IBL, in order to cope with high radiation and higher particle occupancy because of its proximity to the interaction point in the beam pipe [106, 107].

The SCT detector surrounds the pixel detector and consists of four layers in the barrel and nine disks in each endcap. Since the particle density at this stage is lower than at the pixel detector, silicon strips are used instead of pixels to reduce the number of readout channels. A strip pitch of 80 μm was chosen for the rectangular barrel sensors and radial strips of constant azimuth with a mean pitch of $\approx 80\ \mu$m were chosen for the trapezoidal end-cap sensors. Modules are arranged back-to-back with a small stereo angle of 40 mrad to allow for a measurement of the azimuth angle in each layer.

The outermost subsystem of the inner detector, the TRT detector, is a straw-tube tracker. It consists of drift tubes with a diameter of 4 mm that are made from wound Kapton and reinforced with thin carbon fibres. In the centre of each tube there is a gold-plated tungsten wire with a 31 μm diameter. The tubes are filled with a gas mixture of 70% Xe, 27% CO_2, and 3% O_2. The TRT barrel region contains 52544 straw tubes of 1.5 m length, parallel to the beam axis, while the endcaps contain radial 0.4 m long straws that are arranged perpendicularly to the beam axis. When a charged particle passes through the TRT, it ionises the gas inside the straws. The resulting free electrons drift towards the wire, where they are amplified and read out. Furthermore, the spaces between the straws are filled with polymer fibres (barrel) and foils (endcaps) to create transition radiation, which may be emitted by highly relativistic charged particles as they traverse a material boundary. This is especially true for electrons, since this effect depends on the relativistic factor $\gamma = E/m$. Therefore, this effect can be used for particle identification. The design of the TRT makes it complementary to the silicon-based tracking subsystems: although the intrinsic single-point resolution of 120 μm is approximately 10 times worse than that of the silicon trackers, this is compensated by the large number of hits per track (typically more than 30, compared to 3 for pixels of 4 - 9 for the SCT detector) and the long lever arm. Furthermore, the high sampling frequency of the wire signals enables the TRT to provide timing information on the nanosecond level [108].

3.2.3. The Calorimeters

The ATLAS Calorimeter system consists of electromagnetic (EM) and hadronic calorimeters, as shown in Figure 3.5. All calorimeters are sampling calorimeters, i.e. they are a sequence of alternating layers of dense absorber material and active material, where only the latter is used for energy measurements. Calorimeters allow for the generation and containment of electromagnetic and hadronic showers, avoiding a punch-through into the muon system. In that sense, calorimetry is based on a *destructive* method: the energy and the particles get absorbed. Therefore, the optimal absorber materials in electromagnetic calorimeters are usually chosen with high atomic number Z, so that the radiation length [4], X_0, is small enough to contain the electromagnetic shower in a realistic calorimeter depth. In the case of the hadronic calorimeter, the characteristic absorption length is the nuclear interaction length λ, describing the interaction of pions and kaons with the material. For high-Z materials, the interaction length is much longer than the electromagnetic one, i.e. hadronic showers start later and are more diffuse.

The calorimeters cover a wide range, $|\eta| < 4.9$. Over the same η region as the inner detector, the fine granularity of the EM calorimeter allows for precision measurements of electrons and photons.

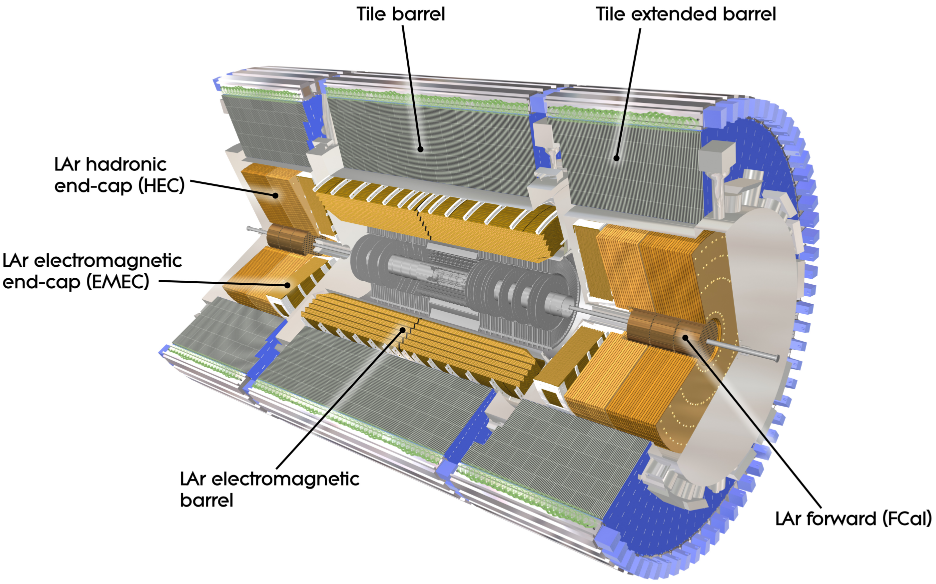

Figure 3.5.: Schematic view of the ATLAS calorimeter system, showing the different electromagnetic and hadronic calorimeters [105].

The Electromagnetic Calorimeter

The EM calorimeter consists of two identical half-barrels, separated by a small gap of 4 mm at $z = 0$, covering up to $|\eta| < 1.475$, and two endcap components, divided into two coaxial wheels each covering the region $1.375 < |\eta| < 2.5$ and $2.5 < |\eta| < 3.2$. It is a lead - LAr (liquid Argon) detector with accordion-shaped kapton electrodes and lead plates used as absorbers. The thickness of the later has been optimised as a function of η to improve the EM calorimeter performance in energy resolution, which is given by $\sigma_E/E = 10\%/\sqrt{E[\text{GeV}]} \oplus 0.7\%$. The accordion shape provides continuous coverage in azimuth and enables fast readout. In the region used for precision physics ($|\eta| < 2.5$), the EM calorimeter is segmented in three sections in depth, for a precise determination of the position of the showers, while for $|\eta| > 2.5$, the wheel has a coarser granularity in both η and ϕ.

---

[4] Mean length of a material to reduce the energy of an electron by a factor $1/e$ via Bremsstrahlung.

In the region of $|\eta| < 1.8$, a presampler detector, consisting of an active LAr layer of thickness 1.1 cm (0.5 cm) in the barrel (endcap) region is used to correct for the energy loss of electrons and photons before entering the calorimeter.

The total thickness of the EM calorimeter is $> 22X_0$ in the barrel and $> 24X_0$ in the endcaps.

The Hadronic Calorimeter

The hadronic tile calorimeter is located directly outside the EM calorimeter. Its barrel covers the region $|\eta| < 1.0$, and the two extended barrels, the range $0.8 < |\eta| < 1.7$. It uses steel as absorber and scintillating tiles as the active material. Wavelength shifting fibres guide the collected light from the scintillating tiles to photomultiplier tubes, which convert the photons into electrons and amplify the electron signal. Both the barrel and extended barrels are divided azimutally into 64 modules. They are segmented in depth in three layers: $\approx 1.5, 4.1$ and $1.8\ \lambda$ thick for the barrel and 1.5, 2.6 and 3.3 λ for the extended barrel. The total detector thickness at $\eta = 0$ of 9.7λ (10λ in the endcap) is sufficient to provide good resolution for high-energy jets.

The LAr hadronic endcap calorimeter (HEC) consists of two wheels per endcap, right behind the endcap EM calorimeter, sharing the same LAr cryostats. The HEC extends out to an $|\eta| = 3.2$, overlapping with the LAr forward calorimeter (FCal) (which starts at $|\eta| = 3.1$), and to an $|\eta| = 1.5$, overlapping with the tile calorimeter. The wheels are built from copper plates as the absorber, interleaved with LAr gaps as the active medium. The FCal is about 10 λ deep and consists of three modules in each endcap: the first made of copper, which is optimised for electromagnetic measurements, and the other two made of tungsten, which are optimised for hadronic interaction energy measurements. The resolution goal in the barrel and endcap hadronic calorimeters is: $\sigma_E/E = 50\%/\sqrt{E[\text{GeV}]} \oplus 3\%$, whereas for the forward calorimeter the resolution is required to be: $\sigma_E/E = 100\%/\sqrt{E[\text{GeV}]} \oplus 10\%$.

3.2.4. The Muon System

The outermost detector system of the ATLAS detector, the muon spectrometer, is based on the magnetic deflection of muon tracks due to the large superconducting toroid magnets to measure its momenta, and consists of separate trigger system and high-precision tracking chambers. An overview of the different components of the muon system and the location of the air-core toroid magnets can be seen in Figure 3.6. In the barrel region, Monitored Drift Tubes (MDTs) are used for tracking and Resistive Plate Chambers (RPCs) for triggering. In the endcap region, Cathode Strip Chambers (CSCs) are used for tracking and Thin Gap Chambers (TGCs) for triggering. In both barrel and encaps, muons traverse typically three longitudinal layers of the muon system. The muon spectrometer is designed in such a way that it can measure muon momenta from 3 GeV up to 3 TeV with good momentum resolution and charge identification. The resolution goal in the muon spectrometer is $\sigma_{p_T}/p_T = 10\%$ at a muon $p_T = 1$ TeV.

The muon system covers the range $|\eta| < 2.7$. Within the range $|\eta| < 1.4$, the muon tracks are bent by the barrel toroid. In the region $1.6 < |\eta| < 2.7$, the magnetic bending is provided by two smaller endcap toroid magnets, which are inserted into both ends of the barrel toroid and line up with the central solenoid. In the remaining gap, covering $1.4 < |\eta| < 1.6$, denoted by the *transition region*, the magnetic bending is due to a combination of barrel and endcap fields. In this way, the magnetic field provided by barrel and endcap toroid magnets is mostly orthogonal to the muon trajectories. Both barrel and endcap toroid magnets consist of eight coils each, assembled radially and symmetrically around the beam axis. The barrel toroid provides 1.5 to 5.5 Tm of bending power in the range $|\eta| < 1.4$, while the endcap toroids provide 1 to 7.5 Tm in the range $1.6 < |\eta| < 2.7$. The overlap region, $1.4 < |\eta| < 1.6$, has lower bending

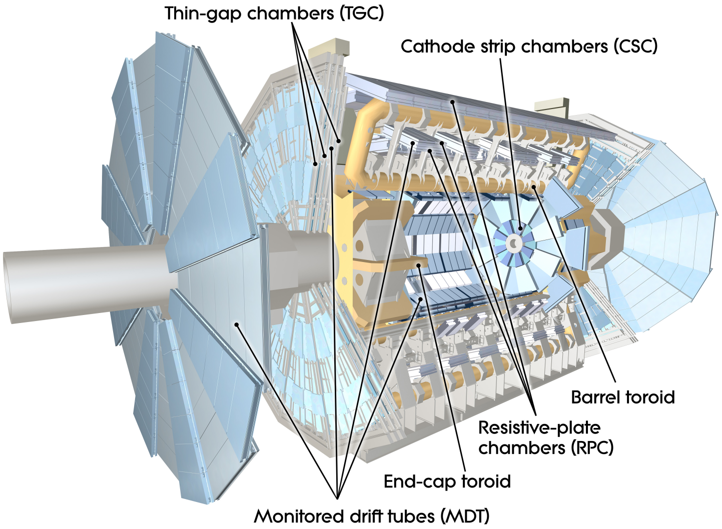

Figure 3.6.: Schematic view of the ATLAS muon system, together with the toroid magnets [105].

power. Approximately 1800 Hall sensors distributed through the muon system volume are used to monitor the magnetic field and to reconstruct the position of the toroid coils in space.

The muon system is divided into eight octants overlapping in ϕ in order to avoid gaps in the detector coverage. In the barrel, the chambers are disposed in three cylindrical layers around the beam axis. In the transition and endcap regions, the chambers are installed in planes in three layers perpendicular to the beam.

The design of the muon spectrometer was driven by the expected high particle flux, in order to allow high precision tracking measurements. Such precision measurement of the muon tracks is provided over most of the η range by MDTs [5], where the mechanical isolation of each sensor wire in the drift tubes ensures the robustness and reliability of the performance of this subsystem. In order to cope with the demanding rate and background conditions, CSCs [6] have higher granularity in the plane covering $2.0 < |\eta| < 2.7$. A stringent relative alignment of the layers of the muon chambers with respect to each other and with respect to the overall detector is needed to ensure a good performance of the muon system. In order to fulfil the performance goal for the stand-alone muon transverse momentum resolution of $\approx 10\%$ for 1 TeV tracks, the locations of MDT wires and CSC strips along a muon trajectory must be known with a precision better than $30\,\mu$m.

The trigger system in the muon spectrometer provides bunch-crossing identification, as well as well-defined p_T thresholds, and complements the muon coordinate measurement of the precision-tracking chambers by measuring the orthogonal coordinate with respect to the one measured by the latter ones. The trigger chambers must provide a fast and highly efficient trigger response. The coverage extends up to an $|\eta| < 2.4$. In the barrel, RPCs [7] provide good spatial and time resolution, while in the endcap regions, the TGCs, based on the same principle as multiwire proportional chambers, provide enough granularity and high rate capabilities for this demanding high particle flux region.

---

[5] In the MDTs, the electrons resulting from ionisation are collected at the central wire, in this case made of tungsten-rhenium.

[6] CSCs are multiwire proportional chambers with cathodes segmented into strips.

[7] The RPC is a gaseous parallel electrode-plate detector.

3.2.5. The Trigger System and Data Acquisition

As was mentioned in the introduction of this section, the collision rate at the LHC is heavily dominated by large cross section QCD processes, in contrast to the interesting physics processes rates at < 10 Hz. For technical and limited-budget reasons, it is not possible to save all the events and perform a posterior selection. Therefore, a fast and efficient selection procedure of physics events is designed to be able to keep the pace of the bunch crossing rate (designed to be 1/[25 ns]).

The ATLAS trigger system is separated in three levels: L1, L2, and the event filter (EF). L2 and the EF are referred to as the High-Level trigger (HLT). Each trigger level performs a stricter selection than in that of the previous level. The L1 trigger is able to make a decision using a limited amount of the detector information in less than 2.5 μs, reducing the rate from the original ≈ 1 GHz [8] to 75 kHz. In the next stages, the event rate is reduced to below 3.5 kHz in L2, and to ≈ 200 Hz after the EF. Compared to the design rates, the actual output rate during Run 1 was on average 400 Hz, as the trigger was able to handle a change of instantaneous luminosity at the LHC of more than 5 orders of magnitude in 2010-2011, and an increase of a factor 2 in 2012 [109].

The L1 trigger uses partial and reduced-granularity information from a subset of detectors: the RPC and TGC for the signature of muons with large transverse momentum, and all the calorimeter subsystems for electromagnetic clusters, jets, τ-leptons, missing and total transverse energy. The results from the L1 triggers are processed by the central trigger processor (CTP), where information from different object types is combined. The CTP processes this information and forms on up to 256 distinct L1 triggers, to which a pre-scale can be applied individually. If any of the 256 triggers fire, a single bit termed L1 Accept (L1A) is produced for that event. The L1 trigger also defines in each event Regions-of-Interest (ROIs): the η and ϕ coordinates of regions in the detector defined as interesting by the trigger selection procedure, where possible trigger objects have been identified by L1.

The L2 trigger uses the ROI information at full granularity and precision to reduce the amount of data to be transferred from the detector readout, needing on average approximately 40 ms to process an event. The event filter further reduces the event rate using offline analysis procedures, with an average event processing time of the order of four seconds, using additional information from the event that requires more complex computation, such as b-jet tagging or precise vertex measurements. The HLT algorithms refine the trigger selection using not only the full information of the calorimeters and muon chamber data, but also information from the inner detector, enhancing the particle identification.

The data acquisition system (DAQ) receives and buffers the event data from each detector readout electronics, at the L1 trigger acceptance rate, over 1600 point-to-point readout links. It transmits the ROI data to the L2 trigger, and an event-building is performed for those events passing the L2 selection criteria. These events are then received by the event filter. Finally, the events fulfilling the event filter selection are moved to permanent event storage at the CERN computer centre. Furthermore, the DAQ allows for configuration, control, and monitoring of the ATLAS detector during data-taking.

Figure 3.7 summarises the flow of data through the ATLAS trigger/DAQ chain. The specified rates should only be considered as orders of magnitudes.

---

[8] Assuming a bunch spacing of 25 ns and approximately 20 inelastic interactions per bunch crossing.

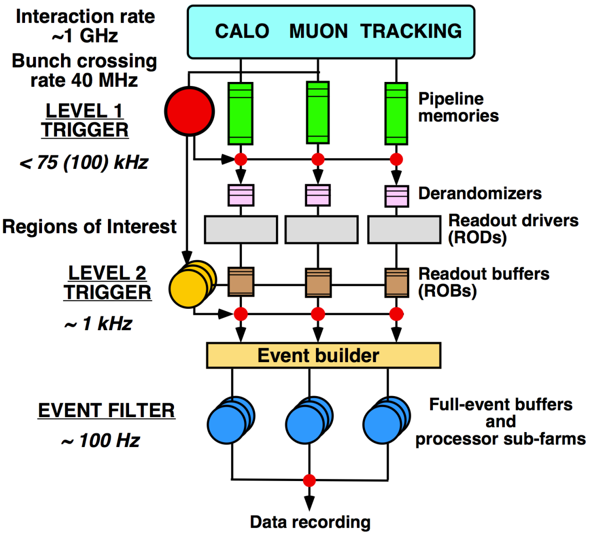

Figure 3.7.: Diagram of the trigger/data acquisition (DAQ) system [110].

3.3. ATLAS Performance in Run 1

The LHC re-started initial commissioning with beam at the end of 2009, after recovering from the accident on September 19th 2008, which mechanically damaged several magnets. Since then, the LHC has had three years of operations. The ATLAS experiment started data taking in 2010 at $\sqrt{s} = 7$ TeV, recording approximately 45 pb^{-1} in that year. The beam energy remained at 3.5 TeV in 2011, but the instantaneous luminosity was significantly increased, reaching a peak luminosity of 3.7×10^{33} $\text{cm}^{-2}\text{s}^{-1}$. The ATLAS detector recorded 5.08 fb^{-1} of the 5.46 fb^{-1} delivered by the LHC, translating into a data taking efficiency of 93%. In 2012, the beam energy was increased to 4 TeV ($\sqrt{s} = 8$ TeV) and the LHC delivered an integrated luminosity of 22.8 fb^{-1}, with a peak luminosity of 7.7×10^{33} $\text{cm}^{-2}\text{s}^{-1}$ [111]. ATLAS recorded 21.3 fb^{-1} with a data taking efficiency of 93.4%, from which 20.3 fb^{-1} fulfilled the ATLAS good data quality (DQ) requirements. This high DQ efficiency (approximately 95% in 2012) was achieved partly due to efficiency recovered during large data reprocessing. The good quality data set is the one used across most analyses. Figure 3.8 summarises the evolution of the cumulative delivered luminosity, showing the recorded and “good for physics” luminosity by ATLAS, as a function of the running time of the LHC.

As can be seen in Figure 3.9, the peak instantaneous luminosity delivered to ATLAS was overall more stable during the year 2012 than in 2011, when the instantaneous luminosity was increased in several steps: increasing bunch spacing time, number of protons per bunch and number of bunches, as well as improving the focusing of the proton beams at the interaction point. Based on experience of the 2011 run, the decision was taken to continue using a bunch spacing of 50 ns, a total number of bunches of around 1380, and tight collimator settings in the year 2012. This allowed the LHC to arrive close to the peak luminosity in a short period of time [113].

The increasing instantaneous luminosity was followed by a larger number of proton-proton collisions in addition to the collision of interest. The pile-up background constitutes of *in-time pile-up*, i.e. additional interactions occurring in the same bunch crossing as the collision of interest, and *out-of-time pile-up*, i.e. additional interactions occurring in bunch crossings just before and after the collision of interest. The increase of the former is due to the increase

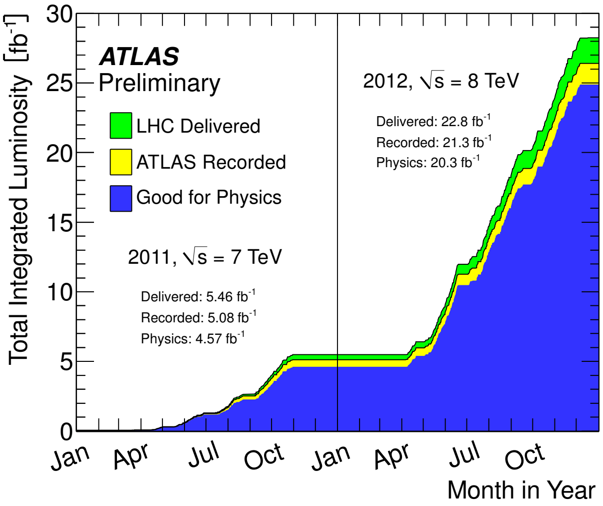

Figure 3.8.: Cumulative luminosity versus time, delivered by the LHC (green), recorded by ATLAS (yellow), and certified to be good quality data (blue) during stable beams for pp collisions at 7 and 8 TeV centre-of-mass energy recorded in 2011 and 2012 [112].

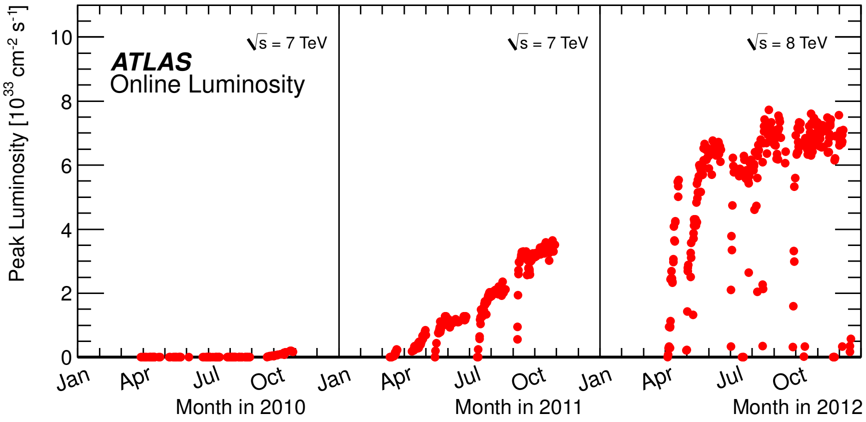

Figure 3.9.: The peak instantaneous luminosity delivered to ATLAS per day versus time, during the pp collisions of 2010, 2011, and 2012 [112].

in the number of protons and better focusing techniques, while the latter originates from the finite readout time of the subdetector systems. The data taking during 2012 was particularly affected by the high pile-up environment, increased by roughly a factor of 2 with respect to the 2011 data taking. Figure 3.10 shows the mean number of interactions per crossing during the 2011 and 2012 data taking periods. The mean number of interactions per crossing is calculated as $\mu = \mathcal{L}_{bunch} \times \sigma_{inel}/f_r$, where $\mathcal{L}_{bunch}$ is the instantaneous luminosity per bunch, σ_{inel} is the inelastic cross section at each centre-of-mass energy, and f_r the LHC revolution frequency. Since pile-up affects the physics object reconstruction and can degrade its performance, ATLAS has optimised the reconstruction in 2012 in order to reduce as much as possible the dependence of the reconstruction performances on the number of interactions per bunch crossing. This will be explained in more detail in Section 4.

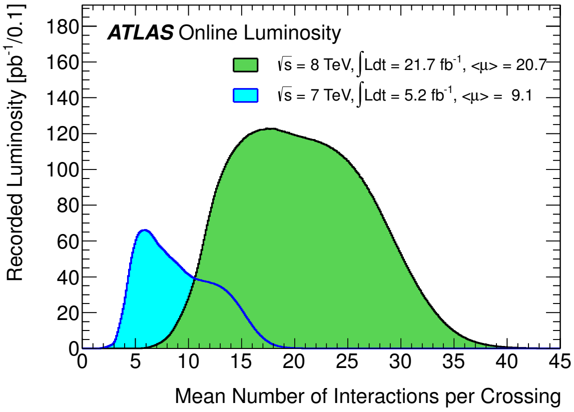

Figure 3.10.: Luminosity-weighted distribution of the mean number of interactions per crossing for the 2011 and 2012 data [112].

The main analysis presented in this thesis analyses the full dataset recorded by ATLAS during 2012 at $\sqrt{s} = 8$ TeV, which fulfils the good run list criteria, corresponding to the integrated luminosity of 20.3 fb^{-1}.

CHAPTER 4

Object definitions and preselection

4.1. Introduction

The measurement of the $t\bar{t}Z$ and $t\bar{t}W$ cross section presented in this thesis is performed with events containing two oppositely-signed charged leptons. The main physics objects used in this measurement are electrons, muons, jets (from which some will be required to be tagged as a jet originating from a b-quark - so called *b-jets*) and missing transverse energy, due to the presence of at least two neutrinos in the final state.

In the following sections, the identification and reconstruction of such objects will be explained.

4.2. Electrons

4.2.1. Definition and Selection

The electron candidates considered in this analysis are reconstructed from energy deposits, called *clusters*, in the EM calorimeter which are associated with reconstructed tracks of charged particles in the inner detector. The reconstruction process consists of three steps:

- *Cluster reconstruction*: the EM clusterisation starts from energy deposits with a total transverse energy above a threshold of 2.5 GeV by using a *sliding-window* algorithm. This algorithm uses a fixed cone, scanning the calorimeter cells in the (η, ϕ) space and chooses the position with the maximum energy deposition within the cone as the cluster position.
- *Track association with the cluster*: tracks with $p_T > 0.5$ GeV are extrapolated from their last measured point in the inner detector to the middle layer of the EM calorimeter. If the distance between the extrapolated track impact point and the EM cluster centre of gravity in the same layer is $|\Delta\eta| < 0.05$, then the track and the cluster are considered matched. Furthermore, the size of the $\Delta\phi$ track-cluster matching window is required to be 0.1 on the side where the extrapolated track bends when passing through the solenoid magnetic field. An electron candidate is considered to be reconstructed when at least one track is matched to the seed cluster. If no matched track is found, the cluster is classified as an unconverted photon candidate.

- *Electron candidate reconstruction*: once a successful track-cluster match is found, the cluster sizes are optimised to take into account the overall energy distribution in the different regions of the calorimeter. The total energy of the electron candidate results from adding the estimated energy deposited in the material *in front* of the EM calorimeter, the measured energy deposited *in* the cluster [1], and the estimated energy deposited *outside* the cluster and *beyond* the EM calorimeter.

The final four-momentum of the electrons combines the information given by the final cluster and the best track matched to the seed cluster; the energy corresponds to the cluster energy, and the (η, ϕ) spatial coordinates are taken from the corresponding track parameters at the interaction vertex [114].

Not all objects resulting from applying the electron reconstruction algorithm are *signal* (isolated) electrons. *Background* electron contributions come from hadrons misidentified as electrons, non-isolated electrons [2], or electrons from photon conversion. Therefore, a further electron identification is needed in order to reject as much background objects as possible, while keeping the efficiency for signal electrons high. For the presented measurement, an electron identification based on a multivariate analysis (MVA) techniques is used. It combines the discriminating power of variables describing different properties in order to make a better selection decision. Specifically, the likelihood (LH) technique was used. It combines the signal and background likelihood, $\mathcal{L}_S$ and $\mathcal{L}_B$, for a given electron into a discriminant $d_{\mathcal{L}}$ as:

$$d_{\mathcal{L}} = \frac{\mathcal{L}_S}{\mathcal{L}_S + \mathcal{L}_B}, \qquad \mathcal{L}_S(\vec{x}) = \prod_{i=1}^{n} P_{s,i}(x_i), \tag{4.1}$$

where $\vec{x}$ is the vector of variable values and $P_{s,i}(x_i)$ $(P_{b,i}(x_i))$, the value of the signal (background) probability density function of the i^{th} discriminating variable evaluated at x_i.

The signal and background probability density functions are obtained from data. For the central electrons, an extensive set of discriminating variables is used, including those describing the longitudinal and transverse shapes of the EM showers in the calorimeters, the properties of the tracks in the inner detector, and the matching between tracks and energy clusters. The electron LH allows to include variables with significant discriminating power but large overlap between signal and background, which would not be feasible in the simple electron cut-based identification (based on sequential explicit cuts on selected variables).

There are three available electron LH selections: LOOSE, MEDIUM and VERY TIGHT. Each of them has similar electron efficiency as the equivalent selection in the cut-based selection menu, but better rejection of light-flavour jets and photon conversions. Each LH selection cuts on a LH discriminant built with a different set of variables. Furthermore, the LH for each operating point is divided in 9 bins in $|\eta|$ and 6 bins in E_T [115]. In the context of the presented measurement, a looser electron selection than the TIGHT cut-based one [3] was pursued in order to increase the electron signal efficiency, while keeping the rate of misidentified leptons low, hence the MEDIUM LH working point was used. In addition, the electron track longitudinal impact parameter with respect to the primary vertex, z_0, is required to be smaller than 2 mm.

In order to further reduce the background from non-prompt electrons (i.e. from decays of hadrons produced in jets), an additional isolation cut not included in the previous identification selection is applied. The electron isolation requirement in this measurement is based on the

---

[1] Corrected for the estimated energy fraction measured by the sampling calorimeter.

[2] Non-isolated electrons can originate from semileptonic decays of heavy-flavour particles.

[3] The recommended electron identification selection at the time.

tracker information only. It requires that the ratio of the sum of transverse momentum of the tracks with $p_T > 0.4$ GeV in a cone of size $\Delta R = 0.3$ around the electron track, denoted by p_T^{cone30}, to the p_T of the electron be less than 0.12 (i.e. $p_T^{cone30}/p_T \leq 0.12$). The tracks considered in the sum must originate from the primary vertex associated to the electron track and be good quality tracks in terms of the number of silicon hits.

The electrons are required to have $|\eta_{\text{cluster}}| < 2.47$, where $|\eta_{\text{cluster}}|$ is the pseudorapidity of the calorimeter cluster associated with the electron candidate. Candidates in the calorimetry transition region between barrel and endcap $1.37 < |\eta_{\text{cluster}}| < 1.52$ are excluded.

4.2.2. Trigger

The electron objects are required to match the logical OR of the lowest unprescaled single lepton trigger during the 2012 data taking, EF_e24vhi_medium1, and the EF_e60_medium1 trigger. These triggers apply a threshold on the cluster E_T at the EF trigger stage of 24 and 60 GeV, respectively. The identification selection of e24_vhi_medium1 is more stringent than for e60_medium1, requiring a loose track isolation, $p_T^{cone20}/E_T < 0.1$. The two triggers are combined with a logical OR to improve the trigger efficiency at higher electron transverse energy ($E_T > 60$ GeV), as can be seen in Figure 4.1.

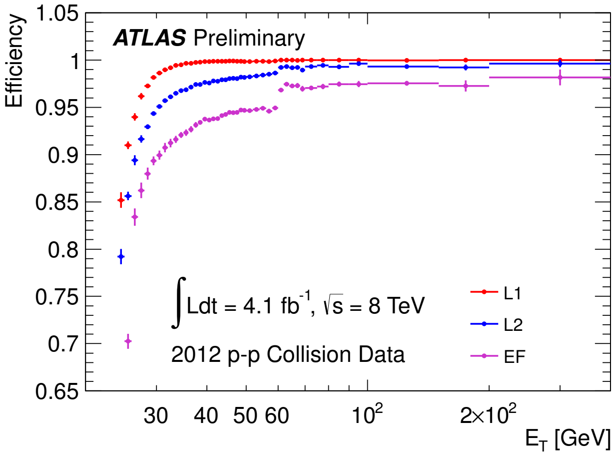

Figure 4.1.: L1, L2 and EF trigger efficiencies as a function of the electron transverse energy for the single electron triggers (e24vhi_medium1 OR e60_medium1) in the 2012 data set [116].

4.2.3. Performance

Reconstruction, Identification and Isolation Efficiencies

In order to measure the identification and reconstruction efficiency, a clean and unbiased sample of electrons is required, such as $Z \to ee$ and $J/\Psi \to ee$ decays. The *tag-and-probe* method is used to derive the electron efficiencies from those events. The method consists of applying strict selection criteria on one of the two decay electrons (called *tag*). The second electron candidate (called *probe*) is used for the efficiency measurement. The efficiency to detect an electron is divided into different components:

$$\epsilon_{total} = \epsilon_{reco} \times \epsilon_{ID} \times \epsilon_{trigger} \times \epsilon_{additional}, \tag{4.2}$$

where:

- ϵ_{reco} is the reconstruction efficiency, measured in $Z \rightarrow ee$ events, which provides the purest selection of probes,
- ϵ_{ID} is the identification efficiency, measured in $Z \rightarrow ee$ events for electrons with $E_T >$ 10 GeV, and in $J/\Psi \rightarrow ee$ events for electrons with 7 GeV $< E_T <$ 20 GeV,
- $\epsilon_{trigger}$ is the trigger efficiency, measured in $Z \rightarrow ee$ events, with respect to the *medium++* electron identification, which is equivalent to the identification working point used at the trigger level, *medium1*, and
- $\epsilon_{additional}$ is the efficiency related to the additional selection criteria, such as isolation.

The efficiencies obtained in data, ϵ_{data}, and in the Monte Carlo (MC) simulated samples, ϵ_{MC}, are compared, and a correction factor, also called *scale factor* (SF) and defined as $SF = \epsilon_{data}/\epsilon_{MC}$, is derived. The SF is applied to MC samples, so that they reproduce the efficiencies in data as closely as possible. Given the dependence of the electron efficiencies on E_T and η, the measurements are performed in two-dimensional bins in the (E_T, η)-plane. SFs are typically a few percent different from unity. This can be seen for the MEDIUM LH electron identification above 20 GeV in Figure 4.2 (left) [4]. Furthermore, Figure 4.2 (right) shows the reasonable stability of the different likelihood-based selection criteria with respect to the number of primary vertices, i.e. pile-up.

The electron isolation SF is set to one, given the looser isolation criteria.

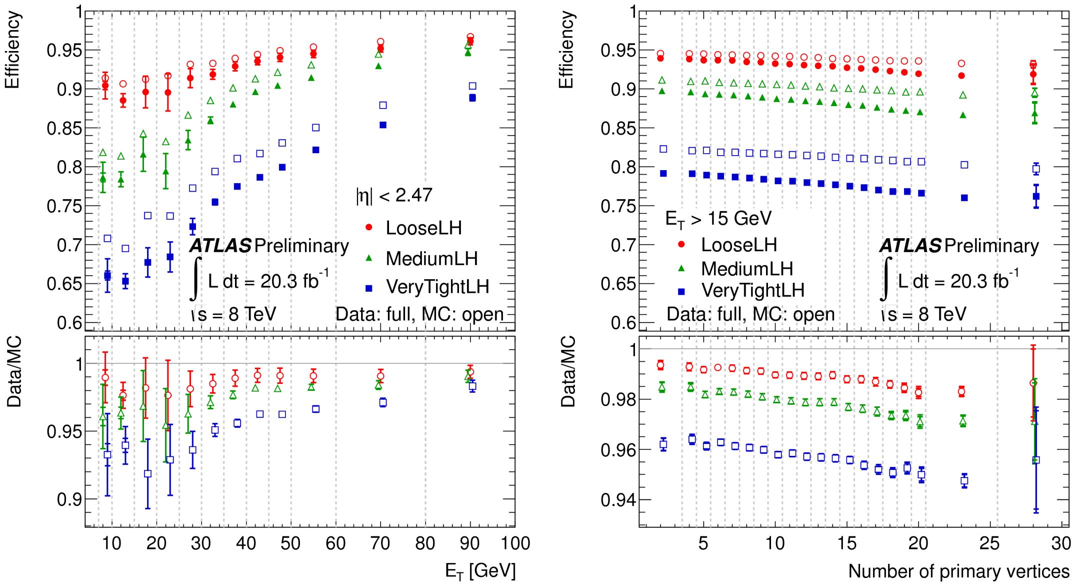

Figure 4.2.: Identification efficiency in data as a function of (left): E_T and (right): the number of reconstructed primary vertices, for the loose LH, medium LH and very tight LH working points, compared to the MC expectation for electrons from $Z \rightarrow ee$ decays [115].

---

[4] Requirements on the minimum p_T of the leptons will be explained in the final selection for the presented analysis.

Energy Scale and Resolution

Energy scale correction factors are derived using a large sample of collected $Z \to ee$ events and the well known Z-boson mass value, and are applied to reconstructed electrons as final energy calibration in data events. An energy smearing is done for simulated events to match the energy resolution in data. Figure 4.3 shows the reconstructed $Z \to ee$ invariant mass in both data and MC after applying the electron energy calibration for the 2011 dataset [115].

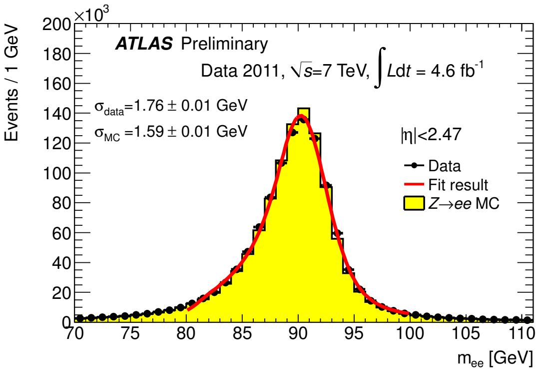

Figure 4.3.: Resolution of the di-electron invariant mass from $Z \to ee$ events after applying all energy corrections in the 2011 data set [117].

4.3. Muons

4.3.1. Definition and Selection

Muon candidates are reconstructed in the ATLAS experiment from track segments in the various layers of the muon spectrometer (MS), and matched with tracks found in the inner detector (ID).

Depending on the reconstruction criteria used for the muon identification, different types of muons are available:

- *Stand-alone (SA)*: the muon trajectory uses information from the MS only. SA muons allow to extend the acceptance range to $2.5 < |\eta| < 2.7$, which is not covered by the ID.
- *Combined (CB)*: track reconstruction is performed independently in the ID and MS; the ID and MS tracks are later combined into one track. This type has the highest muon purity.
- *Segmented-tagged (ST)*: a track in the ID is classified as a muon if, once extrapolated to the MS, it is associated with at least one local track segment in the MDT or CSC chambers. It is useful in cases where muons have low p_T, or cases in which muons fall in regions with reduced MS acceptance.
- *Calorimeter-tagged (CaloTag)*: a track in the ID is classified as a muon if it is associated to an energy deposit in the calorimeter compatible with a minimum ionising particle (MIP) [5]. This type has the lowest purity, but recovers acceptance regions with no MS coverage.

---

[5] Relativistic charged particles with minimum energy loss rates via ionisation when traversing a block of material - typically about 1.5 MeV per g/cm^2. Typical muons are considered to be MIPs.

For the main measurement presented in this thesis, *combined* muons are used. The final candidates are refitted using the complete track information from both detector systems, and are required to have an $|\eta| < 2.5$. Muons are required to have a hit pattern in the inner detector consistent with a well-reconstructed track [118]. The muon track longitudinal impact parameter with respect to the primary vertex, z_0, is required to be smaller than 2 mm. Muons are also required to be separated by $\Delta R > 0.4$ from any selected jet (the jet selection will be presented in Section 4.4).

Furthermore, muons are required to satisfy a p_T-dependent track-based isolation requirement that has good performance under high pile-up conditions and in boosted top quark topologies, where the ΔR distance between the muon and a b-tagged jet scales as $m_{top}/p_{T,top}$. This isolation, denoted as *mini-isolation* [119], is defined as the scalar sum of the p_T of additional tracks, which have a $p_T^{track} > 1$ GeV and fulfil track quality cuts, in a cone of variable radius $\Delta R < 10$ GeV$/{p_T}^{\mu}$ around the muon. The mini-isolation is required to be less than 5% of the muon p_T. Therefore, for higher muon p_T, the cut on the sum of tracks is looser, while the cone radius becomes smaller.

4.3.2. Trigger

The muon objects are required to match the logical OR of two single muon triggers during the 2012 data taking, EF_mu24i_tight and EF_mu36_tight. The former trigger applies a p_T threshold of 24 GeV and an isolation requirement $p_T^{cone20}/{p_T}_{\mu} \leq 0.12$, while the latter only applies a p_T threshold of 36 GeV. Since the mini-isolation requirement is tighter than the one applied in the first trigger, the trigger isolation has no effect on the analysis. The trigger efficiency is measured in $Z \to \mu\mu$ events with the *tag-and-probe* method. Figure 4.4 shows the efficiencies measured for the logical OR of the two single muon triggers used in the 2012 data set and MC simulation, showing an efficiency in the plateau ($p_T > 25$ GeV) of approximately 70% in the barrel region ($|\eta| < 1.05$) and of approximately 86% in the endcap region.

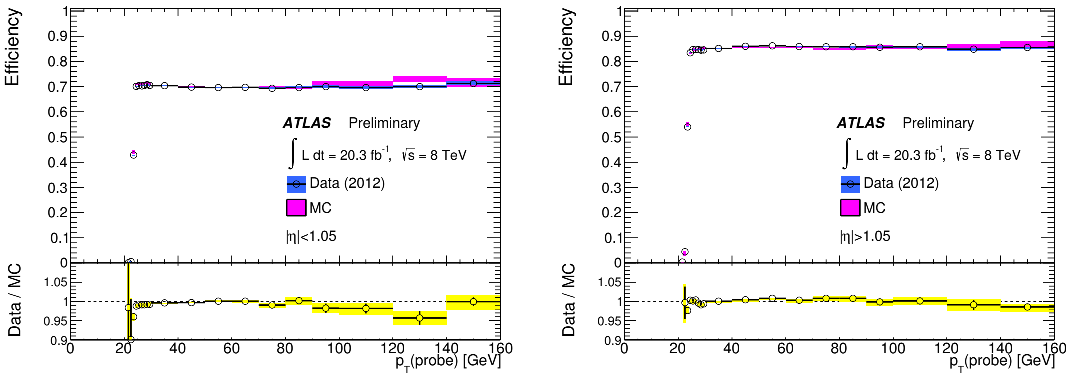

Figure 4.4.: Efficiency of the two single muon triggers, mu24i_tight and mu36_tight, convoluted as an OR between the two, for (left): the barrel and (right): endcap region. The results are shown for both MC simulation and the full 2012 dataset [120].

4.3.3. Performance

Reconstruction, Identification and Isolation Efficiencies

The muon reconstruction efficiencies are computed in data and MC simulation for each muon type in $Z \to \mu\mu$ events using the *tag-and-probe* method, and corresponding SFs are applied to

MC simulation to bring it in agreement with the data efficiency. Figure 4.5 shows the muon ID reconstruction efficiency as a function of η and p_T in the region $|\eta| < 2.5$ for the full 2012 data set and simulation. The largest discrepancy between data and simulation efficiencies can be seen in the region, $1.5 < \eta < 2$. This can be explained by two faulty pixel b-layer (innermost pixel layer) modules that were not disabled correctly in the data reconstruction, causing a lower reconstruction efficiency than that predicted by the simulation. These discrepancies are taken into account with the SFs shown in the lower part of the plots. Other than this region, the overall efficiency is greater than 99%, with very good agreement between data and MC.

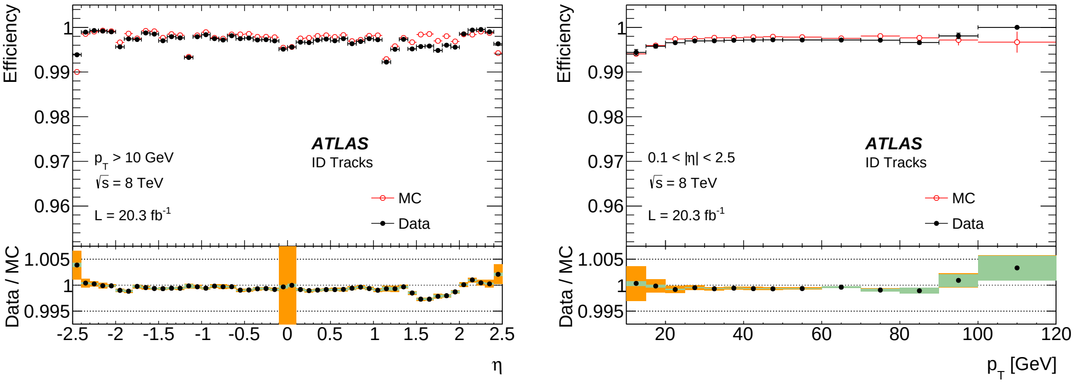

Figure 4.5.: ID muon reconstruction efficiency as a function of (left): η and (right): p_T measured in $Z \to \mu\mu$ events for muons with a p_T > 10 GeV. The panel at the bottom shows the ratio between the measured and predicted efficiencies. The green areas show the pure statistical uncertainty, while the orange areas also include systematic uncertainties [118].

The *tag-and-probe* method is also used in $Z \to \mu\mu$ events to calculate the efficiency of the muon isolation requirement. A dimuon selection is applied, requiring the two muons to have opposite-sign charge, $p_T > 25$ GeV, a distance of $\Delta R \geq 0.4$ to the closest jet and satisfying $80 < m(\mu\mu) < 100$ GeV. The *tag* muon has to pass the isolation requirement, and the isolation efficiency is measured by determining if the *probe* muon fulfils the isolation requirement as well. Since the difference between data and simulation is within 0.5% everywhere, a SF of 1.00 ± 0.5% is assigned for the isolation efficiency.

Energy Scale and Resolution

Due to the large amount of $Z \to \mu\mu$ events collected in 2011 and 2012, a very precise calculation of the muon momentum scale from the Z peak position is possible. The scales are considered separately for the ID and the MS regions, and the corresponding corrections are at the few per mille level.

A smearing of the momentum of the muons is performed in MC simulation in order to make the momentum resolution in MC agree with data. A separate parametrisation is used for the ID and MS region, and the differences in the momentum resolution measurement between the two are also reflected in the smearing correction factor [121]. Figure 4.6 shows the invariant dimuon mass for data and corrected MC using combined muons with $p_T > 25$ GeV.

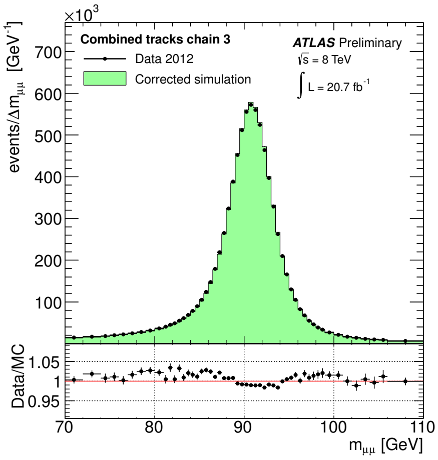

Figure 4.6.: Dimuon invariant mass for combined muons in the full 2012 data set and the corrected MC simulation, after applying smearing and scale corrections to the latter [122].

4.4. Jets

4.4.1. Definition and Selection

As was briefly described in Section 2.2.3, jets are collimated sprays of energetic hadrons as a result of the fragmentation and hadronisation of the original hard partons. They are the dominant characteristic of high energy *pp* collisions at the LHC. When defining a jet, one projects away the multiparticle dynamics, leaving a simpler picture of the event. The definition will depend on the source and the algorithm used to identify a jet. Depending on the input to build the jet, the jet types can be:

- *particle or truth jets*: reconstructed from truth stable particles in MC simulation (with proper lifetimes longer than 10 ps, excluding muons and neutrinos),
- *track-jets*: built from reconstructed charged particle tracks in the inner detector with origin in the primary vertex, insensitive to pile-up effects,
- *calorimeter-tower jets*: built from calorimeter towers, i.e. static grid elements made from calorimeter cells, and
- *topo-clusters*: built from topological calorimeter clusters.

The jets used in this analysis are *topo-clusters*. Topological clusters are groups of calorimeter cells, formed with the topo-cluster formation algorithm. This algorithm starts from a *seed* cell with a signal-to-noise (S/N) ratio required to be $S/N \geq 4$. Neighbouring cells are added iteratively to the seed (or the developing cluster) if $S/N \geq 2$ is fulfilled. Finally, all calorimeter cells neighbouring the topo-cluster are added. In that way, the algorithm efficiently suppresses the calorimeter noise. In 2011, in addition to the electronic noise, a noise component due to pile-up was considered, affecting the energy deposited in a given cell per bunch crossing. The noise induced by pile-up was significantly larger than the electronic noise in the forward calorimeter. In the rest of the calorimeter, the pile-up noise is on average at most, or smaller than, the electronic noise.

The topo-clusters are calibrated in the first stage at the EM scale, which correctly measures the energy deposited by a particle in electromagnetic showers in the calorimeter. Additionally, a second topo-cluster collection is built by calibrating the calorimeter cell such that the response of the calorimeter to hadrons is correctly reconstructed. This calibration uses the local [6] cell signal weighting (LCW or LC in the remainder) method, which classifies topo-clusters as electromagnetic or hadronic, based on the measured energy density and the longitudinal shower depth. It improves the resolution compared to the EM scale by correcting the signal from hadronic deposits, and thus, reducing fluctuations due to the non-compensating nature of the calorimeter.

Jets are then built from these calibrated clusters using a jet algorithm. The jet clustering algorithm used to reconstruct jets in ATLAS is the anti-k_t algorithm [123, 124]. This algorithm belongs to the sequentially-clustering "jet-finders" (successive pair-wise recombination of particles) [123]. The anti-k_t algorithm consists of finding the minimum distance, d_{min}, of all the constructed d_{ij}, d_{iB}, defined as:

$$d_{ij} = \min(k_{ti}^{-2}, k_{tj}^{-2})\frac{\Delta_{ij}^2}{R^2}, \qquad d_{iB} = k_{ti}^{-2} \;\; \text{(distance to the beam)}, \tag{4.3}$$

where $\Delta_{ij} = (y_i - y_j)^2 + (\phi_i - \phi_j)^2$ and k_{ti}, y_i and ϕ_i are the transverse momentum, rapidity and azimuth of particle i. If the minimum is found to be d_{ij}, then i and j are merged into a single particle, summing their four-momenta. Otherwise, if it is d_{iB}, particle i is declared to be a final jet and removed from the particle list. The same procedure is repeated once more with the remaining particles, until no particles are left. The special feature of this algorithm is that soft particles do not modify the shape of the jet, while hard particles do, resulting in almost perfect circular jets with radius R around the hardest particle. If two hard particles are separated by $\Delta_{ij} < 2\text{R}$, the shape of the jets changes slightly due to the overlap, nevertheless, the hardest jet always remains the circular one. A graphic example of the reconstruction of jets using this algorithm can be seen in Figure 4.7

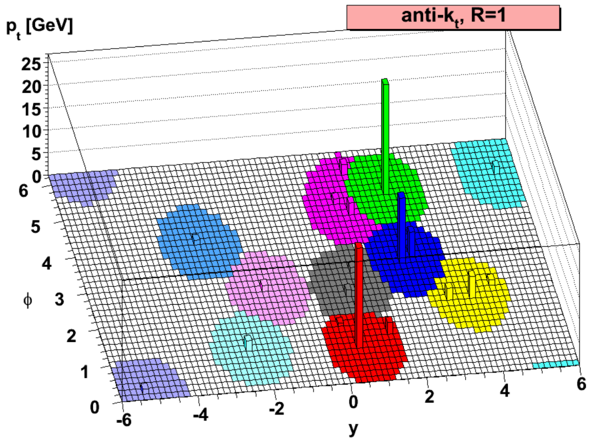

Figure 4.7.: Parton-level event with random soft emissions, clustered with the anti-k_t algorithm [124].

The anti-k_t algorithm is therefore experimentally feasible and theoretically sensible, i.e. it is infrared and collinear safe (is not dependent on additional soft radiation nor on collinear splitting

---

[6] "Local" because the energy corrections are defined without reference to a jet definition.

of the initial parton). In the context of this analysis, the anti-k_t algorithm with $R = 0.4$ was used, implemented in the FASTJET software package [125]. The jet four momentum is defined as the four momentum sum of its constituents. Figure 4.8 summarises the different inputs used to build jets, as well as the most commonly used calibration methods.

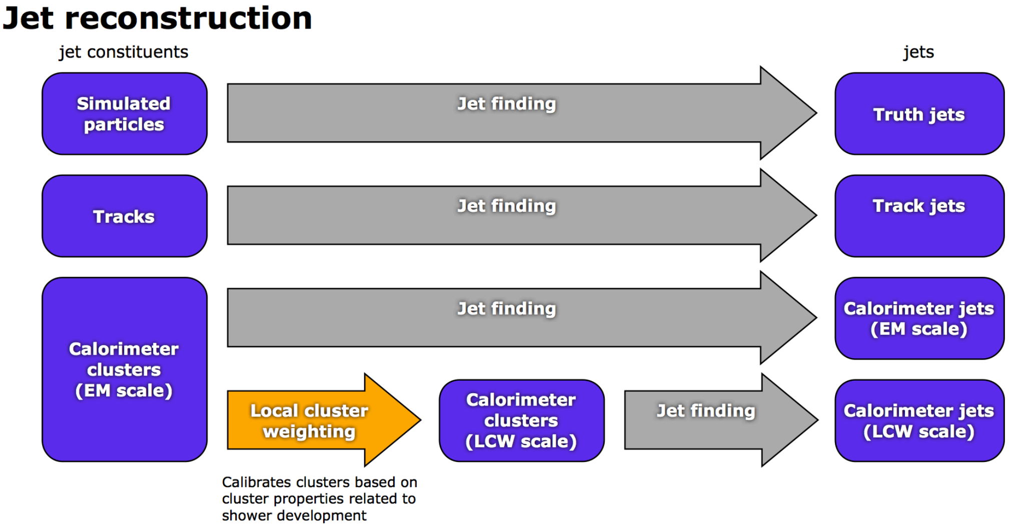

Figure 4.8.: Overview of the jet reconstruction stages in the ATLAS detector. The last row corresponds to the jet reconstruction chain used for this analysis. Calorimeter clusters are calibrated first using the local cluster weighting, and passed to jet finding to produce calorimeter jets at LCW scale [126].

The final jet energy calibration can be applied to both EM scale or LCW calibrated jets, resulting in EM+JES or LCW+JES calibrated jets, respectively. The jet energy scale (JES) is different for each calibration scheme. The final calibration provides the jet energy scale with respect to the energy of jets reconstructed from truth particles, and consists of four steps:

- *Pile-up correction*: correction accounting for the energy offset caused by pile-up interactions. Derived from MC simulations.
- *Origin correction*: correction to the calorimeter jet direction, so that it points to the event primary vertex.
- *Energy and η calibration*: correction of the energy and η from the reconstructed jet to the ones of the matching truth jets in MC simulation.
- *Residual in-situ corrections*: correction applied to jets reconstructed in data, derived using *in-situ* measurements in data and MC simulation.

After the energy calibration, jets are required to have $p_T > 25$ GeV and $|\eta| < 2.5$. During jet reconstruction, no distinction is made between identified electrons and jet energy deposits. Therefore, if any of the jets lie within a ΔR of 0.2 of a selected electron, the single closest jet is discarded in order to avoid double-counting of electrons as jets. Afterwards, electrons which are within a ΔR of 0.4 of remaining jets are removed.

Jet Quality Selection

A set of jet quality selection criteria is required in order to select jets from collisions and reject as many *bad jets* as possible, which can arise from either beam-gas events, beam-halo events, cosmic-ray muons, or calorimeter noise. The discrimination between jets with in-time real energy deposits in the calorimeter and background jets is based on information from the quality of energy reconstruction at the cell level, jet energy deposits in the direction of the shower, and reconstructed tracks matched to the jets. The working point used for this analysis is the *looser* jet quality selection, having the highest jet selection efficiency (greater than 99.8%), and showing a very good agreement between data and MC simulation.

Additionally, in order to further reduce the effect of in-time pile-up, a cut on the Jet Vertex Fraction (JVF) [127] is required. This variable is used to identify the origin vertex of a given jet and is defined for each jet_i with respect to each primary vertex PV_j as:

$$\mathrm{JVF}(jet_i, PV_j) = \frac{\sum_k p_T(track_k^{jet_i}, PV_j)}{\sum_n \sum_l p_T(track_l^{jet_i}, PV_n)}, \tag{4.4}$$

where k runs over all tracks originating from PV_j matched to jet_i, n runs over all primary vertices in the event, and l runs over all tracks originating from PV_n matched to jet_i. Tracks are reconstructed from inner detector information and are required to have a $p_T > 500$ MeV. Once the hard-scatter PV is selected, the JVF variable can be used to select jets having a high probability of originating from that vertex. Figure 4.9 (left) shows the discriminating power of the JVF distribution between hard-scatter and pile-up jets. A value of $JVF = -1$ corresponds to calorimeter jets without associated tracks, and $JVF = 0(1)$, to jets with all associated tracks originating from pile-up vertices (hard-scatter PV). The intermediate region, $0 < JVF < 1$, indicates that some associated tracks originate from the hard-scatter vertex. The cut used for the 8 TeV analysis requires all jets with $p_T < 50$ GeV [7] and $|\eta| < 2.4$ [8] to fulfil a cut of $|JVF| \geq 0.5$, providing a good compromise between pile-up jet rejection and high efficiency selection of hard-scatter jets.

The per-jet efficiency to satisfy the jet vertex fraction requirement is measured in $Z(\rightarrow \ell^+\ell^-)$+1-jet events in data and simulation, where $\ell = e, \mu$, selecting separately events enriched in hard-scatter jets and events enriched in pileup jets. Instead of applying a SF to cover the discrepancies in JVF efficiency between data and simulation, shown to be small in Figure 4.9 (right), a systematic uncertainty is assigned by varying the cut up and down to cover these discrepancies.

B-tagged jets

The identification of jets originating from b-quarks is important for many topics of the LHC program, and in particular, it has a high relevance for top quark physics, since one b-jet per top quark decay is expected. Various b-tagging algorithms available in ATLAS take advantage of the relatively long lifetime of hadrons containing a b-quark (≈ 1.5 ps). This results in a displaced secondary vertex of a B-hadron decay with respect to the primary one, from which several displaced tracks originate, as can be seen in Figure 4.10. The transverse impact parameter, d_0, is the distance of closest approach of the track to the PV in the $x - y$ plane. Equivalently, the longitudinal impact parameter, z_0, is the distance of closest approach of the track to the PV in

---

[7] Pile-up jets are expected to be soft.

[8] Region with good tracking information.

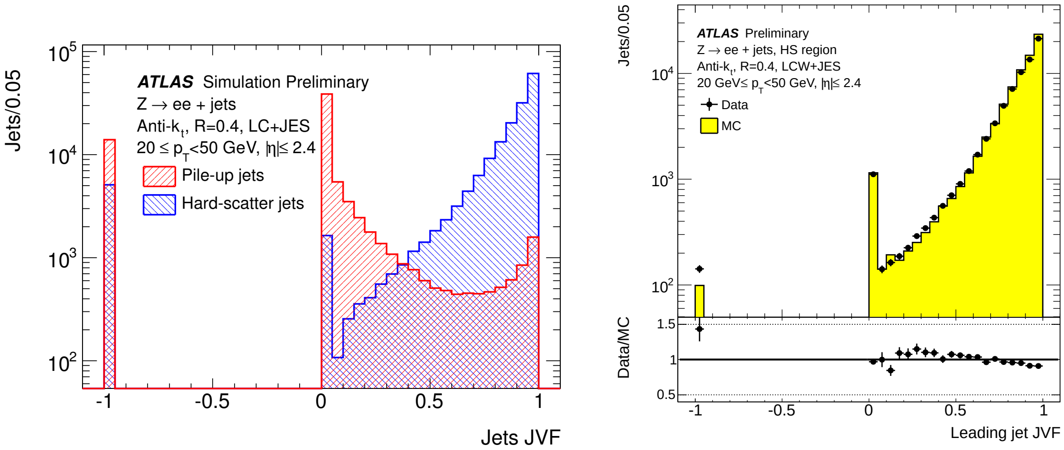

Figure 4.9.: (Left): JVF distribution for hard-scatter jets (blue) and pile-up jets (red) satisfying $20 \leq p_T^{jet} < 50$ GeV and $|\eta| < 2.5$ in simulated Z+jets events [127]. (Right): JVF distribution for LC jets satisfying $20 \leq p_T^{jet} < 50$ GeV and $|\eta| < 2.4$, produced back-to-back with respect to a Z-boson decaying into two electrons (sample with high purity of hard-scatter jets). The distribution is strongly peaked at 1, and a good agreement between data and MC simulation is observed [127].

the z direction. The sign of the impact parameter is positive if the point of minimum approach to the PV is in the same hemisphere as the one defined by the jet direction.

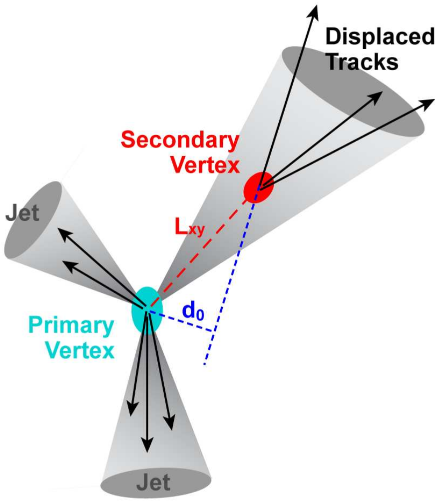

Figure 4.10.: Sketch of the evolution of a B-hadron into a b-jet. L_{xy} is the distance of the secondary vertex from the primary vertex in the plane orthogonal to the proton beam direction, and d_0 is the impact parameter of a track [128].

The b-tagging algorithms rely on either the secondary vertex information or the properties of the displaced tracks, or on the combination of both, in order to tag true b-jets, and reject as many light jets (i.e. reduce the mistag rate [9]) as possible.

---

[9] Fraction of jets originating from light-flavour quarks which are tagged by a b-tagging algorithm.

The following algorithms are available in ATLAS:

- **SV0** [129], based on the decay length significance, and **SV1** [130], extension of SV0, including additional variables, such as the invariant mass of all tracks associated to the vertex, the ratio of the sum of the energies of the tracks in the vertex to the sum of the energies of all tracks in the jet, and the number of two-track vertices, which are combined using a likelihood ratio technique.
- **JetProb** [131], based on the transverse impact parameter significances of the tracks in a jet, **IP3D** [130], based on both the longitudinal and the transverse impact parameter of the tracks in a jet.
- **JetFitter** [132], based on the topological structure of B- and C-hadron decays inside jets.
- **JetFitterCombNN** [130], combines the output of IP3D and JetFitter in a neural network, and **MV1** [133], combines the output of IP3D, SV1 and JetFitterCombNN. Each of the previous two algorithms have a "c" version, JetFitterCombNNc and MV1c, where the respective neural networks are explicitly trained to discriminate between c-jets and b-jets.
- **Soft muon tagging** [134], exploits the presence of a non-isolated muon inside a jet as a good discriminant for b-jet identification.

For each b-tagging algorithm, a set of operating points is defined, in terms of the inclusive b-tag efficiency in a simulated sample of $t\bar{t}$ events. Figure 4.11 shows the corresponding light-jet and c-jet rejection for a given b-jet efficiency for several b-tagging algorithms. The MV1 algorithm provides the best light-jet rejection, and is therefore the one used in the analysis presented in this thesis. The 70 % operating point (0.7 b-tagging efficiency) is used, which corresponds to a light-jet rejection factor of $\sim$ 130 and a c-jet rejection factor of 5, showing a good compromise between b-jet efficiency and rejection.

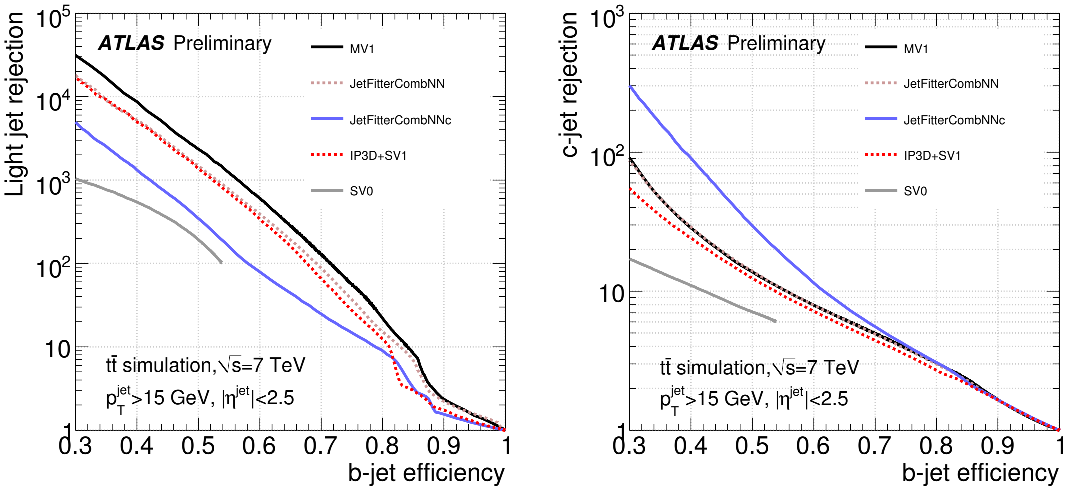

Figure 4.11.: (Left): Light-jet and (right): c-jet rejection as a function of the b-tag efficiency for different b-tagging algorithms [133].

The efficiencies ϵ_b, ϵ_c and mistag rate of each available operating point have been calibrated in data using samples enriched in b-jets, c-jets and light jets, correspondingly. The calibration results are presented in the form of SFs.

The mistag rate, defined as the probability of tagging a jet originating from a light-flavour parton (u-, d-, s-quark or gluon), is measured in an inclusive jet sample using the *negative tag* method [135], which reverses the impact parameter and decay length selections of the b-tagging algorithm. Since the mistag rate depends on the kinematics of the jet, the measurement is performed in bins of jet p_T and η.

The c-tagging efficiency, defined as the efficiency with which a b-tagging algorithm tags jets originating from charm hadrons, is measured using a sample of jets containing D^* mesons [136] (charge-conjugate decays are implicitly included), by comparing the yield of D^* mesons before and after the MV1 tagging cut. The contamination with D^* mesons that result from B-hadron decays is measured with a fit to the pseudo-proper time distribution of the selected candidates. An additional correction factor covering the extrapolation from semileptonic D-meson decays to the inclusive sample is also applied [137].

Finally, a $t\bar{t}$ sample with dileptonically decaying top quark pairs is used to calibrate the b-jet efficiency. A combinatorial likelihood method is used, which considers the correlations between the jets in the events, resulting in reduced uncertainties on the SFs [138]. In order to avoid overlap of the data used for the calibration and the data used for the main analysis of this thesis, also performed in the opposite-sign dilepton channel, the b-tagging calibration derived from the $t\bar{t}$ 2-jet selection is used.

Figure 4.12 shows the calibration SFs for b-, c- and light jet tagging efficiencies for the 70% operating point in MV1 from the 2012 dataset. The final event weight correction applied to the MC sample is the product of the weights from each jet selected in the event:

- If a jet is tagged by the b-tagging algorithm, the corresponding weight is the b-tagging SF of the corresponding jet flavour.
- If a jet fails the b-tagging criteria, a weight corresponding to $(1 - SF * \epsilon_{MC})/(1 - \epsilon_{MC})$ is assigned.

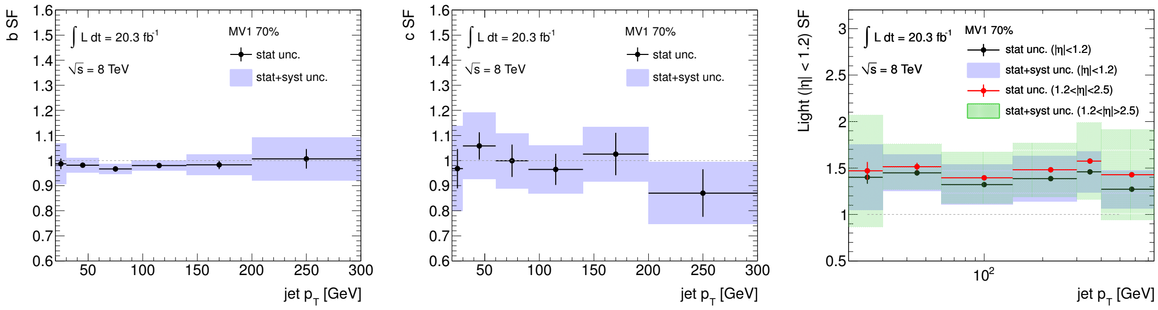

Figure 4.12.: SFs for (left): b-, (middle): c- and (right): light jet tagging efficiencies at the 70 % operating point with the MV1 algorithm. The SFs are measured as a function of jet p_T, and in the case of the light jets, also as a function of $|\eta|$ [139].

4.5. Missing Transverse Energy

Given the initial negligible transverse energy from the colliding partons, a vectorial sum of the energy in the transverse plane of the final state particles is expected to be equal to zero, by energy conservation. Nevertheless, the presence of undetectable particles in the event, such as neutrinos or new weakly-interacting particles, will be translated in a vector momentum imbalance in the transverse plane. The missing transverse energy (E_T^{miss}) is therefore defined as the momentum imbalance in the transverse plane with respect to the beam axis and is obtained from the negative vectorial sum of the momenta of all particles detected from the pp collision. In the $t\bar{t}$ and $t\bar{t}V$ final states with two opposite-sign charged leptons, real E_T^{miss} is expected from the neutrinos originating either from the leptonic W-boson decay, or from the invisible Z-boson decay, for a small fraction of the $t\bar{t}Z$ selected events.

The important requirements for the reliable measurement of the E_T^{miss} are maximum detector coverage and small detector resolution effects. The presence of dead regions and various sources of noise, as well as cosmic-ray and beam-halo muons crossing the detector, can create fake E_T^{miss} [140].

The E_T^{miss} reconstruction [141] takes into account energy deposits in the calorimeter and muons reconstructed in the muon spectrometer. Track information is added to recover the contribution from low-p_T particles which are missed in the calorimeter.

The E_T^{miss} calculation uses reconstructed and calibrated objects. The calorimeter energy deposits associated with a reconstructed and identified high-p_T parent object are considered in the following order: electrons, jets and muons. Hadronically-decaying taus and photons are not considered in this analysis. Deposits not associated with any such objects are also considered in the E_T^{miss} calculation as the *Cell-Out* term. The E_T^{miss} can be then expressed as the sum of the following terms:

$$E_{x(y)}^{miss} = E_{x(y)}^{miss,el} + E_{x(y)}^{miss,jet} + E_{x(y)}^{miss,muon} + E_{x(y)}^{miss,soft-jet} + E_{x(y)}^{miss,cell-out}, \tag{4.5}$$

$$E_T^{miss} = \sqrt{(E_x^{miss})^2 + (E_y^{miss})^2}, \tag{4.6}$$

where the additional term $E_{x(y)}^{miss,soft-jet}$ includes the contribution from jets with $p_T < 20$ GeV [10].

The reconstructed and calibrated jets and muons correspond to the same collection used in the main analysis of this thesis, while for electrons the cut-based *tight++* working point is used for the E_T^{miss} calculation, instead of the likelihood-based *medium*. Studies have shown that the impact of using the specified electron identification method in the E_T^{miss} calculation instead of the one used in the analysis is negligible.

Given that the E_T^{miss} measurement is significantly affected by pile-up effects (especially during 2012 data-taking), methods were developed to suppress such contributions. They are based on tracks, to suppress pile-up in the E_T^{miss} jet term, and on both tracks and the jet area method, to reduce pile-up effects in the E_T^{miss} soft-jet/cell-out terms [140].

4.6. Event Preselection

Once the objects are defined, a set of selection criteria is required to be fulfilled by the events:

Good Run Lists

The Good Run Lists (GRLs) define a set of data-taking runs, each divided in “luminosity blocks”, for which data fulfils good quality criteria in order to be used for analyses. Only data belonging to these GRLs are therefore used.

---

[10] In 2012 data, $E_{x(y)}^{miss,soft-jet}$ and $E_{x(y)}^{miss,cell-out}$ are calculated together.

Lepton Trigger

Only events collected using a single electron or muon trigger (described in Sections 4.2.2 and 4.3.2) are accepted.

Non-collision Background Rejection

After the event has been accepted by the trigger, it is required to have at least one reconstructed vertex with at least four associated tracks with $p_T > 400$ MeV, consistent with the beam collision region in the $x - y$ plane, in order to reduce pile-up. If more than one vertex is found, the primary vertex is taken to be the one which has the largest sum of the squared momenta of its associated tracks. Furthermore, in order to reject cosmic events, the event is discarded if it contains two muons of opposite sign that have a $|d_0| > 0.5$ mm, and are back-to-back, i.e. have a $\Delta\phi > 3.10$.

"Bad Jets" Removal

Events are rejected if a "bad jet" (defined in Section 4.4.1) with $p_T > 20$ GeV and $|\eta| < 4.5$, without any requirements on the JVF, is found.

Opposite-Sign Dilepton Preselection

The dilepton selection used in the main analysis of this thesis additionally requires the event to have two reconstructed leptons (electron or muon) with opposite-sign charges (OS), resulting in the dilepton channels: e^+e^-, $\mu^+\mu^-$, and $e^\pm\mu^\mp$. At least one selected lepton with $p_T > 25$ GeV is required to match a lepton reconstructed by the high-level trigger with a $\Delta R < 0.15$. The p_T requirement on the subleading lepton has been lowered to $p_T > 15$ GeV in the context of the $t\bar{t}V$ analysis in order to increase the signal efficiency. Furthermore, events are rejected if a selected electron and muon share an inner detector track ($\Delta\theta < 0.005$ and $\Delta\phi < 0.005$). Reconstructed leptons are also required to match the leptons in the truth record of the MC simulation, in order to avoid double counting with the fake lepton estimation.

The scalar sum of the transverse momentum of all selected leptons and jets (H_T) is required to be above 130 GeV in the $e\mu$ channel, in order to suppress background contributions from Z/γ^*+jets production (with the Z-boson decaying into leptonically decaying τ leptons).

A cut at low values of the invariant mass of the two selected leptons, m_{ll}, is applied in events with e^+e^- or $\mu^+\mu^-$, requiring $m_{ll} \geq 15$ GeV in order to remove contributions from the weak decay of low-mass hadronic resonances, such as the J/Ψ and Υ, into same-flavour leptons. Furthermore, a cut on the m_{ll} within a 10 GeV window around the Z-boson invariant mass is used to define two analysis categories in the opposite-sign dilepton $t\bar{t}V$ measurement presented in this thesis. Further requirements on the numbers of jets and the number of b-tagged jets will also define different regions within the two above mentioned categories. This additional selection, together with further cuts on the E_T^{miss}, will be described in Section 7, where the $t\bar{t}V$ analysis strategy is introduced.

CHAPTER 5

Modelling of Physics Processes

5.1. Event Simulation

In Section 4, the experimental aspects of object reconstruction and calibration were introduced. However, the majority of measurements or searches for new physics rely at some level on the simulation of the physics processes of interest (signal and background), i.e. on the capability to reproduce the evolution of the hard process to the final object observed in the detector. Stimulated by the study of more complex final states over the past several years, an increasing demand for higher precision descriptions of the physics processes has motivated the rethinking of calculation and simulation paradigms, leading ultimately to new generator tools.

Figure 5.1 is a sketch of an event produced at a hadron collider, which is expected to be described by an event generator. Fortunately, nature allows for the factorisation of such events into different well-defined stages, each corresponding to a different kinematic regime:

- *Hard Scattering*: in general, the key part of the event simulation, which can be calculated at fixed order perturbation theory in the coupling constants. It relies on computations based on matrix elements (ME). This part is process dependent and valid for well-separated hard partons.

- *Parton Showers (PS)*: QCD evolution that links the hard scale of coloured parton creation (high-energy regime) with the hadronisation scale, where colourless hadrons are formed (low-energy regime). It is process independent and valid when partons are collinear and/or soft. The most well-known parton shower MC event generators are PYTHIA [142], HERWIG [143] and SHERPA [144].

- *Hadronisation*: QCD partons are transformed into primary hadrons at the hadronisation scale Λ_{QCD} [1] by applying phenomenological fragmentation models, such as the *string* hadronisation implemented in PYTHIA or the *cluster* hadronisation implemented in HERWIG. These primary hadrons finally decay into particles that will be observed in the detector. Similar to the parton shower, this stage is process independent.

---

[1] Scale at which QCD is no longer perturbative.

- *Underlying Event*: a feature of hadron collisions, where remnants of the incoming hadrons can produce secondary hard or semi-hard interactions. There is no complete first-principles theory available to describe these effects. Their description relies on phenomenological models, that include parameters which need to be tuned to reproduce data, similar to the case of fragmentation models.

- *QED Bremsstrahlung*: photon radiation which can occur at any stage (illustrated by yellow lines in Figure 5.1).

An important aspect that has to be carefully treated in the event generators is the definition of the transition between the matrix element and the parton shower. A generator has to merge these two complementary steps in such a way, that it avoids double counting of the same configurations and ensures smooth distributions. The available parton-jet matching schemes are the CKKW [145, 146, 147] and CKKW-L [148] schemes, which are implemented in different versions of the SHERPA generator, and the MLM scheme [149], implemented in both the ALPGEN [150] and MADGRAPH [151] generators. SHERPA, ALPGEN and MADGRAPH are "multileg" generators, which describe the ME of a $(2 \to n)$ process.

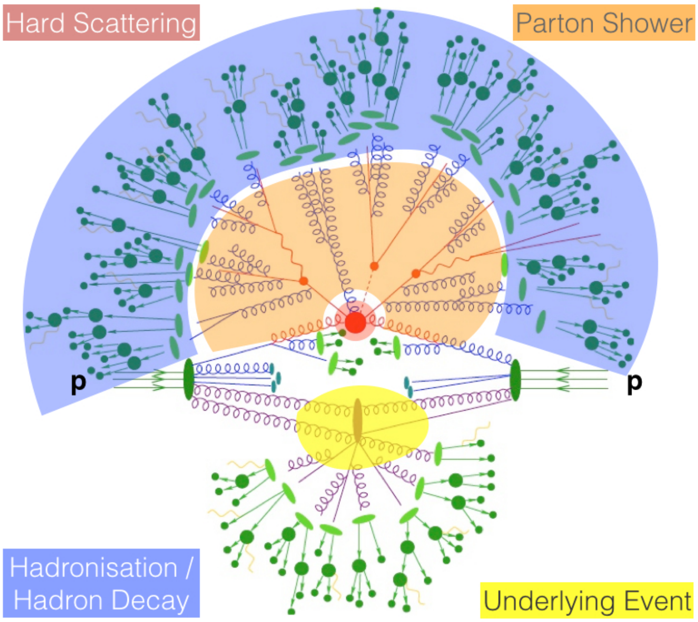

Figure 5.1.: Sketch of a $t\bar{t}H$ event as produced by an event generator. Modified version of figure in [144].

In order to have a complete MC simulation which can be compared to data, the detector response to the generated particles traversing the detector is simulated with GEANT4 [152, 153]. It uses a detailed detector description, but requires a significant running time per event. A faster alternative which is being widely used within the ATLAS collaboration, especially when high MC statistics are required on a short time scale, is the so called "fast simulation", where the detector response is parametrised. In particular, in this analysis, the fast simulated samples use the *ATLFAST-II* simulation, which uses a parameterised calorimeter simulation (FastCaloSim) [154]. Finally, all simulated samples are processed through the same reconstruction software as the data.

Although all MC hard process events are overlaid with minimum bias events to simulate pile-up effects, a further reweighting is applied to MC events to match the distribution of the number of interactions per bunch crossing in the analysed dataset.

In the context of the $t\bar{t}V$ opposite-sign dilepton measurement, both signal and background processes are estimated from MC simulation and normalised to their theoretical cross sections. For the main background processes in this analysis, $t\bar{t}$ and Z+jets, corrections derived from data-driven methods are applied to simulation in order to improve their description of data.

5.2. Signal Processes

The signal samples of $t\bar{t}V$ ($V = W, Z$) production are generated with the Madgraph v5 generator using leading-order (LO) matrix elements with up to one additional parton at matrix element level and the CTEQ6L1 PDF set [155]. Pythia 6.425 with the AUET2B tune [156] is used for hadronisation and to describe the underlying event. Both full and fast simulation samples with a single lepton filter were produced with no statistical overlap between them, and are used in different stages of the analysis, as it will be explained in Section 7.2 and 7.3.

The $t\bar{t}V$ samples are normalised to the inclusive next-to-leading-order (NLO) QCD cross section predictions given in Section 2.4. The top quark mass is assumed to be 172.5 GeV. These samples, generated and validated during the development of the $t\bar{t}V$ measurement presented in this thesis, include the following features and supersede the previous set of signal samples:

- The top quark decay is performed by Madgraph, hence preserving the spin and polarisation effects in the top quark decay products (this information is lost when performing the decay with Pythia). During the validation of the new samples, some interesting asymmetries between the lepton and antilepton η (stemming from the top quarks) were observed, particularly significant in the $t\bar{t}W$ process, as can be seen in Figure 5.2. This can be explained by the fact that the W-boson is emitted from the initial state $q/\bar{q}$, which can therefore only be left/right handed. Thus, the initial $q/\bar{q}$ is turned into polarised beams, and consequently, the top and antitop quarks are produced polarised. As a result, their decay products show asymmetrical distributions in rapidity. This observation triggered an intensive discussion with theorists and inspired a paper about the possibility to study the charge asymmetry between top and antitop quarks in the $t\bar{t}W$ process [2] [157].

- The $t\bar{t}\gamma^*$ contribution, and corresponding interference effects between Z/γ^*, are included in the $t\bar{t}Z$ samples. Given that there is no current NLO calculation of the $t\bar{t}Z/\gamma^*$ cross section, the *k-factor* (σ_{NLO}/σ_{LO}) was computed with aMC@NLO [158] and found to be 1.4 (instead of 1.34) [159].

5.3. Background Processes

As it will be shown in more detail in Section 7, the main background contributions in the opposite-sign dilepton $t\bar{t}V$ channel come from $t\bar{t}$ and Z+jets production. Smaller contributions arise from single top quark, diboson (WW, WZ, ZZ) production, from the associated production of a Higgs boson and a $t\bar{t}$ pair, from the associated production of a single top and a Z-boson, as well as from misidentified leptons.

---

[2] The SM predicts this asymmetry to be much smaller at the LHC than in Tevatron for the $t\bar{t}$ process.

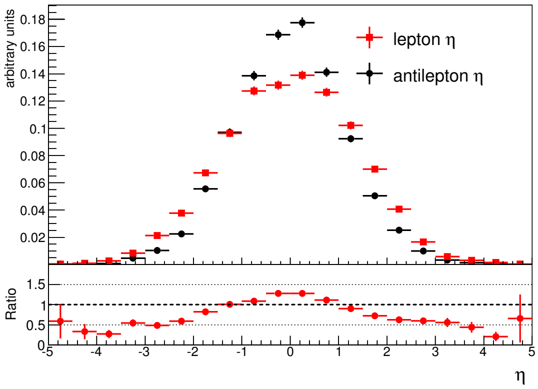

Figure 5.2.: Asymmetric pseudorapidity distribution of the lepton and antilepton originating from the top quark decay, produced from the $t\bar{t}W$ samples decayed with MADGRAPH.

Samples of Z+jets events are generated using the ALPGEN v2.14 LO generator and the CTEQ6L1 PDF set. The parton shower and fragmentation are modelled with PYTHIA 6.425. The Z+jets samples are generated with up to five additional partons, separately for Z+light jets, $Z+b\bar{b}$+jets and $Z+c\bar{c}$+jets. The overlap between $Z+Q\bar{Q}$ ($Q = b, c$) events, also called Z+HF in the following, generated from the matrix element calculation and those generated from parton-shower evolution in the Z+light jet samples is avoided using an algorithm, called *HFOR* (heavy-flavour overlap removal). This algorithm utilises the angular separation between the heavy quarks, such that, if $\Delta R(Q, \bar{Q}) > 0.4$, the matrix-element prediction is used, otherwise the parton shower prediction is employed [3]. The Z+jets background is normalised to the inclusive next-to-next-to-leading-order (NNLO) QCD cross section [160]. The generation details of the Z+jets samples also apply to the simulated W+jets samples, which are used in the estimation of the misidentified lepton background from simulation, as explained in Section 5.3.3.

Simulated $t\bar{t}$ events are generated using the POWHEG generator [76, 77, 78], which implements the NLO matrix element for inclusive $t\bar{t}$ production, with the CT10 PDF set. POWHEG is interfaced to PYTHIA 6.425 with the CTEQ6L1 set of parton distribution functions and the Perugia2011C tune [161]. Given the significant increase in MC statistics, fast simulation $t\bar{t}$ samples generated with a dilepton filter are used in this analysis. The sample is normalised to the theoretical calculation performed at NNLO in QCD that includes resummation of next-to-next-to-leading logarithmic (NNLL) soft gluon terms given in Section 2.3.1.

Unlike "multileg" generators, POWHEG is expected to describe jet multiplicities properly only for $t\bar{t}$ accompanied by up to two jets. Nevertheless, this generator interfaced with PYTHIA provides a good description of the jet multiplicity in data up to much higher multiplicities, as well as the heavy flavour fraction in $t\bar{t}$ production, despite the fact that the heavy flavour component originates only from the parton shower.

Both $t\bar{t}$+jets and Z+jets processes are classified in their light and heavy-flavour (HF) contributions, based on the truth flavour of extra jets matched to B or C hadrons. Particle jets are defined at truth MC level, clustering stable particles using the anti-k_T algorithm with jet radius R=0.4. Muons and neutrinos are excluded from the jets. A b-jet is defined as a jet containing a B-hadron with $p_T > 5$ GeV within a $\Delta R < 0.3$ of the jet axis. In order to identify additional heavy-flavour production, the closest B-hadron to a b-quark originating from top quark decay

---

[3] As explained in Section 5.1, the parton shower gives a better description for collinear partons.

is excluded and jets matching these hadrons are not considered. A jet can contain more than one B-hadron, notably from a collinear gluon splitting where the individual b-quarks are not resolved into separate jets. B-hadrons inside jets are counted and jets are categorised into single hadron (*b-jet*) and double hadron (*B-jet*). Equivalent categorisation is performed for c-jets, if no match to a B-hadron is made.

The $WW/WZ/ZZ$+jets samples are generated using Sherpa with massive b and c-quarks, with up to three additional partons in the matrix element (ME) and parton shower (PS) and are normalised to their NLO QCD theoretical cross sections [162].

Samples of single top quark backgrounds corresponding to the t-channel, s-channel, and Wt production mechanisms are generated with POWHEG using the CT10 PDF set. All samples are interfaced to PYTHIA 6.425 with the CTEQ6L1 PDF set using the Perugia2011C tune. Overlaps between the $t\bar{t}$ and Wt final states are removed using the so-called *diagram removal* (DR) scheme [163]. The single top quark samples are normalised to the approximate NLO+NNLL theoretical cross sections [164, 165, 166] using the MSTW2008 NNLO PDF set.

The production of a single top quark in association with a Z-boson is simulated with MADGRAPH V5 and the CTEQ6L1 PDF set. MADGRAPH is interfaced to PYTHIA 6.425 using the AUET2B tune and the CTEQ6L1 PDF set. The relevant samples are normalised to the NLO predictions obtained from AMC@NLO.

All PYTHIA6 samples use PHOTOS 2.15 [167] to simulate photon radiation and TAUOLA 1.20 [168] to simulate τ decays.

Samples of $t\bar{t}H$ events are simulated using matrix elements obtained from the HELAC-ONELOOP package [79] that correspond to NLO QCD accuracy for the inclusive $t\bar{t}H$ process. POWHEG BOX [76, 77, 78] serves as an interface in order to shower the matrix element calculation. The samples, referred to as POWHEL samples, are produced using the CT10 NLO PDF sets, and the normalisation and Higgs boson decay branching fractions are taken from the NLO QCD calculations from Ref. [169].

Table 5.1 provides a summary of the MC samples used as the nominal prediction in the analysis.

Sample	Generator	PDF	Shower	Normalisation
$t\bar{t}V$	MADGRAPH	CTEQ6L1	PYTHIA 6.427	NLO
$t\bar{t}$+jets	POWHEG	CT10	PYTHIA 6.425	NNLO+NNLL
Z+jets	ALPGEN	CTEQ6L1	PYTHIA 6.426	NLO
Single top	POWHEG	CT10	PYTHIA 6.425	NLO+NNLL
Diboson	SHERPA	CT10	SHERPA	NLO
$t\bar{t}H$	HELAC-Oneloop	CT10	PYTHIA 8.1	NLO
Single Top + Z	MADGRAPH	CTEQ6L1	PYTHIA 6.425	NLO
W+jets	ALPGEN	CTEQ6L1	PYTHIA 6.426	NLO

Table 5.1.: A summary of generators, PDF sets and cross section calculations used for various processes.

5.3.1. $t\bar{t}$ corrections

A measurement of the normalised differential cross sections of $t\bar{t}$ production at $\sqrt{s} = 7$ TeV using the ATLAS detector showed that data distributions of top-quark and $t\bar{t}$ transverse momentum are softer than those predicted by several MC simulations, as can be seen in Figure 5.3 [170].

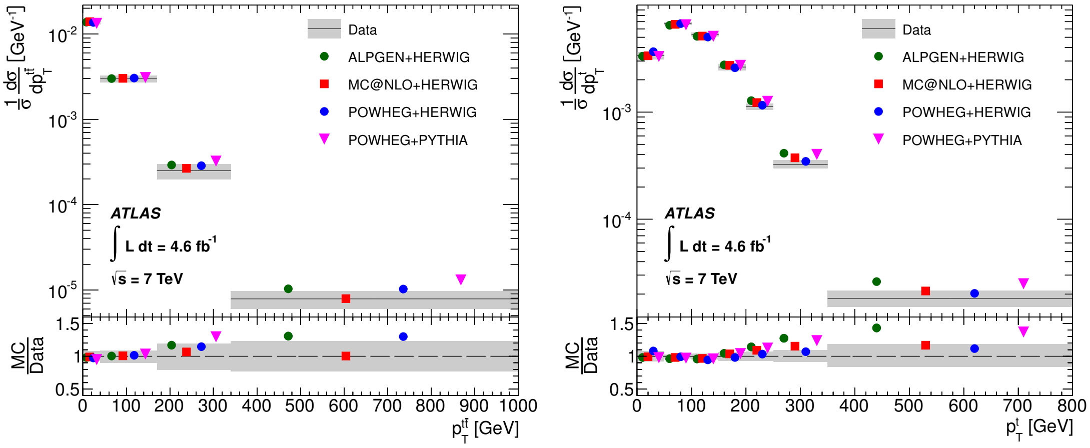

Figure 5.3.: Normalised differential cross sections for (left): the transverse momentum of the $t\bar{t}$ system and (right): the transverse momentum of the hadronically decaying top quark, measured at $\sqrt{s} = 7$ TeV and compared to different MC generators. The results are unfolded to the parton level after QCD radiation [170].

In order to correct for this effect, and improve the agreement between data and simulation in the top pair production dominated regions in the $t\bar{t}V$ analysis, $t\bar{t}$ events simulated with POWHEG+PYTHIA are corrected to reproduce the top quark p_T and $t\bar{t}$ system p_T measured in data. Two event reweighting factors were derived, taking into account the correlation between the corrections for top p_T and $t\bar{t}$ p_T. First, a weight to correct $t\bar{t}$ p_T is applied, followed by a residual correction of top p_T. This procedure is referred to as *sequential reweighting*. The correction is derived for a top mass of 172.5 GeV and is applied to each event at the truth MC level, before parton showering.

Since the correction was derived using 7 TeV data, the top quark and $t\bar{t}$ p_T distributions at 8 TeV were compared to those at 7 TeV for several generators. The ratio of those distributions at 8 TeV to 7 TeV were found to be very stable across generators, showing a maximum deviation of 3 % in both top quark and $t\bar{t}$ p_T. This study proved that the correction derived using 7 TeV data is applicable to the $t\bar{t}V$ analysis at 8 TeV.

After applying the correction to $t\bar{t}$ simulated events at $\sqrt{s} = 8$ TeV, the effect of the reweighting on the agreement between data and MC simulation can be seen in $t\bar{t}$ dominated regions, improving the jet multiplicity distribution (mainly due to the correction of the $t\bar{t}$ p_T distribution), and the transverse momentum of various objects, for example H_T (mainly due to the correction of the top p_T distribution). Figure 5.4 shows the final H_T and jet multiplicity distributions after corrections in the $t\bar{t}$ dominated region within the $t\bar{t}V$ measurement for data and MC simulation, where a good description of the jet multiplicity up to 5 jets can be seen.

5.3.2. Z+jets corrections

Measurements of the $Z(\rightarrow ll)$+jets differential cross section as a function of the transverse momentum of the Z-boson candidate (denoted in the following as p_T(Z), since two leptons are always required in this analysis), have shown that the ALPGEN generator predicts a much harder p_T(Z) spectrum than data. Figure 5.5 (left) shows a comparison between the unfolded measurement of the Z+jets differential cross section and the prediction of several generators, as

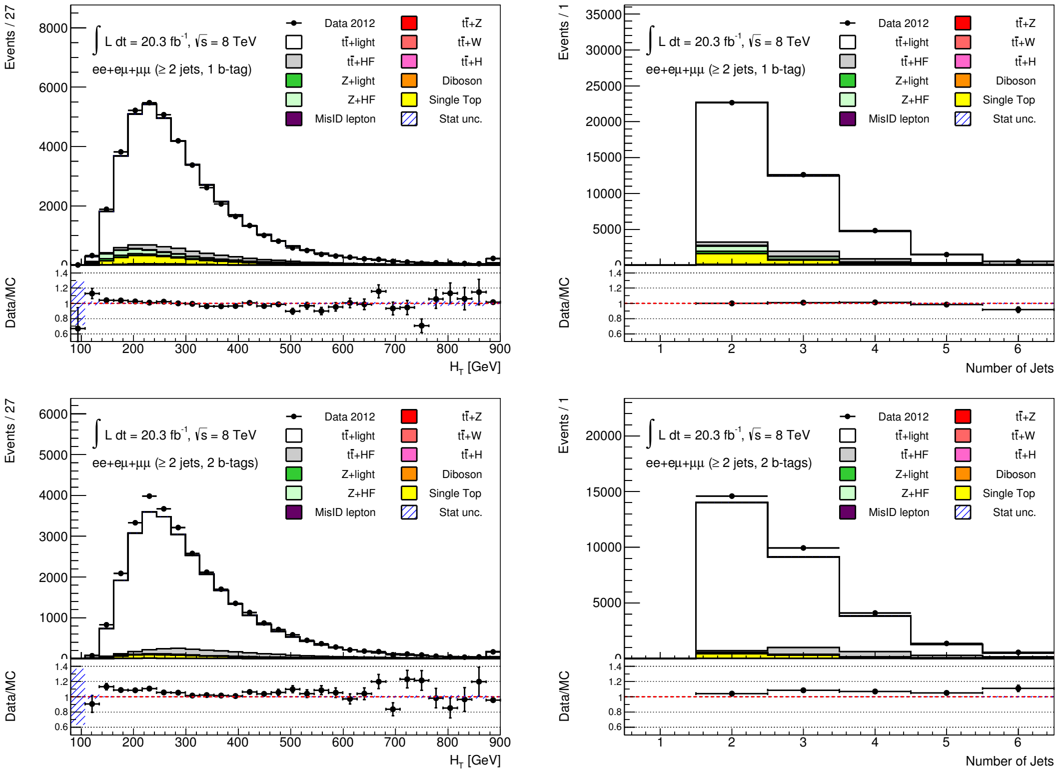

Figure 5.4.: Comparison of data and MC distributions for (left): H_T and (right): jet multiplicity, in the OS dilepton $t\bar{t}$ dominated region with (top): ≥ 2 jets and 1 b-jet, or (bottom): 2 b-jets, after applying corrections on $t\bar{t}$ p_T and top p_T. The error band contains only the statistical error on MC.

a function of p_T(Z), including the nominal generator used in this analysis, Alpgen [4] [171].

To correct for this deficiency, the reconstructed p_T(Z) spectrum was studied in data and simulation at $\sqrt{s}$ = 8 TeV in a Z+jets dominated region. Events with two leptons with the same flavour (ee and $\mu\mu$) are selected, requiring the dilepton invariant mass to be within a Z mass window of 10 GeV, $|m(ll) - m(Z)| < 10$ GeV, and the presence of ≥ 2 jets, none of which are b-tagged. Correction factors, w_Z, were derived bin-by-bin from this comparison, as shown in Figure 5.5 (right), as the ratio:

$$w_Z = \frac{Z(\text{data})}{Z(\text{MC})} = \frac{N_{\text{data}} - N_{\text{other(MC)}}}{N_{Z(\text{MC})}}, \tag{5.1}$$

where N_{data} and $N_{\text{other(MC)}}$ are the number of observed events and expected background events from sources other than Z+jets, respectively, and $N_{Z(\text{MC})}$ is the Z+jets MC prediction, calculated in each bin of the p_T(Z) distribution. Data yield is normalised to the one in simulation to extract a shape-only correction. This correction is applied to Z+jets MC events as an event weight per reconstructed p_T(Z) bin.

The correction factors for p_T(Z) were also derived in other regions as a cross check, such as the exclusive regions with exactly 2 jets and 0 b-jets and the individual dilepton channels (ee and $\mu\mu$), showing a good compatibility between them. The corrections were also derived from

---

[4] In the differential Z+jets measurement, Alpgen is interfaced with Herwig, instead of Pythia

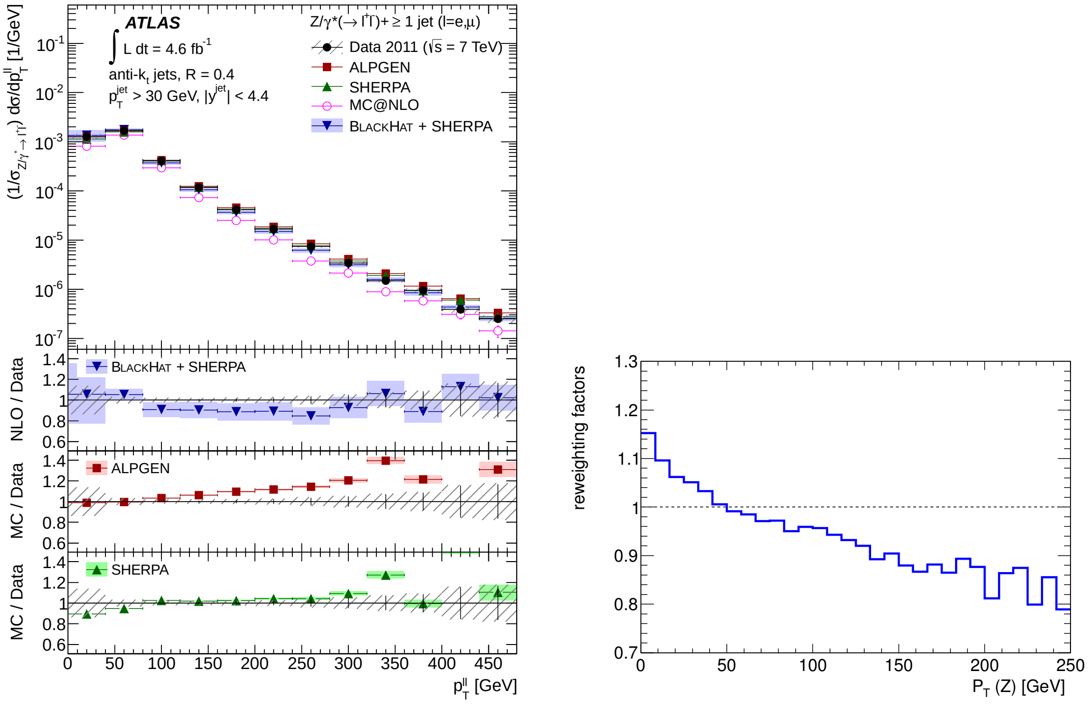

Figure 5.5.: (Left): Measured cross section for $Z(\rightarrow ll)$+jets events as a function of the transverse momentum of the Z candidate (p_T(Z)) in events with at least one jet with $p_T > 30$ GeV and $|\eta| < 4.4$ in the final state, compared to several MC generators at $\sqrt{s} = 7$ TeV [171]. (Right): Derived correction factors $w_Z = \frac{Z(\text{data})}{Z(\text{MC})}$ per p_T(Z) bin in a Z+jets dominated region using Alpgen+Pythia Z+jets prediction at $\sqrt{s} = 8$ TeV.

Z+light and Z+HF jet samples separately. Since both corrections were found to be consistent with one another, a single p_T(Z) correction is applied to Z+jets events inclusively.

Another known deficiency of the Alpgen+Pythia Z+jets generator is the prediction of the heavy flavour content of the jets produced in association with the vector boson. Since the fraction of additional jets originating from heavy-flavour quarks in association with the Z-boson varies significantly between the regions with at least 2 jets and 0 b-jets ($\geq$ 2 j, 0 b) and at least 2 jets and 1 b-jet ($\geq$ 2 j, 1 b), Z+HF and Z+light normalisation corrections can be derived by solving the following system of equations:

$$x * N^{2j0b}_{Z\text{+light}} + y * N^{2j0b}_{Z\text{+HF}} = (N^{2j0b}_{\text{data}} - N^{2j0b}_{\text{other}}),$$
$$x * N^{2j1b}_{Z\text{+light}} + y * N^{2j1b}_{Z\text{+HF}} = (N^{2j1b}_{\text{data}} - N^{2j1b}_{\text{other}}),$$

where x and y are the scale factors for the number of Z+light and Z+HF jets, respectively. The correction factors of $x = 0.94$ for Z+light and $y = 1.50$ for Z+HF contributions were obtained.

Figure 5.6 shows the p_T(Z) distributions for events with exactly 2 jets and 0, 1 and 2 b-tags before any correction (left column) and after applying both the p_T(Z) shape-only and Z+HF/Z+light normalisation corrections (right column). While the agreement in the 2 jet bin with 0 and 1 b-tag is achieved almost by construction, a very good agreement between the data and the corrected MC prediction is obtained in the control region with 2 jet and 2 b-tags.

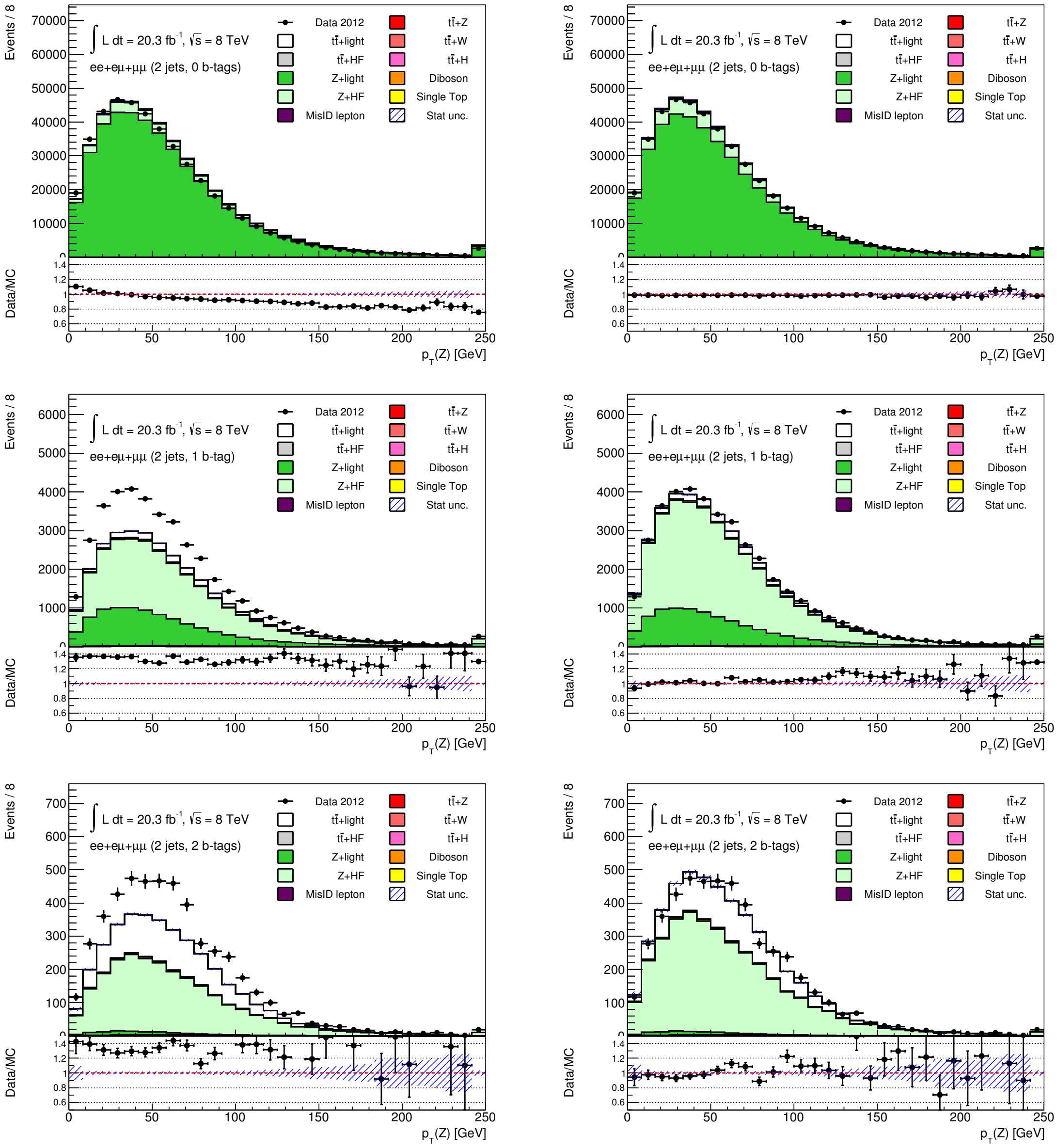

Figure 5.6.: Data and MC distributions of p_T(Z) in a Z-dominated region, (left column): without any corrections, and (right column): with both p_T(Z) and Z+HF/Z+light normalisation corrections applied. The error band contains only the statistical error on MC. The figures from top to bottom highlight the (2 j, 0 b), (2 j, 1 b), and (2 j, 2 b) regions, respectively.

Besides the Alpgen+Pythia Z+jets sample, Z+jets events produced with Alpgen+Herwig and Sherpa with massive b, c quarks were studied. As already seen in Figure 5.5 (left), all generators need a correction of the p_T(Z) distribution to match data. For angular distributions, Alpgen+Pythia shows a clear disagreement between data and MC at low values of the ΔR

between two jets. The distribution of the average ΔR between all dijet systems in the event, shown in Figure 5.7 (top left), is taken as a representative variable to highlight this discrepancy. This low ΔR region is correlated to the low invariant mass region of dijet systems, as can be seen in Figure 5.7 (top right). Given that the low ΔR and M_{inv} (jj) regions are background dominated, a cut on the average distance between two jets $\Delta R^{\rm jj}_{\rm ave} > 0.75$ is applied in the $t\bar{t}V$ analysis to remove the poorly described region by Alpgen+Pythia Z+jets simulation. The distributions after the cut are shown in Figure 5.7 (bottom).

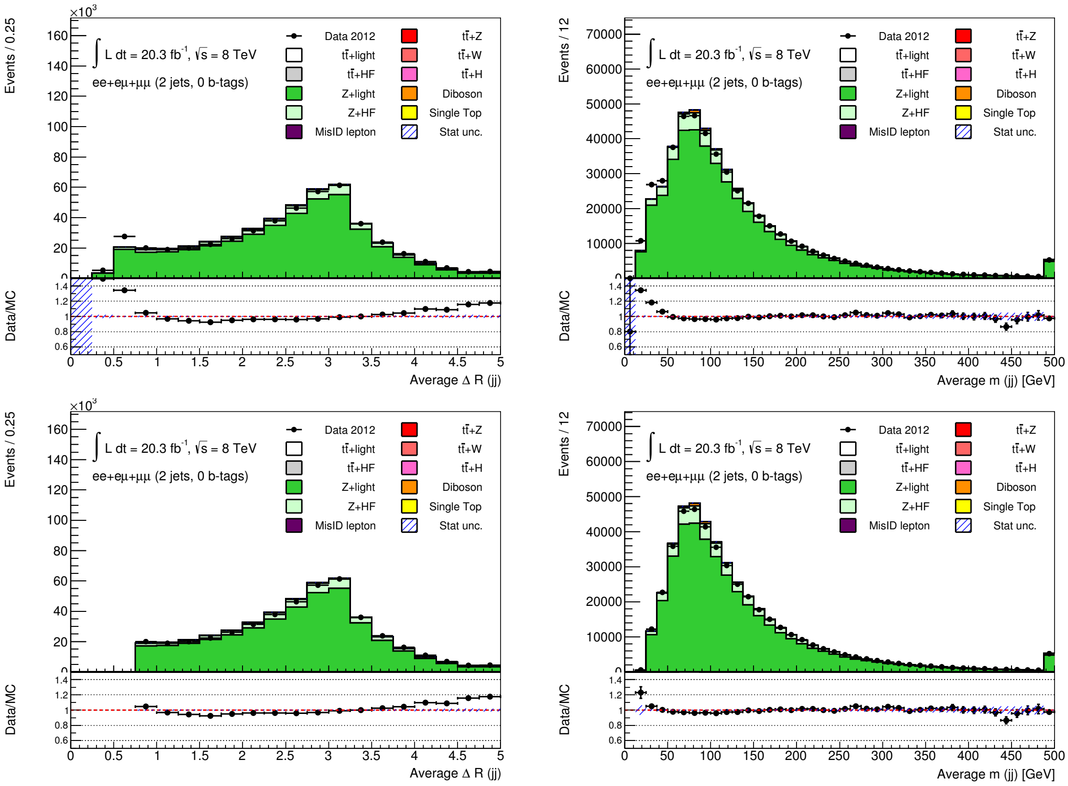

Figure 5.7.: Data and MC distributions of (left): $\Delta R^{\rm jj}_{\rm ave}$ and (right): $M^{\rm jj}_{\rm ave}$, (top): before and (bottom) after the $\Delta R^{\rm jj}_{\rm ave} > 0.75$ cut in events with exactly 2 jets and 0 b-jets. The error band contains only the statistical error on MC.

After all the corrections and the angular cut are applied, Figure 5.8 shows that the Z+jets background is well modelled up to 5 additional jets in the opposite-sign dilepton Z-dominated region. The region with exactly 2 b-jets, Figure 5.8 (right), is one of the $t\bar{t}V$ analysis regions, which will be introduced in Section 7.

5.3.3. Misidentified lepton background

The misidentified lepton background, also called *fakes* or *misID leptons* in the following, originates from different types of sources depending on the lepton flavour. There are several sources of misidentified electrons: (a) *non-prompt* electrons, produced in the showering process rather than in the hard interaction, (b) electrons from photon conversion, (c) electrons from single lepton heavy-flavour hadron decay, (d) jets with a high fraction of their energy deposited in the EM calorimeter identified as electrons. Muon fakes consist of *non-prompt* muons, originating from single lepton B- or C-hadron decays or from decays in flight. In the lepton+jets channel,

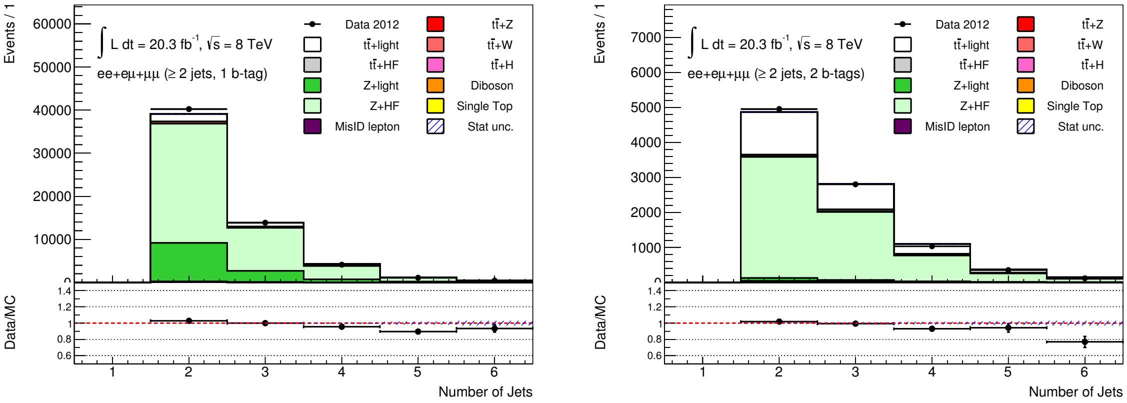

Figure 5.8.: Jet multiplicity spectrum in the OS dilepton Z-dominated region after applying corrections to the Z+jets MC in events with (left): 1 b-jet and (right): 2 b-jets. The last bin includes the overflow (≥ 6 jets). The error band contains only the statistical error on MC.

the main source of misidentified lepton background comes from multijet production. Since its cross section is approximately four orders of magnitude larger than that of the $t\bar{t}$ production, it is an important source of background. In the dilepton channel, on the contrary, single lepton W+jets and $t\bar{t}$ events are the main contributors to the fake lepton background, while the chances of misidentifying two leptons from multijet production are significantly lower.

Two alternative methods were studied in the dilepton channel. The first estimate of fakes was obtained from the same-sign charge (SS) dilepton selection. Assuming that approximately equal number of fakes are expected in the same sign as in the opposite sign (OS) dilepton region, the misID lepton contribution was derived as follows:

$$Fakes = Data(SS) - MC(SS).$$

This approach, however, suffers from the very limited statistics of same-sign dilepton events in high b-tag and jet multiplicity regions. Also, given the subsequent combination with the same-sign dilepton $t\bar{t}V$ channel, it is desirable to avoid using the SS method for the misID lepton background estimation, due to the potential statistical overlap between the channels.

Since the fake background contribution in the OS dilepton channel is negligible in the signal region compared to the total background (approximately 0.2 % of the total background), the second estimate of fakes was obtained from MC simulation and compared with the one from the SS selection. Fake events are required to fail at least one of the lepton truth matching requirements (explained in Section 4.6). The individual contribution of each MC sample to the total misID lepton yields can be seen in Figure 5.9, where events with at least 2 jets are considered. Z+jets and W+jets fakes dominate the low H_T region, while $t\bar{t}$ fakes dominate the high H_T region. Inclusive yields of fakes in the SS method and fakes in MC differ only by 5%. The shape agreement in H_T between the two methods also indicates that MC provides a good estimation of the fake background. The previously introduced corrections for $t\bar{t}$ and Z+jets MC samples have also been applied to obtain the fakes estimate. Small differences in shape between the H_T distribution obtained by the two methods are considered to be a shape uncertainty on the fake background estimate.

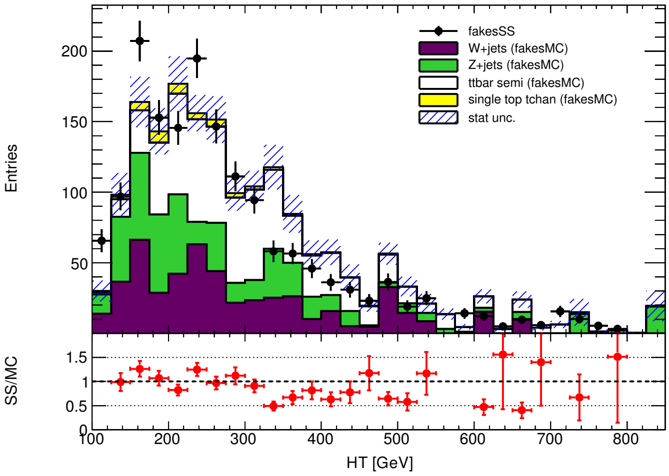

Figure 5.9.: H_T distribution, comparing fakes estimated from the SS dilepton selection and the ones predicted by MC.

CHAPTER 6

Reconstruction of $t\bar{t}$ in the dilepton final state

6.1. Challenges of the dileptonic $t\bar{t}$ system

The $t\bar{t}$ dilepton final state has a very clean signature with two charged leptons originating from the leptonic decays of both W-bosons and two b-jets from the top quark decays. However, the presence of the two neutrinos in the final state, which escape direct detection and can therefore only be inferred as a global E_T^{miss} in the event, leads to an under-constrained kinematic system. Therefore, the kinematic reconstruction of the $t\bar{t}$ dilepton final state is challenging and needs additional assumptions to be solvable. The Neutrino Weighting algorithm provides those additional assumptions and can be used to reconstruct the $t\bar{t}$ dilepton system.

6.1.1. The Kinematic Equations of the $t\bar{t}$ Dilepton System

The $t\bar{t}$ dilepton final signature includes two b-jets, two charged leptons, and two neutrinos, making a total of 6(particles) $\times$ 4(vector components) $=$ 24 degrees of freedom. The “known”, or measured, information includes the masses of all particles, the momenta of the charged leptons and the jets, and the sum of the momenta of the two neutrinos in the x and y direction, denoted as E_x^{miss} and E_y^{miss}. Additionally, there are three kinematic constraints:

- The relationship between the invariant mass of a W-boson, denoted by the index $i = (1, 2)$, and the four-momentum vector of its decay products:

$$M_{W_i}^2 = (E_{\nu_i} + E_{\ell_i})^2 - (\vec{p}_{\nu_i} + \vec{p}_{\ell_i})^2 \quad \text{for } i = 1, 2. \tag{6.1}$$

- A similar relationship between the invariant mass of a top quark, each denoted by the index $i = (1, 2)$, and the four-momentum vector of its decay products, with the additional assumption that $M_t = M_{\bar{t}}$:

$$M_{t_i}^2 = (E_{\nu_i} + E_{\ell_i} + E_{b_i})^2 - (\vec{p}_{\nu_i} + \vec{p}_{\ell_i} + \vec{p}_{b_i})^2 \quad \text{for } i = 1, 2; \tag{6.2}$$

$$M_{t_1} = M_{t_2}. \tag{6.3}$$

Considering all measured information and kinematic constraints, the system of equations is still under-constrained by one degree of freedom.

6.1.2. The Neutrino Weighting Algorithm

The Neutrino Weighting algorithm was originally used by the DØ collaboration [172, 173] as a reconstruction algorithm in the $t\bar{t}$ dilepton final state for the measurement of the top quark mass. Its original formulation adds three assumptions to the kinematic equations:

- The top quark mass is known *a priori.*
- The neutrino and antineutrino pseudorapidities, η_ν and $\eta_{\bar{\nu}}$, are assumed to be distributed as in the SM, which can be described by a Gaussian centred at zero, with a decay width weakly dependent on the top quark mass from MC simulation.

The algorithm ignores the two constraints on the E_x^{miss} and E_y^{miss} in the kinematic equations. With these assumptions, the kinematic system is constrained and the kinematic equations are now solvable [174]. The neutrino momentum is obtained from solving a quadratic equation. Therefore, there are up to two solutions per neutrino and antineutrino, resulting in a fourfold ambiguity .

Once the neutrino momenta solutions are calculated, the expected missing transverse momentum, $E_{x,exp}^{miss}$ and $E_{y,exp}^{miss}$, are derived from those solutions, and compared to the observed missing transverse energy, $E_{x,obs}^{miss}$ and $E_{y,obs}^{miss}$ [1]. The comparison is performed by allowing for a Gaussian missing energy resolution in the x and y direction, $\sigma_{E_x^{miss}}$ and $\sigma_{E_y^{miss}}$. The weight w is thus defined per event as:

$$w = \sum_{i=1}^{N} \exp\left(\frac{-(E_{x,exp,i}^{miss} - E_{x,obs}^{miss})^2}{2\sigma_{E_x^{miss}}^2}\right) \cdot \exp\left(\frac{-(E_{y,exp,i}^{miss} - E_{y,obs}^{miss})^2}{2\sigma_{E_y^{miss}}^2}\right), \tag{6.4}$$

where i runs over all permutations of jet assignments, neutrino rapidity assumptions given an assumed top quark mass [2], and neutrino momentum solutions for a particular neutrino rapidity assumption. Detector resolutions are included in this process by calculating each event and configuration several times with the kinematics of the jets and leptons, fluctuated according to their resolution. All weights resulting from each smeared event are summed.

The weight is calculated for different top quark mass assumptions, and yields a weight distribution as a function of the top quark mass hypothesis per event. The event weight indicates how well the reconstructed event matches a certain top quark mass hypothesis.

6.2. Kinematic Likelihood Fitter

The original Neutrino Weighting algorithm was designed specifically for top quark mass measurements. The idea of the project presented in this thesis was to build a more general reconstruction algorithm based on the Neutrino Weighting algorithm, which would allow not only to measure the top quark mass via summed-weight templates, but also to determine the most probable assignment of pairs of jets and charged leptons originating from the top or antitop quark, as well as the most probable kinematic solution of the neutrinos. Therefore, a likelihood-based reconstruction method was developed within the Kinematic Likelihood Fitter (KLFitter) framework for the kinematic reconstruction of the $t\bar{t}$ dilepton final state, as a project within this thesis.

---

[1] These two constraints were not used in solving the kinematic equations of the event.

[2] A scanning over the η_ν Gaussian distributions for a certain mass is performed, dividing the distribution in such a way, that the same number of top events is expected in each η_ν range.

The KLFitter [175] is a framework for kinematic fitting, based on the Bayesian Analysis Toolkit (BAT) [176]. Several reconstruction algorithms have been implemented within this framework to reconstruct the $t\bar{t}$ system in different decay modes. It initially included the likelihood-based algorithm for the reconstruction of the ℓ+jets $t\bar{t}$ final state, and it grew over the years, incorporating algorithms for other signatures, such as the all-hadronic $t\bar{t}$ final state or single top Wt decaying in the ℓ+jets channel. In order to reconstruct any of the $t\bar{t}$ final states, the best matching of reconstructed jets to partons is required. The different jet-parton assignments are called *permutations*. The *combinatorial background* comprises the incorrect jet-parton assignment. The detector resolution is simulated by smearing the parton-level energies with assumed resolution functions. The KLFitter maximises a likelihood function with respect to a given set of parameters and constraints. Typical parameters are the energies of jets and charged leptons, which are varied in the fit.

Although the dilepton final state is in principle less affected by the combinatorial background, given the presence of only two jets in the event, it includes the additional difficulty of under-constrained kinematics, if no assumptions are made. For the implementation in KLFitter, the Neutrino Weighting assumptions were incorporated in a likelihood, together with additional terms improving finding the best assignment of reconstructed jets to partons.

6.2.1. The Dilepton Likelihood

The likelihood function gives a value for every combination of jet and lepton assignment, based on the kinematic information of the reconstructed objects.

The likelihood for the reconstruction of $t\bar{t}$ events in the dilepton final state is defined as:

$$\begin{aligned}
L = &\left(\prod_{i=x,y} G(E_i^{miss}|p_i^{\nu}, p_i^{\bar{\nu}}, \sigma_i^{miss}(m_{top}, m_W, \eta^{\nu}, \eta^{\bar{\nu}}))\right) \cdot G(\eta^{\nu}|m_{top}) \cdot G(\eta^{\bar{\nu}}|m_{top}) \cdot \\
&W(\widetilde{E}_{jet_1}|E_{b_1}) \cdot W(\widetilde{E}_{jet_2}|E_{b_2}) \cdot \begin{cases} W(\widetilde{E}_{lep_1}|E_{lep_1}) \cdot W(\widetilde{E}_{lep_2}|E_{lep_2}), & ee \text{ channel} \\ W(\widetilde{E}_{lep_1}|E_{lep_1}) \cdot W(\widetilde{p}_{T_{lep_2}}|p_{T_{lep_2}}), & e\mu \text{ channel} \\ W(\widetilde{p}_{T_{lep_1}}|p_{T_{lep_1}}) \cdot W(\widetilde{p}_{T_{lep_2}}|p_{T_{lep_2}}), & \mu\mu \text{ channel} \end{cases} \cdot \\
&(m(lep_1, jet_1) + m(lep_2, jet_2))^{\alpha}
\end{aligned} \tag{6.5}$$

Each line in the likelihood is explained as follows:

- **Neutrino Weighting term**: The product of Gaussian distributions compares the calculated missing transverse energy, given the E_T^{miss} detector resolution, σ^{miss}, with the observed missing transverse energy, E^{miss}, in the x and y direction. This term is based on Equation 6.4. The two remaining Gaussians are the assumed distributions of the neutrino and antineutrino pseudorapidities according to the SM prediction. The likelihood values of each possible neutrino and antineutrino solution are summed internally.

- **Transfer Function terms**: Account for the difference, due to detector resolution and higher order effects, between the energy of the reconstructed object after calibration, denoted as $\widetilde{E}$ or E_{reco}, and the energy at LO parton-level, denoted as E or E_{truth}. In the case of muons, the transfer function is given in terms of the p_T of the reconstructed and truth object. The transfer functions are parametrised by a double-Gaussian as follows [3]:

$$W(E_{reco}, E_{truth}) = \frac{1}{2\imath(p_2 + p_3 p_5)} \left(\exp - \frac{(\Delta E - p_1)^2}{2p_2^2} + p_3 \exp - \frac{(\Delta E - p_4)^2}{2p_5^2} \right), \qquad (6.6)$$

where $\Delta E = (E_{truth} - E_{reco})/E_{truth}$. The parameters $p_1 ... p_5$ are defined as:

$$p_2 = \frac{a_2}{\sqrt{E_{truth}}} + b_2, \quad \text{or} \quad p_2 = a_2 + b_2 p_{T_{truth}} \quad \text{for muons,} \qquad (6.7)$$

$$p_i = a_i + b_i E_{truth} \qquad \text{for i=1,3,4,5,} \qquad (6.8)$$

where a_j and b_j (with $j = 1...5$) are fit parameters determined from MC. The p_2 parameter is based on the detector resolution in the calorimeter, for electrons and jets, or in the inner detector and muon spectrometer, for muons, as seen in Section 3.2. The transfer functions are obtained for each object type (b-jets, light-quark jets, electrons, muons, E_T^{miss}) and for different $|\eta|$ regions, since the resolution of the reconstructed objects is not uniform in $|\eta|$. The transfer functions were derived from $t\bar{t}$ samples generated with MC@NLO. Reconstructed objects are matched to the truth ones when the distance between them is $\Delta R < 0.3$. Figure 6.1 (left) shows the transfer functions for b-jets with $0.8 < |\eta| < 1.5$, parametrised as a function of the fitted parton energy.

Although not included as an explicit transfer function term in the likelihood, the E_T^{miss} resolution is used in the Neutrino Weighting term, as shown in Equation 6.4, and is derived as well from a parametrised function. The E_T^{miss} depends on the scalar sum of deposited energy in the calorimeters projected in the transverse plane, denoted as $\sum E_T$ [141]. Therefore, the width of the difference ($E_{x,y}^{miss} - p_{x,y}^{\nu}$) is parametrised as a function of $\sum E_T$, using a sigmoid function:

$$\sigma(\sum E_T) = p_0 + \frac{p_1}{1 + e^{-p_2(\sum E_T - p_3)}}. \qquad (6.9)$$

Figure 6.1 (right) shows the transfer functions for neutrinos, or E_T^{miss}, parametrised as a function of $\sum E_T$.

- **Additional term**: The sum of the invariant masses of each pair of lepton and jet is included as an additional term in the likelihood to increase the reconstruction efficiency. If the pairing of jet and charged lepton is correct, that is, if the paired jet and charged lepton are both decay products from the top quark, or both from the antitop quark, the invariant mass is expected to be smaller than in the case of a wrong pair assignment. Given that a higher likelihood value indicates a higher probability of a certain permutation to be correct, the α tuning parameter is negative, and is found to provide optimal separation for $\alpha = -2$.

The positively-charged lepton is associated to the top quark, while the negatively-charged lepton is assigned to the antitop quark. Therefore, only the assignment of jets to charged leptons needs to be determined. Since there are two jets in the LO $t\bar{t}$ dilepton final state, a total of two permutations of jets is possible.

---

[3] For muons, the equivalent is valid, replacing the energy with a p_T parametrisation, unless specified otherwise.

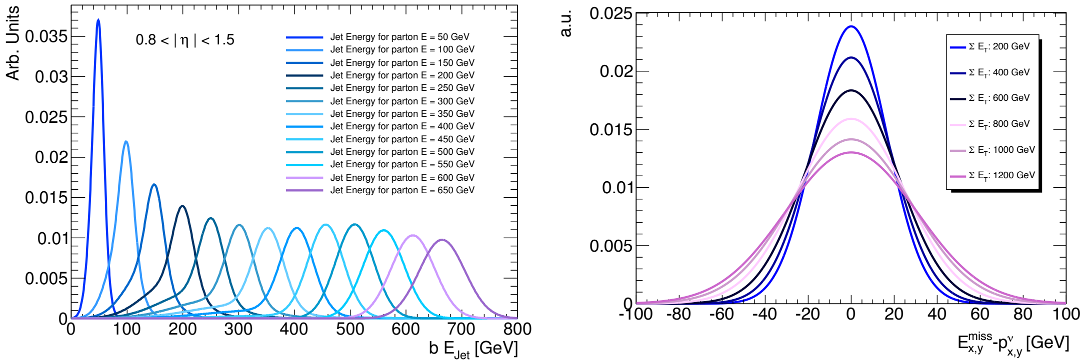

Figure 6.1.: (Left): Example of transfer functions for the entire fitted parton energy range for b-jets in the middle $|\eta|$ region [177]. (Right): Transfer functions for neutrinos (or E_T^{miss}), parametrised as a function of $\sum E_T$ [178].

The likelihood is maximised for each permutation of jets. The permutation which has higher log$L$ compared to the other one, is chosen as the correct jet ordering in the event. Alternatively, the likelihood values for each permutation can be summed, providing a similar output to that of the original Neutrino Weighting, introduced in Section 6.1.2.

The top quark mass can either be fixed, or considered as a free parameter in the likelihood. If the top quark mass is not fixed, there are 7 parameters in the fit: M_{top}, the energy of the two jets, the energy or p_T of the two charged leptons, and the η from the neutrino and antineutrino.

The Bayesian Analysis Toolkit offers several minimisation methods. The choice depends on the use case of the reconstruction algorithm within an analysis. The two minimisation methods considered in the studies of this thesis are:

- *Markov Chain Monte Carlo (MCMC)*: It aims to sample the posterior probability [4] from a Bayesian analysis, by constructing a random walk heading towards regions with larger probability. A Markov Chain of elements $x^{(1)}, ..., x^{(n)}, x^{(n+1)}$ is constructed in such a way that step $x^{(n+1)}$ depends only on the transition probability from the previous step n to n+1, denoted as $T(x^{(n+1)} \leftarrow x^{(n)})$. The transition probability used in the studies of this thesis is the Metropolis algorithm [179]. The MCMC distributions are expected to converge to the underlying function. In practice, the convergence of multiple chains is tested with respect to each other using the Gelman and Rubin criterion [180], to determine at which iteration to stop so that convergence is reached. The Gelman and Rubin criterion calculates the within-chain and between-chain variance for a given parameter, reaching convergence when both quantities are similar enough, converging for infinite number of iterations to the true variance of the parameter.

  While sampling, the MCMC can find the mode of the distribution. It also allows to marginalise the posterior probability, that is, to integrate over all parameters, except the one of interest, for example: the top quark mass. Therefore, the MCMC is able to "project" the posterior probability onto the parameter of interest while sampling. Other functions of the parameters can also be calculated while sampling via error propagation, such as the mass of the $t\bar{t}$ system, or the $\cos\theta^*$. Despite the various functionalities of the method, it is computationally expensive.

---

[4] This can be a difficult task, if it depends on a large number of parameters.

- *Simulated Annealing (SA) [181]*: It aims to find the global minimum of a function, $f(x)$. It is a modification of the Metropolis algorithm, incorporating the concept of *annealing*: the physical process of heating a material and then slowly lowering the temperature to decrease defects, thus minimising the energy of the system. At each iteration of the simulated annealing algorithm, a new point is randomly generated, and the temperature of the system decreases. The distance of the new point from the current point is based on a probability distribution with a scale proportional to the temperature. The algorithm accepts the new point, $x^{(n+1)}$, with a probability, p_A, dependent on the previous point, $x^{(n)}$, and on the temperature at the n^{th} iteration, T_n, in the form:

$$p_A = \min\left(1, \exp\left(\frac{f(x^{(n+1)}) - f(x^{(n)})}{T_n}\right)\right). \tag{6.10}$$

  This allows, at the beginning of the global minima search when the temperature is high, to explore globally for better solutions and avoid being trapped in local minima, and settling for the global minimum when the temperature decreases.

In order to minimise the $-\log L$ and find the best permutation, both minimisation methods can be used. Nevertheless, given the significant gain in speed using SA in comparison to MCMC, the former is preferred for this purpose. The MCMC is only recommended to obtain marginalised histograms or to use the error propagation for calculating the marginalised probability distribution of a new variable per event.

6.2.2. Performance

The performance of the reconstruction algorithm in the $t\bar{t}$ dilepton final state can be evaluated considering different aspects of the reconstruction: the efficiency to correctly pair the jet and lepton, and the estimation of the fitted parameters, such as the p_T of the b-jets and the (η, ϕ) position of the neutrinos and top quarks.

As mentioned in Section 6.1.2, the neutrino momentum is obtained within the Neutrino Weighting algorithm from solving a quadratic kinematic equation. This implies that:

- Even if the correct jet assignment is determined, there remains an ambiguity in the specific four-momentum vector of the neutrino and the antineutrino. This will be discussed further in the remainder of this section.
- Because the neutrino momentum solution is obtained by solving a quadratic equation, it might happen that there are no (real) solutions for a given event.

The latter case occurs in approximately 2% of the events used for performance studies, resulting in a solution efficiency of 98%.

Selection and Sample All performance studies have been performed at the simulation level, using the corresponding object calibrations and transfer functions at $\sqrt{s} = 7$ TeV. The dilepton selection is equivalent to the one described in Section 4.6, with an additional Z-boson veto cut, $|m(\ell\ell) - m(Z)| < 10$ GeV, and requiring at least 2 good jets, from which at least one is a b-jet. The $t\bar{t}$ sample considered is simulated using the MC@NLO event generator [182], interfaced with Herwig and Jimmy [183] to model the parton showering and the underlying event. The CT10 PDF and the AUET2 tune [184] are used. The sample is generated for an assumed top quark mass of 172.5 GeV.

Matching efficiency One important aspect to consider, before testing any performance of the reconstruction algorithm itself, is the criteria to select the two jets that are considered in the reconstruction algorithm. The $t\bar{t}$ dilepton events can have more than two jets, due to effects such as pile-up or additional radiation. Three options are studied:

- **p_T-order**: The two jets with the highest p_T are considered.
- **b-jets and p_T-order**: First, the b-jets with the highest p_T are considered. If the number of b-jets is smaller than 2, the untagged jet with highest p_T is considered.
- **b-tagging weight order**: the two jets with the highest b-tagging weight are considered.

The efficiency of each option is assessed with its matching efficiency. An event is considered *matched* if the leptons entering the KLFitter reconstruction are matched to the truth ones within a $\Delta R < 0.1$, and if the jets entering the KLFitter reconstruction are matched to the truth $b/\bar{b}$-quarks within a $\Delta R < 0.3$.

Table 6.1 shows the matching efficiencies for each option and for the different dilepton flavour channels. The highest matching efficiency is achieved when providing the jets ordered by b-tagging weight. Therefore, this criterium is used for studying the reconstruction performance of the algorithm. Events are always required to be matched in the remainder of the performance studies.

	p_T-order	**b-jets and p_T-order**	**b-tagging weight order**
$e\mu$ channel	54.7%	64.8%	67.2%
$\mu\mu$ channel	52.4%	63.1%	65.7%
ee channel	51.2%	62.1%	64.8%

Table 6.1.: Matching efficiencies for different criteria used to select input jets to the KLFitter reconstruction algorithm, when there are more than 2 jets in the event. The matching efficiencies are compatible and show the same trend in all the dilepton flavour channels.

Correctly pairing jet and lepton Given that in the $t\bar{t}$ dilepton final state there are only two possible permutations of jets, there is a 50% probability to get the correct assignment of jet and lepton pairs from a simple guessing in matched events.

Table 6.2 shows the efficiency to correctly assign a jet to a lepton, for the three dilepton flavour channels, and for both the cases where the top quark mass is free or fixed to $M_{top} = 170$ GeV in the likelihood. A slight improvement in efficiency is observed when the top mass parameter is fixed. The correct assignment due to this algorithm is significantly higher than the 50% probability from a simple guessing.

Transverse momentum of the fitted b-jets The reconstruction algorithm in the KLFitter provides not only the permutation with the highest likelihood value, but also the fitted four-momentum vector of the objects. Figure 6.2 compares the truth p_T of the b- and $\bar{b}$-quark with the reconstructed (fitted) p_T of the matched jet before (after) the KLFitter reconstruction. Since the fitted parameters contain the detector resolution correction from the transfer functions, the fitted distribution is closer to the truth one, as expected.

	M_{top} **free**	M_{top} **fixed**
$e\mu$ channel	78.8%	81.3%
$\mu\mu$ channel	79.0%	82.0%
ee channel	81.3%	84.3%

Table 6.2.: Efficiencies of pairing the jet with the correct lepton, where the pair originates from the top or antitop quark. The matching efficiencies are compatible and show the same trend across the dilepton flavour channels.

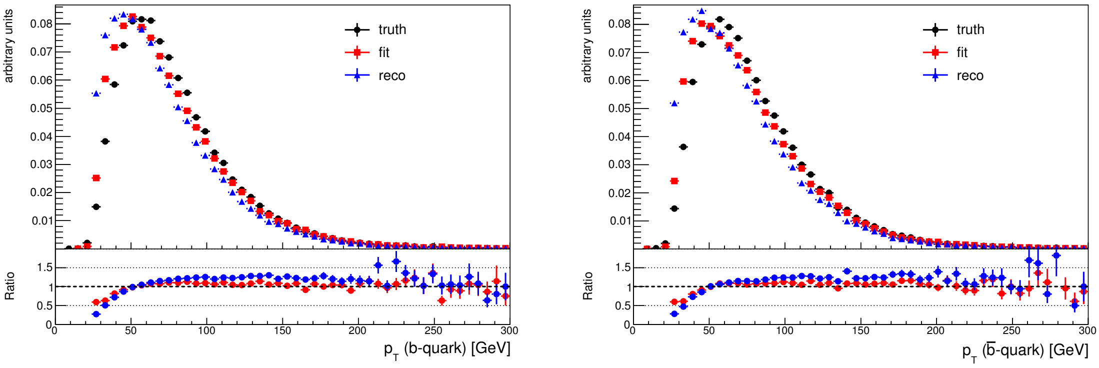

Figure 6.2.: Comparison of the truth transverse momentum of the (left): b-quark and (right): $\bar{b}$-quark, with the reconstructed (before KLFitter) and fitted (after KLFitter) p_T of the corresponding matched jets. The top quark mass parameter is fixed to $M_{top} = 170$ GeV. The bottom plot shows the ratio of the reconstructed and fitted distributions to the truth one.

ΔR efficiencies for neutrino and top quark The ambiguity of the up-to-four possible neutrino and antineutrino solutions is solved by computing the kinematic likelihood component related to the Neutrino Weighting for each solution after maximising the likelihood, including the fitted parameters of the chosen permutation, and keeping the neutrino and antineutrino solutions with the highest likelihood value.

Figure 6.3 shows the distance, ΔR, between the truth and the fitted top and antitop, and between the truth and fitted neutrino and antineutrino, in a two-dimensional histogram (left) or overlaid in a one-dimensional histogram (right). The ΔR distribution for the neutrino and antineutrino is much broader than the one corresponding to the top and antitop. This can be explained by the fact that the top four-momentum vector results from the sum of the four-momentum vector of the corresponding fitted b-quark, charged lepton, and neutrino, and therefore, might be dominated by the other two objects with uniquely-defined four-momentum vectors from the fit. The fraction of events with $\Delta R(\text{truth } t, \text{fitted } t) < 0.4$ is 47%, whereas the fraction of events with $\Delta R(\text{truth } \nu, \text{fitted } \nu) < 0.4$ is 22%. Similar numbers are obtained for the antitop and the antineutrino. These ΔR efficiencies are comparable to other implementations of the Neutrino Weighting algorithm in the ATLAS Collaboration.

6.2.3. Conclusions

A likelihood-based reconstruction algorithm for the $t\bar{t}$ dilepton final state was implemented within the KLFitter framework, based on the Neutrino Weighting algorithm. The implementa-

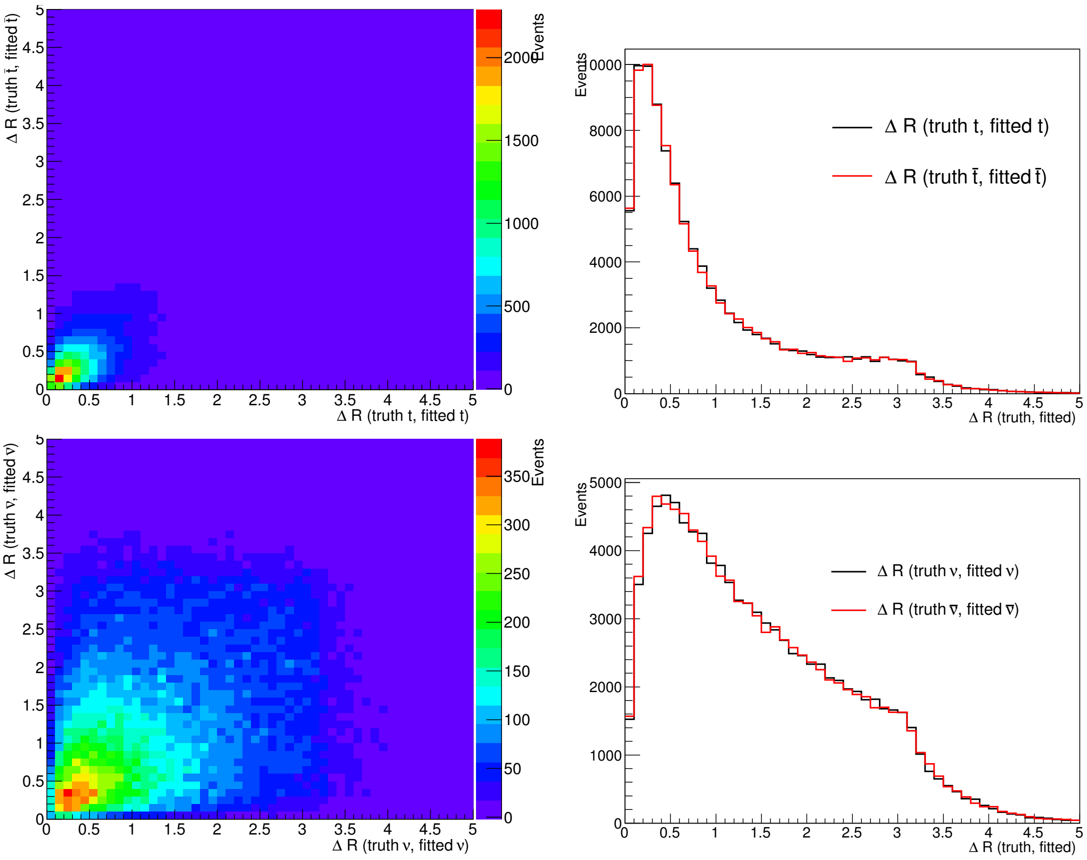

Figure 6.3.: (Left): Two-dimensional distributions of the distance, ΔR, between the truth and the fitted (top): top quark on the $x-axis$, and antitop quark on the $y-axis$, and (bottom): neutrino on the $x-axis$, and antineutrino on the $y-axis$. (Right): Distance ΔR between the truth and the fitted (top): top quark in black, and antitop quark in red, and (bottom): neutrino in black, and antineutrino in red. The events are matched and the top quark mass parameter is fixed at $M_{top} = 170$ GeV.

tion within the KLFitter allows any analyser in the ATLAS collaboration to use the reconstruction algorithm as a standalone library. Furthermore, the algorithm is flexible enough to be used for top quark mass measurements, or for measurements of top quark properties in $t\bar{t}$ dilepton events.

In a first stage of the $t\bar{t}V$ measurement in the opposite-sign dilepton channel, the reconstruction of the $t\bar{t}V$ system with the KLFitter was considered, by extending the $t\bar{t}$ dilepton likelihood with additional terms related to the jets originating from the associated Z or W-boson. This could be useful in the case where the main background is the $t\bar{t}$ process decaying into two leptons. Nevertheless, as it will be explained in Section 7, the region with highest sensitivity to $t\bar{t}Z$ is dominated by Z+jets background. Studies have shown that neural networks, built using kinematic variables with high discriminating power between signal and background, provide better sensitivity than the event reconstruction of high jet multiplicity processes, such as $t\bar{t}V$. Therefore, KLFitter was not used in the presented $t\bar{t}V$ analysis.

CHAPTER 7

Analysis Strategy

7.1. Introduction

The OS dilepton $t\bar{t}V$ measurement is based on data collected by the ATLAS experiment in pp collisions at $\sqrt{s} = 8$ TeV between April and October 2012. The dataset corresponds to an integrated luminosity of 20.3 fb^{-1}. The results of this analysis, together with the combined results described in Section 8.4, were presented as a conference note for ICHEP 2014 in Reference [185].

7.2. Event Selection

After applying the event preselection described in Section 4.6, the dilepton events are further categorised according to the lepton flavour: ee, $\mu\mu$ and $e\mu$ samples. There are numerous possible final states corresponding to the various decay modes of $t\bar{t}Z$ and $t\bar{t}W$ processes. Two orthogonal analysis regions are defined in order to separate the $t\bar{t}Z$ and $t\bar{t}W$ final states involving two leptons with opposite-sign charge, as summarised in Table 7.1.

	2ℓOSZveto	2ℓOSZ
Z mass window cut	$\lvert m_{\ell\ell} - m_Z\rvert > 10$ GeV	$\lvert m_{\ell\ell} - m_Z\rvert < 10$ GeV
dilepton flavour channels	ee, $\mu\mu$, $e\mu$	ee, $\mu\mu$
signal processes	mix of $t\bar{t}Z$ and $t\bar{t}W$	$t\bar{t}Z$
dominant background process	$t\bar{t}$+jets	Z+jets
other selection cuts	$m_{ll} \geq 15$ GeV (ee, $\mu\mu$) $\Delta R^{\text{jj}}_{\text{ave}} > 0.75$ $E_T^{miss} > 40$ GeV(ee, $\mu\mu$) H_T> 130 GeV($e\mu$)	$m_{ll} \geq 15$ GeV (ee, $\mu\mu$) $\Delta R^{\text{jj}}_{\text{ave}} > 0.75$

Table 7.1.: Definition and characteristics of the two orthogonal analysis regions, 2ℓOSZveto and 2ℓOSZ, in the $t\bar{t}V$ OS dilepton channel.

The so called 2ℓOSZveto analysis region contains events in the ee and $\mu\mu$ channels with the dilepton invariant mass outside a window of 10 GeV centred at the Z-boson mass, $|m_{\ell\ell} - m_Z| >$

10 GeV, and the so called 2ℓOSZ region, contains ee and $\mu\mu$ events fulfilling the orthogonal cut: $|m_{\ell\ell} - m_Z| < 10$ GeV. A further cut on the low missing transverse energy of the event, $E_T^{miss} > 40$ GeV, is applied in the 2ℓOSZveto region in the ee and $\mu\mu$ dilepton channels to reduce the Z+jets contribution in this region. This cut has a negligible effect on the signal acceptance, while it helps to disentangle the main background contribution between the 2ℓOSZveto and 2ℓOSZ regions, making the interpretation of the fit results easier. Dilepton $e\mu$ events are also included in the 2ℓOSZveto region. However, no $m_{\ell\ell}$ cut is applied in this channel, since in the $Z \to \tau^+\tau^-$ decay, τ leptons decay to e and μ only in a fraction of the events, and some of their momentum is carried away by the neutrinos. Thus, the Z peak is no longer identifiable in the dilepton mass distribution. In both 2ℓOSZveto and 2ℓOSZ regions, the cut on the average distance between two jets $\Delta R^{\mathrm{jj}}_{\mathrm{ave}} > 0.75$ is applied, as discussed in Section 5.3.2.

Events with additional reconstructed leptons with $p_T > 15$ GeV and $|\eta| < 2.5$ are rejected to avoid statistical overlap in the combination with the trilepton channel, as will be discussed in Section 8.4.

Figure 7.1 shows all possible decay modes for the $t\bar{t}Z$ and the $t\bar{t}W$ process, resulting from the different decay modes of $t\bar{t}$, as already discussed in Section 2.3.2, and the decay modes of the Z and the W-bosons. Given the structure of the coupling of these vector bosons to the fermions, as explained in Section 2.2.1, the branching ratio (BR) of the W-boson to hadronic final states is $BR(W \to q\bar{q'}) = 67.5\%$, decaying otherwise into a lepton and the corresponding antineutrino (or antilepton and neutrino). The branching ratios of the Z-boson to the different final states are as follows: $BR(Z \to q\bar{q}(\text{hadrons})) \approx 69\%$, $BR(Z \to \nu\bar{\nu}) \approx 21\%$ and $BR(Z \to l^+l^-) \approx 10\%$ [1].

In Figure 7.1, in particular, the final states contributing to the two analysis regions in the $t\bar{t}V$ OS dilepton channel are highlighted with the red and the blue boxes. The 2ℓOSZveto region is dominated by the dileptonic $t\bar{t}$ final state and hadronic Z/W-boson decay mode and by the semileptonic $t\bar{t}$ final state and leptonic W-boson decay mode. The $t\bar{t}Z$ final state where $t\bar{t}$ decays dileptonically and the Z-boson decays into neutrinos, therefore called "invisible" Z-boson decay mode, contributes significantly less, due to the small BR of that $t\bar{t}Z$ final state. The 2ℓOSZ region is dominated by the hadronic $t\bar{t}$ final state and leptonic Z decay mode, hence this region is primarily sensitive to the $t\bar{t}Z$ production.

7.2.1. Classification of Event Categories

Events fulfilling the aforementioned selection are further categorised according to the number of jets and the number of b-jets.

In the 2ℓOSZveto region, events with at least three jets with one or two b-jets are split into three exclusive regions according to the jet multiplicity: events with exactly 3 jets, exactly 4 jets, and at least 5 jets, from which 1 or 2 are b-jets, denoted by $(3\mathrm{j}, 1\mathrm{b}+2\mathrm{b})$, $(4\mathrm{j}, 1\mathrm{b}+2\mathrm{b})$, and $(\geq 5\mathrm{j}, 1\mathrm{b}+2\mathrm{b})$, respectively. These regions have different signal (S) over background (B) rates. Since regions with one or two b-jets have similar S/B and $S/\sqrt{B}$, as shown in Figure 7.2, they are merged together into one region. In the 2ℓOSZ region, events with at least three jets and exactly two b-jets are split in three exclusive regions according to the jet multiplicity: events with exactly 3 jets, exactly 4 jets, and at least 5 jets, from which 2 are b-jets, denoted by $(3\mathrm{j}, 2\mathrm{b})$, $(4\mathrm{j}, 2\mathrm{b})$, and $(\geq 5\mathrm{j}, 2\mathrm{b})$, respectively. Depending on the S/B ratio, the categories are classified as *signal regions* (high S/B and high $S/\sqrt{B}$) or as *control regions* (low S/B or low $S/\sqrt{B}$).

Figure 7.3 shows the background composition of the 2ℓOSZveto and 2ℓOSZ regions. As mentioned previously, the main background in the 2ℓOSZveto region is from $t\bar{t}$+light jets events, since $t\bar{t}$ already contains two b-jets from the top and antitop quark decays. On the other hand, the main background in the 2ℓOSZ region is Z+HF jets, since the two b-jets must come from

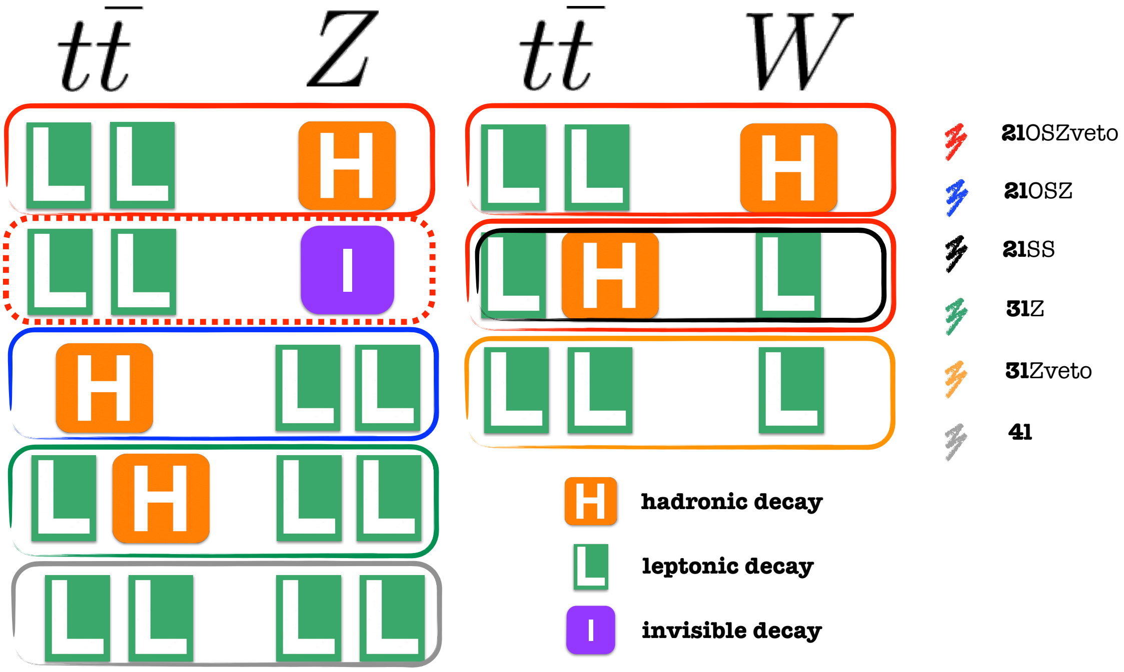

Figure 7.1.: Overview of all the possible SM final states of the $t\bar{t}Z$ and $t\bar{t}W$ processes, split into the decay modes of the $t\bar{t}$ system and the Z/W boson. The boxes indicate which event selection (right legend) each of the final states mainly contributes to. The box with the red dashed line indicates that the relative contribution of that decay mode to the 2ℓOSZveto selection is significantly smaller compared to the other contributing final states.

additional jets, given that the Z-boson is required to decay leptonically to fulfil the OS dilepton selection.

After applying the OS dilepton selection, the MC modelling of basic kinematic distributions is compared to data in the analysis regions. Figure 7.4 shows the p_T and η distributions of the leading and subleading leptons and jets in the 2ℓOSZ $(3\text{j}, 2\text{b})$ control region, after applying all corrections to the main backgrounds. Figure 7.5 shows other kinematic distributions in the same region, such as $m_{\ell\ell}$, $E_T^{miss}$and p_T(Z), as well as the number of events of different leptons flavours. The same distributions are shown in Figures 7.6 and 7.7 for the 2ℓOSZveto $(3\text{j}, 1\text{b})$ control region. All variables are well described by the MC simulation within statistical uncertainties, after applying the corrections discussed in Section 5.3.

All six regions are considered in the final statistical analysis, introduced in Section 8.1. The event yields for the combined ee+jets, $\mu\mu$+jets and $e\mu$+jets samples for the different regions are summarised in Table 7.2 for the 2ℓOSZveto region, and in Table 7.3 for the 2ℓOSZ region. The uncertainty in those tables includes both MC statistical uncertainties and systematic uncertainties before the fit procedure. A detailed explanation of the different systematic uncertainty sources will be provided in Section 8.2.

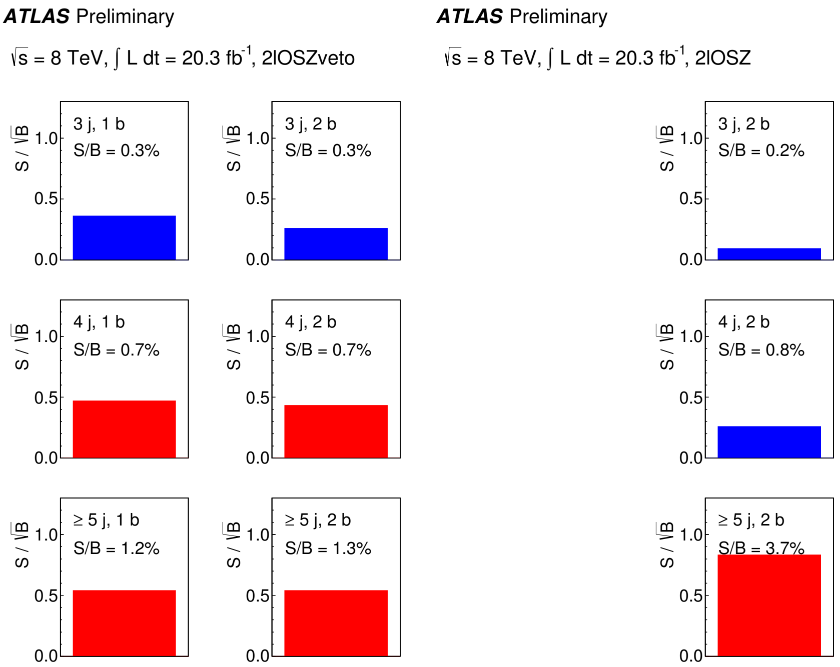

Figure 7.2.: $S/\sqrt{B}$ and S/B ratio for each of the categories after the OS dilepton $t\bar{t}V$ event selection, assuming SM cross sections at $\sqrt{s} = 8$ TeV. Each row shows the plots for a specific jet multiplicity $(3, 4, \geq 5)$, and the columns show the b-jet multiplicity $(1, 2)$ for the 2ℓOSZveto region, and 2 b-jet multiplicity for the 2ℓOSZ region. Signal regions are shown in red, while the control regions are shown in blue.

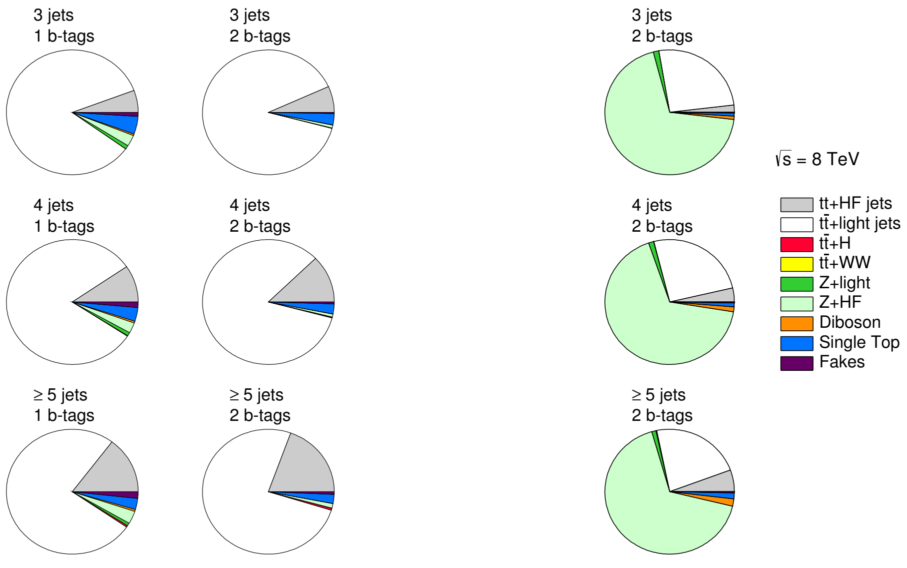

(a) (b)

Figure 7.3.: Pie charts showing the fractional contributions of the various backgrounds to the total background prediction in the OS dilepton regions: **(a)** 2ℓOSZveto and **(b)** 2ℓOSZ. Each row shows the plots for a specific jet multiplicity (3, 4, $\geq$5), and the columns show the b-jet multiplicity.

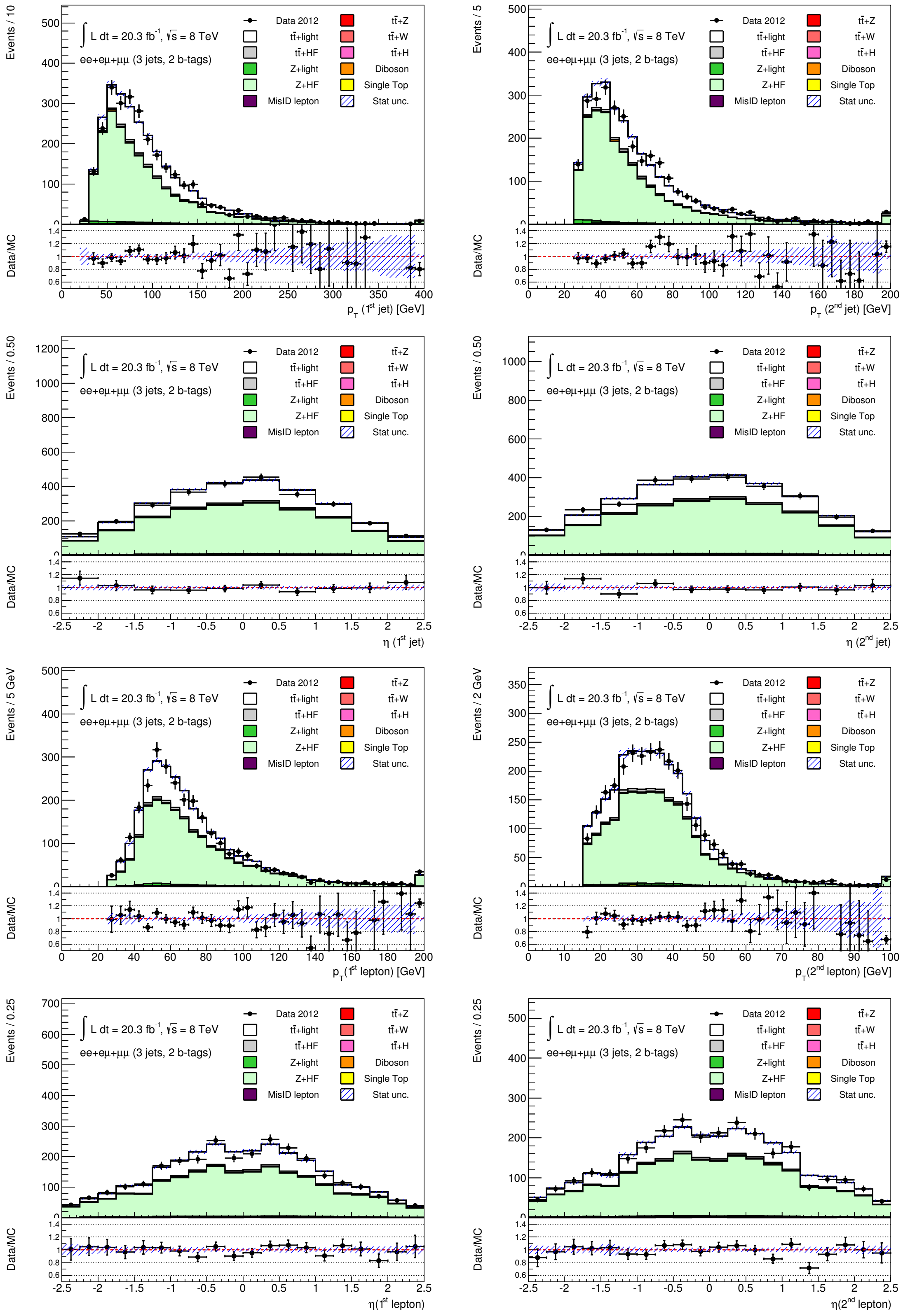

Figure 7.4.: (Top four plots): p_T and η distributions of (left): leading jet and (right): second leading jet. (Bottom four plots): p_T and η distributions of (left): leading lepton and (right): second leading lepton. All distributions are shown in the 2ℓOSZ $(3\text{j}, 2\text{b})$ control region, after applying all corrections to the Z+jets and $t\bar{t}$ MC. The error band contains only the statistical error on MC.

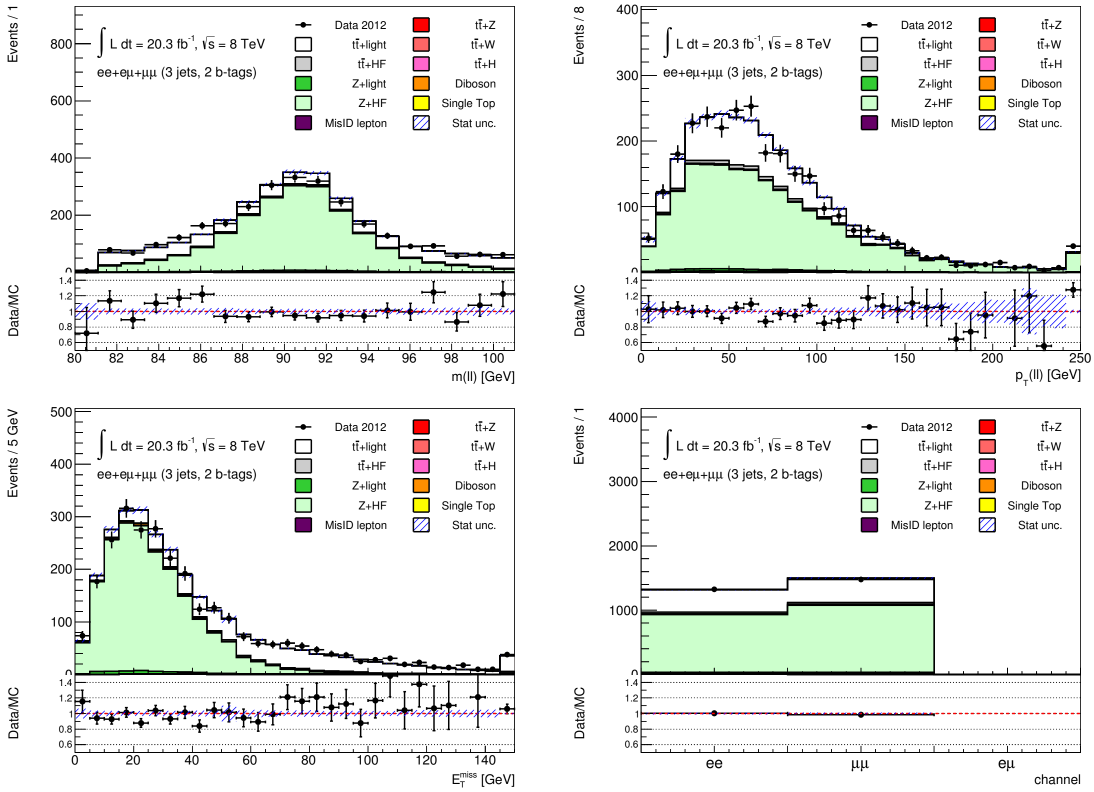

Figure 7.5.: (Top left): Invariant mass and (top right): transverse momentum distributions of the dilepton system, (bottom left): missing transverse energy and (bottom right): the normalisation per dilepton channel in the 2ℓOSZ $(3\mathrm{j}, 2\mathrm{b})$ control region, after applying all corrections to the Z+jets and $t\bar{t}$ MC. The error band contains only the statistical error on MC.

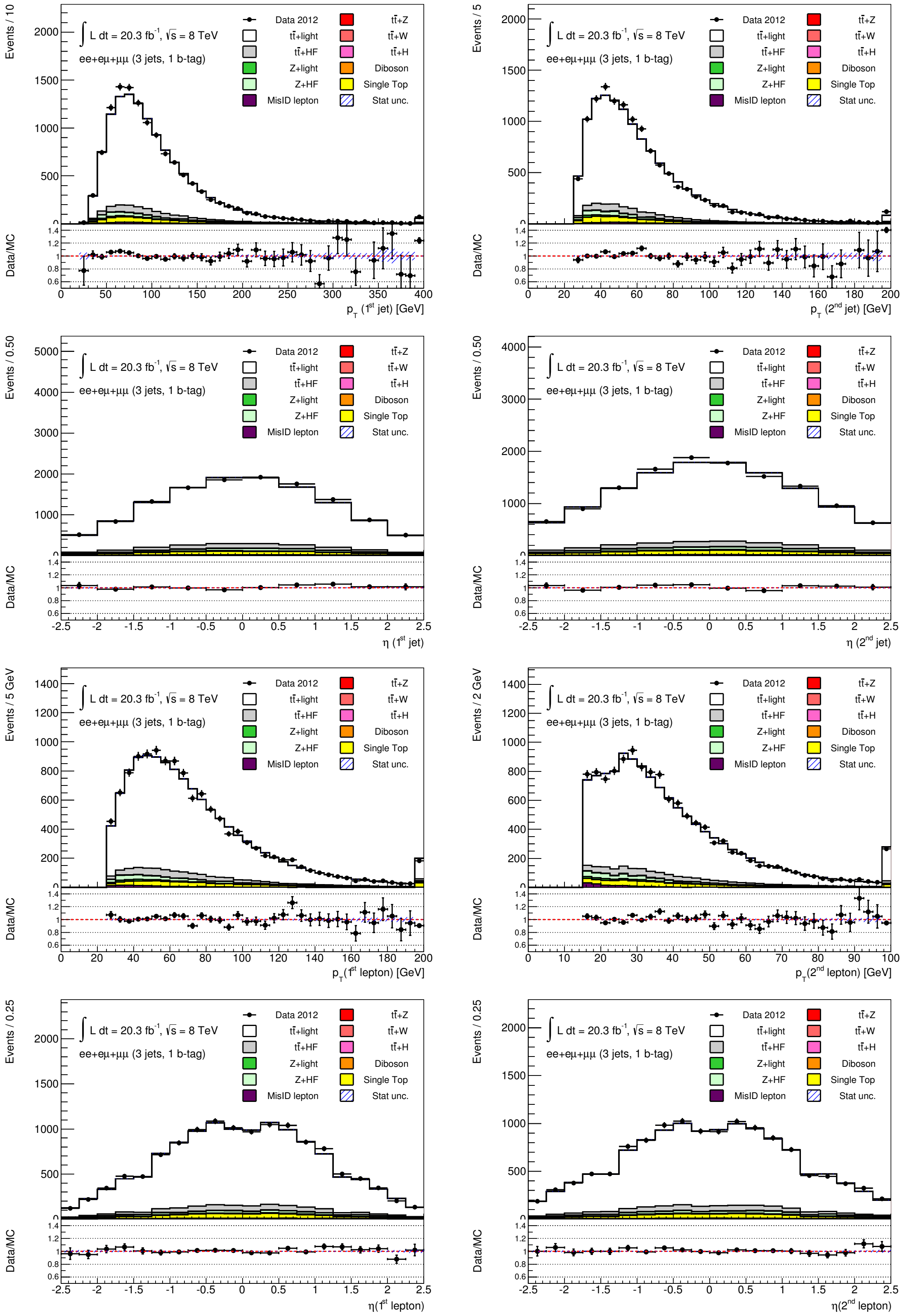

Figure 7.6.: (Top four plots): p_T and η distributions of (left): leading jet and (right): second leading jet. (Bottom four plots): p_T and η distributions of (left): leading lepton and (right): second leading lepton. All distributions are shown in the 2ℓOSZveto (3j, 1b) control region, after applying all corrections to the Z+jets and $t\bar{t}$ MC. The error band contains only the statistical error on MC.

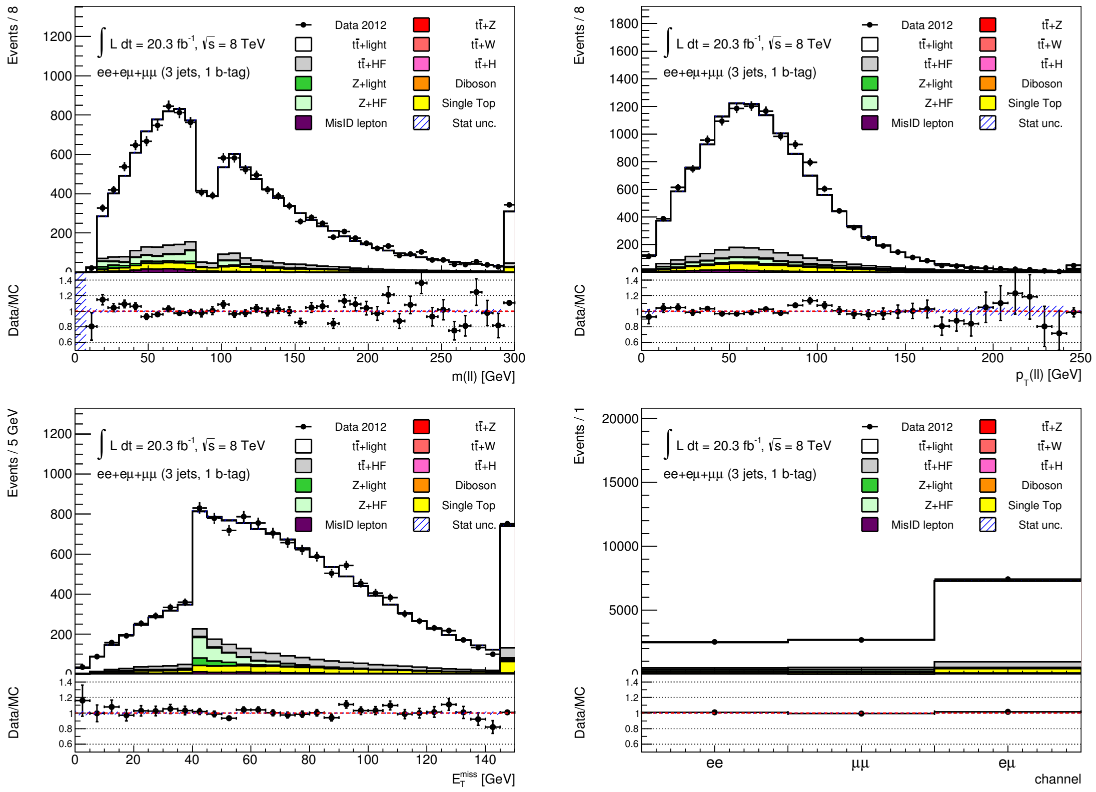

Figure 7.7.: (Top left): Invariant mass and (top right): transverse momentum distributions of the dilepton system, (bottom left): missing transverse energy and (bottom right): the normalisation per dilepton channel in the 2ℓOSZveto $(3\mathrm{j}, 1\mathrm{b})$ control region, after applying all corrections to the Z+jets and $t\bar{t}$ MC. The error band contains only the statistical error on MC.

	3 j, 1 b + 2 b	4 j, 1 b + 2 b	$\geq$ 5 j, 1 b + 2 b
$t\bar{t}Z$	23 ± 1	22 ± 1	22 ± 2
$t\bar{t}W$	42 ± 3	37 ± 2	25 ± 2
$t\bar{t}$	20000 ± 3000	8000 ± 1000	3600 ± 800
Z+jets	600 ± 200	220 ± 90	90 ± 40
$t\bar{t}H$	11 ± 2	13 ± 2	17 ± 2
Single top	800 ± 100	260 ± 50	100 ± 30
Diboson	60 ± 20	27 ± 7	12 ± 4
tZ	4 ± 2	2 ± 1	1.9 ± 1.0
MisID lepton	160 ± 80	80 ± 40	50 ± 20
Total Bkgd	22000 ± 3000	9000 ± 1000	3800 ± 900
Data	22585	8909	3901

Table 7.2.: Estimated event yields for signal and backgrounds, as well as the observed data in the 2ℓOSZveto region. The quoted uncertainties on expected event yields include both MC statistical and systematic uncertainties.

	3 j, 2 b	4 j, 2 b	$\geq$ 5 j, 2 b
$t\bar{t}Z$	3.7 ± 0.4	7.3 ± 0.6	18 ± 1
$t\bar{t}W$	1.2 ± 0.1	1.3 ± 0.1	0.9 ± 0.1
$t\bar{t}$	800 ± 100	330 ± 60	160 ± 30
Z+jets	2000 ± 900	800 ± 400	300 ± 200
$t\bar{t}H$	0.49 ± 0.07	0.63 ± 0.08	0.9 ± 0.1
Single top	19 ± 3	7 ± 2	3 ± 1
Diboson	26 ± 7	14 ± 4	10 ± 3
tZ	4 ± 2	5 ± 2	3 ± 3
MisID lepton	4 ± 2	2 ± 1	1.4 ± 0.7
Total Bkgd	2800 ± 900	1100 ± 400	500 ± 200
Data	2806	1031	471

Table 7.3.: Estimated event yields for signal and backgrounds, as well as the observed data in the 2ℓOSZ region. The quoted uncertainties on expected event yields include both MC statistical and systematic uncertainties.

7.2.2. Tag Rate Function Method

Since the selection requires that events have up to 2 b-jets with a 70% b-tagging efficiency and a mistag rate of about 1%, only 1 out every 10000 MC events with no real b-quarks will populate the 2 b-tag region. This reduces the MC statistics drastically, especially in the *signal regions*, where both high jet and high b-jet multiplicity are required. The shortage of events, in particular for the backgrounds weighted with large cross sections, can lead to large fluctuations in the resulting distributions. Since this analysis relies on the shape information in each of the event categories, this behaviour can negatively affect the sensitivity of the analysis, given that the corresponding statistical uncertainties on the background templates are taken into account in the fit. It can also lead to unreliable systematic uncertainties in the shape of the distributions.

The method, called the *tag rate function* (TRF), is used to mitigate this problem. Instead of cutting events based on the values of the MV1 algorithm, the TRF method assigns a weight to every event, corresponding to the probability of the given event to have the requested number of b-jets. Therefore, all MC events are used, regardless of the b-tagging requirement.

The TRF weight uses the tagging efficiency, parametrised as a function of η, p_T and the true flavour of the jet. For instance, the probability of a given event with N jets to have 1 b-tag can be expressed as:

$$P_{=1b} = \sum_{i=1}^{N} \left(\varepsilon_i \prod_{i \neq j} (1 - \varepsilon_j) \right) , \tag{7.1}$$

where, $\varepsilon_i = \varepsilon(\text{flavour}_i, |\eta|_i, p_{Ti})$, is the tagging probability of the i^{th} jet. If it is necessary to know which of the N jets in the event is the b-tagged one, continuing with the previous example, one of the permutations in the product loop in Equation 7.1 has to be selected. The criteria to select a given permutation consist of two steps:

- First, the sum of the probabilities (or *TRF weights*) of all permutations corresponding to the requested number of b-jets is calculated, denoted as S_{TOT}, as well as each partial sum, denoted as $S_{1,\ldots,N}$. S_2, for instance, is the sum of the probability of the first and the probability of the second permutation.
- Second, a random number uniformly distributed between $[0, S_{TOT}]$ is thrown.
- The permutation k that corresponds to the partial sum S_k, which is equal or greater than the thrown random number, is chosen.

This procedure ensures that the probability to pick a certain permutation is proportional to its TRF weight.

Validation

The TRF method was applied to all MC samples used in the analysis. This allows the use of all events in the pre-b-tagged sample to predict the normalisation and shape after b-tagging.

As a validation of the method, kinematic distributions were compared when applying the b-tagging cut, to those using the TRF weights, and were found to agree within the statistical uncertainty. Figure 7.8 shows the comparison of the cut-based, denoted as “MV1 cut”, and TRF H_T distribution in the high jet and high b-jet multiplicity regions for $t\bar{t}$+light (top left) and $t\bar{t}$+HF (top right) in the 2ℓOSZveto region, and Z+HF (bottom) in the 2ℓOSZ region.

Given that the agreement is reasonable between both approaches, no extra systematic uncertainty is added due to the use of the TRF technique.

7.3. Multivariate Analysis

Despite of the splitting of events into jet and b-jet multiplicity categories in order to isolate regions with higher S/B ratio, these values are not large enough to perform a counting experiment in the OS dilepton channel. For this reason, a multivariate analysis (MVA) is performed, where the shape information of several distributions showing high discrimination between signal ($t\bar{t}V$) and background is used to build a powerful discriminant using a multivariate algorithm.

In this analysis, three neural network (NN) discriminants are built using the NeuroBayes [186, 187] package in the three aforementioned *signal regions*: the 2ℓOSZveto $(4\text{j}, 1\text{b} + 2\text{b})$ and $(\geq 5\text{j}, 1\text{b} + 2\text{b})$ regions, and the 2ℓOSZ $(\geq 5\text{j}, 2\text{b})$ region.

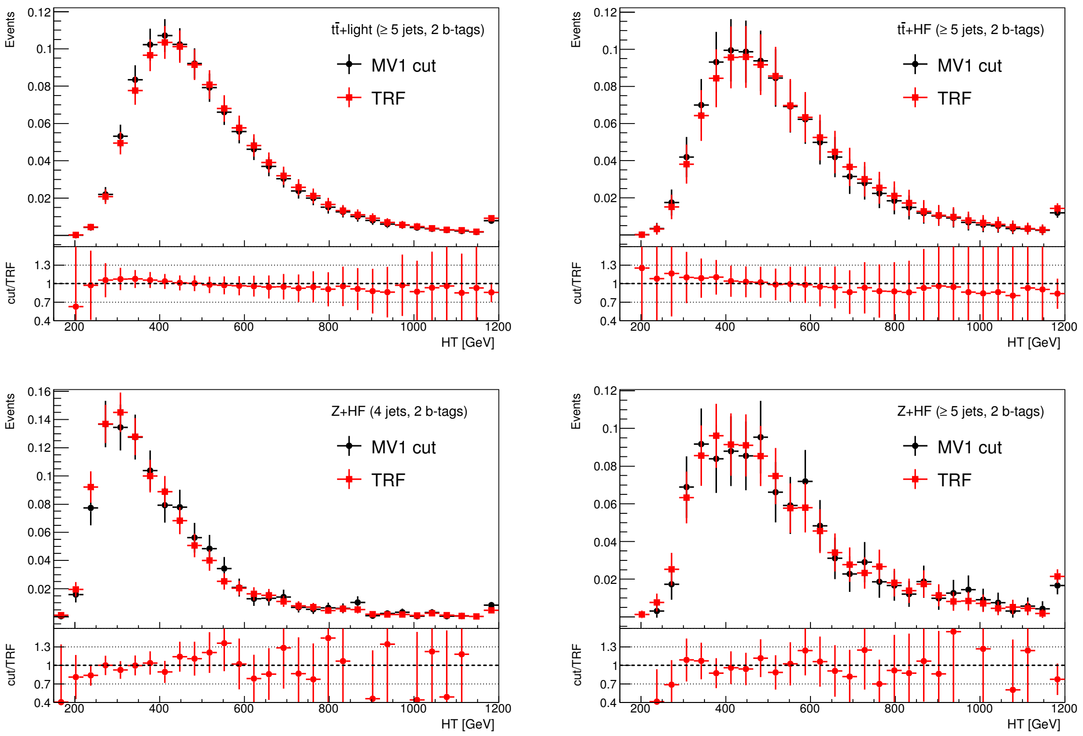

Figure 7.8.: Comparison of the cut-based and the TRF procedure in the H_T distribution for (top left): $t\bar{t}$+light and (top right): $t\bar{t}$+HF in the 2ℓOSZveto $(\geq 5\text{j}, 2\text{b})$ region, and for (bottom left): Z+HF in the 2ℓOSZ $(4\text{j}, 2\text{b})$ region and (bottom right): Z+HF in the 2ℓOSZ $(\geq 5\text{j}, 2\text{b})$ region. There is a reduction in the MC statistical uncertainty when using the TRF technique.

7.3.1. Introduction to the MVA

Given a data sample, composed of two sets of events, H_0 and H_1, there exists a set of D input variables $x_1, x_2, ..., x_D$ that provide discrimination between the two sets of events. It is important to find the optimal boundary conditions in order to discriminate against the two sets. Figure 7.9 (1), highlights possible boundaries in the (x_1, x_2) phase space. This is precisely the goal of a multivariate analysis: to find the most optimal way to separate one set of events from another. Therefore, a mapping from a D-dimensional input space, which can also be a *feature space* [1], to a one dimensional output $y(x)$ has to be performed, given a certain type of model class.

The quality of a classification procedure can be characterised with the area under the *receiver operating characteristic* (ROC) curve, as shown in Figure 7.9 (2). The ROC curve shows the background rejection as a function of the signal efficiency. Each possible cut on the $y(x)$ output would correspond to a point in the corresponding ROC curve. According to the *Neyman-Pearson lemma* [188], the curve maximising the area under the ROC curve is the one corresponding to the likelihood ratio $y(\mathbf{x}) = \frac{p(\mathbf{x}|H_0)}{p(\mathbf{x}|H_1)}$, where H_0 is the signal-type and H_1 the background-type, and p is the corresponding probability density function. Nevertheless, the true probability density functions for signal and background are typically unknown and the likelihood ratio estimator is

---

[1] Transformation of the initial set of input variables to a new set ϕ_i, where a linear decision boundary is optimal.

not useful in practice. Instead, the $y(x)$ output is obtained in an automatic way learning from "known" and already classified events, such as signal and background MC samples, in order to use the resulting $y(x)$ output properties to determine the nature of "unknown" events, such as a data sample. This learning process is hence called *supervised machine learning*.

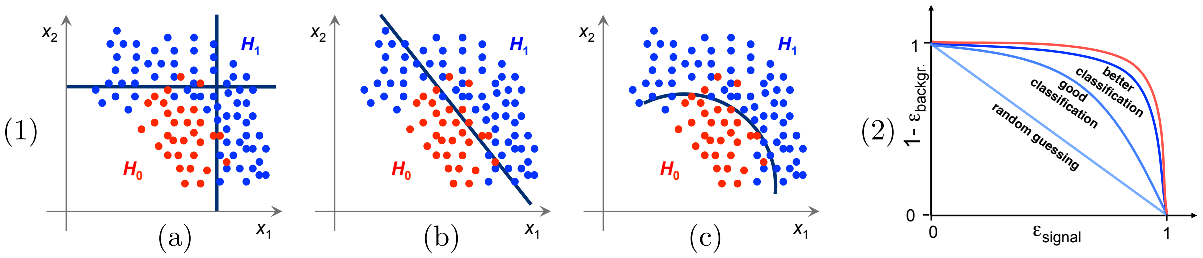

Figure 7.9.: (1) Example of possible decision boundaries using variables x_1 and x_2 to select events of type H_0: (1.a) rectangular cuts, (1.b) linear boundary, (1.c) non-linear boundary. (2) Examples of receiver operating characteristic (ROC) curves as a function of the signal efficiency (*x-axis*) and the background rejection (*y-axis*); the one maximising the area under the ROC curve is given by the likelihood ratio (red curve) [188]. Figures taken from [189].

7.3.2. Neural Network

From the various multivariate methods available, the NN method has been chosen for the presented analysis. Inspired by the fact that the information is coded in the interconnections between neurons in the human brain, allowing self-learning capabilities from examples, the NN method calculates the final output from the input variables via one or more intermediate hidden layers, as shown in the example in Figure 7.10. The output of a node j in layer n is calculated from a weighted sum of outputs in the previous layer $n-1$:

$$x_j^n = f(\sum w_{i,j}^n x_i^{n-1} + w_{0,j}^n), \tag{7.2}$$

where $w_{i,j}^n$ is the weight associated with the connection between node i in layer $n-1$ and node j in layer n, $w_{0,j}^n$ is a bias associated to node j in layer n, and $f(x)$ is a non-linear transfer function, called *activation function*, applied to the output of each node, mapping the interval $(-\infty, \infty)$ to a finite one. This kind of architecture is called a *feed-forward* NN, since each node can only be connected to the successive layer, allowing the information transfer from input to output.

The training is the process that searches for the best set of weights based on the known set of events, by minimising the error/loss function. The most commonly used error functions are:

- *Quadratic loss function*: $\chi^2 = \sum_j \frac{1}{2} \sum_i^{events} (T_{ji} - o_{ji})^2$, or
- *Entropy loss function*: $E_D = \sum_j \sum_i^{events} -log(\frac{1}{2}(1 + T_{ji} o_{ji})$,

where T_{ji} denotes the true target value (-1 and 1 for background and signal, respectively), and o_{ji} denotes the output value for the output node j in event i.

The hidden layer can be understood as the set of transformed inputs ϕ_i that create the *feature space*. Although the NN can contain many hidden layers, it has been shown that a single hidden layer with a sufficiently large number of nodes can approximate very well the

Bayes optimal decision boundary [190]. In practice, the number of nodes in the hidden layer can be increased in order to improve the network's learning ability. Nevertheless, too many hidden nodes can increase significantly the training time and, given the finite amount of training data, the estimates can be sensitive to statistical fluctuations. The latter phenomena is called *overtraining*. One procedure to control and reduce the overtraining consists on including a so called *regularisation term* in the error function that penalises the overfitting.

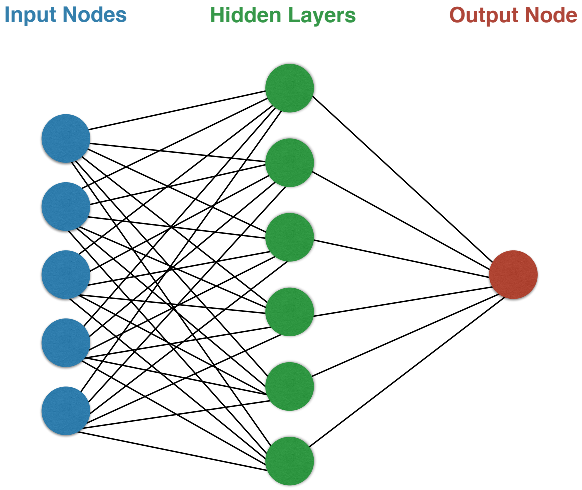

Figure 7.10.: Sketch of a three-layer feed-forward NN. Each connection has an associated weight and each node a bias.

7.3.3. NeuroBayes package

The NeuroBayes package [186, 187] is used to build the NN discriminants in this analysis. It is a commercial package that uses a three-layer feed-forward NN architecture. Given that the first layer has as many input nodes as input variables considered, N_I, the hidden layer is chosen to have $N_I + 2$ nodes, and the final layer, 1 output node.

Before performing the training, a preprocessing of the input variables is performed and a ranking of the initial input variables is provided.

Preprocessing of the input variables

Given that minimising in a large number of dimensions can be a complex task, a preprocessing step is performed in order to prepare the input variables in a way that the NN can handle easily, thus improving the stability and robustness of the following steps. The *global preprocessing* procedure consists of the following steps:

- Firstly, the input variables are *equalised*: the original input variable may be distributed according to an arbitrary probability density function. This distribution is then flattened by a non-linear transformation.
- Afterwards, the flat distribution is transformed into a Gaussian with mean zero and standard deviation of 1.
- At this stage, the variables are ranked, as it will be described in the following.

- Finally, a further preprocessing procedure de-correlates the input variables from each other.

The *individual variable preprocessing* modifies the procedure for single variables before the stage of ranking and de-correlation. This can be useful in order to provide information to the preprocessing procedure if the variable is discrete (such as the jet multiplicity) or continuous.

Ranking of input variables

The ranking of the input variables takes into account not only the individual discriminating power of each variable, but also its correlation to the rest of the input variables. After the variables have been preprocessed, the correlation matrix of the N input variables and the total correlation of the set of input variables to the target are computed.

In an iterative process, one variable at the time is removed from the list of inputs and the correlation to target is re-computed, so that the variable causing the smallest loss of correlation to target, and therefore the least discriminating one, is discarded, leaving an $N-1$ set of variables where the same process is repeated. The iterative process continues until one variable, the most significant one, remains. The ranking of the input variables is then based on their significance, which is defined as the loss of correlation when the variable is removed from the input set, multiplied by $\sqrt{n}$, where n is the sample size.

Training

The training used in the NB setup for this analysis makes use of the relationships between nodes described in Equation 7.2, taking a modified sigmoid function of type:

$$f(x) = \frac{2}{1+e^{-x}} - 1, \tag{7.3}$$

as the activation function, mapping the output of the node to the range $[-1, 1]$. The entropy loss function is used to derive the best set of weights, and the minimisation is performed with the BFGS algorithm [191]. This algorithm uses the approximate second derivatives of the error function to determine in which “direction” to adjust the node weight.

In order to reduce the overtraining, a Bayesian regularisation method is used during the training stage, so that only the weights supported by data are intensified, while pruning away those connections that are insignificant. With this procedure, the architecture of the NN is changed, and the number of free parameters is lowered. To evaluate potential overtraining effects, a statistically independent sample to the one used for training is used for the testing of the performance and the evaluation of the NN discriminant. In the case of the $t\bar{t}V$ signal, the fast simulation AFII samples are used for training, while the full simulation ones are used for testing and evaluation. For the backgrounds, the selected samples are divided in two sets, depending on the parity of the event number: one set is used for training and the other one for evaluation. In the case of the Z+jets background, where the available statistics after the selection is significantly reduced, an alternative method, called *cross-training*, is used. It consists of dividing the sample into two sets, performing the training twice using each half of events, and adding the resulting NN outputs. Equivalently, the evaluation is performed in the opposite halves, and the final NN is the sum of both outputs. This procedure allows to significantly reduce the statistical uncertainty of the NN discriminant output.

Discriminating Variables as input in the NN analysis

The NN algorithm is run independently in each of the three signal regions. The initial collection of variables is different for each signal region. When two highly correlated variables are in the input list, either of the variables may appear in the final set, depending on small changes in the limited statistics of the sample. Therefore, different variable sets were tested in the ranking, removing in each case variables with high correlations.

Several classes of variables have been considered:

- **Object kinematics**: p_T and η of each lepton and jet.
- **Global event variables**: the scalar sum of the transverse momentum of jets (H_T^{had}), the invariant mass of the vector combination of all the objects in the event (M_{eff}), the number of jets above a given p_T threshold (40, 60 and 80 GeV), and the missing transverse energy (E_T^{miss}).
- **Event shape variables**: combinations of the eigenvalues of the linear momentum tensor (sphericity, aplanarity), centrality, and the Fox-Wolfram moments.
- **Object pair properties**: p_T, invariant mass and ΔR of the jet pair with the largest vectorial sum p_T (*_maxPt*), the largest invariant mass (*_maxM*) or the smallest ΔR (*_min*ΔR).

Global and event shape variables have the advantage that they can be examined in all jet and b-jet multiplicity categories, and are less sensitive to the loss of jets by mis-reconstruction. For each variable, three possible definitions have been tested: one that makes use of the leptons and jets in the event to build the variables (no suffix), another one using only the jets (with suffix "*_jet*") and the last one considering only the b-jets (with suffix "*_b*").

The Fox-Wolfram moments were originally designed to analyse geometric patterns in QCD [192], but are currently used in many analyses at the LHC. They are defined as [193]:

$$H_\ell = \sum_{i,j} \frac{|\vec{p_i}||\vec{p_j}|}{E^2} P_\ell(cos\theta_{ij}), \tag{7.4}$$

where i, j sums over all final state objects in the event, $|\vec{p_i}|$ is the absolute value of the three momentum vector of the i^{th} object, E is the sum of the energy of all considered objects, P_ℓ are the Legendre polynomials of ℓ^{th}-degree, and $\cos\theta_{ij}$ is the angle between objects i and j.

The centrality is defined as: $C = \sum p_T / \sum E$, and sphericity and aplanarity are combinations of the eigenvalues of the momentum tensor with its elements defined as:

$$M^{\alpha\beta} = \frac{\sum_i p_i^\alpha p_i^\beta}{\sum_i |p_i|^2}, \tag{7.5}$$

where i runs over all particles considered, and α, β indices run over the x, y, z component of the particle vector momentum.

For the variables characterising object pair properties, pairs containing any type of jets (j, j), a tagged jet and any jet (b, j), two tagged jets (b, b), or two untagged jets (u, u), are considered in separate variables.

In the signal regions with at least five jets, $(\geq 5\text{j}, 1\text{b} + 2\text{b})$ and $(\geq 5\text{j}, 2\text{b})$, input variables are built using a maximum of 5 jets in the 2ℓOSZveto region and 6 jets in the 2ℓOSZ region, since the nominal number of jets in $t\bar{t}(\rightarrow jj)Z(\rightarrow ll)$ is six. Firstly, all tagged jets are used, and then

Variable	Definition
$M_{\text{uu}}^{\text{Pt}_{\text{ord}}}$	mass of the two untagged jets with the highest p_T in events with exactly two tagged jets or mass of the two untagged jets with the highest p_T after discarding the jet with second highest b-tagging weight in events with exactly one tagged jet
Cent_{jet}	Sum of p_T divided by sum of E for all jets
H1	2^{nd} Fox-Wolfram moment
H1_{jet}	2^{nd} Fox-Wolfram moment built from jets only
$M_{\text{jj}}^{\text{MindR}}$	mass of the combination between any two jets with the smallest ΔR
max $M_{\ell\text{b}}^{\text{MindR}}$	maximum mass between a lepton and the tagged jet with the smallest ΔR
$p_T{}^{\text{jet3}}$	third leading jet p_T
$p_T{}^{\text{jet4}}$	fourth leading jet p_T
$\Delta R_{\text{ave}}^{\text{jj}}$	average ΔR for all jet pairs
$N_{\text{jets}}^{\lvert M_{jj}-M(V)\rvert<30}$	number of jet pairs with mass within a window of 30 GeV around 85 GeV
N_{40}^{jet}	number of jets with $p_T \geq 40$ GeV
$M_{\text{bb}}^{\text{MaxPt}}$ ($M_{\text{bj}}^{\text{MaxPt}}$)	mass of the two tagged jets (one tagged jet and any jet) system with the largest vector sum p_T
$\Delta R_{\ell\ell}$	ΔR between the two leptons

Table 7.4.: The highest-ranked input variables considered to build the NN discriminant in the $t\bar{t}V$ OS dilepton signal regions.

the untagged jets with the highest p_T are incorporated until the maximum number of jets is reached.

In each signal region, the seven highest ranked variables were selected for the NN analysis. The choice of a relatively small number of variables per region is the result of a balance between limiting the complexity of the analysis, keeping the NN robust against overtraining, and obtaining the largest separation between signal and background. The list of selected variables is given in Table 7.4. Table 7.5 shows the lists of variables used in each region and their ranking.

Although the training is performed separately in each of the three signal regions, Table 7.5 shows that the discriminating variables chosen in the two signal regions of the 2ℓOSZveto region, $(4\text{j}, 1\text{b}+2\text{b})$ and $(\geq 5\text{j}, 1\text{b}+2\text{b})$, are mostly the same, which confirms that the kinematics are similar in these two regions. Furthermore, the event shape variables Cent_{jet} and H1 (or H1_{jet}) appear in the list of highest-ranked variables for all three signal regions.

The discriminating power of many of the variables can be understood from the kinematic properties of the dominant signal decay modes and dominant background process in each region.

In the 2ℓOSZveto region, the dominant signal decay modes consist of a dileptonic $t\bar{t}$ decay, with the associated Z/W-boson decaying hadronically, or alternatively the single lepton decay of a $t\bar{t}$ pair and a leptonic W-boson decay. The main background process is the dileptonic $t\bar{t}$ decay. This signal and background composition explains the discriminating power of the following selected variables:

- $M_{\text{uu}}^{\text{Pt}_{\text{ord}}}$: $t\bar{t}$ events contain two b-jets from the $t \to Wb$ decay of the top quark, corresponding to the two jets with the highest b-tag weight. The two untagged jets with the highest p_T are expected to be the hadronic decay products from the vector bosons. The invariant mass of those jets in the signal samples shows a narrow peak around the invariant mass of the vector bosons.

Variable	2ℓOSZveto		2ℓOSZ
	$(4\mathrm{j}, 1\mathrm{b}+2\mathrm{b})$	$(\geq 5\mathrm{j}, 1\mathrm{b}+2\mathrm{b})$	$(\geq 5\mathrm{j}, 2\mathrm{b})$
$M_{\mathrm{uu}}^{\mathrm{Pt}_{\mathrm{ord}}}$	1	7	-
$\mathrm{Cent}_{\mathrm{jet}}$	2	1	6
H1	3	2	-
$M_{\mathrm{jj}}^{\mathrm{MindR}}$	4	6	-
max $M_{\ell\mathrm{b}}^{\mathrm{MindR}}$	5	5	-
${p_T}^{\mathrm{jet3}}$	6	-	-
${p_T}^{\mathrm{jet4}}$	-	3	-
$\Delta R_{\mathrm{ave}}^{\mathrm{jj}}$	7	-	-
$N_{\mathrm{jets}}^{\lvert M_{jj}-M(V)\rvert<30}$	-	4	2
N_{40}^{jet}	-	-	1
$M_{\mathrm{bb}}^{\mathrm{MaxPt}}$	-	-	3
$\Delta R_{\ell\ell}$	-	-	4
$M_{\mathrm{bj}}^{\mathrm{MaxPt}}$	-	-	5
$\mathrm{H1}_{\mathrm{jet}}$	-	-	7

Table 7.5.: The lists and rankings of the variables in each of the three signal regions in the OS dilepton channel.

- $M_{\mathrm{jj}}^{\mathrm{MindR}}$: similar to $M_{\mathrm{uu}}^{\mathrm{Pt}_{\mathrm{ord}}}$, the closest pair of jets in ΔR corresponding to the decay products of the vector bosons will have a higher invariant mass than extra radiation jets from the $t\bar{t}$ background.
- max $M_{\ell\mathrm{b}}^{\mathrm{MindR}}$: this variable was designed to separate mainly the $t\bar{t}W$ decay mode where $t\bar{t}$ decays into the lepton plus jets channel and the associated W-boson decays leptonically, from the rest of signal and background processes. In the case of the $t\bar{t}$ background, the maximum invariant mass between the lepton and the closest tagged jet, corresponding to the decay products of the top or antitop quark, is smaller than in the case of the $t\bar{t}W$ signal, where the maximum invariant mass corresponds to a lepton from the associated W boson and a tagged jet from the top.

In the 2ℓOSZ region, the dominant signal decay mode is the one where $t\bar{t}$ decays hadronically and the Z-boson decays leptonically. The main background process is Z+HF jets. Therefore, the following variables are expected to show high discriminating power between signal and background:

- $\Delta R_{\ell\ell}$: although the two opposite-sign leptons originate from the Z-boson in both signal and Z+jets background, the boost of the Z-boson decay products is different in each case, which is reflected in the ΔR between the two leptons.
- $M_{\mathrm{bb}}^{\mathrm{MaxPt}}$ and $M_{\mathrm{bj}}^{\mathrm{MaxPt}}$: these two variables exploit the feature of the signal having two real hard b-jets originating from $t\bar{t}$, while in Z+HF events, the b-jets do not originate from any heavy particle.

Given the poor description of ΔR between jets by Z+jets MC simulation, all variables related to the ΔR between jets were removed from the initial ranking list provided for the 2ℓOSZ region.

Figure 7.11 shows the distribution of the two highest-ranked discriminating variables in each signal region for data and MC simulation.

The separation power between signal and background of each of the seven input variables can be seen in Figures 7.12, 7.13 and 7.14 for the signal regions $(4\mathrm{j}, 1\mathrm{b}+2\mathrm{b})$, $(\geq 5\mathrm{j}, 1\mathrm{b}+2\mathrm{b})$ and $(\geq 5\mathrm{j}, 2\mathrm{b})$, respectively. The discrimination power for each variable in the figures is defined as:

$$S = \frac{1}{2} \cdot \sum_{i}^{bin} \frac{(N_i^{signal} - N_i^{background})^2}{(N_i^{signal} + N_i^{background})^2}, \tag{7.6}$$

where N_i^{signal} and $N_i^{background}$ are the corresponding entries in each bin after the histograms have been normalised to unity.

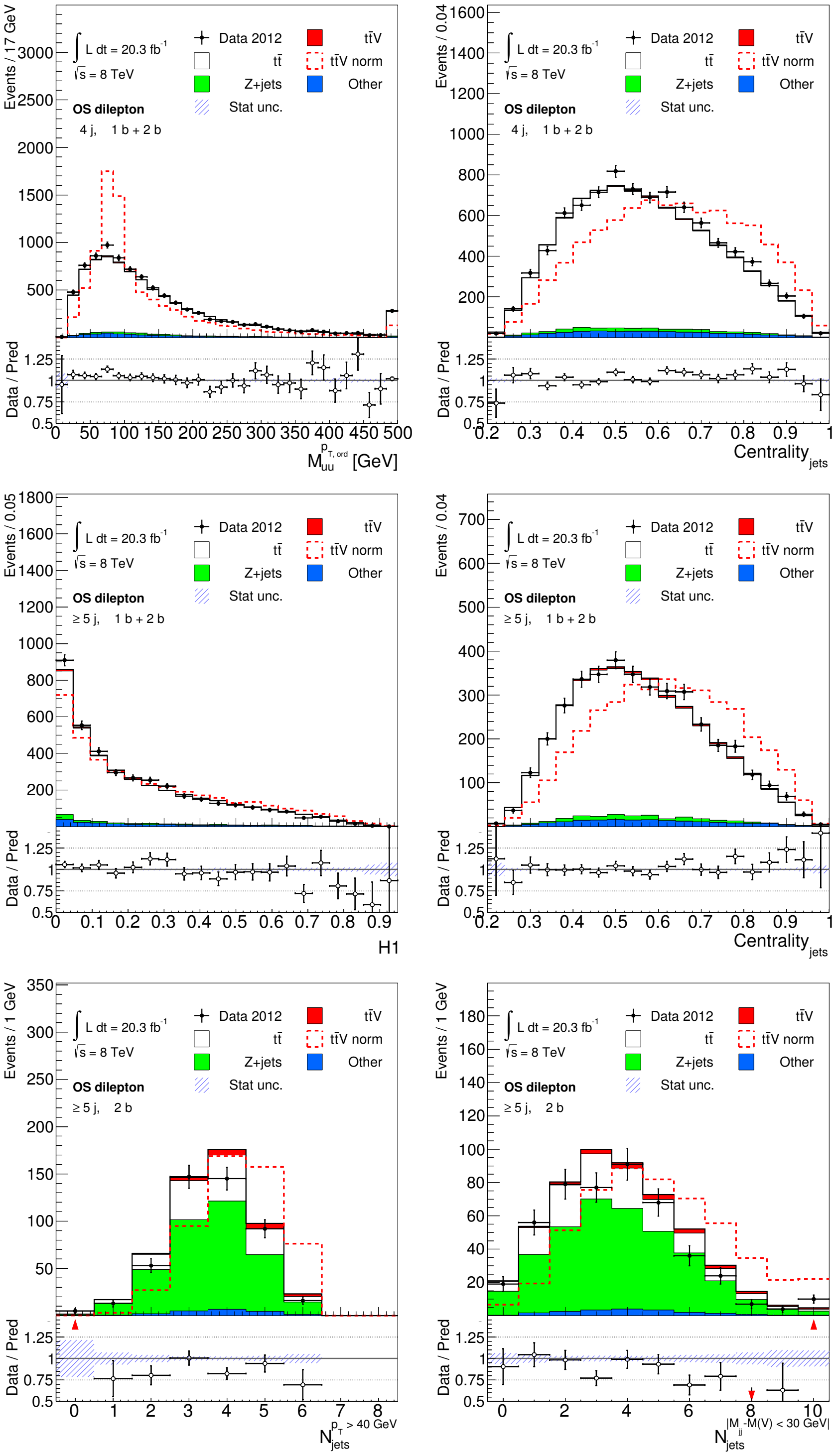

Figure 7.11.: The distributions of the two highest ranked variables in the 2ℓOSZveto (4j, 1b+2b) region (top), the 2ℓOSZveto (≥ 5j, 1b+2b) region (middle) and the 2ℓOSZ (≥ 5j, 2b) region (bottom). The red dashed line shows $t\bar{t}V$ signal normalised to the background yield. The error band includes only statistical uncertainties. The arrow in the bottom panel indicates that the central value of the ratio between data and total prediction in that bin is outside the specified range. The last bin in each histogram includes the overflow.

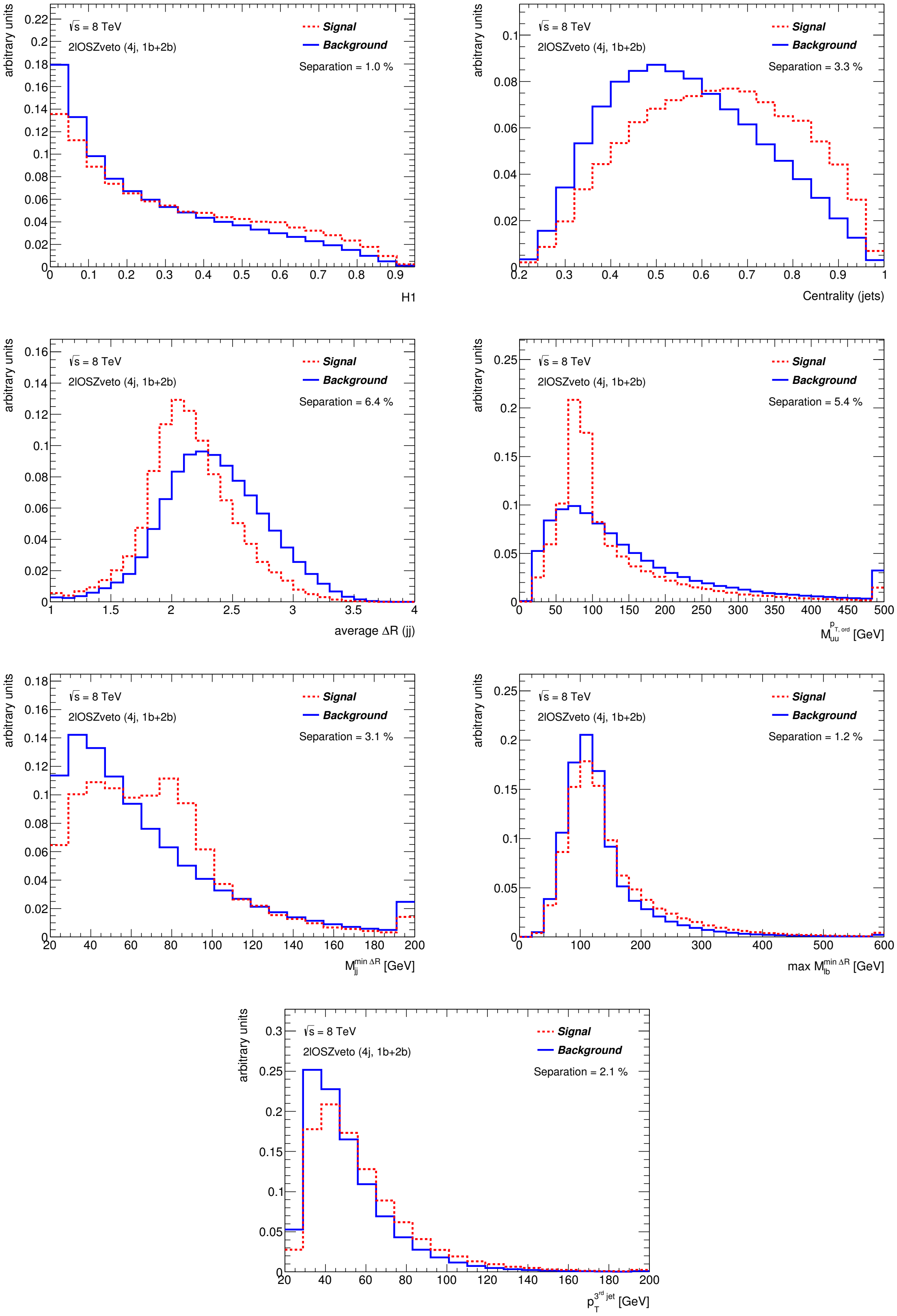

Figure 7.12.: Separation between signal and background for each input variable in the 2ℓOSZveto $(4\mathrm{j}, 1\mathrm{b}+2\mathrm{b})$ region. From top to bottom (left): H1 Fox-Wolfram moment, $\Delta R^{\mathrm{jj}}_{\mathrm{ave}}$, $M^{\mathrm{MindR}}_{\mathrm{jj}}$, ${p_T}^{\mathrm{jet3}}$, and (right): $\mathrm{Cent}_{\mathrm{jet}}$, $M^{\mathrm{Pt_{ord}}}_{\mathrm{uu}}$, max $M^{\mathrm{MindR}}_{\ell\mathrm{b}}$.

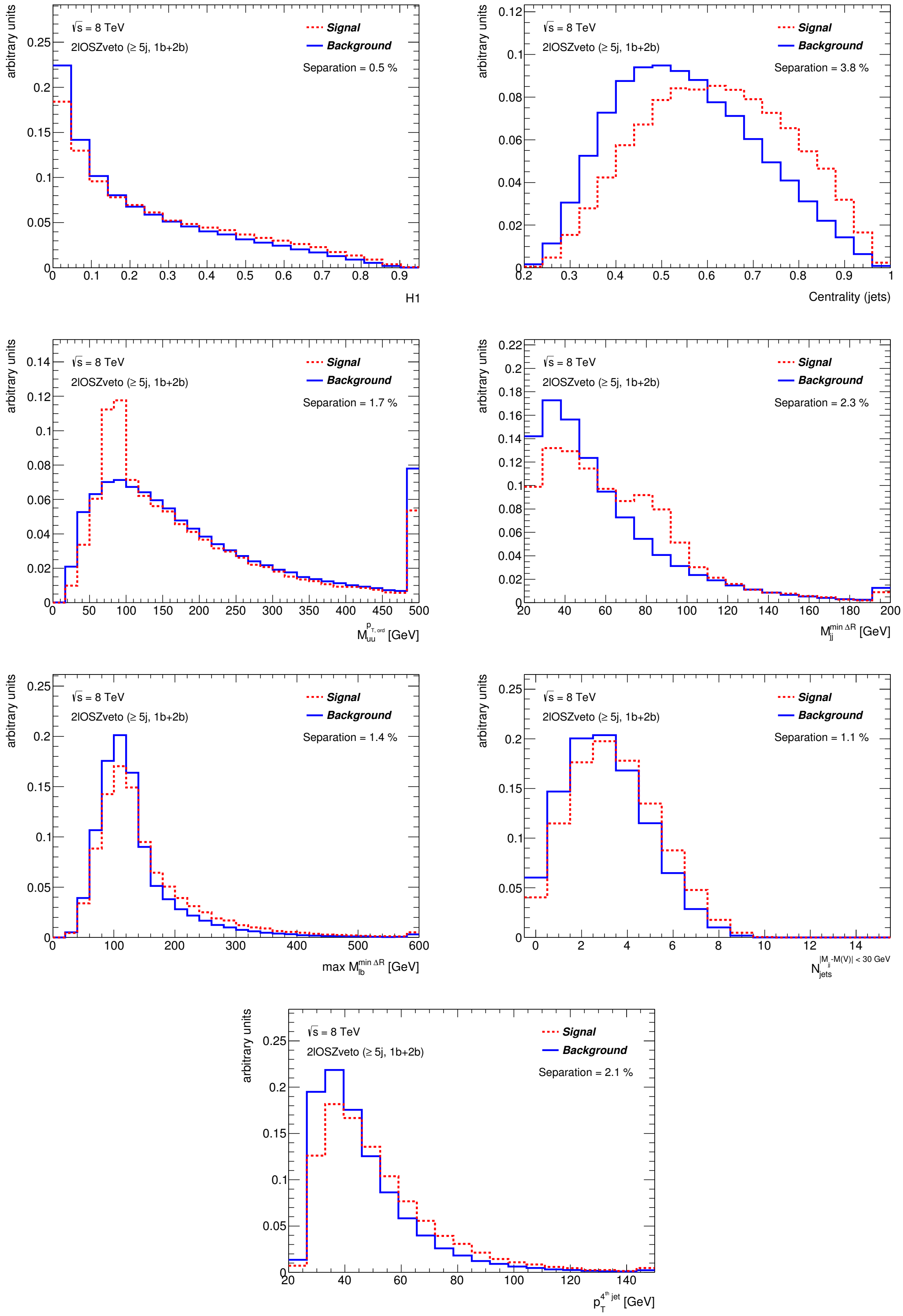

Figure 7.13.: Separation between signal and background for each input variable in the 2ℓOSZveto ($\geq$ 5j, 1b + 2b) region. From top to bottom (left): H1 Fox-Wolfram moment, $M_{\mathrm{uu}}^{\mathrm{Pt_{ord}}}$, max $M_{\ell\mathrm{b}}^{\mathrm{MindR}}$, $p_T{}^{\mathrm{jet4}}$, and (right): $\mathrm{Cent_{jet}}$, $M_{\mathrm{jj}}^{\mathrm{MindR}}$, $N_{\mathrm{jets}}^{|M_{jj}-M(V)|<30}$.

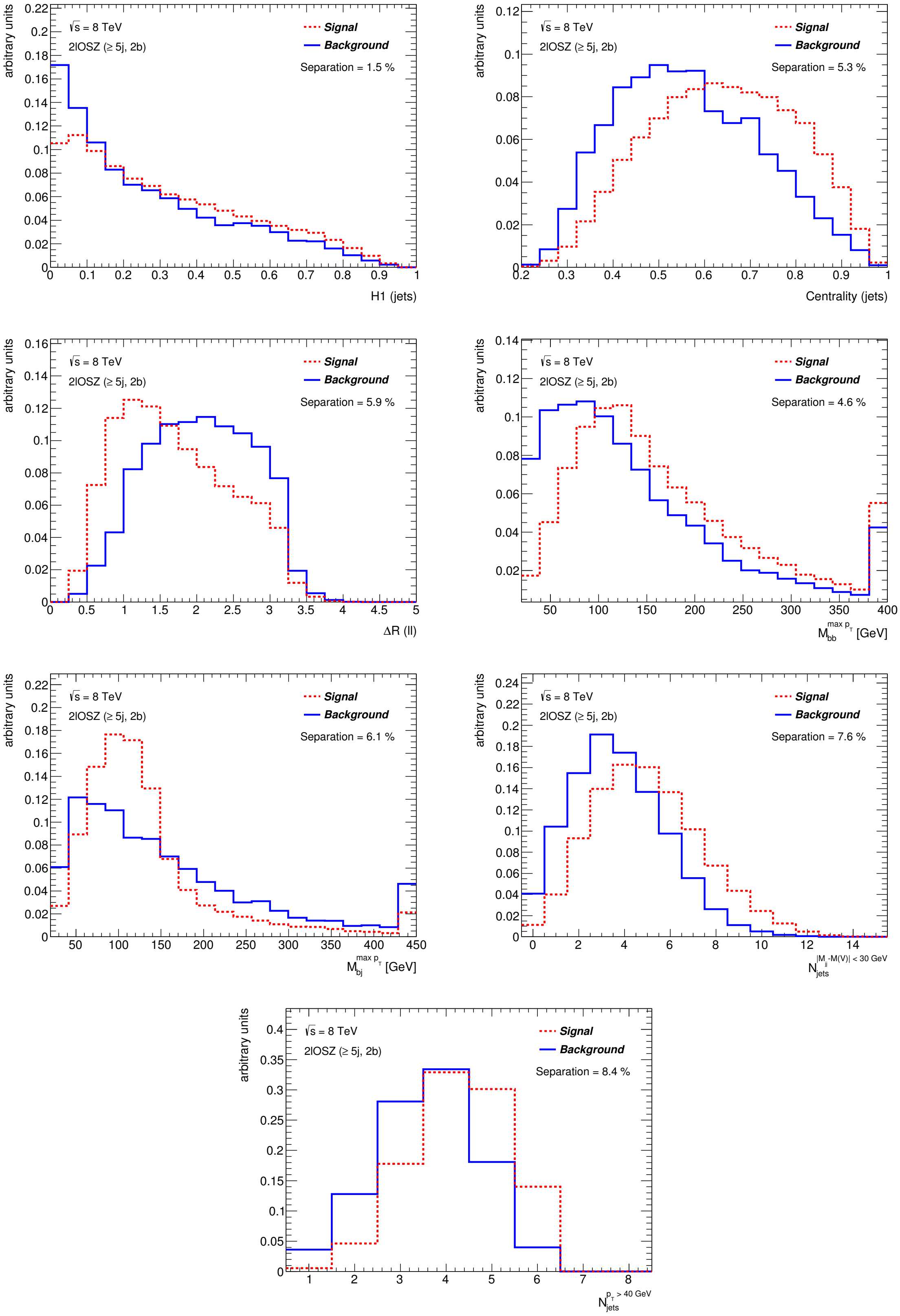

Figure 7.14.: Separation between signal and background for each input variable in the 2ℓOSZ ($\geq$ 5j, 2b) region. From top to bottom (left): $\mathrm{H1}_{\mathrm{jet}}$ Fox-Wolfram moment, $\Delta R_{\ell\ell}$, $M_{\mathrm{bj}}^{\mathrm{MaxPt}}$, N_{40}^{jet}, and (right): $\mathrm{Cent}_{\mathrm{jet}}$, $M_{\mathrm{bb}}^{\mathrm{MaxPt}}$, $N_{\mathrm{jets}}^{|M_{jj}-M(V)|<30}$.

Validation of correlation

Even though the NeuroBayes program is able to deal with the correlation between the input variables, the consistent modelling of such correlations in data and MC simulation needs to be checked. In Figures 7.15, 7.16 and 7.17, linear correlation factors between variables for data, background and their difference are shown. In general, they are found to be consistent between data and MC simulation. The largest deviation in correlation between data and background is 12 % in the 2ℓOSZ $(\geq 5\text{j}, 2\text{b})$ region, as can be seen in Figure 7.17. Given the limited data statistics (≈ 500 events) in this region, larger statistical fluctuations can occur and therefore the correlation matrix of the difference between data and MC is less flat than for the higher-statistics regions in the 2ℓOSZveto region.

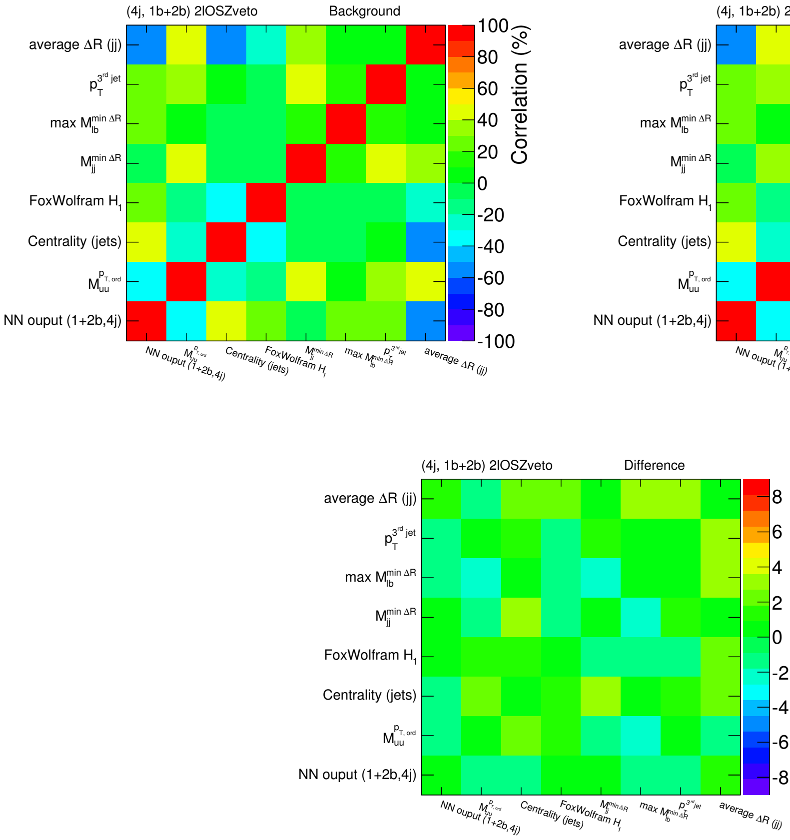

Figure 7.15.: Linear correlations between pairs of input variables in the 2ℓOSZveto $(4\text{j}, 1\text{b}{+}2\text{b})$ region for (top left): background, (top right): data, and (bottom): the difference (data-background).

Final NN discriminants

The output of the NN training phase is a set of weights that can be applied to the input variables and, subsequently, derived quantities in order to yield -1 for background and 1 for signal. This file of weights and the response function can be applied to any signal or background process, even if it was not used in the training, to determine if the process is *background-like* or

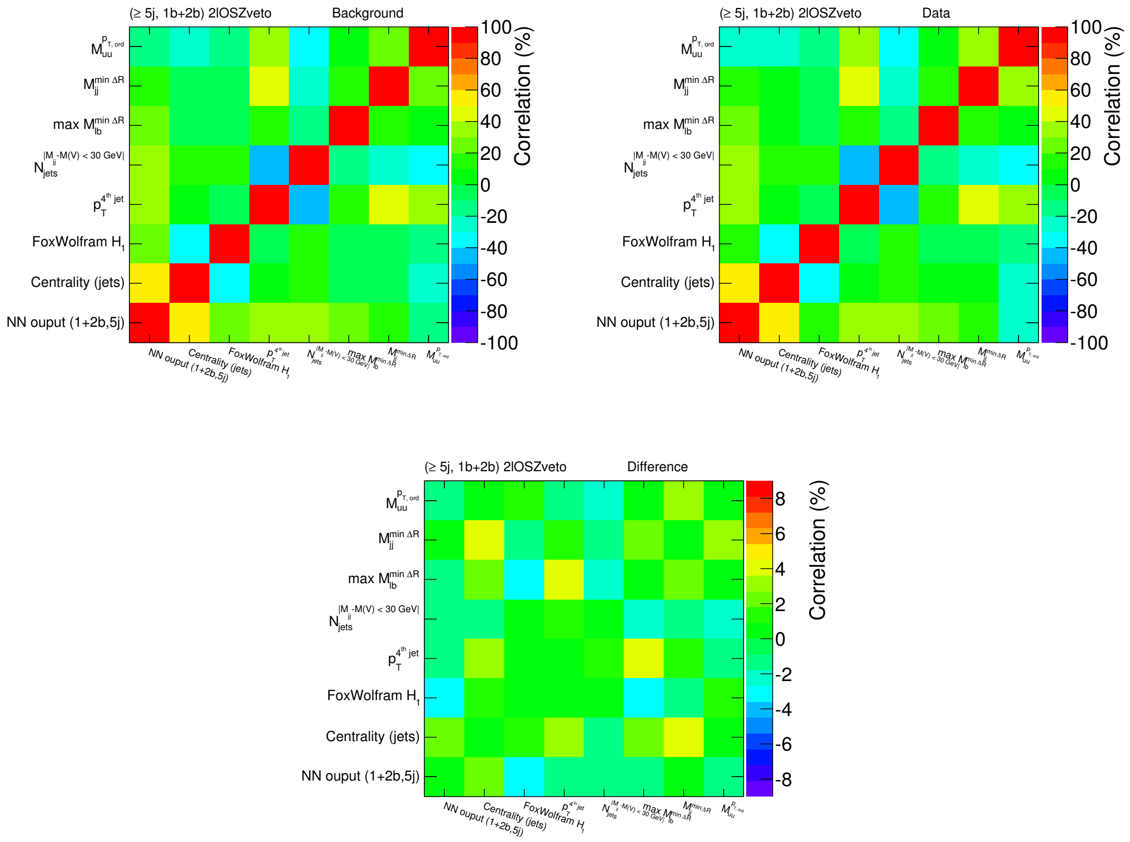

Figure 7.16.: Linear correlations between pairs of input variables in the 2ℓOSZveto ($\geq$ 5j, 1b+2b) region for (top left): background, (top right): data, and (bottom): the difference (data-background).

signal-like. The algorithm is then applied to the data to separate the signal from background in the signal regions.

Figure 7.18 illustrates the discrimination between the $t\bar{t}V$ signal and background provided by the NN discriminant in each signal region. In the 2ℓOSZveto region, the signal contribution comes from $t\bar{t}W$ and $t\bar{t}Z$ production with hadronic W and Z decays respectively. As both contributions are comparable in size and have similar kinematics, they result in a similar NN discriminant shape. In the 2ℓOSZ region, the $t\bar{t}W$ contribution is negligible. Thus the NN discriminant shape in ($\geq$ 5j, 1b + 2b) is driven by the $t\bar{t}Z$ signal.

Figure 7.19 shows the NN output distributions in data and MC in the aforementioned signal regions. A good agreement between data and MC is expected for the NN discriminants, as a result of the good description of the selected input variable distributions in data by the MC simulation. The distributions of the input variables, as well as of the NN distributions in the 2ℓOSZ control regions and in the 2ℓOSZveto signal regions in events with exactly 1 b-jet and 2 b-jets separately, can be found in Appendix A.

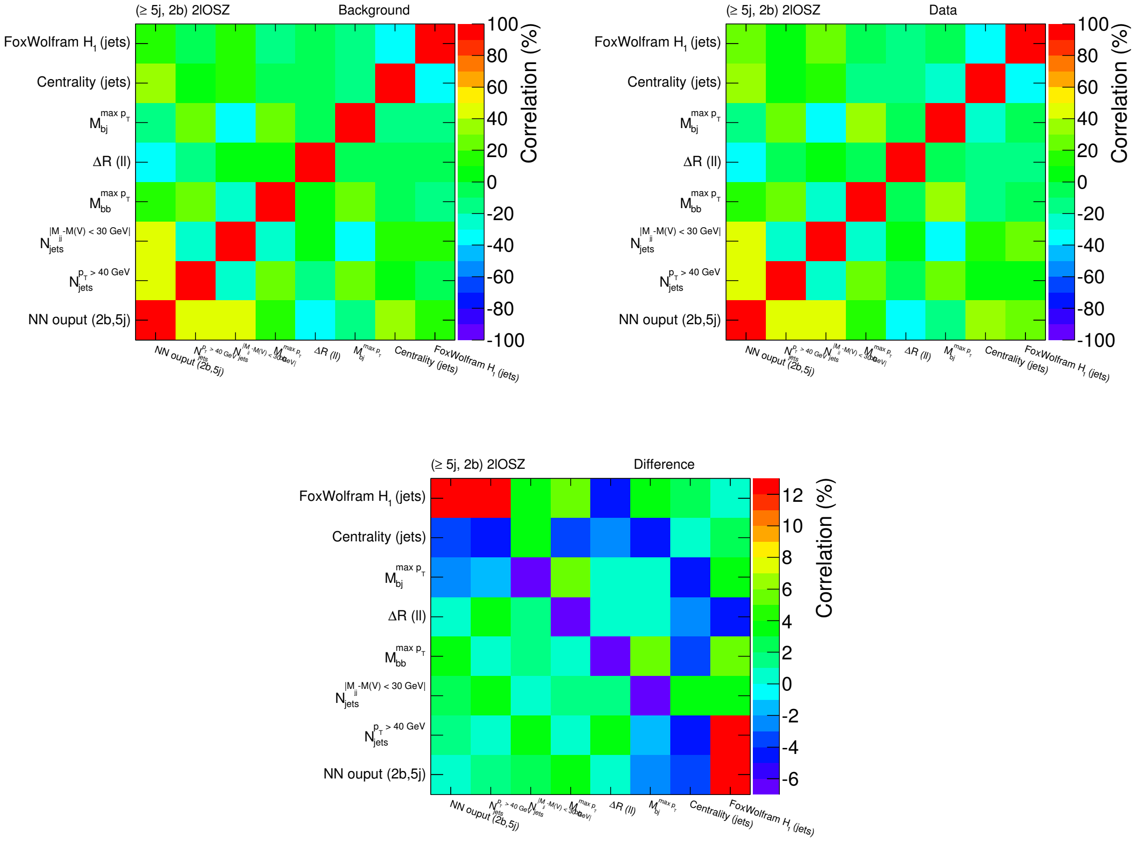

Figure 7.17.: Linear correlations between pairs of input variables in the 2ℓOSZ $(\geq 5\text{j}, 2\text{b})$ region for (top left): background, (top right): data, and (bottom): the difference (data-background).

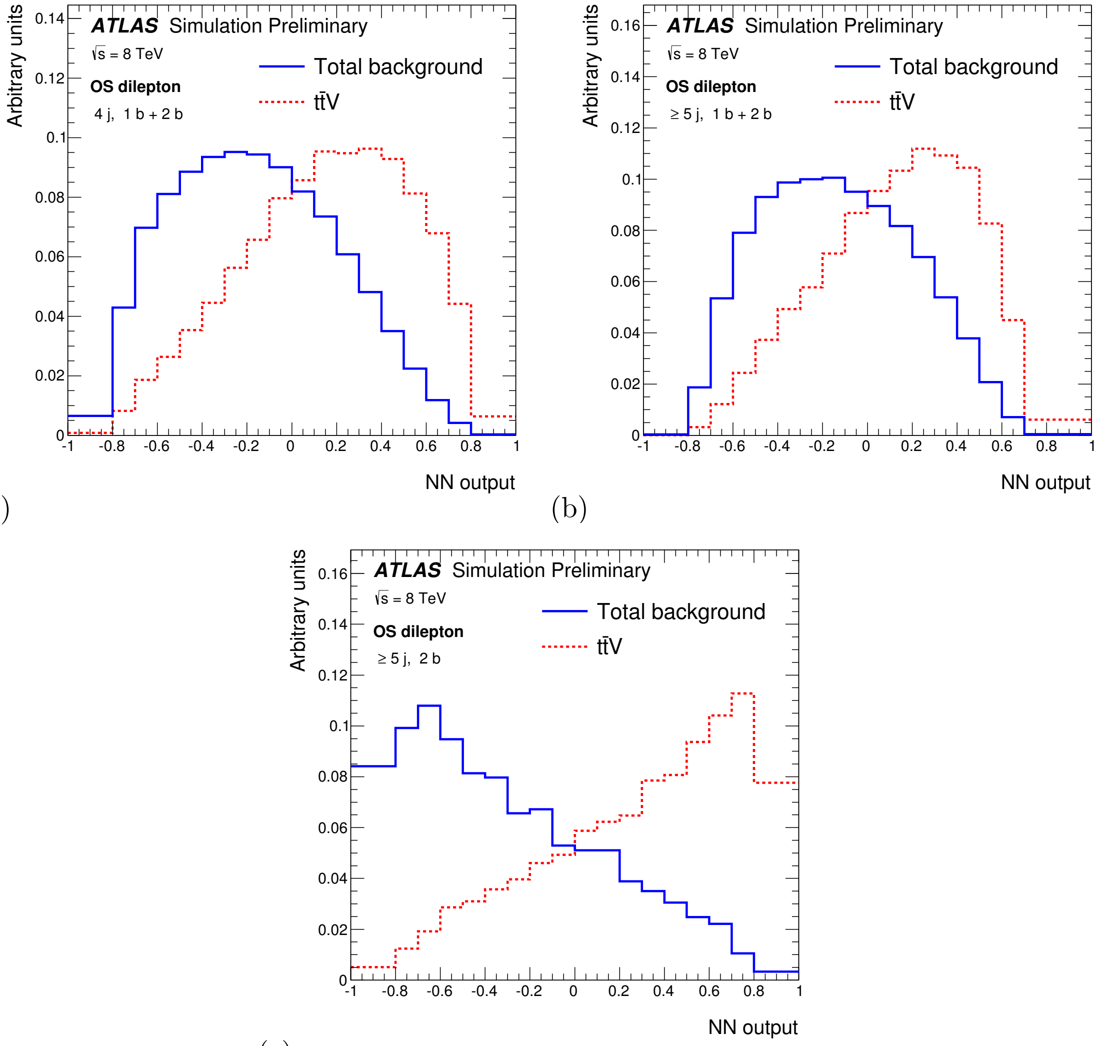

(a)

(b)

(c)

Figure 7.18.: Expected distribution of the NN discriminant for the background (blue) and signal (red dashed) in **(a)** the 2ℓOSZveto $(4\text{j}, 1\text{b}+2\text{b})$ region, **(b)** the 2ℓOSZveto $(\geq 5\text{j}, 1\text{b}+2\text{b})$ region, and **(c)** the 2ℓOSZ $(\geq 5\text{j}, 2\text{b})$ region.

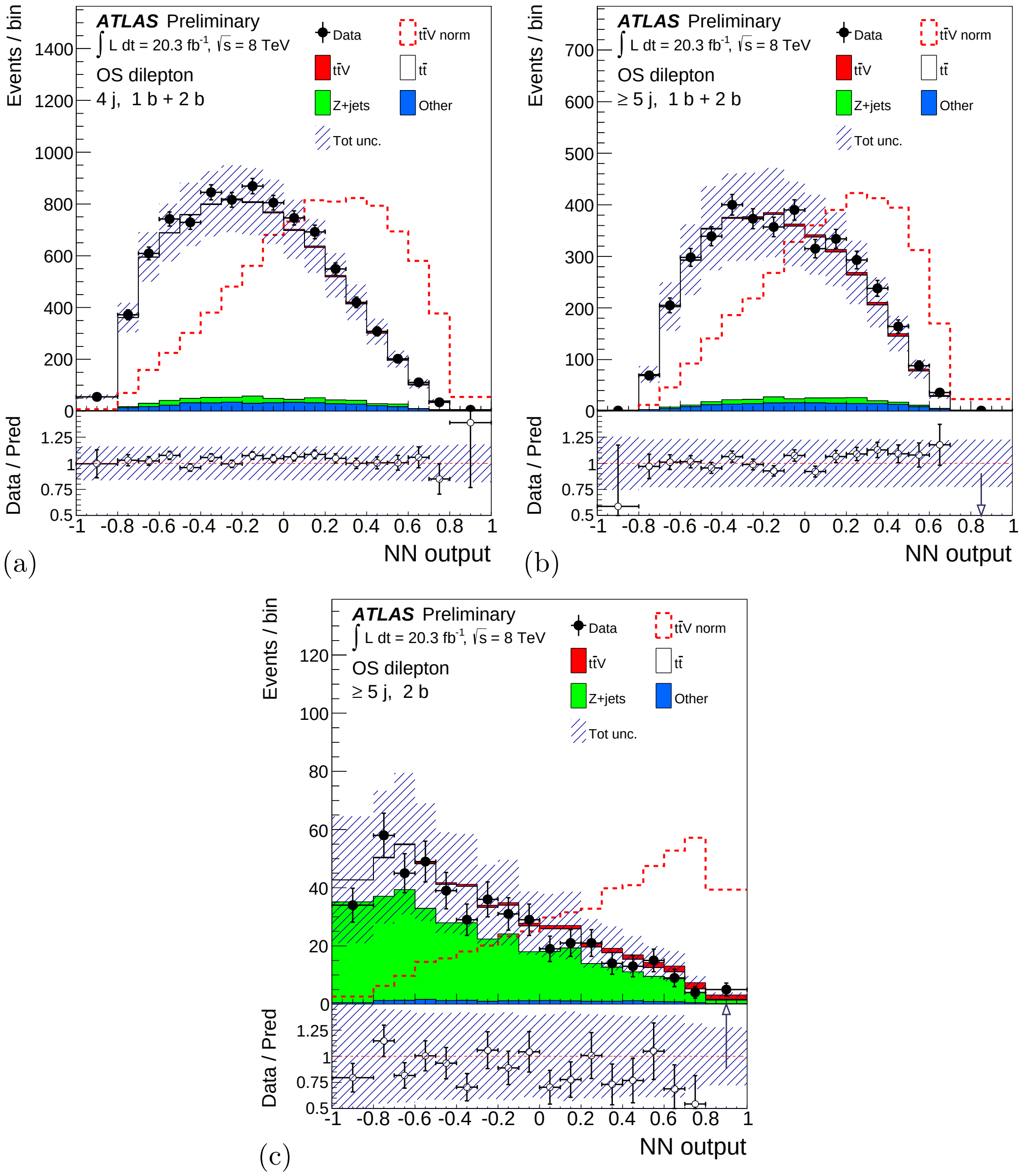

(a) (b) (c)

Figure 7.19.: NN output distributions in data and MC simulation in **(a)** the 2ℓOSZveto ($4\text{j}, 1\text{b} + 2\text{b}$) region, **(b)** the 2ℓOSZveto ($\geq 5\text{j}, 1\text{b} + 2\text{b}$) region, and **(c)** the 2ℓOSZ ($\geq 5\text{j}, 2\text{b}$) region. The uncertainty bands include both MC statistical uncertainty and systematic uncertainties before the fit procedure. The red dashed line shows the $t\bar{t}V$ signal normalised to the background yield.

Partial blinding of the analysis

In the first stage of the analysis, a partial blinding of the analysis was performed. The “blinding” procedure consists of “hiding” the most signal-enriched regions when validating the agreement between data and MC simulation, in order to not bias the measurement by optimising or correcting the MC model based on the region where a signal is expected [2].

The *partial blinding* used in this analysis exploits the separation between signal and background provided by the NN outputs in the signal regions. The blinding is defined by excluding events with high NN values, corresponding to the signal-enriched region. The advantage of this procedure compared to a drastic blinding of the whole signal region is that it allows to understand the behaviour of the background at high jet and b-jet multiplicity regions, without including the signal-like events.

The regions with the highest S/B, the 2ℓOSZveto $(\geq 5\mathrm{j}, 1\mathrm{b}+2\mathrm{b})$ region and the 2ℓOSZ $(\geq 5\mathrm{j}, 2\mathrm{b})$ region, were partially blinded. Figure 7.20 (top) shows the expected S/B for each bin of the NN in those regions. The cut on the NN is chosen requiring a $S/B < 2\%$. In the $(\geq 5\mathrm{j}, 1\mathrm{b}+2\mathrm{b})$ region it corresponds to a cut value of 0.2, and in the $(\geq 5\mathrm{j}, 2\mathrm{b})$ region it corresponds to a cut value of -0.3.

Figure 7.20 (bottom) shows the integrated S/B as a function of the NN values. With the chosen blinding procedure, the expected signal contamination in the considered regions is well below 1%.

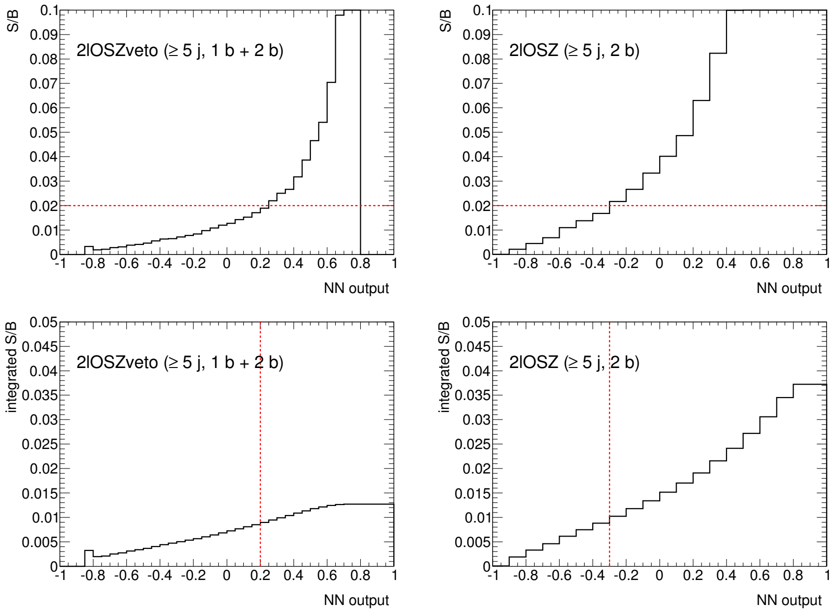

Figure 7.20.: The S/B as a function of the NN output in (top left): the 2ℓOSZveto $(\geq 5\mathrm{j}, 1\mathrm{b}+2\mathrm{b})$ region, and in (top right): the 2ℓOSZ $(\geq 5\mathrm{j}, 2\mathrm{b})$ region. The red lines correspond to a $S/B = 2\%$. The integrated S/B as a function of the NN distribution in (bottom left): the 2ℓOSZveto $(\geq 5\mathrm{j}, 1\mathrm{b}+2\mathrm{b})$ region, and in (bottom right): the 2ℓOSZ $(\geq 5\mathrm{j}, 2\mathrm{b})$ region. The red lines represent the position of the chosen cut on the NN output.

---

[2] It has to be noted that the “measurement” of the $t\bar{t}V$ production process started as a search.

CHAPTER 8

Statistical Analysis and Results

8.1. The Fit

The Profile Likelihood Fit

The fitting procedure used in this analysis is based on the maximisation of a likelihood function. The likelihood function represents the probability that a given hypothesis is supported by data. The hypothesis is represented by the *signal strength* parameter, μ, defined as:

$$\mu = \frac{\sigma_{t\bar{t}V}}{\sigma_{t\bar{t}V}^{SM}} = \begin{cases} 0 & \text{background-only hypothesis} \\ 1 & \text{SM } t\bar{t}V \text{ signal hypothesis} \end{cases} . \quad (8.1)$$

A simplified version of a binned likelihood function in terms of μ, which is the parameter of interest in the fit, and the observed data, without considering contributions from systematic uncertainties, can be expressed as the product of the Poissonian probability of observing n_k data events when $(\mu s_k + b_k)$ events are expected, for each bin k in the fit:

$$L_{Pois}(\mu) = \prod_{k \in Allbins} Pois(n_k | (\mu s_k + b_k)) = \prod_{j}^{reg} \prod_{i}^{bins(j)} \frac{(\mu s_{ij} + b_{ij})^{n_{ij}}}{n_{ij}!} \exp\left(-(\mu s_{ij} + b_{ij})\right), \quad (8.2)$$

where s_{ij} and b_{ij} are the expected number of signal and background events in bin i of the fitted distribution in the fit region j, respectively.

In the presented analysis, the systematic uncertainties are included in the likelihood as a set of continuous parameters, θ, called *nuisance parameters*. They parameterise the effect of each systematic uncertainty on the template distributions in each region. As it will be discussed in Section 8.2, most of the systematic uncertainties, in particular those related to the physics objects, are estimated from auxiliary measurements, which provide the nominal and the $\pm 1\sigma$ variations. In the case of systematic uncertainties related to theory or modelling, the difference between the alternative and the nominal model is taken as $+1\sigma$ variation, and is then symmetrised to obtain the -1σ variation. The nominal template corresponds to a value of the nuisance parameter $\theta = 0$, while the $\pm 1\sigma$ variation of the systematic uncertainty corresponds to $\theta = \pm 1$. In order to define a continuous parameterisation of the systematic uncertainties from these templates, an interpolation and extrapolation procedure is used for the ranges $|\theta| \leq 1$ and $|\theta| \geq 1$, respectively. The component of the uncertainty affecting the shape of the template, and the component modifying the overall normalisation of a template within a fit region are treated internally in the fit with different methods [1]. Both methods use a 6^{th} order polynomial interpolation function, and a linear extrapolation function, in order to create a continuous set for each systematic uncertainty [194]. With these choices, a continuity of θ over the whole range is ensured. For the component of the uncertainty affecting the shape of the discriminants, a *vertical template morphing* is implemented, performing the interpolation and extrapolation independently per-bin [195].

Each nuisance parameter is included in the likelihood function with a Gaussian (or log-normal) distribution constrain, with mean equal to zero and a standard deviation equal to 1, representing the prior knowledge of them. Since a value of $\theta \neq 0$ modifies the nominal template distributions, s_{ij} and b_{ij}, and as a result also L_{Pois}, depend on θ.

Given the finite MC statistics of the templates used in the fit, an additional set of nuisance parameters, γ, is included in the likelihood function. Each γ corresponds to the MC statistical uncertainty per template bin. If this uncertainty is not large, these nuisance parameters can enter in the likelihood with a Gaussian prior with mean equal to 1 and a standard deviation, $\sigma_{\gamma,ij}$, equal to the relative statistical uncertainty of the sum of all templates in the bin i of the fitted distribution in region j.

The complete likelihood function is therefore expressed as:

$$L(\mu,\theta) = L_{Pois}(\mu,\theta) \cdot \prod_p \frac{1}{\sqrt{2\pi}} \exp\left(-\frac{\theta_p^2}{2}\right) \cdot \prod_{i,j} \frac{1}{\sqrt{2\pi}\sigma_{\gamma,ij}} \exp\left(-\frac{(\gamma_{ij}-1)^2}{2\sigma_{\gamma,ij}^2}\right), \tag{8.3}$$

where p runs over all nuisance parameters related to the systematic uncertainties included in the fit.

When maximising $L(\mu,\theta)$, or minimising the $-\log L$, a simultaneous measurement of the parameter of interest, μ, and the nuisance parameters is performed. The values of those parameters that maximise the likelihood function are called “best fit” values and are denoted by $\hat{\mu}$ and $\hat{\theta}$.

The process of including the nuisance parameters in the fit is referred to as “profiling”: the best fit estimate and the corresponding $\pm 1\sigma$ fitted uncertainty on μ is extracted from the scan of the $-\log L$ with respect to μ, computing and minimising the $-\log L$ for each μ value.

This scan over the parameter of interest, μ, can be also understood in terms of the *profile likelihood ratio*, λ, defined as [196]:

$$\lambda(\mu) = \frac{L(\mu,\hat{\hat{\theta}})}{L(\hat{\mu},\hat{\theta})}, \tag{8.4}$$

where the denominator is the maximised unconditional [2] likelihood function, the “best fit” values $\hat{\mu}$ and $\hat{\theta}$ are their maximum likelihood estimators, and the numerator is the maximised conditional likelihood, where $\hat{\hat{\theta}}$ denotes the values of θ that maximise the likelihood function for the specified μ.

---

[1] However, both shape and normalisation effects enter as one nuisance parameter in the fit, unless stated otherwise.

[2] The maximisation of a likelihood function is denoted as unconditional (conditional), when the parameter of interest is considered a free (fixed) parameter in the likelihood.

Wilk's theorem shows that $-2\log\lambda(\mu)$ is asymptotically distributed as a chi-square distribution [197]. Therefore, the profile likelihood curve has a parabolic shape [198]:

$$-2\log\lambda(\mu) = -2(\log L(\mu, \hat{\hat{\theta}}) - \log L(\hat{\mu}, \hat{\theta})) = \left(\frac{\mu - \hat{\mu}}{\sigma_\mu}\right)^2, \tag{8.5}$$

where σ_μ represents the Gaussian standard deviation of the parameter of interest, μ. In other words, the best fit value for μ can be extracted from minimising the $-\log\lambda(\mu)$, and the fitted $\pm 1\sigma_\mu$ are the values of μ that correspond to $-\log\lambda(\mu) = 0.5$ in the profile likelihood curve. The presence of the nuisance parameters broadens the profile likelihood curve as a function of μ, reflecting the loss of information about μ due to the systematic uncertainties.

The profile likelihood fit allows a reduction of the impact from systematic uncertainties on the signal sensitivity by including high-statistics signal-depleted control regions, allowing data to improve the initial knowledge of systematic uncertainties, and extrapolating that knowledge to the signal-enriched regions. The fit to data can:

- *shift*, or *pull*, a nuisance parameter's central value to improve the data/MC agreement, and/or
- *reduce*, or *constrain*, a nuisance parameter's uncertainty with respect to the nominal value, if the initial large uncertainty effect is not supported by data.

In the fit procedure, correlations between the different nuisance parameters are established, allowing a further reduction of the total effect of the systematic uncertainties on the measured μ.

This powerful fit procedure requires a good understanding of the effect of each systematic uncertainty on the distributions in each fit region and for each process. This also allows a proper interpretation of the fit results.

Search as a Statistical Test

In order to discover a new signal process, such as $t\bar{t}Z/W/V$, a *null hypothesis* is defined as the *background-only hypothesis*, where the corresponding $\mu = 0$. To quantify the level of disagreement between the data and the background-only hypothesis, the p_0-value is computed. The p_0-value refers to the probability of the observed data to be caused by a fluctuation in the background-only hypothesis. This information can be also expressed as the *significance*, Z_0, defined as:

$$Z_0 = \Phi^{-1}(1 - p_0), \tag{8.6}$$

where Φ^{-1} is the inverse of the cumulative distribution of the standard Gaussian. Therefore, the correspondence between the significance, Z_0, and p_0 is such that a Gaussian distributed variable found Z_0 standard deviations above the background-only hypothesis ($\mu = 0$) has an upper-tail probability equal to p_0. For instance, a rejection of the background-only hypothesis with a significance of $Z = 5$, considered within the particle physics community as an appropriate value to constitute a discovery of a new signal, corresponds to $p_0 = 2.87 \times 10^{-7}$.

The p_0 value is computed from the test statistic q_0, which is defined as:

$$q_0 = \begin{cases} -2ln\lambda(0) & \hat{\mu} \geq 0 \\ 0 & \hat{\mu} < 0 \end{cases} \tag{8.7}$$

where $\lambda(0)$ is the aforementioned profile likelihood ratio for $\mu = 0$.

The p_0 value is defined as:

$$p_0 = \int_{q_{0,\mathrm{obs}}}^{\infty} f(q_0|0)\, dq_0, \tag{8.8}$$

where $f(q_0|0)$ is the probability density function of q_0 under the assumption of $\mu = 0$, and $q_{0,\mathrm{obs}}$ is the observed test statistic value.

In the asymptotic limit, the aforementioned Wilk's theorem can be used, and $Z_0 = \sqrt{q_0} = \hat{\mu}/\sigma$, where σ is the fitted Gaussian error on $\hat{\mu}$. However, this approximation is not completely valid for the data sample size of the additional channels entering the combination with the OS dilepton channel. Therefore, for consistency across channels, the complete calculation of the significance is performed in the OS dilepton channel, as well as for the combined result.

The Fit Model

In order to exploit the profile likelihood fit capabilities, the fit regions include both signal and control regions as defined in Section 7.2.1. Table 8.1 summarises the discriminants used in each fit region. The discriminant used in the three signal regions are the NN distributions presented in Section 7.3. In the control regions, the H_T^{had} variable is used (scalar sum of the transverse momentum of the jets), since it is sensitive to systematic variations and can therefore allow the data to limit the effect of the systematic uncertainties in the signal regions. For the control region $(3\mathrm{j}, 1\mathrm{b}+2\mathrm{b})$, only the normalisation information is used, due to a non-negligible data/MC disagreement in the H_T^{had} distribution prior to the fit [3]. Since that fit region is the one with highest statistics, including the shape information of H_T^{had} produces artificial shifts of nuisance parameters in the fit, to minimise the data/MC disagreement.

	2ℓOSZveto	2ℓOSZ
	$1b + 2b$	$2b$
$3j$	norm	H_T^{had}
$4j$	NN	H_T^{had}
$\geq 5j$	NN	NN

Table 8.1.: Summary of the fit regions and the corresponding discriminating variables used in each of the regions.

All six regions enter the final statistical analysis, resulting in a total of 92 bins in the likelihood function. The nuisance parameters corresponding to the MC template statistics are only considered for bins with a relative MC statistical uncertainty larger than 1%.

The fitted signal strength, $\hat{\mu}$, is allowed to be negative in the fit, with the condition that the Poisson mean values, $\mu s_{ij} + b_{ij}$, remain non-negative [196].

Figure 8.1 shows the distributions of the six discriminants in the corresponding fit region before the fit procedure. The uncertainty band includes both MC statistical and systematic uncertainties.

---

[3] The relative loss of sensitivity when replacing the H_T^{had} with a 1-bin normalisation template is negligible.

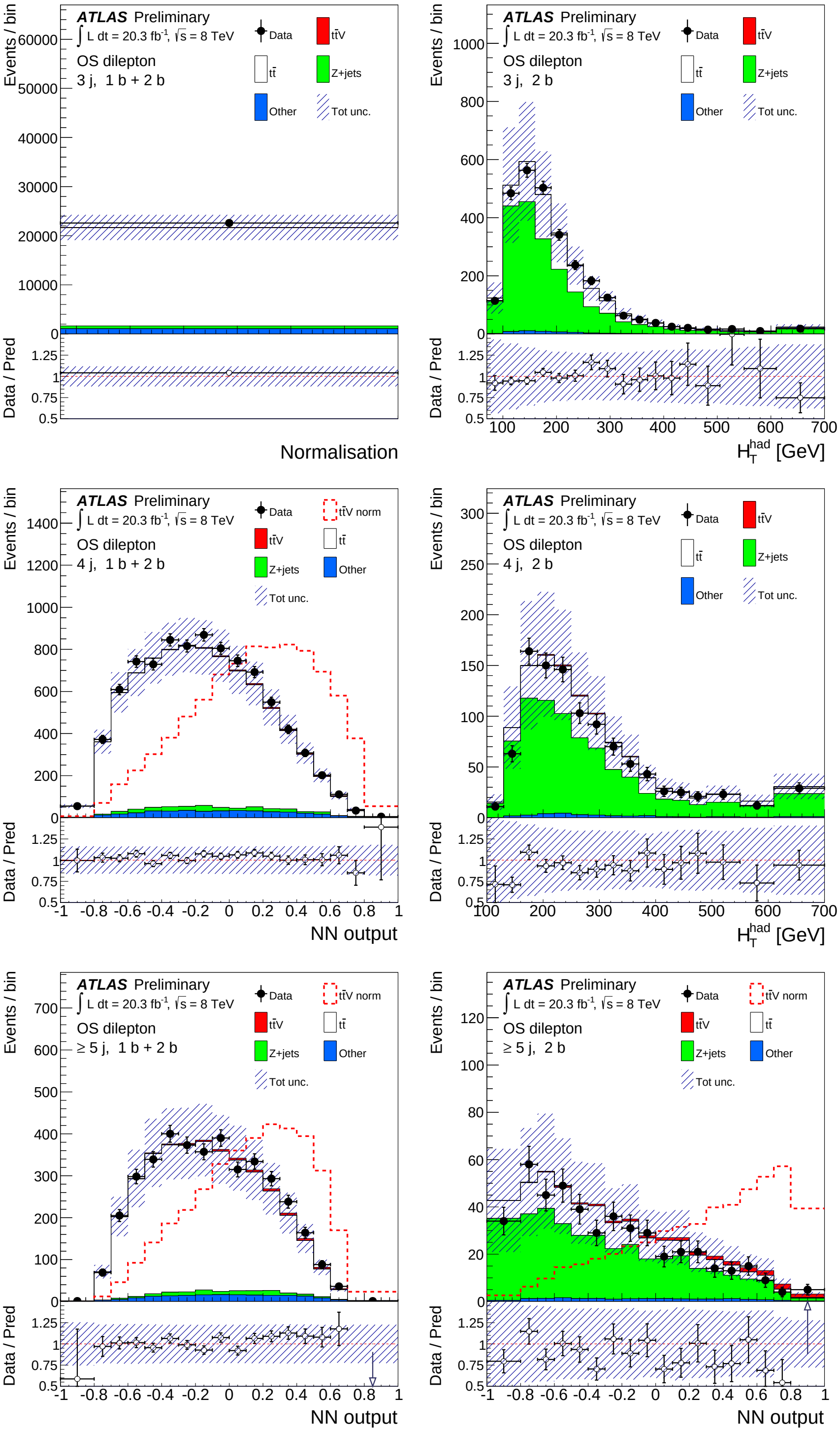

Figure 8.1.: Pre-fit distributions for each of the six regions included in the fit. The left (right) column shows distributions in the 2ℓOSZveto (2ℓOSZ) region. The red dashed line shows the $t\bar{t}V$ signal normalised to the background yield. The top left plot shows the $(3\text{j}, 1\text{b} + 2\text{b})$ region, where only event counting is used in the fit, while the top right plot shows the $(3\text{j}, 2\text{b})$ region with the H_T^{had} distribution. The middle plots show the $(4\text{j}, 1\text{b} + 2\text{b})$ and $(4\text{j}, 2\text{b})$ regions, where a NN and the H_T^{had} distribution is used, respectively. The bottom two plots show the $(\geq 5\text{j}, 1\text{b} + 2\text{b})$ and $(\geq 5\text{j}, 2\text{b})$ regions, where a NN discriminant is used in each of them.

8.2. Systematic Uncertainties

Several sources of systematic uncertainties are considered that can affect the normalisation of signal and background and/or the shape of their discriminant distributions. Individual sources of systematic uncertainty are considered uncorrelated. Correlations of a given systematic uncertainty are maintained across processes and channels.

Each background normalisation is controlled by a nuisance parameter containing the theoretical uncertainty on the cross section, and a variation of such a parameter yields an overall change of the normalisation of the corresponding background. The overall normalisation of the signal process is determined by a free-floating parameter in the fit, μ.

Table 8.2 presents a summary of the systematic uncertainties considered in the analysis indicating whether they are taken to be normalisation-only (N), shape-only (S), or both shape and normalisation (SN). The breakdown of systematic uncertainties, such as the 22 subcomponents of the Jet Energy Scale, provide flexibility to the fit model. It allows to decouple systematic effects that, if the envelope would be considered instead, would create artificial over-constraints of the nuisance parameters. The breakdown of the systematic uncertainties related to physics objects into sub-components was provided as external inputs. Other effects related to the modelling of the backgrounds, such as the ALPGEN scale variation in the Z+jets modelling or the generator uncertainty on the $t\bar{t}$ modelling, are split into sub-components within the $t\bar{t}V$ analysis, as will be explained in Section 8.2.2.

The following sections describe each of the systematic uncertainties considered in the analysis, classified in three categories: detector-related systematics, background modelling systematics, and signal modelling systematics.

	Systematic uncertainty	Type	Components
	Luminosity	N	1
Physics Objects	Electron	SN	5
	Muon	SN	6
	Jet vertex fraction	SN	1
	Jet energy scale	SN	22
	Jet energy resolution	SN	1
	Jet reconstruction efficiency	SN	1
	E_T^{miss} systematics	SN	2
	b-tagging efficiency	SN	6
	c-tagging efficiency	SN	6
	Light jet-tagging efficiency	SN	12
Signal and Background Modelling	Z cross section	N	1
	Z modelling: p_T(Z) reweighting	S	1
	Z modelling: Alpgen scale	SN	2
	Z modelling: generator/parton shower	N	1
	$t\bar{t}$ cross section	N	1
	$t\bar{t}$ modelling: reweighting	SN	9
	$t\bar{t}$ modelling: generator	SN	2
	$t\bar{t}$ modelling: parton shower	N	1
	$t\bar{t}$+heavy-flavour normalisation	N	1
	$t\bar{t}H$ cross section	N	1
	$t\bar{t}H$ model	SN	2
	Single top cross section	N	1
	Single top modelling	SN	1
	Diboson+jets normalisation	N	1
	Diboson+heavy-flavour normalisation	N	1
	tZ cross section	N	1
	Fake background	SN	2
	$t\bar{t}V$ modelling	SN	1
	$t\bar{t}V$ PDF	SN	1

Table 8.2.: List of systematic uncertainties considered. An “N” means that the uncertainty is taken as normalisation-only for all processes and channels affected, whereas an “S” denotes systematics that are considered shape-only in all processes and channels. An “SN” means that the uncertainty is taken as both shape and normalisation. Some of the systematic uncertainties are split into several different components for a more accurate treatment, indicating the number under the column labeled as “Components”.

8.2.1. Detector Systematics

Luminosity

The luminosity estimate has an uncertainty of 2.8%, determined using beam-separation scans, also known as *van der Meer* scans, where the absolute luminosity can be inferred from direct measurements of the beam parameters [199, 200]. This systematic uncertainty is applied to all contributions obtained from MC simulation.

Uncertainties on Physics Objects

Leptons Uncertainties associated with the lepton selection arise from the trigger, reconstruction, identification, isolation and lepton momentum scale and resolution. In total, uncertainties associated with electrons (muons) include 5 (6) components.

The uncertainty on the reconstruction, identification and trigger efficiency of electrons and muons are derived by applying the *tag-and-probe* techniques on $Z \to \ell^+\ell^-$ ($\ell = e, \mu$) events, as already introduced in Section 4.2 and 4.3.

The accuracy of the lepton momentum scale and resolution in simulation is checked using reconstructed distributions of the $Z \to \ell^+\ell^-$ and $J/\psi \to \ell^+\ell^-$ masses. In the case of electrons, E/p studies, using the combined measurement of track momentum in the inner detector p and the energy in the calorimeter E, are also used, profiting from the large statistics $W \to e\nu$ sample. In the case of muons, uncertainties on both the momentum scale and resolutions in the muon spectrometer and the tracking system are considered, and varied separately.

Jet Energy Scale The jet energy scale (JES) uncertainty is split into 22 uncorrelated sources which model the p_T and η dependencies of the JES uncertainty [126] and are treated independently:

- **In situ calibration techniques**: the residual in situ corrections outlined in Section 4.4.1 exploit the transverse momentum balance between the jet and a well-measured reference object, and is defined as:

  $$\mathcal{R}(p_T^{\text{jet}}, \eta) = \frac{(p_T^{\text{jet}}/p_T^{\text{ref}})_{\text{data}}}{(p_T^{\text{jet}}/p_T^{\text{ref}})_{\text{MC}}}. \tag{8.9}$$

  Jets in the central region are calibrated using photons or Z-bosons ($Z \to e^+e^-$) as reference objects up to a transverse momentum of 800 GeV. For higher p_T jets, a calibration using a system of low-p_T jets recoiling against a high-p_T jet is used. The corresponding uncertainties on the jet response ratio $\mathcal{R}$ for each in situ technique in the central region as a function of the jet p_T can be seen in Figure 8.2, showing the jet p_T range that each technique covers. The different components of this uncertainty are split depending on their source and correlated into the categories: detector description (DET), statistics/method (STAT), physics modelling (MODEL), and mixed detector and modelling (MIXED). From the initial 54 in situ components, a reduced set of 12 is obtained while retaining the information on the correlations with a "diagonalisation and reduction" method [126]. In each category, the components are ordered by their effect, beginning with the largest.

  The calibration of jets in the forward η region of the detector relative to jets in the central η region, denoted as **η-intercalibration**, exploits the transverse momentum balance in dijet events with a well calibrated jet in the central region and a jet in the forward region.

In this way, the dependence of the detector response to jets within $0.8 \leq |\eta| < 4.5$ is removed, by equalising it with the one for jets within $|\eta| < 0.8$. The uncertainties are divided into a statistical component and a MC modelling component, the latter being the dominant one in the forward η region.

- **Single Particle Response**: the uncertainty in the calorimeter response to jets can be obtained from the response uncertainty in the individual particles constituting the jet. In situ measurements of the single hadron response in pp collisions and test-beam data significantly reduce the uncertainty due to a limited knowledge of the detector geometry, such as the presence of dead material, and the modelling of the interaction of particles with the detector [201].
- **Pile-up correction**: uncertainties on the pile-up correction to the jet energy are obtained from the comparison of in situ measurements of the slopes $\alpha = \partial p_T/\partial N_{PV}$ and $\beta = \partial p_T/\partial \mu$ with the corresponding simulation and the results based on a MC simulation only approach, where N_{PV} is the number of reconstructed primary vertices, a measure of the in-time pile-up, and μ is the average number of pile-up interactions per bunch crossing, a measure of the out-of-time pile-up. Hence, the uncertainty covers possible systematic biases due to mismodelling of the effect of pile-up on simulated jets.
- **Flavour related**: the calorimeter response is different for different jet flavour types: gluon, or light jets. This can be attributed to the difference in the fragmentation and showering properties of the jet origin, or flavour. The derived uncertainties on the flavour composition and flavour response are dependent on the topology.
- **Jets with heavy-flavour content**: the main observable, r_{trk}, used to study jets from b-quarks, is defined as:

$$r_{trk} = \frac{|\sum \overrightarrow{p}_T^{track}|}{p_T^{jet}}, \tag{8.10}$$

  where $\overrightarrow{p}_T^{track}$ is the sum of the transverse momentum vectors from all tracks in the jet cone, and p_T^{jet} is the calorimeter jet transverse momentum. Comparisons between data and MC simulations show agreement within systematic uncertainties of approximately 3%, with a weak dependence on the jet p_T [126].

Figure 8.3 shows the fractional contribution of each component to the total JES uncertainty from the 2012 dataset. As expected, the uncertainty on the pile-up correction dominates at low jet p_T, whereas it is negligible at higher jet p_T. At high jet p_T, the uncertainty is driven by the in situ JES uncertainty. The uncertainty in the forward η region is dominated by the contribution of the in situ η-intercalibration, while in the central region, the uncertainty on the flavour response of jets originating from quarks or gluons dominates.

Jet Vertex Fraction As mentioned in Section 4.4.1, the JVF uncertainty is evaluated and propagated to the analysis by varying the nominal JVF cut value up and down to cover the discrepancies in JVF efficiency between data and simulation. Figure 8.4 shows the relative variations of the JVF uncertainty, $\pm 1\sigma$, with respect to the nominal JVF cut, for the Z+jets (top) and $t\bar{t}$ (bottom) background processes in the 2ℓOSZ and 2ℓOSZveto fit regions, respectively. By construction, the JVF uncertainty is not expected to be symmetric, and shows significantly larger variations in the low H_T^{had} region, corresponding to low p_T jets. The overall normalisation variation per fit region goes up to 8% in the high jet multiplicity regions, $(\geq 5\mathrm{j}, 1\mathrm{b}+2\mathrm{b})$ and $(\geq 5\mathrm{j}, 2\mathrm{b})$.

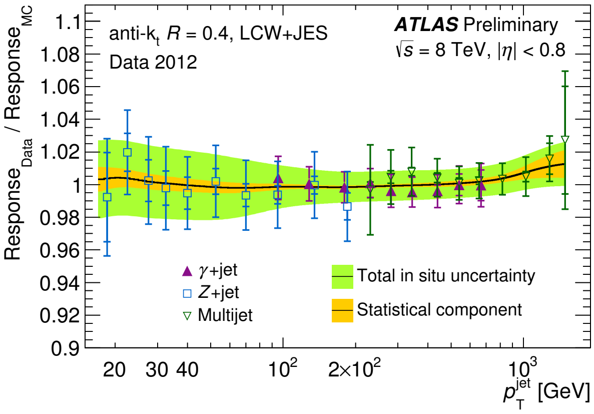

Figure 8.2.: Jet response ratio of data to the MC simulation as a function of p_T for three in situ techniques, which are combined to determine the in situ energy scale correction: Z+jet (squares), γ+jet (full triangles) and multijet (empty triangles). The error bars indicate the statistical and the total uncertainties. The results are shown for LCW+JES calibrated jets. The dark line shows the combination of the in situ techniques, with the total in situ uncertainty band (green) and the statistical uncertainty fraction band (orange) [202].

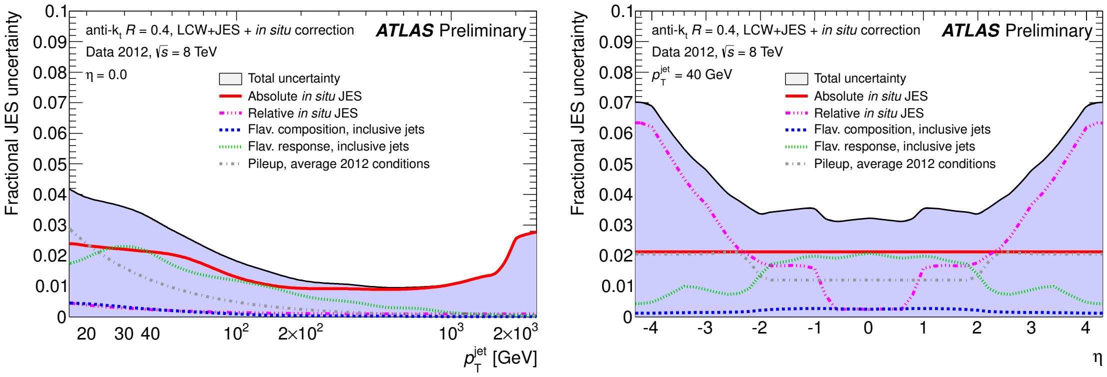

Figure 8.3.: Fractional jet energy scale systematic uncertainty components as a function of (left): p_T for jets at $|\eta| = 0.0$, and (right): η for jets with $p_T = 40$ GeV, using the LCW+JES calibration scheme. The total uncertainty (all components summed in quadrature) is shown as a filled blue region topped by a solid black line. Average 2012 pile-up conditions were used, and topology dependent components (flavour response and composition) were taken from inclusive dijet samples [202].

Jet Energy Resolution The jet energy resolution is measured using the in situ technique called the *bisector method* [203]. The method is based on a transverse balance vector $\vec{P}_T$, defined as the sum of the momenta of the two leading jets in dijet events, $\vec{p}_{T,1}$ and $\vec{p}_{T,2}$. This vector is projected along an orthogonal coordinate system in the transverse plane, (Ψ, η), where η is chosen in the direction that bisects the angle formed by $\vec{p}_{T,1}$ and $\vec{p}_{T,2}$. Different sources can cause fluctuations from the perfectly balanced dijet event, $\vec{P}_T = 0$, giving rise to a non-zero variance on its Ψ and η components.

Figure 8.5 shows the fractional jet energy resolution as a function of the average jet p_T in the central η region for the bisector technique. The jet energy resolution in MC agrees in general with

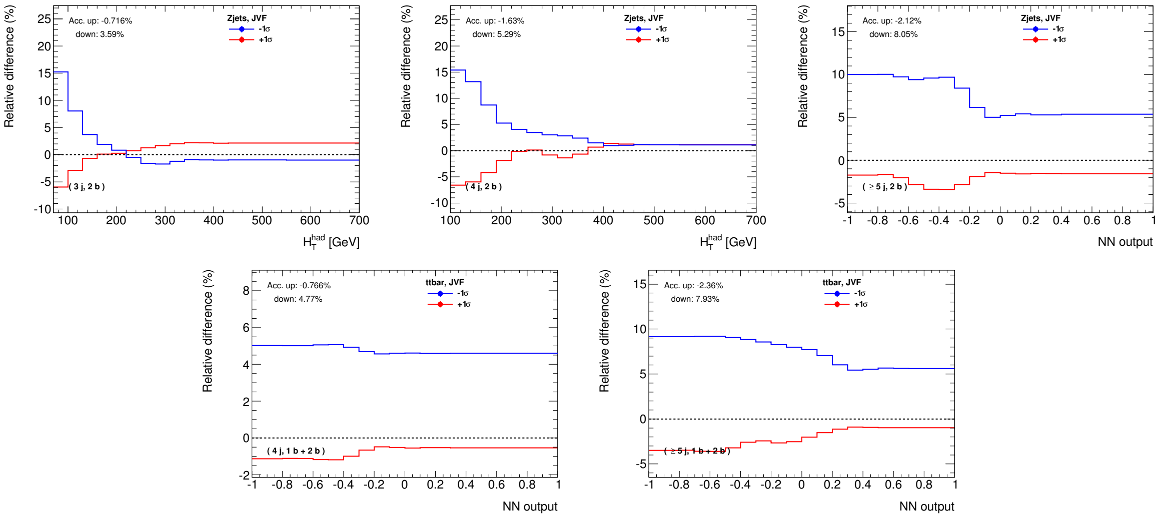

Figure 8.4.: Relative differences of the JVF uncertainty on the Z+jets discriminants in the three fit regions in the 2ℓOSZ region, (top left): $(3\text{j}, 2\text{b})$, (top middle): $(4\text{j}, 2\text{b})$, and (top right): $(\geq 5\text{j}, 2\text{b})$, and on the $t\bar{t}$ discriminants in the two fit regions using shape information in the 2ℓOSZveto region, (bottom left): $(4\text{j}, 1\text{b} + 2\text{b})$ and (bottom right): $(\geq 5\text{j}, 1\text{b} + 2\text{b})$.

the one measured in data, except for some small differences in some p_T and η regions. Therefore, instead of applying a smearing to the nominal measurement, a systematic uncertainty is defined as the difference in quadrature between the jet energy resolutions for data and simulation. To estimate the impact of this systematic uncertainty on this analysis, the energy of each jet in the simulation is smeared by this residual difference, and the changes in the normalisation and shape of the final discriminant are compared to the default prediction. Since jets in the simulation cannot be "under-smeared", the resulting uncertainty is one-sided by definition, i.e. only the "up" variation exists, and then the effect of the systematic uncertainty on the discriminant is symmetrised.

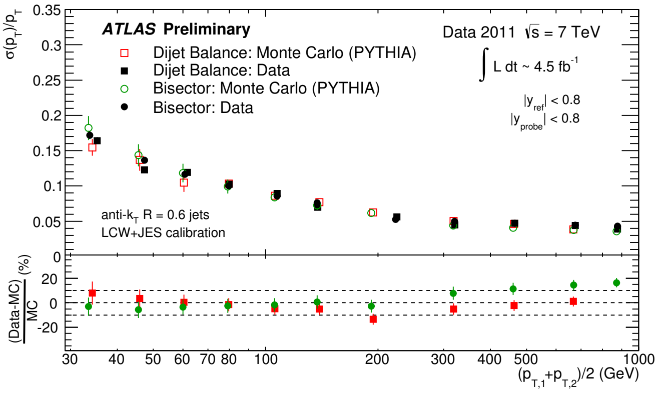

Figure 8.5.: Fractional jet energy resolution as a function of the average jet transverse momenta measured with and bisector (circles) techniques using the LCW+JES calibration in MC simulation and 2011 data. The bottom plot shows the relative difference between data results and MC simulation (green) [204].

Jet Reconstruction The jet reconstruction efficiency is found to be about 0.2% lower in the simulation than in data for jets below 30 GeV, and consistent between data and MC simulation for higher jet p_T. To evaluate the effect of this inefficiency, 0.2% of the jets with p_T below 30 GeV are removed randomly and all jet-related kinematic variables are recomputed, and the event selection is updated accordingly. The effect of this systematic uncertainty is also symmetrised as in the jet energy resolution.

Heavy- and Light-Flavour Tagging The uncertainties on the b-tagging efficiency of jets originating from b, c and light quarks or gluons, which are measured for the different jet types, as explained in Section 4.4.1, are split into sub-components using the *eigenvector method*. This method uses a diagonalisation procedure, preserving the correlation among jet p_T bins from the measured SFs and providing components that can be treated as uncorrelated. There are as many independent systematic uncertainty components as p_T bins used in the efficiency measurement: six components for each b-jet and c-jet efficiency (for the six jet p_T bins), and twelve components for the mistag rate, since the efficiency is parametrised in six bins in jet p_T, and in two η regions. In each jet type category, the components are labelled with an index to order them according to their absolute eigenvalue obtained from the diagonalisation procedure, beginning with the smallest effect.

Missing Transverse Energy Given that an explicit cut on the E_T^{miss} distribution is applied in the 2ℓOSZveto region, systematic uncertainties on the calculation of the E_T^{miss} are included in the fit, in particular uncertainties on the scale and resolution of the soft terms (*soft-jets* and *cell-out*), introduced in Section 4.5.

8.2.2. Background Modelling Systematics

Z+jets

Four sources of uncertainties are considered: theoretical cross section uncertainty, uncertainty due to the p_T(Z) correction, uncertainty due to scale choice for QCD emissions in ALPGEN, and the uncertainty due to the choice of the generator.

- An NNLO QCD cross section uncertainty of 5% is applied to the Z+jets contribution [160].
- A systematic uncertainty equal to the full size of the p_T(Z) correction (described in Section 5.3.2), comparing the final distributions with and without applying the p_T(Z) correction in the analysis. This is included in the fit as a shape-only systematic.
- Z+jets MC samples with separately varied renormalisation and factorisation scales were studied to assess the uncertainty due to the extrapolation of the Z+jets simulation prediction to high jet multiplicity. The variation of the scale associated with the strong coupling α_s in the matrix element in ALPGEN, varied by a factor of two up and down, is found to have the largest effect and is considered as a systematic uncertainty in the analysis. The corresponding NP is denoted by the suffix *ktfac*.
- The choice of matrix element generator and parton shower on Z+jets modelling is evaluated by using a SHERPA Z+jets MC sample with massive b, c-quarks as an alternative model. In the analysis, the effect of this model uncertainty is described as an uncertainty

parameter affecting the normalisation in each jet multiplicity, since a significant discrepancy between data and MC simulation is observed in the H_T^{had} distribution in the high statistics 2ℓOSZ (3j, 2b) region.

Given that the fit regions in the 2ℓOSZ region are dominated by the Z+HF background contribution, no dedicated systematic uncertainty is assigned to the normalisation correction for Z+light and Z+HF described in Section 5.3.2. The normalisation of the Z+HF background already enters as nuisance parameter in the fit.

The Z+HF sub-composition, defined according to the heavy flavour classification presented in Section 5.3, was studied across fit regions. The HF sub-composition can be divided into several categories, according to the additional HF jets. The three dominant categories are: b, when a jet is matched to one B-hadron; bb, when two jets are matched to two B-hadrons, and B, when one jet is matched to two B-hadrons. In all fit regions in the 2ℓOSZ region, $Z + bb$ is the dominant process, and is found to be 3 times larger than $Z + b$ across all jet multiplicities (60% $Z + bb$, 20% $Z + b$). $Z + c/cc/C$ accounts for only 12% in the (3j, 2b) region to 15% in the ($\geq$ 5j, 2b) region, and $Z + B(+B)$ for only 1-3%.

Z+jets Sherpa has a different relative composition of Z+b and Z+bb than Alpgen+Pythia: it contains a higher fraction of Z+b and lower fraction of Z+bb compared to Alpgen+Pythia, but is still dominated by $Z + bb$ across all jet multiplicities, as shown in Table 8.3.

Region	$Z + b$	$Z + bb$
(3j, 2b)	1.22	0.91
(4j, 2b)	1.20	0.92
($\geq$ 5j, 2b)	1.15	0.94

Table 8.3.: Fractions of $Z + b$ and $Z + bb$ in Sherpa Z+jets relative to the corresponding fractions in Alpgen+Pythia Z+jets in the three fit regions in the 2ℓOSZ region.

Given that there is no relative change of the $Z + b$ and $Z + bb$ fractions across jet multiplicities in the fit regions, and that Z+jets Sherpa normalisation variation per jet bin allows an indirect handle on the relative contribution of $Z + b$ and $Z + bb$, a single Z+HF normalisation correction is justified as a starting point for the fit. Furthermore, since the fit is allowed to vary the normalisation per jet multiplicity based on the variation of the *ktfac* parameter and the Sherpa variations, varying in opposite directions of one another, this covers all possible variations on the Z+HF modelling.

Figure 8.6 shows the relative variations in the shape of the corresponding discriminants in the three fit regions in the 2ℓOSZ region for the Z+jets process, when comparing Alpgen+Pythia Z+jets with a modified *ktfac* parameter, and Alpgen+Pythia Z+jets without the p_T(Z) correction, with the nominal Alpgen+Pythia Z+jets.

$t\bar{t}$+jets

Several systematic uncertainties affecting the modelling of $t\bar{t}$+jets are considered in this channel: the uncertainty on the cross section, uncertainties due to the choice of the generator and the parton shower, and uncertainties due to the reweighting procedure applied to correct the $t\bar{t}$ MC modelling. An additional uncertainty is assigned to account for the limited knowledge of the $t\bar{t}$ production in association with heavy flavour jets.

- An uncertainty of +5%/-6% is assumed for the inclusive $t\bar{t}$ production cross section, as described in Section 2.3.1.

- The systematic uncertainties assigned to the top quark and $t\bar{t}$ p_T corrections, described in Section 5.3.1, are derived based on the largest systematic uncertainties of the differential $t\bar{t}$ cross section measurement at $\sqrt{s} = 7$ TeV [170]. Nine different sources of systematic uncertainties related to the $t\bar{t}$ correction, accounting for approximately 95% of the total experimental uncertainty of the $t\bar{t}$ measurement at $\sqrt{s} = 7$ TeV, are included in the fit, which modify the shape and amplitude of the correction.

  The sources of uncertainties associated with the measurement of the differential cross section for $t\bar{t}$ and top p_T used to correct the $t\bar{t}$ MC model include:

  - *Detector-related*: b-tagging efficiency [4] **(ttbarDataRwBTagEff)**, jet energy resolution **(ttbarDataRwJER)**, JES close-by jets [5] **(ttbarDataRwJetCloseby)**, the largest in situ JES uncertainty in the category DETECTOR **(ttbarDataRwJet-Det1)**, JES η-intercalibration **(ttbarDataRwJetEtaCalibration)**, JES b-quark jets **(ttbarDataRwJetFlavB)**.
  - *Model-related*:
    - initial and final state radiation: ALPGEN+PYTHIA $t\bar{t}$ samples with varied radiation settings **(ttbarDataRwIFSR)**,
    - MC generator: MC@NLO+HERWIG $t\bar{t}$ as an alternative model to the nominal ALPGEN+HERWIG **(ttbarDataRwMCgen)**,
    - parton shower and hadronisation: ALPGEN+PYTHIA compared to ALPGEN+HERWIG $t\bar{t}$ **(ttbarDataRwFragmentation)**.

  The largest uncertainties on the measurement of the differential distributions arise from radiation modelling in $t\bar{t}$ events (up to 12% uncertainty on the overall normalisation of $t\bar{t}$ in the $(\geq 5\text{j}, 1\text{b} + 2\text{b})$ region), the choice of the generator to simulate $t\bar{t}$ production, and uncertainties on the components of the jet energy calibration, jet resolution, and jet flavour tagging. Figure 8.7 shows the effect of the envelope of all nine sources of data-driven reweighting uncertainties on the top quark and $t\bar{t}$ p_T. Figure 8.8 shows the relative variations in shape and rate on the NN discriminants in the two signal regions in the 2ℓOSZveto region, when comparing the $t\bar{t}$ *ttbarDataRwFragmentation* uncertainty with the nominal corrected $t\bar{t}$ MC.

- An uncertainty due to the choice of the generator is evaluated by comparing a sample generated using MADGRAPH interfaced with PYTHIA to the default $t\bar{t}$ POWHEG+PYTHIA sample. Effects on the shapes are compared, symmetrised and applied to the shapes predicted by the default model after correcting both samples to match top quark p_T and $t\bar{t}$ p_T distributions as measured in the differential cross section analysis.

- An uncertainty due to the choice of the parton shower and hadronisation model is derived by comparing events produced by POWHEG interfaced with PYTHIA or HERWIG. Only the effect on normalisation per jet multiplicity is considered from this source, since the effect on the shape is found to be similar to the one from MADGRAPH+PYTHIA, as shown in Figure 8.9.

- A systematic uncertainty of 50% is applied to the $t\bar{t}$+HF normalisation component of $t\bar{t}$+jets background obtained from the POWHEG+PYTHIA MC simulation.

---

[4] In the $t\bar{t}$ differential measurement, the envelope of the b-tagging efficiency uncertainty is considered.

[5] This systematic is not considered as a separate component in the JES uncertainty breakdown at $\sqrt{s} = 8$ TeV.

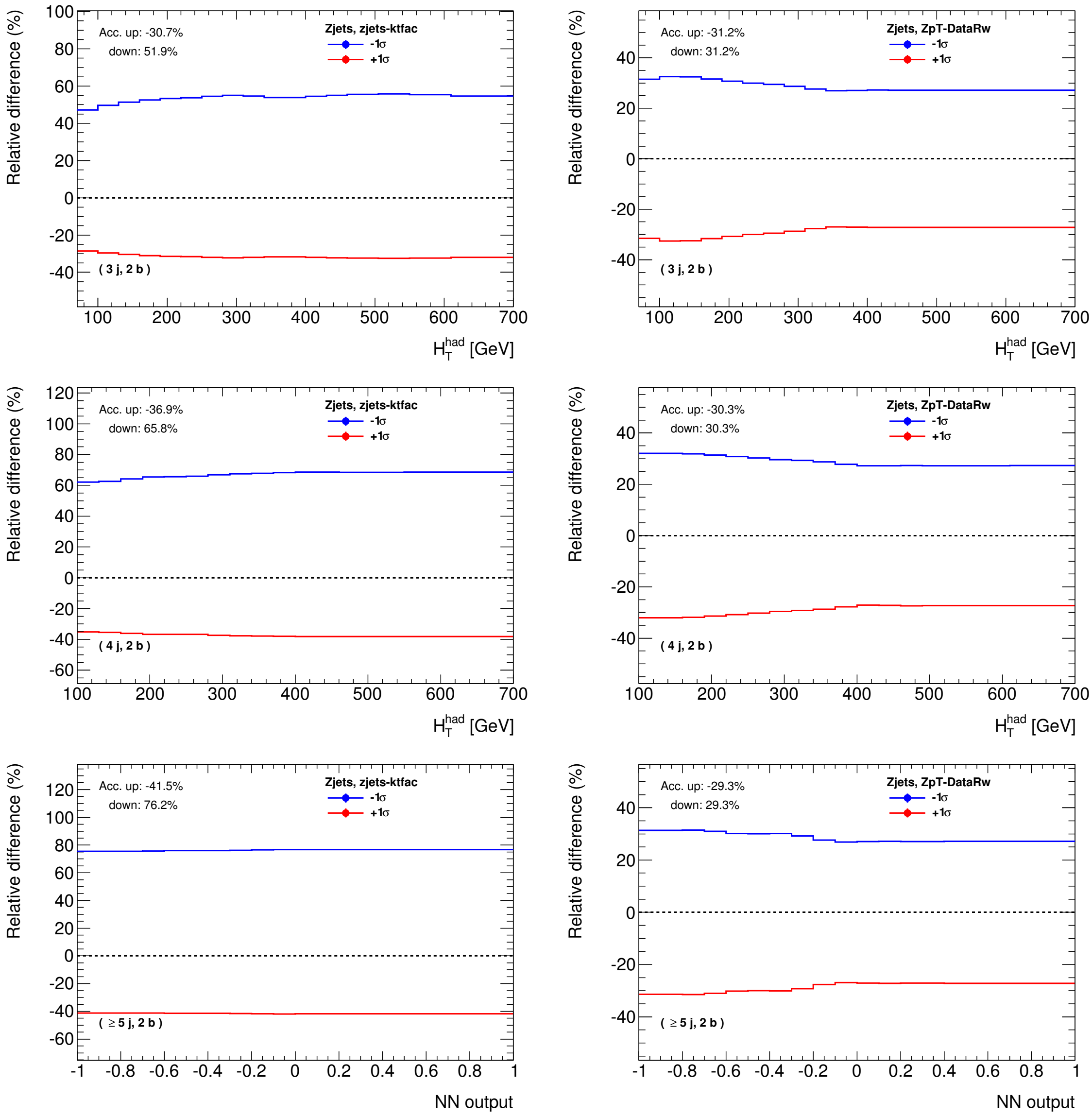

Figure 8.6.: Relative differences of (left column): the *ktfac* varied sample, and (right column): the Z+jets sample without p_T(Z) correction, compared to the nominal corrected Z+jets ALPGEN+PYTHIA, on the Z+jets discriminants in the (top): 2ℓOSZ $(3\text{j}, 2\text{b})$, (middle): 2ℓOSZ $(4\text{j}, 2\text{b})$, and (bottom): 2ℓOSZ $(\geq 5\text{j}, 2\text{b})$ regions. For the p_T(Z) correction, only the shape of the systematic uncertainty is considered.

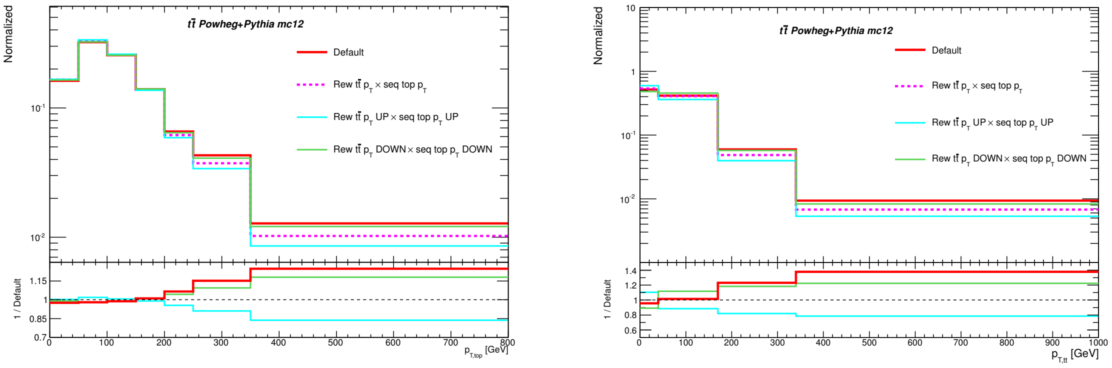

Figure 8.7.: The effect of the full envelope of the data-driven uncertainties on (left): top p_T and (bottom): $t\bar{t}$ p_T distributions.

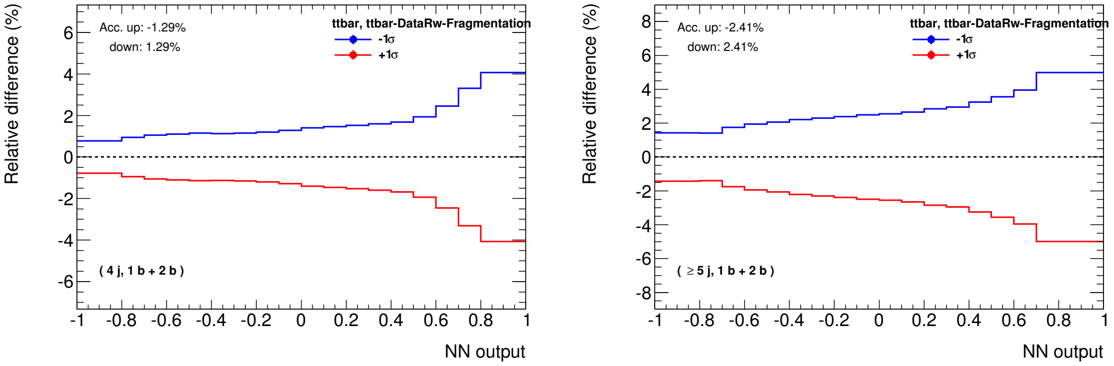

Figure 8.8.: Relative differences of the fragmentation uncertainty related to the top and $t\bar{t}$ correction on $t\bar{t}$ Powheg+Pythia, compared to the nominal $t\bar{t}$ Powheg+Pythia, in the fit regions in the 2ℓOSZveto region, (left): $(4\text{j}, 1\text{b} + 2\text{b})$ and (right): $(\geq 5\text{j}, 1\text{b} + 2\text{b})$, where the shape information of the discriminant is used.

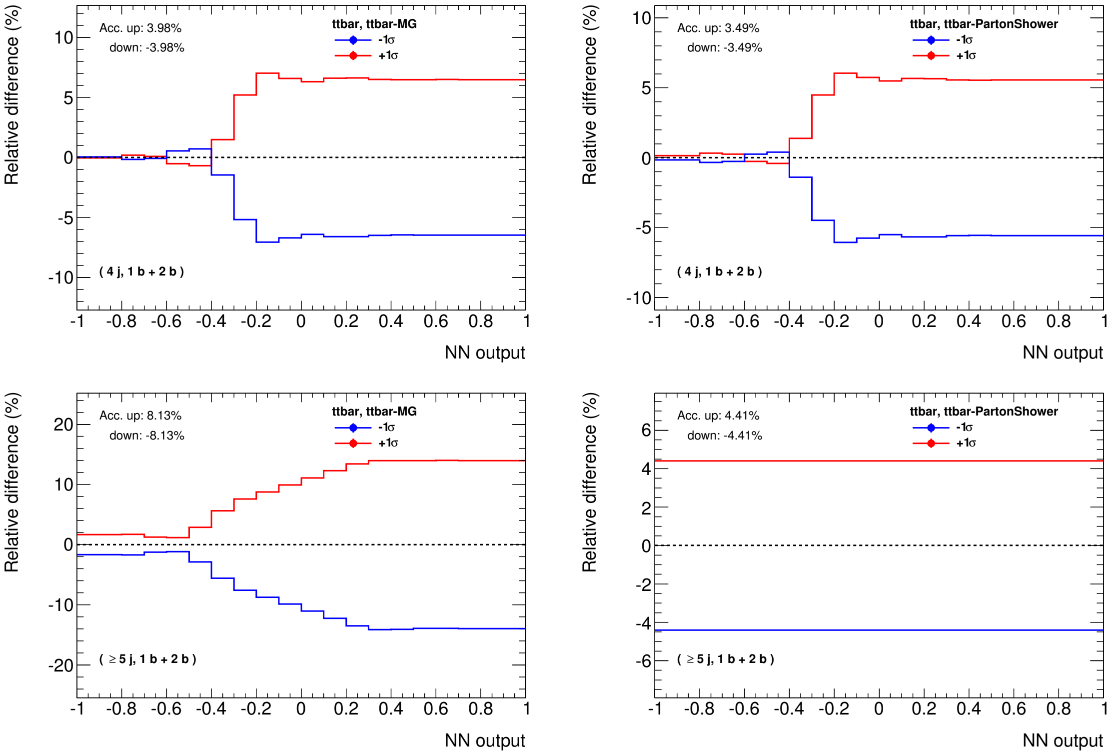

Figure 8.9.: Relative differences of (left column): $t\bar{t}$ Madgraph+Pythia and (right column): $t\bar{t}$ Powheg+Herwig, compared to the nominal $t\bar{t}$ Powheg+Pythia, in the fit regions in the 2ℓOSZveto region, (left): $(4\text{j}, 1\text{b} + 2\text{b})$ and (right): $(\geq 5\text{j}, 1\text{b} + 2\text{b})$, where the shape information of the discriminant is used. It can be seen that $t\bar{t}$ Powheg+Herwig has the same shape variation as Madgraph+Pythia in the $(4\text{j}, 1\text{b} + 2\text{b})$ region, and no shape variation in the $(\geq 5\text{j}, 1\text{b} + 2\text{b})$ region.

Categories of modelling systematic uncertainties on the dominant backgrounds Table 8.4 categorises the modelling uncertainties on the main background processes in this analysis, $t\bar{t}$ and Z+jets, according to their effect on the shape, the normalisation across the number of jets, or the heavy flavour content. Given that both $t\bar{t}$ MADGRAPH+PYTHIA and Z+jets varied sample according to the ALPGEN parameter *ktfac*, have a significant impact on both the rate per jet multiplicity bin and the shape of the discriminant within each fit region, the two effects are treated separately in the fit, assigning to each systematic source two uncorrelated nuisance parameters, one for the shape-only variation and one for the rate-only variation. This procedure prevents situations where, for instance, only the *ktfac* shape effect is needed to be pulled by the fit, but since it implies a big normalisation shift associated with this systematic, other nuisance parameters will be shifted to compensate this normalisation variation.

Uncertainties	$t\bar{t}$	Z**+jets**
Cross-section	+5%/-6%	5%
Corrections	nine sources for top/$t\bar{t}$ p_T	p_T(Z)
Extrapolation to high jet multiplicity	ttbarDataRWIFSR MADGRAPH+PYTHIA POWHEG+HERWIG	*ktfac* SHERPA
Shape of the discriminant in each fit region	uncertainties on top/$t\bar{t}$ p_T MADGRAPH+PYTHIA	*ktfac* p_T(Z)
Flavour fraction	50% on $t\bar{t}$+HF	SHERPA

Table 8.4.: Summary of the modelling systematic uncertainties on the $t\bar{t}$ and Z+jets background in this analysis, categorised according to their effect on the discriminants in the fit regions.

Figure 8.10 shows the relative difference in rate with respect to the nominal of those modelling uncertainties affecting the normalisation per jet multiplicity bins of the $t\bar{t}$ process in the 2ℓOSZveto region (left), and of Z+jets process in the 2ℓOSZ region (right). The alternative $t\bar{t}$ generator, MADGRAPH, yields the largest normalisation variation for $t\bar{t}$ in the 2ℓOSZveto $(3\text{j}, 1\text{b} + 2\text{b})$ region, the region which has the largest data statistics. In the 2ℓOSZ region, the systematic uncertainty related to the *ktfac* parameters has the largest variation per jet multiplicity on Z+jets events: from +50%/-30% relative variation in $(3\text{j}, 2\text{b})$, to +70%/-40% relative variation in $(\geq 5\text{j}, 2\text{b})$. As a result, the corresponding nuisance parameter is expected to be largely constrained by the fit.

Single Top

An uncertainty of 6.8% is assumed for the cross section of the single top production [205] corresponding to the theoretical uncertainty on the Wt-channel cross section, the only process contributing to the opposite-sign dilepton final state. An additional modelling uncertainty on the Wt production is obtained from a simulated sample which uses the alternative *diagram subtraction (DS)* approach in the Wt-channel production to avoid overlap between single top quark and $t\bar{t}$ final states. While the *diagram removal* approach used in the nominal sample removes doubly-resonant diagrams from the calculation of the Wt amplitude, the *diagram subtraction* alternative approach subtracts a gauge invariant term from the Wt cross section that removes the doubly resonant contributions from $t\bar{t}$ final states. Each approach has its disadvantages: the DR

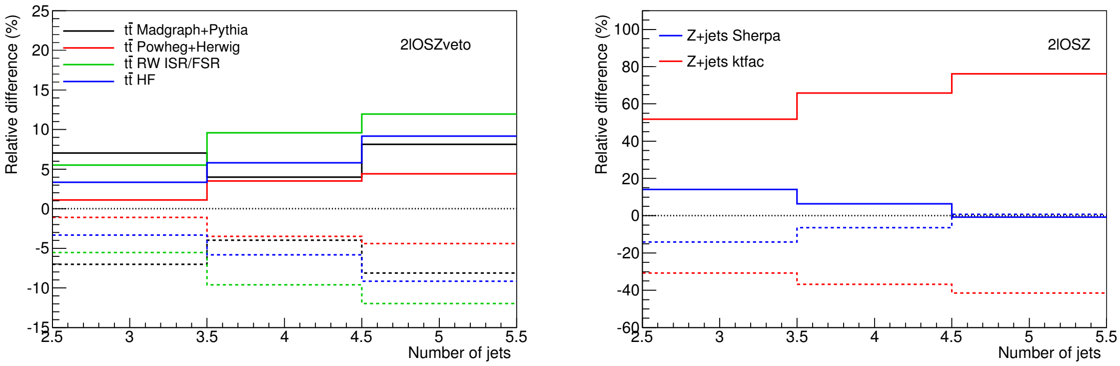

Figure 8.10.: Relative differences on (left): the normalisation of $t\bar{t}$ per fit region in the 2ℓOSZveto region, and (right): the normalisation of Z+jets per fit region in the 2ℓOSZ region, for each of the relevant modelling systematics.

approach violates gauge invariance, while the DS approach does not eliminate the interference term between Wt and $t\bar{t}$, since the subtraction is performed at the cross section level.

Figure 8.11 shows the shape and rate variation on the NN discriminants in the two signal regions in the 2ℓOSZveto region, where single top contributes the most, when comparing the alternative DS single top model with the nominal DR single top model.

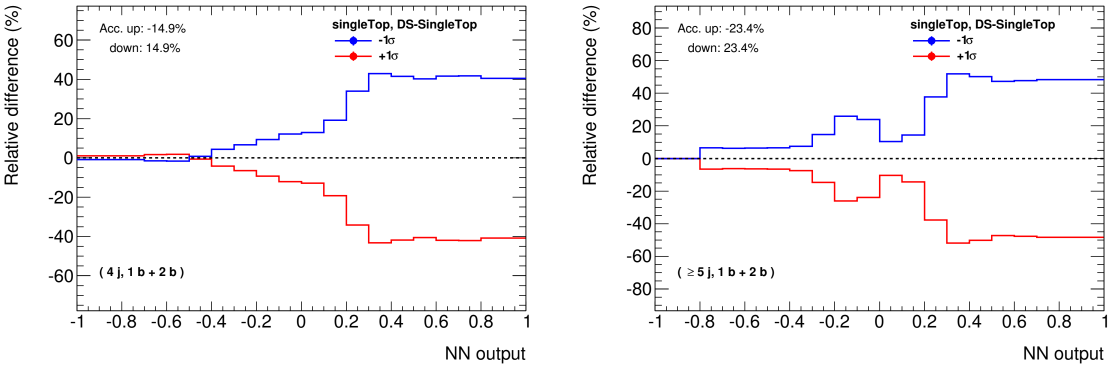

Figure 8.11.: Relative difference on the NN discriminants in the fit regions (left): 2ℓOSZveto $(4\mathrm{j}, 1\mathrm{b}+2\mathrm{b})$ and (right): 2ℓOSZveto $(\geq 5\mathrm{j}, 1\mathrm{b}+2\mathrm{b})$, when comparing the single top Wt production, using the alternative DS approach, with the nominal single top Wt model, using the DR approach.

tZ

An uncertainty of 20% is assumed for the theoretical cross section of the tZ background, obtained from aMC@NLO calculations of all tZ subchannels. Only uncertainties from scale variation are included.

$\mathbf{t\bar{t}H}$

An uncertainty of 12% is assumed for the theoretical cross section of $t\bar{t}H$ production, including the maximum scale variation, when varying the μ_r and μ_f scales in parallel by a factor of 2, the PDF envelope uncertainty and the uncertainty on $\alpha_S(M_Z)$ [169]. Additional uncertainties associated with the choice of factorisation and renormalisation scales and the functional form of the scale in $t\bar{t}H$, which affect $t\bar{t}H$ kinematics, are included in the fit. The effect of the variations is studied at particle level and the nominal PowHel $t\bar{t}H$ MC sample is reweighted to reproduce these variations.

Diboson

The uncertainty on the diboson background (WW, WZ and ZZ) includes a 20% uncertainty estimated from the agreement between data and prediction in a control region dominated by WZ background contribution, consisting of events with three leptons, requiring the invariant mass of the lepton pair with same lepton flavour and opposite sign charge to fulfil $|m(\ell,\ell) - m(Z)| <$ 10 GeV, and from the observed uncertainty in the WZ prediction when theory assumptions are varied. An additional uncorrelated uncertainty of 40% is assigned to account for the modelling of diboson production associated with heavy flavour jets.

Misidentified lepton background

An uncertainty of 50% is applied to the misidentified lepton yields across all selected regions to cover the maximum difference between yields obtained from the MC simulation and from SS dilepton events in data. An additional uncertainty is applied to cover the difference in shape of the H_T distributions in the MC simulation and SS data events, as discussed in Section 5.3.3.

8.2.3. Signal Modelling Systematics

Scale and radiation

To assess the scale uncertainties on the $t\bar{t}V$ modelling, the factorisation and renormalisation scales are varied by a factor of two up and down with respect to the nominal values. Radiation uncertainties are assessed by varying the strong coupling α_s in the matrix element calculation by a factor of two up and down with respect to the nominal value, while simultaneously varying the amount of initial state radiation in Pythia [206]. In addition, the jet p_T matching threshold is varied up and down by a factor of two as well as the amount of the radiation in Pythia in the Madgraph+Pythia $t\bar{t}V$ simulation. Alternative Madgraph+Pythia samples representing such variations were generated at the particle level and the propagation of these uncertainties to the baseline sample is performed with a reweighting procedure in kinematic variables such as top quark p_T and η, $t\bar{t}$ p_T and η, W and Z p_T and η, and the number of jets between the nominal and alternative samples.

The dominating systematic uncertainty on the $t\bar{t}V$ modelling comes from the variation associated with the strong coupling α_s in the matrix element calculation, controlled by the Madgraph parameter *alpsfact*, with a simultaneous variation of the amount of initial state radiation in Pythia. This variation has a significant effect on the distribution of the number of jets in $t\bar{t}V$ events. Figure 8.12 shows the jet multiplicity for the $t\bar{t}Z$ process for variations of the *alpsfact* scale, and 8.13 illustrates the corresponding $t\bar{t}Z$ p_T and η distribution and $t\bar{t}$ and top p_T distributions. To account for the shape uncertainty coming from the *alpsfact* variation, the p_T distributions of both the $t\bar{t}Z$ and $t\bar{t}W$ system are reweighted to match distributions in the alternative samples with *alpsfact* varied up and down. After this reweighting, differences in other distributions become negligible.

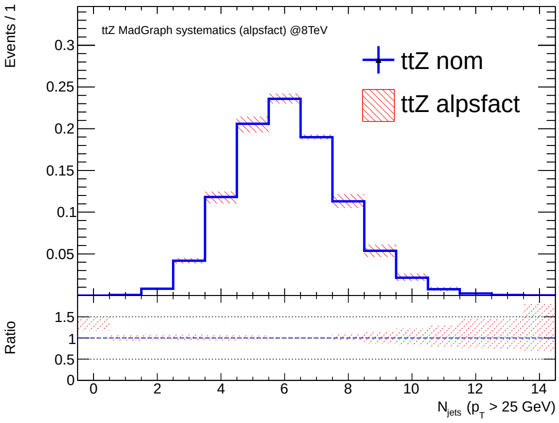

Figure 8.12.: Jet multiplicity distribution for variations of the *alpsfact* parameter in the $t\bar{t}Z$ Madgraph process.

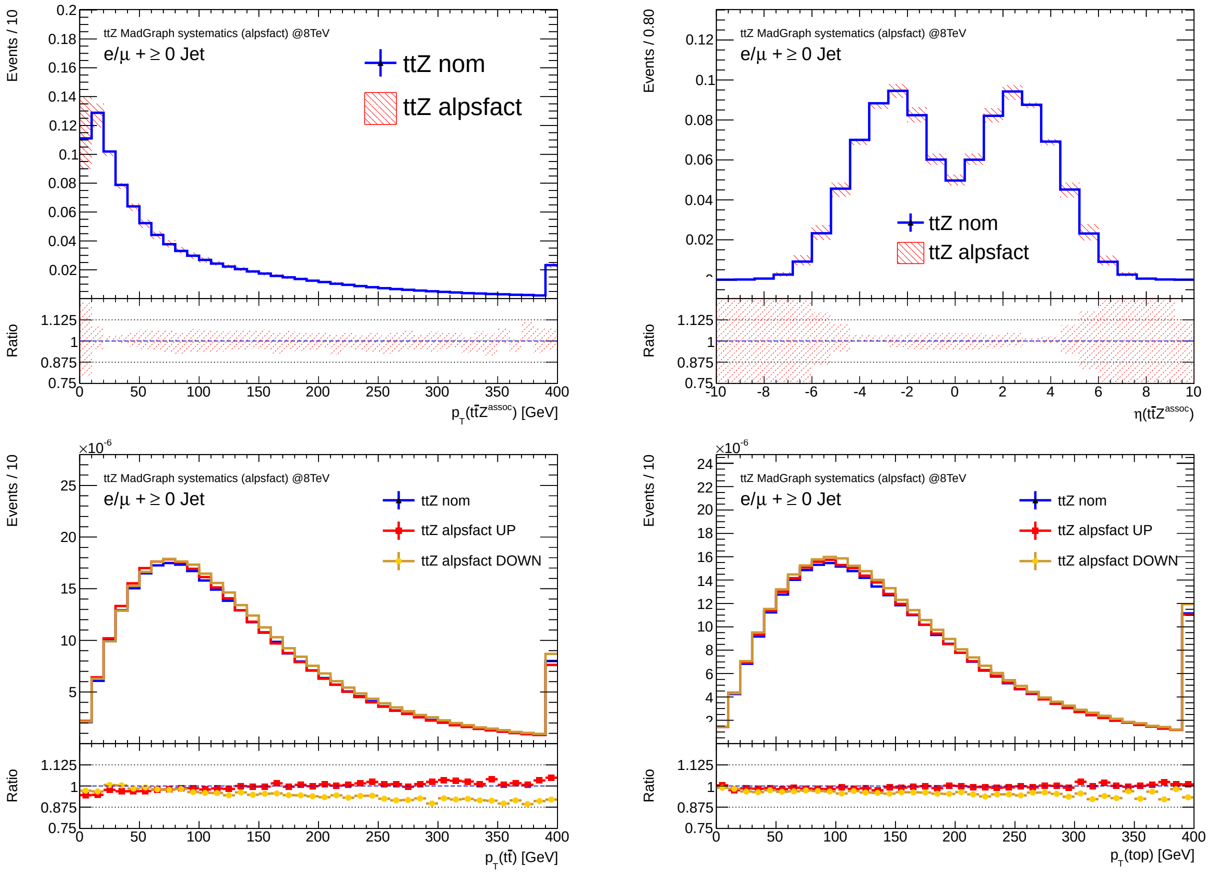

Figure 8.13.: Kinematic distributions for the $t\bar{t}Z$ events at truth level for variations of the *alpsfact* parameter. (Top left): p_T of the $t\bar{t}Z$ system, (top right): η of the $t\bar{t}Z$ system, (bottom left): p_T of the $t\bar{t}$ system, and (bottom right): p_T of the top quark. Distributions for $t\bar{t}Z$ system p_T and η are normalised to unity while $t\bar{t}$ and top p_T distributions are normalised to the corresponding cross sections.

PDF

Systematic uncertainties on the $t\bar{t}V$ modelling due to the PDF choice are evaluated using the uncertainty sets of the CT10 NLO [41], MSTW2008 68% CL NLO [51, 52] and NNPDF 2.3 NLO [53] sets. The final PDF uncertainty is calculated as half the envelope of (a) *intra-PDF uncertainty*, which evaluates the changes due to the variation of different PDF parameters within a single PDF error set, and (b) *inter-PDF uncertainty*, which evaluates differences between different PDF sets. The uncertainty is evaluated by reweighting the signal MC to the different PDF sets and evaluating the change in acceptance as a function of the variables that are used in the final fit (either H_T^{had} or the NN discriminant). The different variations are then combined following the PDF4LHC recommendations [50]. The largest change on the overall normalisation in this analysis is found to be 2% in the 2ℓOSZ region.

8.2.4. Treatment of nuisance parameters

Prior to performing the fit, a treatment is applied to some of the systematic variation templates, called "smoothing", and another to the total number of nuisance parameters affecting each process and each region, called "pruning".

Smoothing

Many systematic uncertainties used in the fit have a non-negligible MC statistical component. For instance, some of the 22 components of the JES uncertainty show variations which are smaller than the statistical error in the tails of distributions. In such cases, statistical fluctuations are convoluted into the systematic templates. Moreover, in some low MC statistic bins, both "up" and "down" variations fluctuate in the same direction, making the nuisance parameter variation one-sided. This can be problematic for the fit.

The goal is to smooth artificial fluctuations in small backgrounds, while keeping the real shape variations in high statistic samples. A compromise between smoothness and closeness to the original distribution has to be found. The algorithm chosen in the $t\bar{t}V$ analysis re-bins the effect of the systematic uncertainty until the number of local maximum/minimum is less than three, and as such, is referred to as *maxVariations3*. To test the performance of the algorithm on systematics in this analysis, the smoothed template distributions from the largest variations of shape were compared to the original raw distribution. Some examples are shown before and after the smoothing algorithm in Figure 8.14 for the $t\bar{t}$ MADGRAPH+PYTHIA variation in the 2ℓOSZveto $(4\mathrm{j}, 1\mathrm{b}+2\mathrm{b})$ and $(\geq 5\mathrm{j}, 1\mathrm{b}+2\mathrm{b})$ regions, and in Figure 8.15 for the Z+jets "up" variation of the JES sub-component *JESMODEL1* in the three fit regions in the 2ℓOSZ region. The results show that the algorithm performs quite well in balancing between random fluctuations and the original shape of the systematic uncertainty. The normalisation variation in each systematic template is preserved by the smoothing algorithm.

Pruning

The fit model used in the current analysis includes approximately 100 nuisance parameters, 8 processes and 6 fit regions. Evaluating this large amount of variations in the fit is very computationally expensive. Therefore, it is desirable to remove negligible variations that do not change the fit result, increasing the speed of the fitting procedure, as well as easing the minimisation procedure. This goal is achieved by the *pruning* algorithm.

The effect on both the normalisation and shape of every systematic uncertainty is compared to the nominal discriminant. If the normalisation variation of a certain systematic uncertainty in a

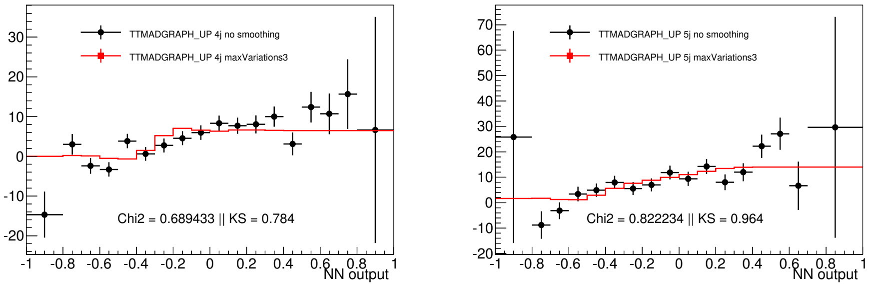

Figure 8.14.: Relative shape variations of $t\bar{t}$ MADGRAPH+PYTHIA with (red curve) and without (black curve) smoothing using the *maxVariations3* algorithm with respect to the nominal $t\bar{t}$ in the two fit regions using shape information in the 2ℓOSZveto region, (left): $(4\text{j}, 1\text{b} + 2\text{b})$, and (right): $(\geq 5\text{j}, 1\text{b} + 2\text{b})$. The chi-square (Chi2) and Kolmogorov-Smirnov (KS) test values are presented to quantify the agreement between the two distributions.

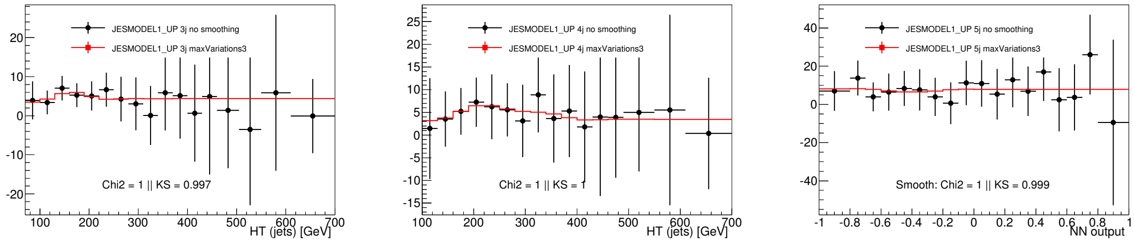

Figure 8.15.: Relative shape variations of Z+jets *JESMODEL1 UP* systematic (red curve) with and without (black curve) smoothing using the *maxVariations3* algorithm with respect to the nominal Z+jets in the three fit regions in the 2ℓOSZ region, (left): $(3\text{j}, 2\text{b})$, (middle): $(4\text{j}, 2\text{b})$, and (right): $(\geq 5\text{j}, 2\text{b})$. The chi-square (Chi2) and Kolmogorov-Smirnov (KS) test values are presented to quantify the agreement between the two distributions.

given region for a given process varies by less than 0.5%, the systematic uncertainty is "pruned", removed prior to the fit. In a similar manner, if a given systematic uncertainty does not change any bin of the fitted distribution by more than 0.5% with respect to the nominal value, then the shape component of that systematic uncertainty for that process in that fit region is ignored. The choice of the conservative threshold of 0.5% is based on the small S/B values in the signal regions in this analysis, so that relative systematic variations in the main backgrounds of the order of the signal are kept. Figures showing the detailed list of systematic uncertainties pruned away in each fit region and process can be found in Appendix C. This treatment is shown to have no effect on the fit result.

8.3. Results

8.3.1. Introduction

Given that the OS dilepton $t\bar{t}V$ channel has sensitivity to both $t\bar{t}W$ and $t\bar{t}Z$ signal processes, the same fit model can be used to perform measurements of different types of signal, under different assumptions:

1. measure $\mu_{t\bar{t}V}$,
2. measure $\mu_{t\bar{t}Z}$, assuming SM $t\bar{t}W$ production,
3. measure $\mu_{t\bar{t}W}$, assuming SM $t\bar{t}Z$ production,
4. measure simultaneously $\mu_{t\bar{t}Z}$ and $\mu_{t\bar{t}W}$.

The full details of the expected behaviour of the fit and the fit to data are shown for the first option. The fitted signal strength, the compatibility with the background-only hypothesis, as well as the breakdown of the fitted uncertainty on the signal strength, are shown for all options. Options 1-3 involve one parameter of interest, μ, in the fit, while option 4 includes two parameters of interests in the fit, $\mu_{t\bar{t}Z}$ and $\mu_{t\bar{t}W}$, and the result will therefore be presented as a contour plot. A simultaneous measurement of $\mu_{t\bar{t}W}$ and $\mu_{t\bar{t}Z}$ allows to measure both cross sections without any assumption on the production.

8.3.2. Expected Fit Performance

The expected performance of the fit is studied using the *Asimov dataset*. In the Asimov dataset, the data are set to the expected signal-plus-background ($S+B$) from the MC prediction. This procedure replaces the *ensemble testing* with MC pseudo-experiments by a single dataset representative of the prediction, such that the "best fit" values of the parameters correspond to the true parameter values [196].

The fit to the Asimov dataset under the signal-plus-background hypothesis yields a signal strength of $\mu_{t\bar{t}V} = 1.0 \pm 0.7$. By construction of the $S+B$ Asimov dataset, the fitted signal strength is equal to 1, and all fitted mean values of the nuisance parameters are equal to 0. The fitted error on the signal strength gives an estimate of the expected sensitivity of the analysis, while the fitted errors on the nuisance parameters show the expected constraints on the systematic sources with the current fit model. The Asimov fit result is shown in Figure 8.16. The list of nuisance parameters is split into two parts for better visibility. The first part contains detector systematics, and the second part shows mostly nuisance parameters related to backgrounds and signal modelling. The fitted nuisance parameters are shown with their constraints compared to the nominal standard deviation of 1. These constraints are expected due to the fit configuration, pre-fit size of the systematic uncertainties and the observed data statistics.

The large pre-fit Z+jets *ktfac* scale variation uncertainty, as shown in Figure 8.10, is expected to be constrained by the fit, given the large data statistics in the 2ℓOSZ region.

As seen in Figure B.3, the offset in normalisation when using the alternative Z+jets generator SHERPA, is of the order of 15% in the 2ℓOSZ $(3\text{j}, 2\text{b})$ fit region. As a result, the data is expected to constrain the nuisance parameter related to the SHERPA Z+jets generator uncertainty in the fit.

Analogously, $t\bar{t}$ MADGRAPH has a large normalisation offset of the order of 7%, 3% and 8% in the 2ℓOSZveto $(3\text{j}, 1\text{b}+2\text{b})$, $(4\text{j}, 1\text{b}+2\text{b})$, and $(\geq 5\text{j}, 1\text{b}+2\text{b})$ region, respectively. Therefore, the constraint on $t\bar{t}$ MADGRAPH normalisation is expected.

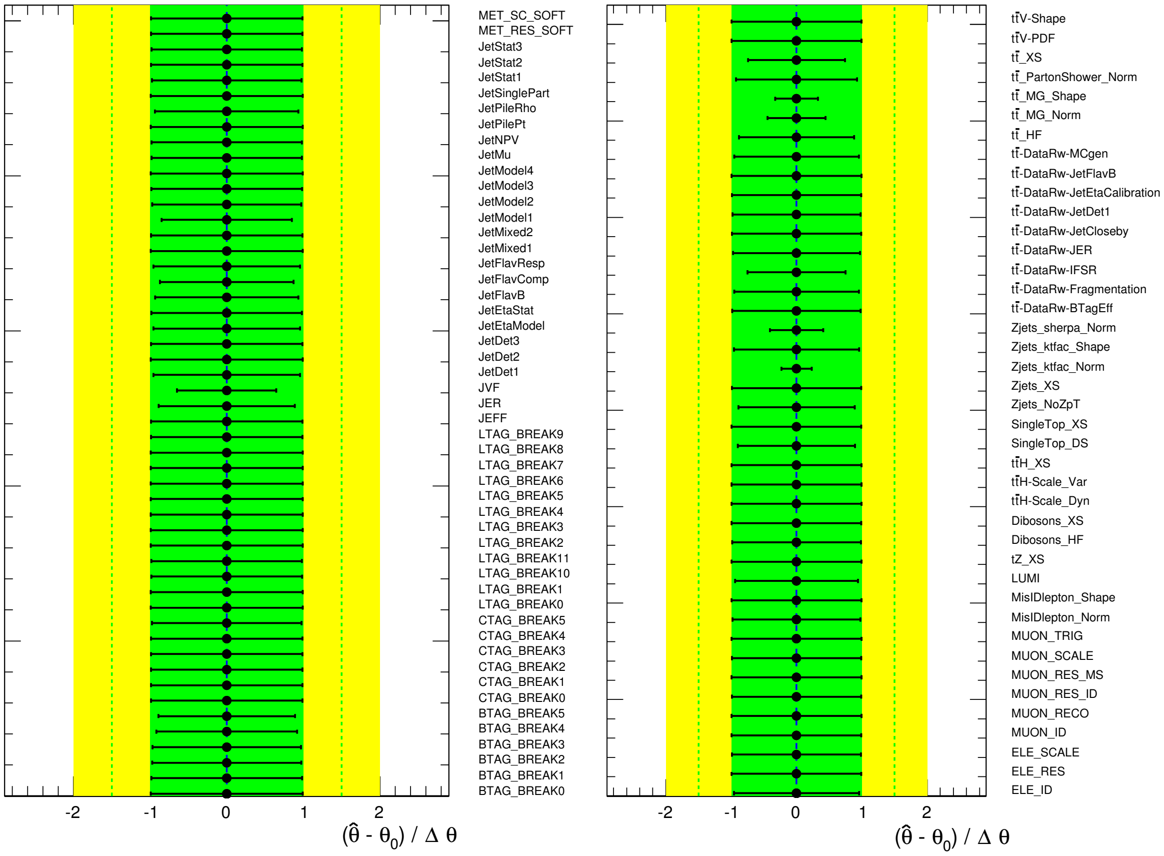

Figure 8.16.: Pull distribution of the fitted nuisance parameters in the $S + B$ hypothesis to the Asimov dataset for the fit of the six regions. As expected, all nuisance parameters' mean values fit at the expectation of 0. The expected constraints of the nuisance parameters can be read directly from the figure, relative to the pre-fit 1σ green band.

The constraint on $t\bar{t}$ MadGraph shape is also expected, since the shape variations are very large with respect to the MC statistical uncertainty. This is especially pronounced in the 2ℓOSZveto ($\geq$ 5j, 1b + 2b) fit region, as can be seen in Figure 8.9, where there is up to a 15% relative variation in the tail of the NN distribution.

From the detector-related systematics, it can be seen that the JVF uncertainty is slightly constrained. As explained in Section 8.2.1, this can be understood from its quite asymmetric shape variation, and from the large relative difference at low H_T^{had} values, which can reach 15%.

As a further cross check of the fit results, the correlations between the nuisance parameters in the Asimov fit are shown in Figure 8.17. Only correlations above 25% are included in the figure, which shows no significant correlations of nuisance parameters built in the fit model.

8.3.3. Fit to Data

In order to understand better the fit behaviour when performing the fit to data, the fit result to data in the six fit regions under the signal-plus-background hypothesis, where signal in this case is $t\bar{t}V$, is shown in comparison with the fit to the three fit regions in the 2ℓOSZveto region in Figure 8.18, and the fit to the three fit regions in the 2ℓOSZ region in Figure 8.19. By splitting

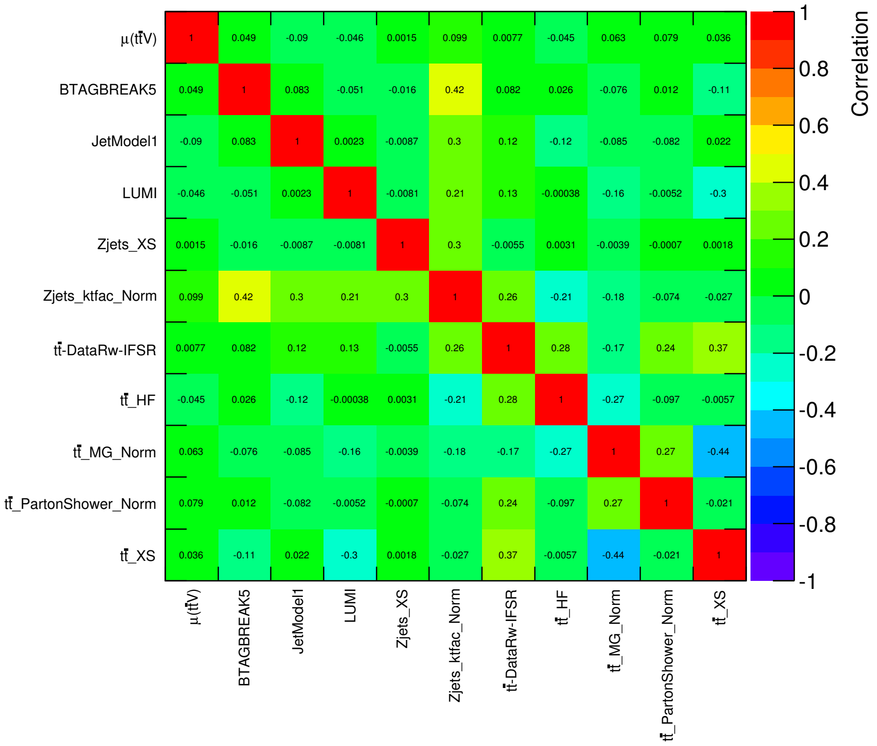

	μ(tt̄V)	BTAGBREAK5	JetModel1	LUMI	Zjets_XS	Zjets_ktfac_Norm	tt̄-DataRw-IFSR	tt̄_HF	tt̄_MG_Norm	tt̄_PartonShower_Norm	tt̄_XS
μ(tt̄V)	1	0.049	-0.09	-0.046	0.0015	0.099	0.0077	-0.045	0.063	0.079	0.036
BTAGBREAK5	0.049	1	0.083	-0.051	-0.016	0.42	0.082	0.026	-0.076	0.012	-0.11
JetModel1	-0.09	0.083	1	0.0023	-0.0087	0.3	0.12	-0.12	-0.085	-0.082	0.022
LUMI	-0.046	-0.051	0.0023	1	-0.0081	0.21	0.13	-0.00038	-0.16	-0.0052	-0.3
Zjets_XS	0.0015	-0.016	-0.0087	-0.0081	1	0.3	-0.0055	0.0031	-0.0039	-0.0007	0.0018
Zjets_ktfac_Norm	0.099	0.42	0.3	0.21	0.3	1	0.26	-0.21	-0.18	-0.074	-0.027
tt̄-DataRw-IFSR	0.0077	0.082	0.12	0.13	-0.0055	0.26	1	0.28	-0.17	0.24	0.37
tt̄_HF	-0.045	0.026	-0.12	-0.00038	0.0031	-0.21	0.28	1	-0.27	-0.097	-0.0057
tt̄_MG_Norm	0.063	-0.076	-0.085	-0.16	-0.0039	-0.18	-0.17	-0.27	1	0.27	-0.44
tt̄_PartonShower_Norm	0.079	0.012	-0.082	-0.0052	-0.0007	-0.074	0.24	-0.097	0.27	1	-0.021
tt̄_XS	0.036	-0.11	0.022	-0.3	0.0018	-0.027	0.37	-0.0057	-0.44	-0.021	1

Figure 8.17.: Correlation matrix showing the correlations between the nuisance parameters built in the fit model, and with the signal strength, $\mu_{t\bar{t}V}$. Only nuisance parameters with at least one correlation above 25% are shown.

the fit by region, a shift or constraint of a fitted nuisance parameter can be associated with a given region. The black points and error bands correspond to the combined six-regions fit, and the red ones correspond to the fit in the 2ℓOSZveto region in Figure 8.18, and to the fit in the 2ℓOSZ region in Figure 8.19.

There are no over-constraints in the fit to data that are not expected from the fit to the Asimov dataset. In general, the fit output shows very little movement of the nuisance parameters' central value with respect to 0.

When performing the fit in the 2ℓOSZveto and 2ℓOSZ regions separately, it can be seen that the constraints on the systematic uncertainties related to $t\bar{t}$ originate from the data in the 2ℓOSZveto region, while the constraints on the systematic uncertainties related to Z+jets originate from the data in the 2ℓOSZ region. Similarly, it can be seen that the leading pulls originate from the analysis regions where the $t\bar{t}$ and Z+jets are dominant backgrounds.

The large data statistics available in the 2ℓOSZveto (4j, 1b+2b) and ($\geq$ 5j, 1b+2b) fit regions allow to constrain the $t\bar{t}$ Madgraph+Pythia uncertainty to 40% of its initial value. The reduced post-fit uncertainties, as well as the modified background and signal yields according to the fitted nuisance parameters' central values and signal strength $\mu_{t\bar{t}V}$, can be seen in the post-fit distributions in Figure 8.20. After the fit, the agreement between data and prediction improves significantly, and the differences are covered by the post-fit uncertainty band.

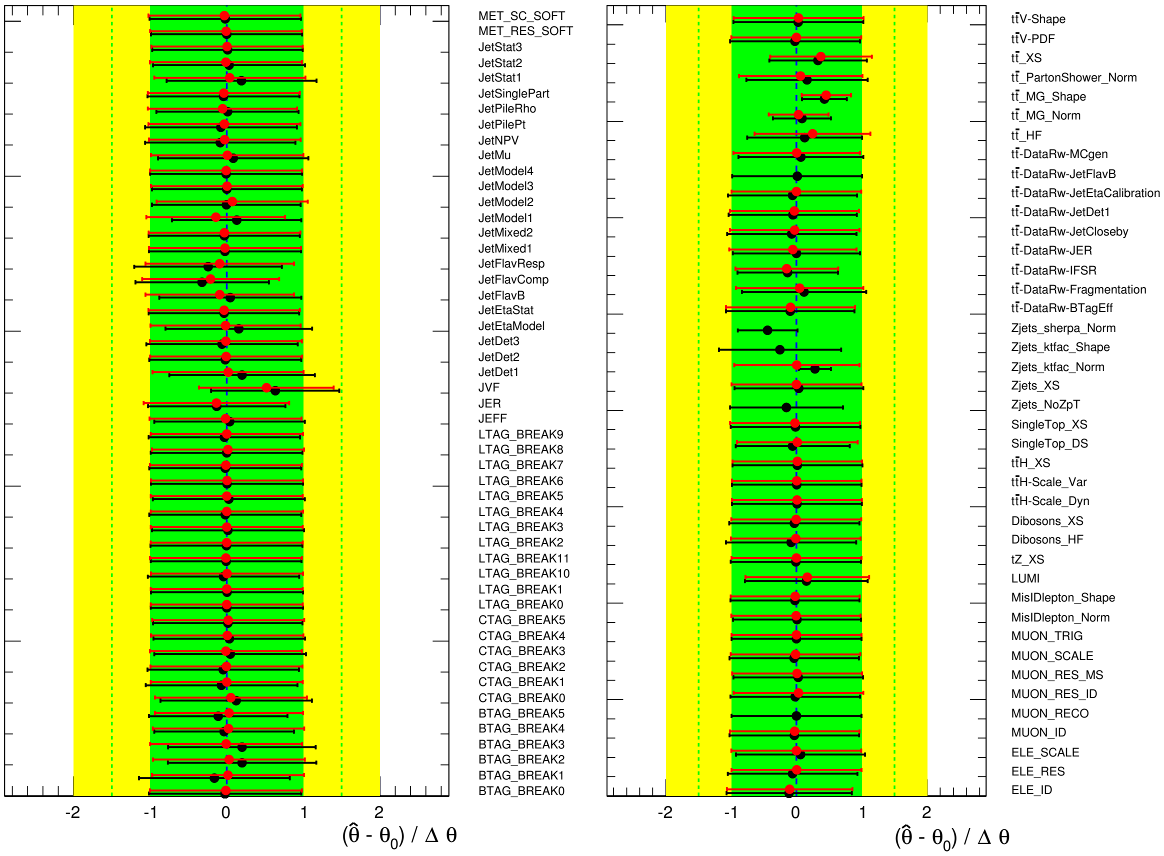

Figure 8.18.: Pull distributions of the fitted nuisance parameters in the $S + B$ hypothesis to the data for the combined six-regions fit (black) and for the fit in the 2ℓOSZveto region only (red). The fitted nuisance parameters are shown with their pulls and constraints compared to the nominal central value of 0 and standard deviation of 1. If a nuisance parameter appears with no red line, it means that the nuisance parameter did not pass the pruning selection in the 2ℓOSZveto region, and is therefore not included in the corresponding fit.

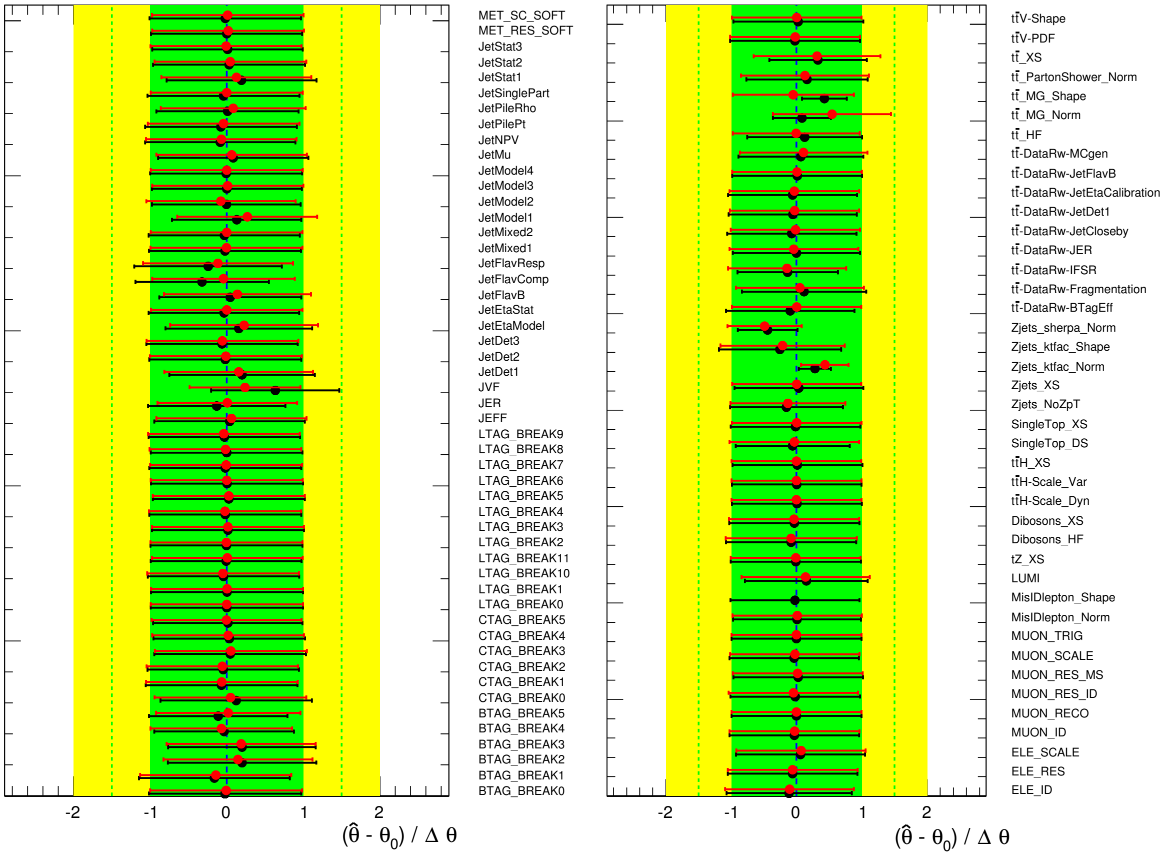

Figure 8.19.: Pull distributions of the fitted nuisance parameters in the $S + B$ hypothesis to the data for the combined six-regions fit (black) and for the fit in the 2ℓOSZ region only (red). The fitted nuisance parameters are shown with their pulls and constraints compared to the nominal central value of 0 and standard deviation of 1. If a nuisance parameter appears with no red line, it means that the nuisance parameter did not pass the pruning selection in the 2ℓOSZ region, and is therefore not included in the corresponding fit.

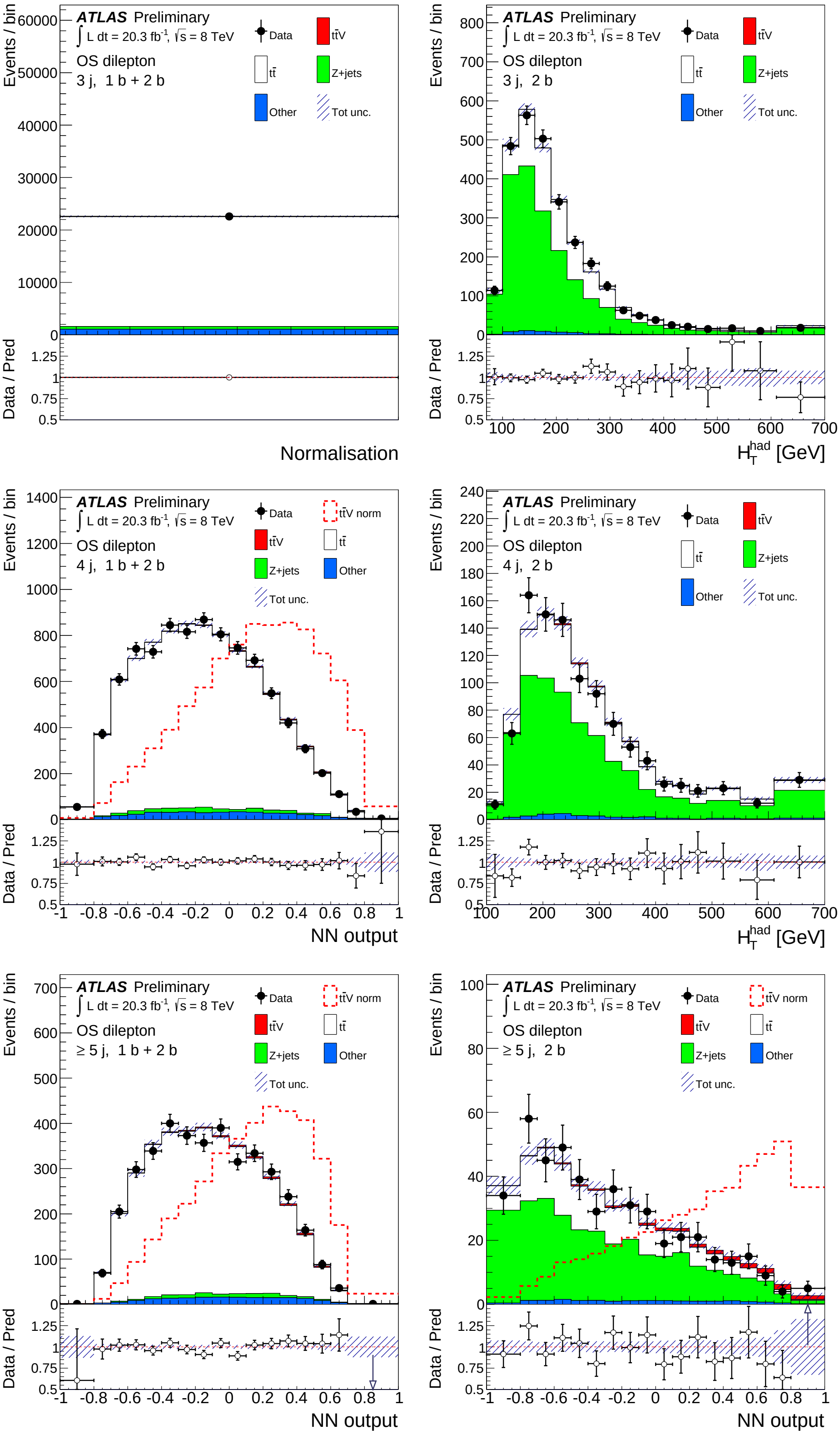

Figure 8.20.: Post-fit distributions for each of the six fit regions in the OS dilepton channel. The left (right) column shows the distributions in the 2ℓOSZveto (2ℓOSZ) regions. The red dashed lines show the $t\bar{t}V$ signal normalised to the background yield. The top left plot shows the $(3\text{j}, 1\text{b} + 2\text{b})$ region, where only the event count is used in the fit. The error band includes the final post-fit uncertainties on signal and background.

The post-fit event yields for the combined ee+jets, $\mu\mu$+jets and $e\mu$+jets samples in the six fit regions are summarised in Table 8.5 for the 2ℓOSZveto region, and in Table 8.6 for the 2ℓOSZ region.

	3 j, 1 b + 2 b	4 j, 1 b + 2 b	$\geq$ 5 j, 1 b + 2 b
$t\bar{t}V$	52 ± 3	46 ± 2	36 ± 2
$t\bar{t}$	21000 ± 200	8300 ± 100	3660 ± 90
Z+jets	510 ± 60	190 ± 10	80 ± 20
$t\bar{t}H$	11 ± 2	13 ± 2	17 ± 2
Single top	800 ± 100	260 ± 40	100 ± 20
Diboson	60 ± 10	26 ± 7	12 ± 3
tZ	4 ± 2	3 ± 1	1.9 ± 1.0
MisID lepton	160 ± 80	90 ± 40	50 ± 20
Total Bkgd	22600 ± 200	8900 ± 100	3910 ± 80
Data	22585	8909	3901

Table 8.5.: Post-fit event yields under the signal-plus-background hypothesis for signal, backgrounds and data in each of the three fit regions in the 2ℓOSZveto region. The quoted uncertainties are the sum in quadrature of post-fit statistical and total systematic uncertainties on the yields, taking into account correlations among nuisance parameters and among processes.

	3 j, 2 b	4 j, 2 b	$\geq$ 5 j, 2 b
$t\bar{t}V$	4.0 ± 0.3	6.8 ± 0.4	14.5 ± 0.9
$t\bar{t}$	830 ± 40	340 ± 20	163 ± 8
Z+jets	1900 ± 70	670 ± 30	290 ± 20
$t\bar{t}H$	0.5 ± 0.07	0.64 ± 0.08	0.9 ± 0.1
Single top	20 ± 3	7 ± 1	3 ± 1
Diboson	25 ± 7	14 ± 4	9 ± 3
tZ	4 ± 2	4 ± 2	3 ± 3
MisID lepton	4 ± 2	2 ± 1	1.4 ± 0.7
Total Bkgd	2790 ± 50	1040 ± 30	470 ± 20
Data	2806	1031	471

Table 8.6.: Post-fit event yields under the signal-plus-background hypothesis for signal, backgrounds and data in each of the three fit regions in the 2ℓOSZ region. The quoted uncertainties are the sum in quadrature of post-fit statistical and total systematic uncertainties on the yields, taking into account correlations among nuisance parameters and among processes.

The agreement between data and prediction is also checked in the kinematic variables, which are not used in the fit. Figure 8.21 shows the post-fit distributions for the two highest-ranked input variables used for the NN discriminant in each signal region: the 2ℓOSZveto $(4\text{j}, 1\text{b} + 2\text{b})$ and $(\geq 5\text{j}, 1\text{b} + 2\text{b})$ regions, and the 2ℓOSZ $(\geq 5\text{j}, 2\text{b})$ region. The small discrepancies remaining between data and prediction are covered by the post-fit uncertainty band.

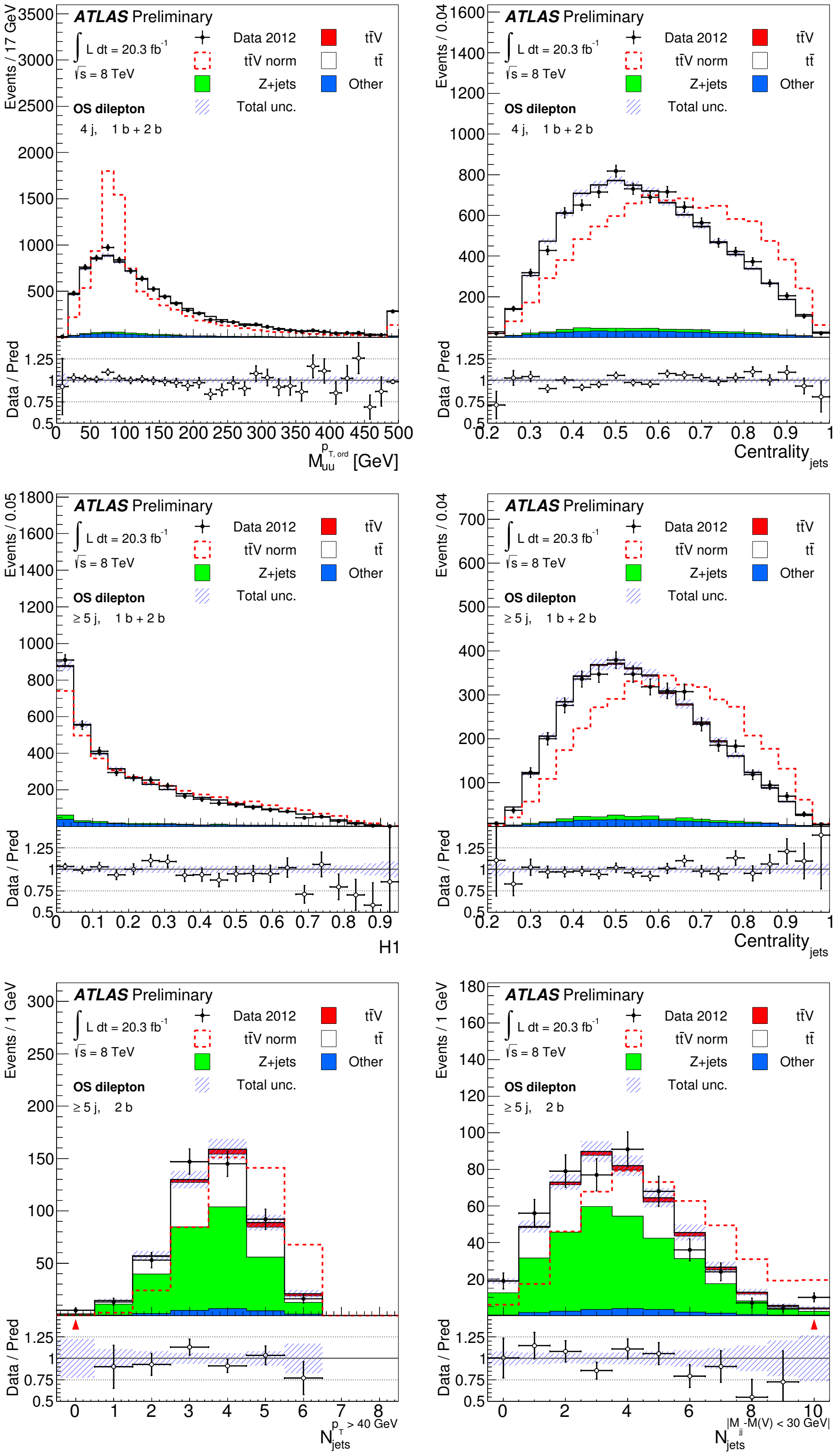

Figure 8.21.: The post-fit distributions of the highest two ranked variables in (top): the 2ℓOSZveto $(4\mathrm{j}, 1\mathrm{b}{+}2\mathrm{b})$ region, (middle): the 2ℓOSZveto $(\geq 5\mathrm{j}, 1\mathrm{b}{+}2\mathrm{b})$ region, and (bottom): the 2ℓOSZ $(\geq 5\mathrm{j}, 2\mathrm{b})$ region. The red dashed line shows $t\bar{t}V$ signal normalised to the background yield. The error band includes both statistical and systematic post-fit uncertainties. The arrow in the bottom panel indicates that the central value of the ratio between data and total prediction in that bin is outside the specified range.

In order to identify the systematic uncertainties with the largest post-fit impact on the fitted signal strength, $\mu_{t\bar{t}V}$, a ranking of the nuisance parameters is performed, and shown in Figure 8.22. The procedure to obtain such a ranking consists of repeating the fit fixing one nuisance parameter at a time to its post-fit $+1\sigma$, and then to the post-fit -1σ uncertainty. The post-fit impact of the nuisance parameter, shown with the blue dashed band, corresponds to the difference of the fitted μ values. If the same is performed but fixing the nuisance parameters to the pre-fit $\pm1\sigma$ values, the pre-fit yellow band is obtained. The upper $x - axis$ shows the absolute difference in the fitted μ. The lower $x - axis$ and the black lines show the aforementioned pull distribution of the nuisance parameters in the fit result.

The nuisance parameters corresponding to the leading modelling systematics on the main backgrounds are ranked in the first positions, as expected. The high ranking of the nuisance parameter related to the alternative DS approach for single top background can be understood given the "signal-like" shape variation in the NN distribution in the 2ℓOSZveto $(4\text{j}, 1\text{b} + 2\text{b})$ and $(\geq 5\text{j}, 1\text{b} + 2\text{b})$ regions, as shown in Figure 8.11. Moreover, it has a significant normalisation variation per fit region, which is not constrained by the fit.

The fitted signal strengths and its total uncertainty with respect to the NLO QCD calculation described in Sections 2.4 and 5.2, as well as the corresponding expected and observed compatibility with the background-only hypothesis in each case, are summarised in Table 8.7 for options 1-3. From the expected significances, it can be seen that the OS dilepton analysis is more sensitive to the $t\bar{t}Z$ signal process, than to the $t\bar{t}W$ process. This can be understood by the presence of the 2ℓOSZ region in the fit, which has the most discriminating NN in the signal region $(\geq 5\text{j}, 2\text{b})$.

Process	Signal Strength	Observed σ	Expected σ
$t\bar{t}V$	$0.77^{+0.63}_{-0.56}$	1.4	1.7
$t\bar{t}Z$	$0.77^{+0.69}_{-0.59}$	1.4	1.5
$t\bar{t}W$	$0.57^{+2.48}_{-2.30}$	0.3	0.4

Table 8.7.: The observed signal strength and its total uncertainty relative to the corresponding NLO QCD prediction, and the observed and expected significance of the $t\bar{t}V$, $t\bar{t}W$ and $t\bar{t}Z$ signals, expressed in terms of the standard deviations from the background-only hypothesis.

Table 8.7 shows that the total fitted uncertainties are slightly asymmetric. This follows from the negative *log* of the profile likelihood ratio curve as a function of μ, $-\log\lambda(\mu)$. Figure 8.23 shows in red the $-\log\lambda(\mu_{t\bar{t}V})$ curve, and the black dashed lines indicate the $\mu_{t\bar{t}V}$ values for which the likelihood curve has a value of 0.5, corresponding to the $\pm1\sigma$ fitted uncertainty on $\mu_{t\bar{t}V}$. The "real" asymmetric curve is compared to the symmetric blue dashed profiled likelihood curve, when imposing a symmetric uncertainty on μ. The divergence between the two curves is more pronounced the more the μ value is shifted from the minimum of the curve, for instance at $\mu = 0$. The "asymmetric" nature of the profile likelihood curve comes mainly from the statistical component of the total uncertainty, as can be seen in Table 8.8.

Table 8.8 provides a breakdown of the uncertainties on the measured signal strengths of the $t\bar{t}Z$ and $t\bar{t}W$ processes. It provides equivalent information to the post-fit impact bands from the systematic uncertainties on the fitted signal strength in Figure 8.22, grouped into categories. Furthermore, the statistical uncertainty (data and template statistics) is shown in the table. The

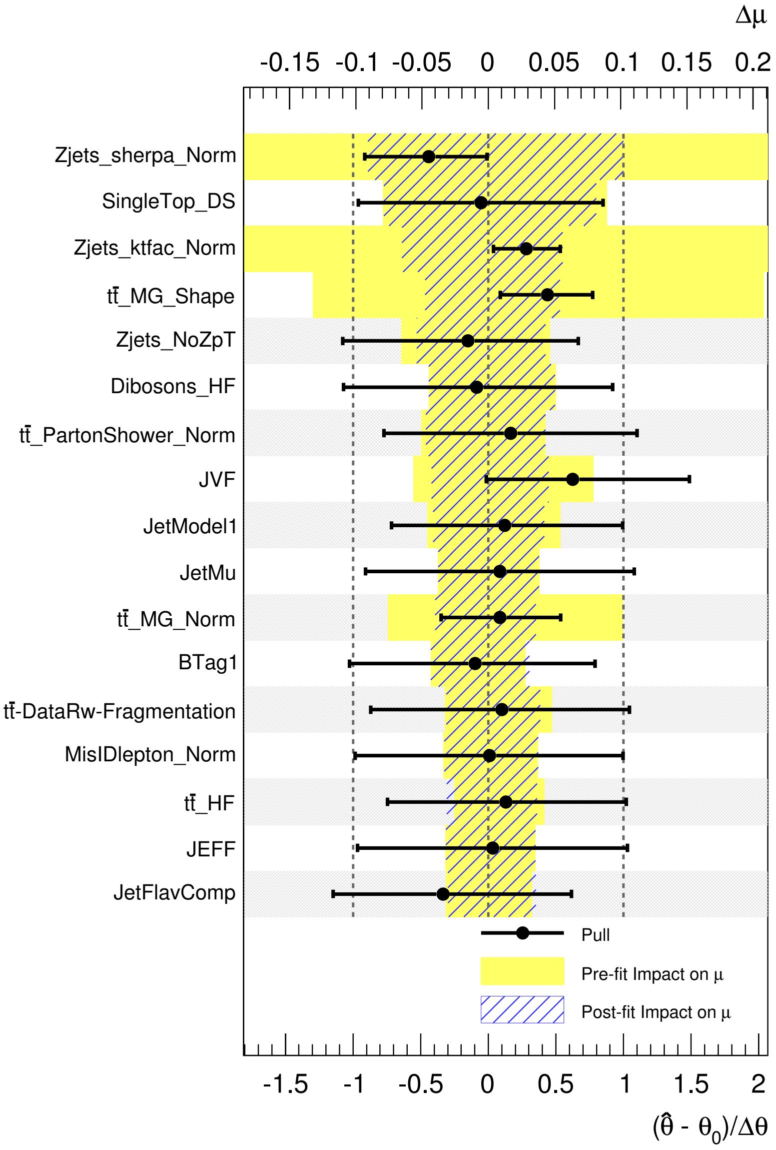

Figure 8.22.: Ranking of the nuisance parameters based on the fit to data according to their effect on the fitted signal strength. The top 18 parameters are shown. The yellow band corresponds to its pre-fit impact, and the dashed blue band, to its post-fit impact. They are plotted relative to the top horizontal axis in terms of the difference between the fitted signal strength values, $\Delta\mu$. The ranking from top to bottom is based on the post-fit impact on μ. The bottom axis shows the pull of the nuisance parameters from the fit result.

main contribution to the total uncertainty for the $t\bar{t}Z$ measurement arises from the limited data statistics, and from systematic variations for the $t\bar{t}W$ measurement. The dominating systematic uncertainty in both cases comes from the modelling of the backgrounds.

The results of the simultaneous fit of the $t\bar{t}Z$ and $t\bar{t}W$ processes are presented together with the combined results with the trilepton and same-sign dilepton channels in Section 8.4.

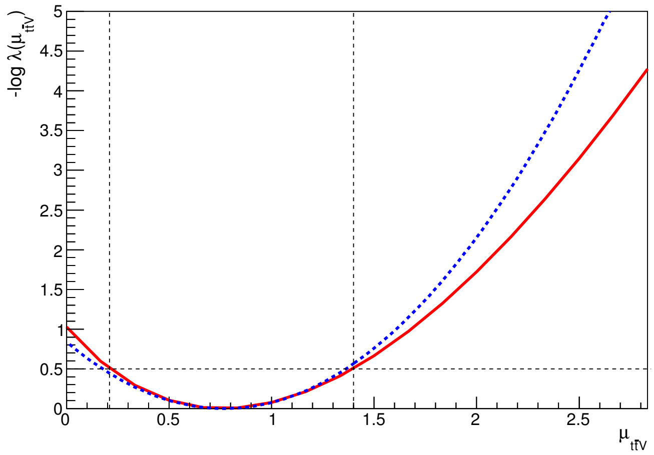

Figure 8.23.: Profiled likelihood curve $-\log\lambda(\mu_{t\bar{t}V}) = -(\log L(\mu_{t\bar{t}V}) - \log L(\hat{\mu}_{t\bar{t}V}))$ as a function of the $t\bar{t}V$ signal strength, $\mu_{t\bar{t}V}$. The red solid curve corresponds to the "real" asymmetric likelihood, and the blue dashed curve corresponds to the symmetric likelihood, when imposing a symmetric uncertainty on $\mu_{t\bar{t}V}$. The minimum value of the curve corresponds to the "best-fit" signal strength, $\hat{\mu}_{t\bar{t}V}$. The $\mu_{t\bar{t}V}$ values corresponding to the intersection between $-\log\lambda(\mu_{t\bar{t}V}) = 0.5$ and the profiled curve, indicated with the horizontal and vertical black dashed lines, correspond to the error on the signal strength, $\hat{\mu}_{t\bar{t}V} \pm 1\sigma$.

Uncertainty	$\mu_{t\bar{t}Z}$	$\mu_{t\bar{t}W}$
Detector	0.11	0.36
Background from simulation	0.20	1.28
MisID lepton	0.02	0.32
Signal modelling	< 0.01	0.10
Total systematics	0.33	2.06
Statistics	$+0.59-0.51$	$+1.20-1.18$
Total	$+0.69-0.59$	$+2.48-2.30$

Table 8.8.: Breakdown of uncertainties on the measured signal strength of $t\bar{t}Z$ and $t\bar{t}W$ processes from the 1-parameter-of-interest fit. Due to (anti)correlations between the different sources of uncertainties, the total systematic uncertainty can be different from the sum in quadrature of the individual sources. Systematic uncertainties are given symmetrised.

8.4. Combined Results

The OS dilepton $t\bar{t}V$ channel is combined with the three-lepton, or *trilepton*, final state, and with the final state with two leptons with same-sign charge, or *SS dilepton*. In the SS dilepton channel, only the di-muon events are used, motivated by a negligible contribution of background processes where the charge of one of the leptons is misidentified. The estimation of the charge lepton misidentification in electrons is difficult and non-negligible, and as a result, for the purposes of the conference note, the ee and $e\mu$ channels were not included in the SS dilepton result.

Table 9.1 summarises the characteristics of the trilepton and SS di-muon final states, comparing them with those from the OS dilepton channel. The trilepton final state is split into two regions, 3ℓZ and 3ℓZveto, similarly to the OS dilepton channel, based on the invariant mass of the same-flavour opposite-sign lepton pair, so that each region has sensitivity to $t\bar{t}Z$ or $t\bar{t}W$, respectively. The main $t\bar{t}V$ decay modes contributing to the 3ℓZ region are: $t\bar{t}$ decaying into lepton+jets, and the Z-boson decaying into two leptons. For the 3ℓZveto region, $t\bar{t}$ decays predominantly into a dilepton final state, and the W-boson decays leptonically. The SS di-muon channel is sensitive to $t\bar{t}W$, since the main decay mode contributing to that selection criteria is $t\bar{t}$ decaying into lepton+jets, and the W-boson decaying leptonically, so that both leptons have same-sign charge.

The main difference in the analysis strategy of the trilepton and SS di-muon channels, compared to the OS dilepton channel, is that the former have comparable signal and background contributions, so that the S/B is large enough to perform a counting experiment. Therefore, the OS dilepton channel is the only multivariate analysis, and the fit regions provided by the trilepton and SS di-muon channels contain only event counting information. No “control regions” from the trilepton and SS di-muon channels are included in the fit, though they are used to estimate the largest background contributions.

	Trilepton		**Same-sign di-muon**	**Opposite-sign dilepton**	
Channels	3ℓZ	3ℓZveto	2μSS	2ℓOSZveto	2ℓOSZ
Signal	$t\bar{t}Z$	$t\bar{t}W$	$t\bar{t}W$	$t\bar{t}Z$ and $t\bar{t}W$	$t\bar{t}Z$
Main Bkgds	tZ, WZ,	$t\bar{t}Z$, $t\bar{t}H$		$t\bar{t}$+jets	Z+jets
	lepton misID				
Fit regions	3	1	1	3	3

Table 8.9.: Overview of the final state channels included in the combination of the $t\bar{t}V$ measurements at $\sqrt{s} = 8$ TeV. The suffices “Z” and “Zveto” refer to the lepton invariant mass requirement $|m_{\ell\ell} - m_Z| < 10$ GeV and $|m_{\ell\ell} - m_Z| > 10$ GeV, respectively, corresponding in the trilepton case, to the invariant mass of the same-flavour opposite-sign lepton pair.

A simultaneous fit to the data is performed under the signal plus background hypothesis using the distributions of the discriminating variable in each of the six fit regions in the OS dilepton channel, and the event counts from the one fit region in the SS dilepton channel and the four fit regions in the trilepton channel. The RooStats project [198] allows to perform the combination of fit models easily by combining the corresponding *workspaces*, where the data and the fit model (processes, fit regions, fit bins) is stored.

Before performing the combination, the list of systematic uncertainties that are correlated across channels is specified, leaving the rest uncorrelated across channels.

All uncertainties grouped as “Physics Objects”-related in Table 8.2 are correlated across channels, except for the systematics related to the b, c and light-tagging efficiency, since the trilepton and SS di-muon channel use the corresponding envelope uncertainty [6]. From the uncertainties grouped as “Background Modelling”, only the $t\bar{t}H$ and tZ cross section uncertainties are correlated. The reason for this is the different background composition in each channel, and the different treatment of them within each analysis. All “Signal Modelling” uncertainties are correlated. The signal PDF uncertainty was not included in the combined fit.

Table 8.10 summarises the observed signal strength μ with respect to the NLO QCD prediction, and the corresponding observed and expected significance, σ, for the three 1-parameter-of-interest measurements presented in Section 8.3.1.

	1-parameter-of-interest combined fit results		
Process	Signal Strength	Observed σ	Expected σ
$t\bar{t}V$	$0.89^{+0.23}_{-0.22}$	4.9	4.9
$t\bar{t}W$	$1.25^{+0.57}_{-0.48}$	3.1	2.4
$t\bar{t}Z$	$0.73^{+0.29}_{-0.26}$	3.2	3.8

Table 8.10.: The observed signal strength relative to the SM prediction and its total uncertainty, and the observed and expected significance of the $t\bar{t}V$, $t\bar{t}W$ and $t\bar{t}Z$ signals for the combination of all channels. The combined $t\bar{t}V$ result assumes SM ratio of $t\bar{t}Z$ to $t\bar{t}W$ cross sections, the $t\bar{t}W$ result assumes SM $t\bar{t}Z$ production rate and the $t\bar{t}Z$ result assumes SM $t\bar{t}W$ production rate.

Table 8.11 provides a breakdown of the total uncertainty on the measured signal strengths of the $t\bar{t}Z$ and $t\bar{t}W$ processes, for the 1-parameter-of-interest fit. In both cases, the measurement is limited by the statistical uncertainty, followed by the uncertainties due to modelling of the detector effects.

The result of the simultaneous fit of the signal strengths of both $t\bar{t}Z$ and $t\bar{t}W$ processes compared to the NLO QCD expectation, is shown in Figure 8.24. The results are shown for the fit to all channels combined in black, for the fit to the OS dilepton channel in magenta, and for the fit to the trilepton and SS di-muon channels in red. The NLO QCD expectation is shown with a blue cross. The solid and dashed curves show the 68% and 95% CL uncertainty contours. The overlaid contours demonstrate the relative sensitivity to $t\bar{t}Z$ and $t\bar{t}W$ production for each individual measurement.

The results from the fit shown in Figure 8.24 for the individual channels and their combination are summarised in Table 8.12. The observed and expected significances are calculated with respect to a no-$t\bar{t}Z$ and no-$t\bar{t}W$ background hypothesis.

Table 8.13 shows the fitted signal strengths translated in measured $t\bar{t}Z$ and $t\bar{t}W$ cross sections, and their uncertainties, split into the statistical and systematic contributions, as well as the observed and expected signal significances for $t\bar{t}Z$ and $t\bar{t}W$ separately, from the simultaneous combined fit. The significances for each signal process are calculated assuming the null hypothesis for one of them and treating the other as a free parameter in the fit.

---

[6] Since these channels do not rely on shape information in each fit region, there is no need to use the breakdown in sub-components of these systematics.

Uncertainty	$\mu_{t\bar{t}Z}$	$\mu_{t\bar{t}W}$
Detector	0.07	0.13
Background from simulation	0.08	0.09
MisID lepton	0.03	0.09
Signal modelling	< 0.01	< 0.01
Total systematics	0.10	0.24
Statistics	$+0.26-0.24$	$+0.49-0.43$
Total	$+0.29-0.26$	$+0.57-0.48$

Table 8.11.: Breakdown of uncertainties on the measured signal strength of $t\bar{t}Z$ and $t\bar{t}W$ processes from the corresponding 1-parameter-of-interest fits. Systematic uncertainties are symmetrised.

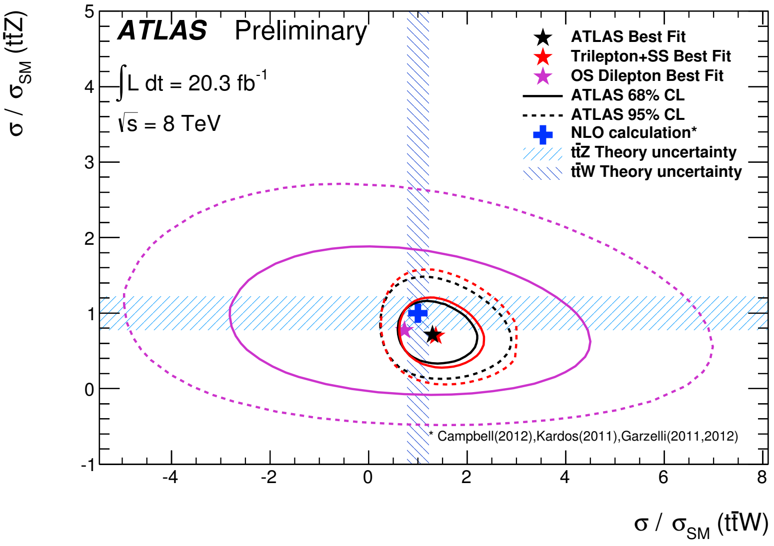

Figure 8.24.: The result of the combined simultaneous fit of the $t\bar{t}Z$ and $t\bar{t}W$ signal strengths along with the 68% CL and 95% CL uncertainty contours compared to the fit results in the OS dilepton and trilepton plus SS di-muon channels. The χ^2 quantile for two degrees of freedom is used to define the likelihood contours. The dashed area corresponds to the 22% uncertainty on the NLO QCD theoretical calculations of $\sigma(t\bar{t}Z)$ and $\sigma(t\bar{t}W)$.

The measured signal strengths and significances in the simultaneous fit are close to those obtained from the fits using 1-parameter-of-interest, due to the very small correlation between the $t\bar{t}Z$ and $t\bar{t}W$ measurements, as seen in Figure 8.24. In both types of measurements, with 1 or 2 parameters-of-interest in the fit, the $t\bar{t}Z$ and $t\bar{t}W$ processes are observed with significance larger than 3 standard deviations from the background-only hypothesis, providing **evidence** for both $t\bar{t}Z$ and $t\bar{t}W$ production for the first time with the ATLAS experiment.

Channel	$\mu_{t\bar{t}Z}$	$\mu_{t\bar{t}W}$	Observed σ	Expected σ
Trilepton and SS di-muon	$0.70^{+0.30}_{-0.28}$	$1.37^{+0.62}_{-0.51}$	4.1	4.1
OS dilepton	0.77 ± 0.65	0.71 ± 2.41	0.4	0.6
Combination	$0.71^{+0.28}_{-0.26}$	$1.30^{+0.59}_{-0.48}$	4.4	4.4

Table 8.12.: The observed signal strength for $t\bar{t}Z$ and $t\bar{t}W$ production from the simultaneous fit of two parameters of interest, and the observed and expected significance of the signals for each individual channel and the combination. The signal significance is calculated with respect to a no-$t\bar{t}Z$ and no-$t\bar{t}W$ background hypothesis. The result for the $t\bar{t}W$ ($t\bar{t}Z$) signal strength is obtained treating the $t\bar{t}Z$ ($t\bar{t}W$) signal strength as a nuisance parameter.

	Summary of combined simultaneous fit results		
Process	Measured cross-sections	Observed σ	Expected σ
$t\bar{t}Z$	150^{+58}_{-54}(total) $= 150^{+55}_{-50}$(stat.) $\pm$ 21(syst.) fb	3.1	3.7
$t\bar{t}W$	300^{+140}_{-110}(total) $= 300^{+120}_{-100}$(stat.)$^{+70}_{-40}$(syst.) fb	3.1	2.3

Table 8.13.: The measured cross-sections and total uncertainty, and the observed and expected significance of the individual $t\bar{t}W$ and $t\bar{t}Z$ signals from the simultaneous fit of 2-parameters-of-interest for the combination of all channels. The significances for each signal process is calculated assuming the null hypothesis for one of them and treating the other as a free parameter in the fit.

CHAPTER 9

Conclusions $t\bar{t}V$ Results

9.1. Discussion of Results

Measurements of the production cross section of a top quark pair in association with a W- or Z-boson using 20.3 fb^{-1} of data collected at $\sqrt{s}$ = 8 TeV by the ATLAS detector have been presented in this thesis. The combined results, with final states with two or three charged leptons, were obtained in various scenarios. All measurements are consistent with the NLO QCD theoretical calculations. Evidence of both $t\bar{t}Z$ and $t\bar{t}W$ processes was obtained when measuring each process individually, and, most importantly, when measuring both processes simultaneously. Furthermore, this is the first time, that evidence of the $t\bar{t}W$ production mechanism is obtained.

A summary of the most precise cross section measurements from processes predicted by the SM, performed by ATLAS up to July 2014, can be seen in Figure 9.1. The last two entries on the right side of the plot correspond to the combined $t\bar{t}Z$ and $t\bar{t}W$ production cross section measurements presented in this thesis. The figure highlights, as well, how rare the $t\bar{t}V$ processes are, compared to, for example, the $t\bar{t}$ production; 1 $t\bar{t}Z/W$ event is expected for 1000 $t\bar{t}$ events at $\sqrt{s} = 8$ TeV.

9.1.1. Comparison with CMS $t\bar{t}V$ Measurements

It is interesting to compare the combined $t\bar{t}V$ production cross section measurements presented in this thesis to the results obtained by CMS at $\sqrt{s}$ = 8 TeV, presented in Section 2.4.1. In order to understand the differences in sensitivity to $t\bar{t}Z$ and $t\bar{t}W$ between the ATLAS and CMS measurements, a summary of the multi-leptonic channels considered by each experiment is shown in Table 9.1.

The most sensitive channel to the $t\bar{t}Z$ production is the trilepton 3ℓZ region, whereas the most sensitive channel to $t\bar{t}W$ production is the 2μSS region. Both experiments include those channels in their combination results. However, ATLAS split the 3ℓZ region into three fit regions, based on the jet and b-jet multiplicities, in order to separate regions with different S/B; CMS, on the contrary, includes only one of those fit regions in the combination. This aspect, together with the different treatment of the backgrounds, leads to a higher expected significance of the $t\bar{t}Z$ measurement in ATLAS than in CMS, as shown in Table 9.2. Concerning the sensitivity to the $t\bar{t}W$ production, although CMS performs a finer splitting of the 2μSS region and includes all

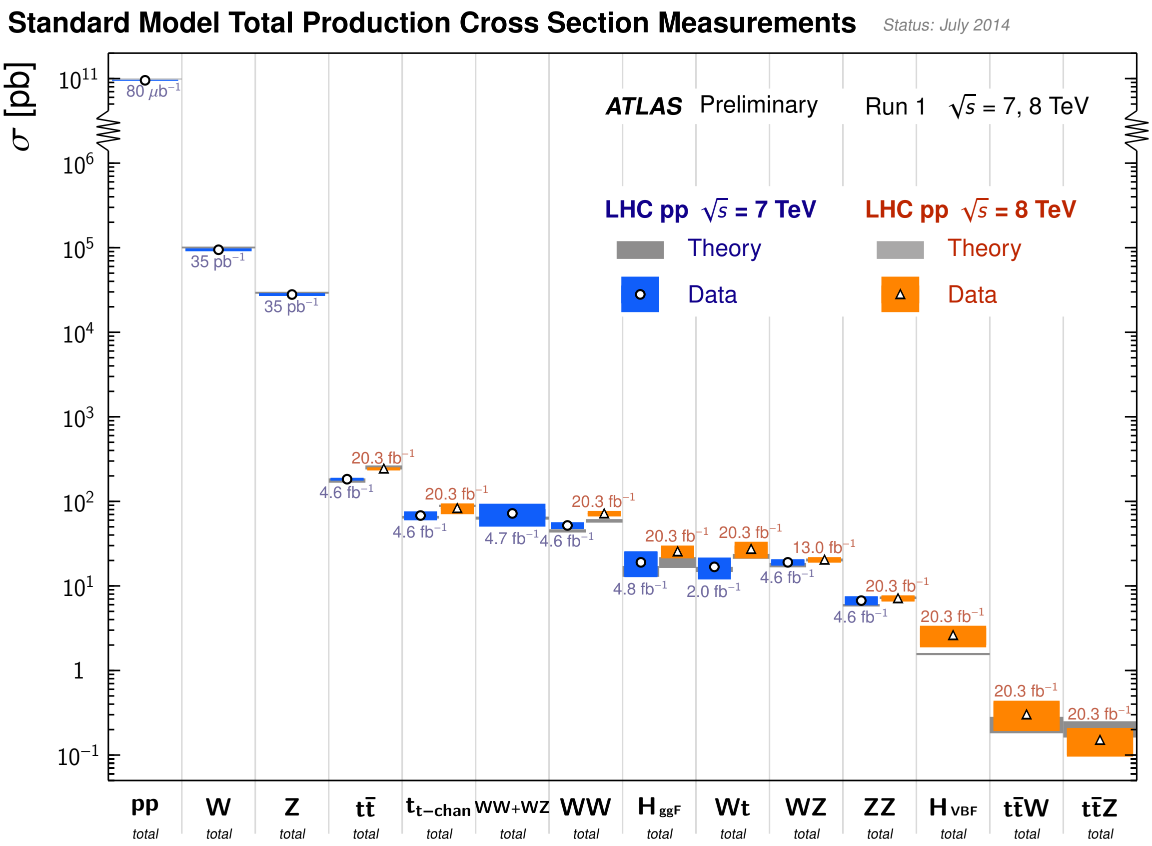

Figure 9.1.: Summary of several total production cross section measurements from processes predicted by the SM, performed by ATLAS at $\sqrt{s} = 7$ and 8 TeV up to July 2014. The measurements are compared to the corresponding theoretical expectations, which were calculated at NLO or higher order in QCD. The combined measurements of $t\bar{t}Z$ and $t\bar{t}W$ production cross sections at $\sqrt{s} = 8$ TeV presented in this thesis are shown in the last two bins of the plot [207].

lepton flavours, ATLAS treats the 2μSS and 3ℓZveto regions separately in the fit, and performs separate optimisation in each region. As a result, the expected sensitivity to $t\bar{t}W$ is comparable between ATLAS and CMS.

To understand the observed significances shown in Table 9.2, Figure 9.2 and Figure 9.3 highlight the pre-fit normalisation in the trilepton and SS dilepton regions, for ATLAS and CMS, respectively. A slight deficit (excess) is seen in the expected pre-fit event yields with respect to data in the two first bins (last bin) in Figure 9.2, corresponding to the regions sensitive to $t\bar{t}Z$ ($t\bar{t}W$). This explains the differences between expected and observed significances for the $t\bar{t}Z$ and $t\bar{t}W$ production processes in the ATLAS analysis. On the other hand, the pre-fit event yields in the CMS analysis in the trilepton and SS dilepton channels are similar between data and prediction, and therefore the observed significances are close to the expected ones.

The OS dilepton channel (ATLAS) and the four-lepton channel (CMS) add to the respective combinations an expected sensitivity to the $t\bar{t}Z$ process of 1.5 and 2.0, respectively. Furthermore, the OS dilepton channel improves slightly the sensitivity to $t\bar{t}W$ in the ATLAS combined result. Both ATLAS and CMS perform a combination of the channels and measure $t\bar{t}Z$, $t\bar{t}W$ and

	Trilepton		**Same-sign dilepton**	**Four lepton**	**Opposite-sign dilepton**	
Channels	3ℓZ	3ℓZveto	2μSS	4ℓ	2ℓOSZveto	2ℓOSZ
Signal	$t\bar{t}Z$	$t\bar{t}W$	$t\bar{t}W$	$t\bar{t}Z$	$t\bar{t}Z$ and $t\bar{t}W$	$t\bar{t}Z$
Main Bkgds	tZ, WZ	$t\bar{t}Z$, $t\bar{t}H$	charge misID (CMS)	ZZ	$t\bar{t}$+jets	Z+jets
	lepton misID					
Fit regions:						
ATLAS	$(3\text{j}, \geq 2\text{b})$ $(\geq 4\text{j}, 1\text{b})$ $(\geq 4\text{j}, \geq 2\text{b})$	$(3\text{j} + 2\text{j}, \geq 2\text{b})$	1 region: $(\mu\mu)$ in $(\geq 2\text{j}, \geq 2\text{b})$	-	$(3\text{j}, 1\text{b} + 2\text{b})$ $(4\text{j}, 1\text{b} + 2\text{b})$ $(\geq 5\text{j}, 1\text{b} + 2\text{b})$	$(3\text{j}, 2\text{b})$ $(4\text{j}, 2\text{b})$ $(\geq 5\text{j}, 2\text{b})$
CMS	$(\geq 4\text{j}, \geq 2\text{b})$	*[included in 2μSS]*	6 regions: $(e^{\pm}e^{\pm}), (\mu^{\pm}\mu^{\pm})$, $(e^{\pm}\mu^{\pm})$ in $(\geq 3\text{j}, \geq 1\text{b})$	(1b) (2b)	-	-

Table 9.1.: Overview of final state channels used in the ATLAS and CMS $t\bar{t}V$ production cross section measurements at $\sqrt{s} = 8$ TeV. The suffices “Z” and “Zveto” refer to the lepton invariant mass requirement, $|m_{\ell\ell} - m_Z| < 10$ GeV and $|m_{\ell\ell} - m_Z| > 10$ GeV, respectively, where in the trilepton case, the $m_{\ell\ell}$ is the invariant mass of the same-flavour opposite-sign lepton pair. The fit regions are split into jet multiplicity, denoted by “j”, and b-jet multiplicity, denoted by “b”. Regions are exclusive unless given with a “$\geq$”.

	Sensitivity trilepton + SS dilepton			
	$t\bar{t}Z$		$t\bar{t}W$	
	Observed σ	Expected σ	Observed σ	Expected σ
ATLAS	2.8	3.4	3.0	2.3
CMS	2.3	2.4	1.6	2.0

Table 9.2.: The observed and expected significance for $t\bar{t}Z$ and $t\bar{t}W$ production when performing the fit with the trilepton and SS dilepton channels, as defined by ATLAS and CMS. For ATLAS, only the SS dimuon channel is considered [185, 84].

$t\bar{t}V$ production cross sections, performing a profile likelihood fit in each case. The simultaneous measurements for both experiments indicate a small correlation between $t\bar{t}Z$ and $t\bar{t}W$ production cross sections. All combined cross section measurements are statistically limited.

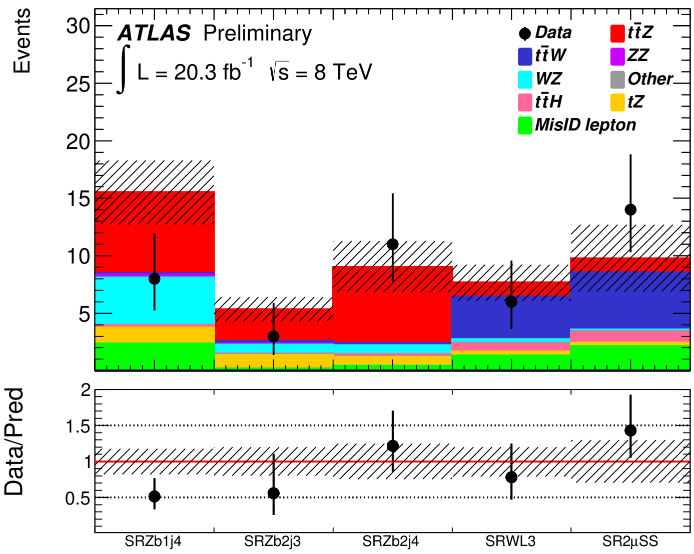

Figure 9.2.: Summary of the pre-fit observed and expected numbers of events in the fit regions considered in the trilepton and same-sign dilepton channels in the ATLAS analysis at $\sqrt{s} = 8$ TeV. The three first bins correspond to the 3ℓZ regions, sensitive to the $t\bar{t}Z$ production, whereas the last two bins correspond to the 3ℓZveto and 2μSS regions, sensitive to the $t\bar{t}W$ production. The shaded bands include all pre-fit systematic uncertainties [185].

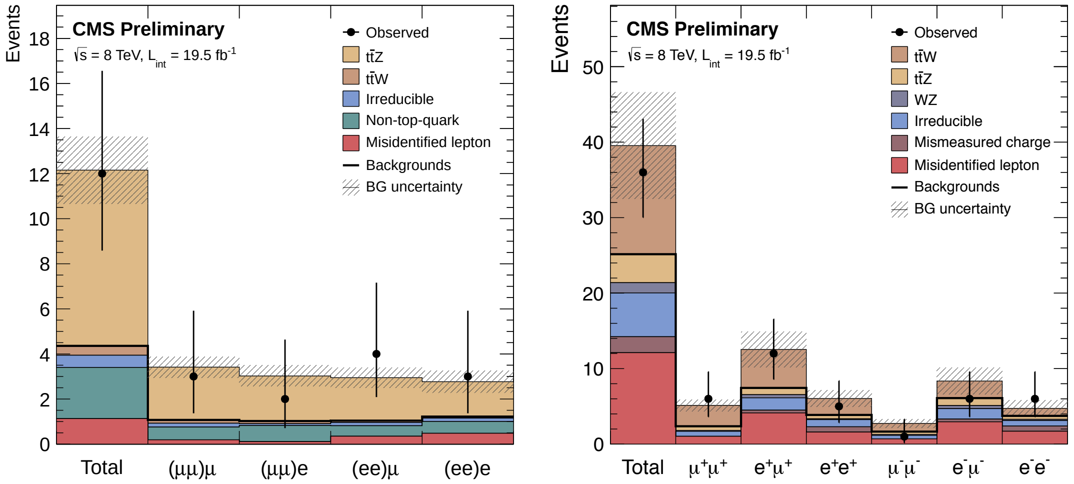

Figure 9.3.: Pre-fit observed and expected event yields in the (left): trilepton, and (right): SS dilepton channels, split into the lepton flavours, in the CMS analysis at $\sqrt{s} =$ 8 TeV. While for the trilepton channel, the "Total" corresponds to one fit region, each lepton flavour channel in the SS dilepton region is included in the fit as separate regions [84].

9.2. Outlook

Given the encouraging results obtained at $\sqrt{s} = 8$ TeV with 20.3 fb^{-1} of data collected by the ATLAS experiment, the $t\bar{t}V$ process observation is expected to be one of the highlights of the early physics program of ATLAS during the second run of the LHC. Already at the early stage of the second run, when the LHC is planning to collide protons at $\sqrt{s} = 13$ TeV, the observation of $t\bar{t}Z$ with 5σ significance is one of the milestones of both ATLAS and CMS Collaborations. As shown in Figure 2.12, the cross section of the $t\bar{t}Z$ production at $\sqrt{s} = 13$ TeV is expected to increase by a factor of 4 with respect to that at $\sqrt{s} = 8$ TeV. Therefore, the same number of $t\bar{t}Z$ data events, which were analysed at $\sqrt{s} = 8$ TeV with the full dataset of 20.3 fb^{-1}, is expected to be collected in ≈ 5 fb^{-1} of data at $\sqrt{s} = 13$ TeV. Since the measurement performed at $\sqrt{s} = 8$ TeV is statistically limited, it can be assumed that the significance scales with $\sqrt{N_{data}}$. Under the assumption that (a) the cross sections of the main background processes scale similarly to $t\bar{t}Z$ with the centre-of-mass energy, and (b) the systematic uncertainties remain the same at $\sqrt{s} = 13$ TeV as in $\sqrt{s} = 8$ TeV, one expects to observe the $t\bar{t}Z$ production with a significance of 5σ with only ≈ 14 fb^{-1} data collected at $\sqrt{s} = 13$ TeV [1]. However, the sensitivity to the $t\bar{t}Z$ process is expected to increase significantly by adding the four-lepton channel to the combination, and increasing data statistics will allow to develop better data driven methods to derive the background contributions and reduce the uncertainties. This would lead to an observation with less data.

Concerning the analysis prospects of the OS dilepton $t\bar{t}V$ channel, several improvements can be exercised in order to achieve higher sensitivity to both $t\bar{t}Z$ and $t\bar{t}W$ processes. In the 2ℓOSZ region, a further splitting of the $(\geq 5\text{j}, 2\text{b})$ region into $(5\text{j}, 2\text{b})$ and $(\geq 6\text{j}, 2\text{b})$ is expected to increase the S/B by a factor of 2 in the $(\geq 6\text{j}, 2\text{b})$ region. This improvement, which was not implemented on the timescale of the conference note due to limited Z+jets MC statistics, would increase the sensitivity to the $t\bar{t}Z$ process. However, the modelling of the Z+jets background by MC simulation in the higher jet multiplicity region, $(\geq 6\text{j}, 2\text{b})$, needs to be carefully validated prior to the fit. In order to improve the sensitivity to the $t\bar{t}W$ process, the NN should be trained in the 2ℓOSZveto region to separate not only $t\bar{t}V$ from $t\bar{t}$, but also $t\bar{t}Z$ from $t\bar{t}W$. Alternatively, a kinematic variable that discriminates between $t\bar{t}Z$ and $t\bar{t}W$ could be used to further separate fit regions mostly sensitive to either $t\bar{t}Z$ or $t\bar{t}W$.

---

[1] Without considering a combination with the 8 TeV dataset.

CHAPTER 10

Precision Measurement of the $t\bar{t}$ Production Cross Section in the Single Lepton Channel

10.1. Introduction

Prior to the measurement of the $t\bar{t}V$ production cross section, it is important to measure the cross section of one of the leading background processes, $t\bar{t}$ production. A precision measurement of the $t\bar{t}$ production cross section was performed at $\sqrt{s} = 7$ TeV in the ℓ+jets channel, using an integrated luminosity of 0.7 fb^{-1}. The results were presented as a conference note for LP 2011 in Reference [208]. Differently than the $t\bar{t}V$ production cross section measurement, which started as a search, the large sample of $t\bar{t}$ events collected in the analysed dataset allows for a high precision measurement of the cross section. Although there are clear differences between the presented $t\bar{t}V$ and $t\bar{t}$ production measurements, such as the energy, the channel, the background composition, and the S/B in the analysis regions, both measurements are based on a similar analysis approach: they profit from MVA techniques, and extract the signal cross section from a profile likelihood fit. In the following sections, the similarities and differences between the two measurements are highlighted, reflecting also the evolution of the understanding of the methods, the simulation of the physics processes, and the reconstruction of the physics objects, between the early analysis in 2011 and the full 8 TeV dataset analysis in 2013.

10.2. The Analysed Dataset

The presented $t\bar{t}$ cross section measurement uses an integrated luminosity of 0.7 fb^{-1}, corresponding to the data set collected between March and July 2011 at $\sqrt{s} = 7$ TeV. As it was shown in Figure 3.9, the instantaneous luminosity increased significantly from $\sqrt{s} = 7$ TeV to $\sqrt{s} = 8$ TeV data-taking (approximately 5 times with respect to the peak luminosity in July 2011), and therefore the pile-up conditions were harsher at $\sqrt{s} = 8$ TeV. This aspect was the leading motivation to improve the object isolation requirements at $\sqrt{s} = 8$ TeV.

At $\sqrt{s} = 7$ TeV, an electron candidate is considered isolated, if the energy in a cone of $\Delta R = 0.2$ around the electron, excluding the energy of the electron itself, is less than 3.5 GeV, $E_T^{cone20} < 3.5$ GeV. Instead of using a likelihood-based electron identification, an electron identification based on cuts applied to electron quality variables is used, corresponding to the *tight* operating point. In contrast to the *mini-isolation* requirement used at $\sqrt{s} = 8$ TeV, muons are required to fulfil a track and a calorimeter isolation requirement at $\sqrt{s} = 7$ TeV, corresponding to $p_T^{cone30} < 4$ GeV and $E_T^{cone30} < 4$ GeV, respectively. Similar isolation requirements with respect to the overlap with jets are required, as in the $t\bar{t}V$ analysis at $\sqrt{s} = 8$ TeV. The definition of good jets is also common between both measurements.

10.3. The $t\bar{t}$ Signature

The $t\bar{t}$ signature in the ℓ+jets channel consists of an isolated charged lepton, genuine E_T^{miss} from the neutrino originating from the W-boson decay, and four jets, from which two are b-jets. This channel provides a good balance between high statistics, given the relatively high branching ratio of the decay mode, and manageable background, given the presence of a charged lepton and E_T^{miss} in the event. The event selection used for this measurement requires one electron (muon) with $E_T > 25$ GeV ($p_T > 20$ GeV), fulfilling the isolation requirements described in Section 10.2. The events are separated according to the lepton flavour in e+jets and μ+jets. At least three jets with $p_T > 25$ GeV are required. Differently than the $t\bar{t}V$ measurement, no b-tag requirements are imposed. This deteriorates signal purity, but avoids the large sources of systematic uncertainties related to the b-jet identification [1].

10.4. Signal and Main Background

The dominant background contribution comes from the W+jets process. It is simulated with Alpgen, in the same way as the Z+jets and W+jets samples in the $t\bar{t}V$ measurement, including the $W + b\bar{b}/c\bar{c}/c$ samples, but with Herwig/Jimmy, instead of Pythia, for fragmentation, parton shower, and underlying event model. Since it is not expected that the MC simulation predicts the W+jets normalisation correctly, the normalisation is derived from a data-driven method, which exploits the charge asymmetry of the W-boson production in pp collisions, and the low theoretical uncertainty on the ratio $r_{MC} = \frac{\sigma(pp \to W^+)}{\sigma(pp \to W^-)}$. Given that W^+ (W^-) bosons are produced from parton level processes such as $u\bar{d} \to W^+$ ($d\bar{u} \to W^-$), and that the parton distribution functions for the "up" and "down" quarks are different in a proton, a charge asymmetry is expected in the production of the W+jets process: a higher W^++jets production rate than that of W^-+jets [210]. With this method, the W+jets estimate, $N_{W^+} + N_{W^-}$, can be determined from:

$$N_{W^+} + N_{W^-} = \frac{r_{MC} + 1}{r_{MC} - 1}(D^+ - D^-), \tag{10.1}$$

where D^+ (D^-) are the number of events in data with a positively (negatively) charged-lepton. Small charge asymmetric contributions, originating from single top and diboson processes, are evaluated with MC simulation and subtracted from D^+ and D^-. Furthermore, the relative HF fraction of the W+jets is also corrected, similarly to Z+jets in the $t\bar{t}V$ measurement. The corrections are derived in a W+2 jets measurement from data, and extrapolated to events with higher jet multiplicities, resulting in the multiplication of the $W + b\bar{b}/c\bar{c}$ contribution by a factor of 1.63, and $W + c$ by a factor of 1.11. The shape of W+jets is taken from the MC simulation.

In contrast to the $t\bar{t}V$ dilepton channel, the misidentified lepton background is the second dominant background in the $t\bar{t}$ ℓ+jets channel and originates from multijet QCD processes.

---

[1] This systematic source limited the precision of a previous $t\bar{t}$ cross section measurement using b-jet identification [209].

Due to different contributions from the multijet QCD background, different cuts on the E_T^{miss} distribution are applied in the e+jets and μ+jets channels: events are required to have an $E_T^{miss} > 35$ GeV ($E_T^{miss} > 25$ GeV) in the electron (muon) channel. To further suppress the contamination from the multijet QCD background, a cut on the transverse mass of the leptonically-decaying W-boson is applied, defined as $m_T(W) = \sqrt{2p_T^{\ell}p_T^{\nu}(1-\cos(\phi^{\ell}-\phi^{\nu}))}$. The events are required to have an $m_T(W) > 25$ GeV in the e+jets channel, and to fulfil the triangular cut, $E_T^{miss} + m_T(W) > 60$ GeV, in the μ+jets channel.

The multijet QCD background is estimated from data using the *matrix method* (MM) technique [211]. The method defines two samples of events, one requiring *tight* leptons and the other *loose* leptons. *Tight* leptons are those used in the analysis selection, whereas *loose* leptons are leptons fulfilling less stringent requirements: a looser isolation cut of $E_T^{cone20} < 6$ GeV, for electrons, and no track/calorimeter isolation cut, for muons. Distinguishing between *real* and *fake* leptons, the method builds the following system of equations:

$$N^{loose} = N^{loose}_{real} + N^{loose}_{fake}, \tag{10.2}$$

$$N^{tight} = \epsilon_{real}N^{loose}_{real} + \epsilon_{fake}N^{loose}_{fake}, \tag{10.3}$$

where ϵ_{real} and ϵ_{fake} are the efficiencies for a loose real and loose fake lepton to fulfil the tight selection criteria, respectively. After measuring the real efficiencies in $Z \to \ell\ell$ data events, and the fake efficiencies in QCD multijet-enriched control samples in data, the number of fake leptons passing the tight lepton selection is determined as:

$$N^{tight}_{fake} = \frac{\epsilon_{fake}}{\epsilon_{real} - \epsilon_{fake}}(N^{loose}\epsilon_{real} - N^{tight}). \tag{10.4}$$

The MM technique can not be easily applied to the $t\bar{t}V$ analysis, since the electron selection used at $\sqrt{s} = 8$ TeV is already too loose to have a “looser” version, for events that passed the trigger.

Other background contributions from EW processes, such as Z+jets, single top quark and diboson production, are estimated using MC simulation.

The $t\bar{t}$ signal process is simulated with the MC@NLO generator, interfaced with Herwig and Jimmy to model the parton showering and the underlying event (see Section 6.2.2). Later measurements of the $t\bar{t}$ production cross section, as a function of the jet multiplicity at $\sqrt{s} =$ 7 TeV with the full dataset of 4.6 fb^{-1}, showed that the MC@NLO $t\bar{t}$ generator predicts too few events at higher jet multiplicities (six or more $p_T > 25$ GeV jets) [212]. Therefore, the Powheg+Pythia generator has been used as the default $t\bar{t}$ generator for later measurements.

The sample composition for events categorised by the jet multiplicity and lepton flavour is summarised in Tables 10.1 and 10.2, based on the predictions before applying the fitting procedure.

	1 Jet	2 Jet	3 Jet	4 Jet	≥ 5 jet
$t\bar{t}$	225 ± 61	1005 ± 247	1934 ± 332	1835 ± 281	1463 ± 472
W+jets	161569 ± 53156	43165 ± 19921	10832 ± 6348	2485 ± 1749	1033 ± 842
QCD	10715 ± 5358	4757 ± 2379	1589 ± 795	507 ± 254	177 ± 89
Single Top	570 ± 137	711 ± 165	391 ± 105	156 ± 51	65 ± 26
Z+jets	3732 ± 1541	2444 ± 1288	996 ± 636	333 ± 233	148 ± 126
Diboson	599 ± 66	538 ± 137	178 ± 41	45 ± 16	10 ± 6
Total Pred.	177408 ± 54659	52620 ± 20916	15919 ± 6869	5361 ± 2018	2893 ± 1176
Data Obs.	179469	51820	15614	5398	2812

Table 10.1.: Selected number of events in the $e+$jets channel split according to the jet multiplicity. Both statistical and systematic uncertainties before the fit procedure are included in the quoted uncertainties on the expected event yields.

	1 Jet	2 Jet	3 Jet	4 Jet	≥ 5 jet
$t\bar{t}$	319 ± 74	1342 ± 336	2734 ± 495	2714 ± 388	2030 ± 522
W+jets	38223 ± 121118	93436 ± 42653	20140 ± 11661	4643 ± 3194	1075 ± 878
QCD	24628 ± 12314	10942 ± 5471	3147 ± 1575	868 ± 434	294 ± 147
Single Top	995 ± 248	1148 ± 531	594 ± 154	210 ± 65	84 ± 34
Z+jets	17267 ± 5642	5492 ± 2557	1510 ± 886	436 ± 302	149 ± 121
Diboson	1093 ± 129	1009 ± 113	308 ± 64	69 ± 21	18 ± 9
Total Pred.	427526 ± 124569	113369 ± 44486	28434 ± 12438	8938 ± 3547	3650 ± 1287
Data Obs.	433931	111741	28643	8680	3814

Table 10.2.: Selected number of events in the $\mu+$jets channel split according to the jet multiplicity. Both statistical and systematic uncertainties before the fit procedure are included in the quoted uncertainties on the expected event yields.

10.5. Analysis Strategy

Six analysis regions are defined in the presented $t\bar{t}$ production cross section measurement based on the lepton flavour ($e+\text{jets}$ or $\mu+\text{jets}$), and the jet multiplicity (3, 4, and ≥ 5). Table 10.3 shows the S/B for each analysis region.

	$\mu+\text{jets}$	$e+\text{jets}$
3 jets	0.11	0.14
4 jets	0.44	0.52
≥ 5 jets	1.25	1.02

Table 10.3.: S/B ratio for the six analysis regions, split according to the jet multiplicity (3, 4, and ≥ 5), and the lepton flavour ($e+\text{jets}$ or $\mu+\text{jets}$).

To extract the $t\bar{t}$ signal in this measurement, kinematic variables which can separate the signal from the background are selected, and a likelihood discriminant is built from them using the TMVA package [213]. The MVA technique used to build the likelihood discriminant is the *projective likelihood* (see Equation 4.1), also used for the likelihood-based electron identification, as shown in Section 4.2.1. Similarly to the NN procedure in the $t\bar{t}V$ analysis, a training step is performed to derive the discriminant function, based on the separation between $t\bar{t}$ and the main background, W+jets [2]. This is followed by an evaluation step, applied to data, signal, and all background contributions, to build the template distributions used in the fit. In order to avoid overtraining effects, the $t\bar{t}$ and W+jets MC statistics are split in two; one half used in the training, and the other half in the evaluation step.

The discriminant is constructed from four input variables, chosen based on their power to discriminate the largest background, W+jets, and their sensitivity to the dominant systematic uncertainties. The latter is crucial to be able to constrain the corresponding nuisance parameters in the profile likelihood fit.

The chosen variables are:

- The pseudorapidity of the lepton: η^{ℓ}.
- The p_T of the jet with highest p_T: p_T(leading jet).
- The event aplanarity, $\mathcal{A}$, defined as 1.5 times the smallest eigenvalue of the momentum tensor (see Equation 7.4).
- The variable $H_{T,3p}$, defined as $H_{T,3p} = \frac{\sum_{i=3}^{N_{jets}} |p_{T,i}|}{\sum_{j=1}^{N_{objects}} |p_{z,j}|}$, where the numerator is the sum of the transverse momentum of all jets except the two leading ones, and the denominator is the sum of all the longitudinal momenta in the event. The longitudinal momentum of the neutrino is obtained from solving the event kinematics, and taking the smallest neutrino p_z solution [209].

The variables $H_{T,3p}$ and $\mathcal{A}$ are transformed to $\exp[-4\times H_{\mathrm{T,3p}}]$ and $\exp[-8\times\mathcal{A}]$, respectively, to have a more uniform and smoother distribution for building the likelihood discriminant. Similar

---

[2] Since the analysis does not distinguish between W+light and W+HF jets, and the W+HF samples were simulated with very low MC statistics, only W+light events are used in the training.

to the $t\bar{t}V$ measurement, the number of jets entering the calculation of $H_{T,3p}$ and $\mathcal{A}$ is limited to the four with highest p_T, in order to reduce the dependence on modelling of soft radiation and pile-up.

Figure 10.1 and Figure 10.2 show the η^{μ} and the $\exp[-8\times\mathcal{A}]$ distributions in the μ+jets channel, respectively. Figure 10.3 and Figure 10.4 show the $\exp[-4\times H_{\mathrm{T,3p}}]$ and the leading jet p_T distributions in the $e+$jets channel, respectively. All distributions are shown before the fitting procedure for the signal regions (3, 4, and ≥ 5 jets), and for the control region (2 jets).

The discriminant is evaluated for each physics process, and the corresponding templates are obtained from MC simulation or data, as explained in Section 10.4. Given that the projective likelihood approach assumes that the probability densities of the discriminating input variables are uncorrelated, the correlation between the input variables was studied, observing a maximum linear correlation of $\approx 60\%$ between the $\exp[-8\times\mathcal{A}]$ and the $\exp[-4\times H_{\mathrm{T,3p}}]$ variables in the different analysis regions.

Figure 10.5 shows the discriminating power, between $t\bar{t}$ and W+jets, of the resulting likelihood distribution in each of the six analysis regions. The discriminant templates in each analysis region for each process contain 20 bins, resulting in a combined template of 120 bins.

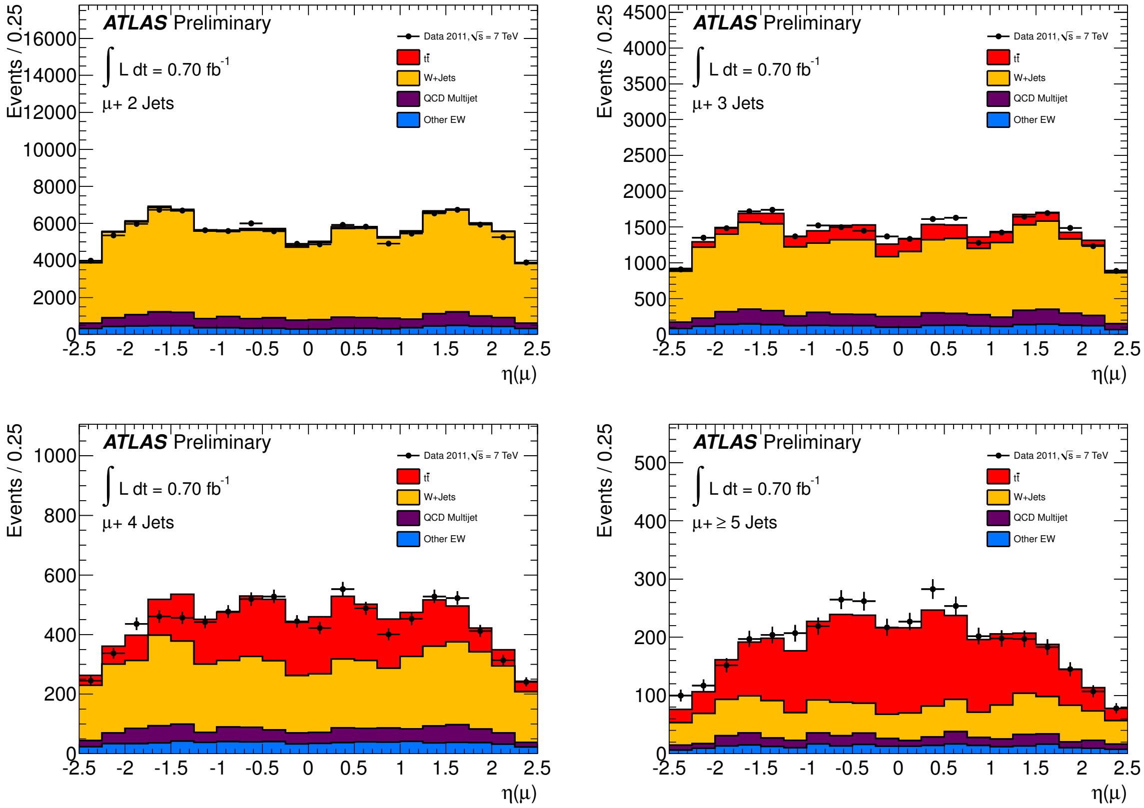

Figure 10.1.: (Top left): the input variable $\eta(\mu)$ for the $\mu+$jets channel in the 2 jets bin control region, and in the signal regions: (top right): 3 jets, (bottom left): 4 jets, and (bottom right): ≥ 5 jets, before the fit procedure.

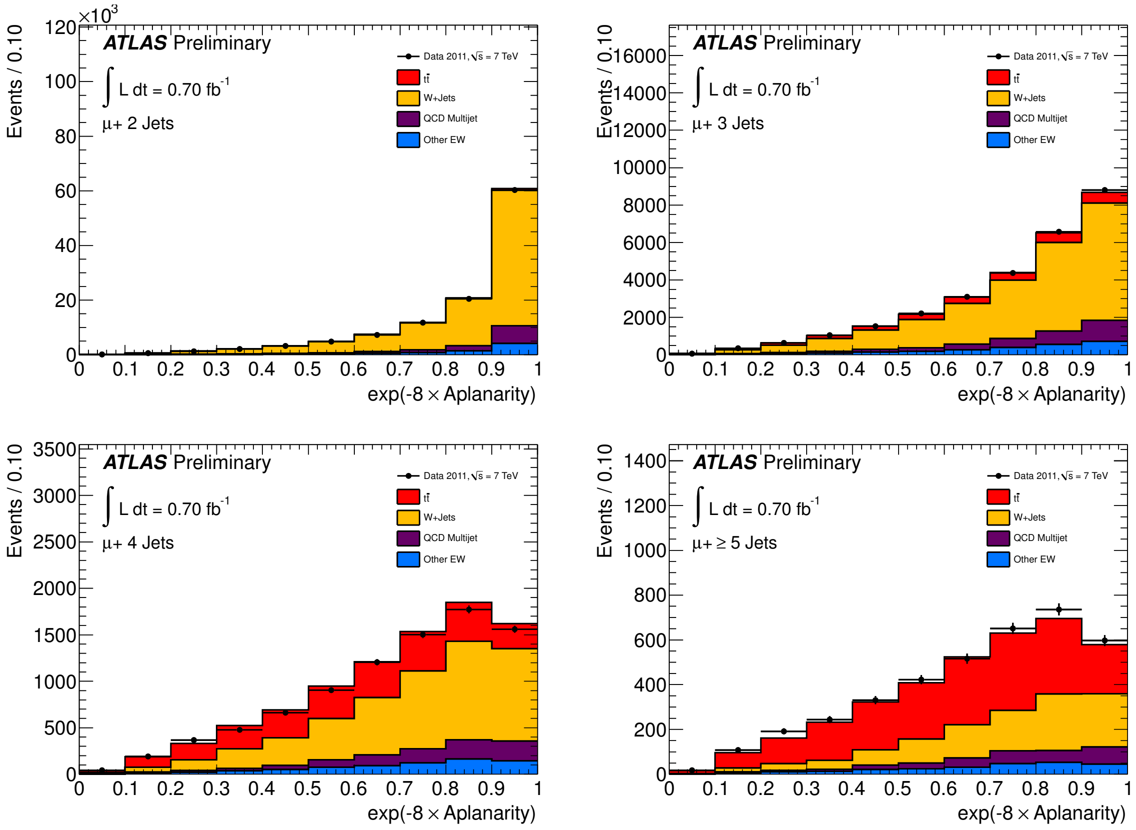

Figure 10.2.: (Top left): the input variable $\exp[-8 \times \mathcal{A}]$ for the $\mu +$jets channel in the 2 jets bin control region, and in the signal regions: (top right): 3 jets, (bottom left): 4 jets, and (bottom right): $\geq$ 5 jets, before the fit procedure.

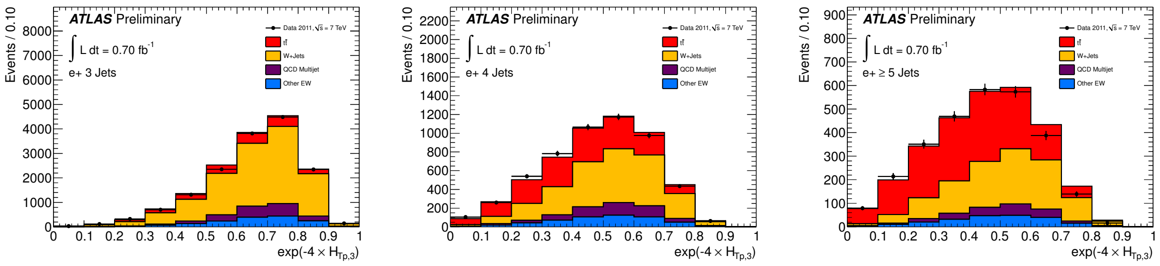

Figure 10.3.: The input variable $\exp[-4 \times H_{\mathrm{T,3p}}]$ for the $e +$jets channel in the signal regions: (left): 3 jets, (middle): 4 jets, and (right): $\geq$ 5 jets, before the fit procedure. The $\exp[-4 \times H_{\mathrm{T,3p}}]$ variable is not defined in the 2 jets control region.

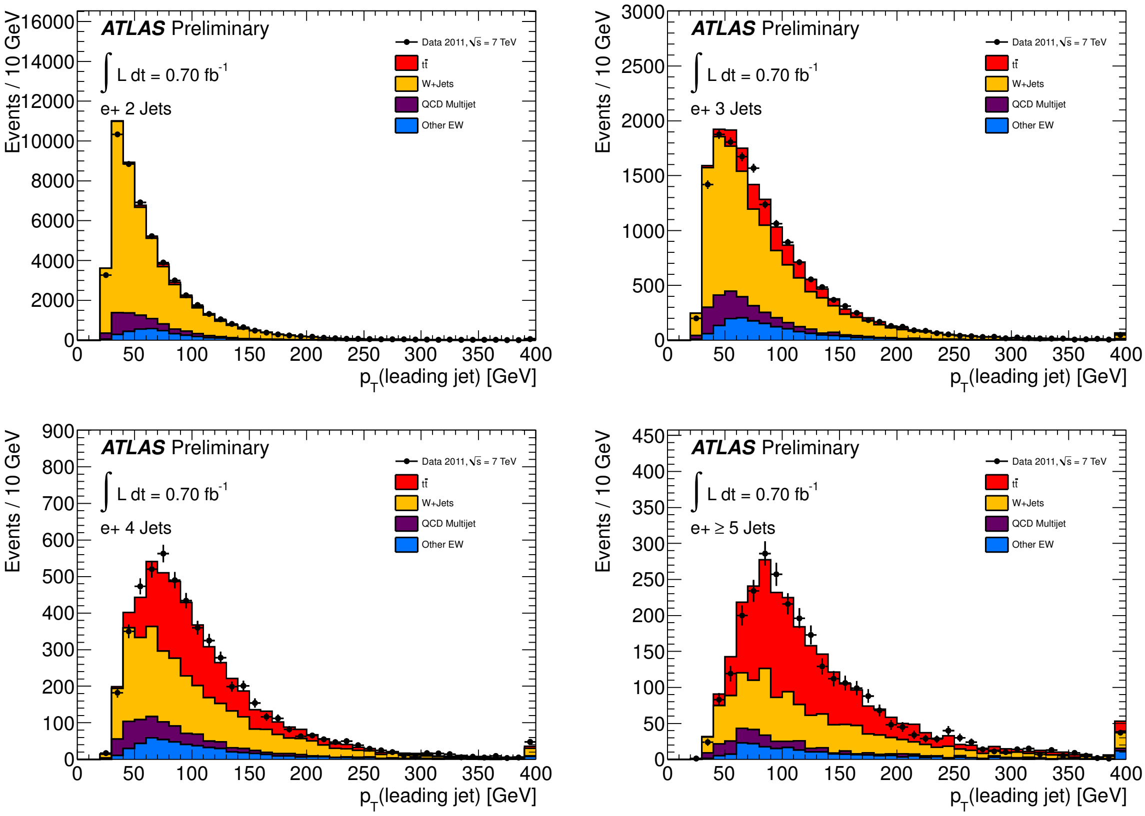

Figure 10.4.: (Top left): the input variable p_T(leading jet) for the $e+$jets channel in the 2 jets bin control region, and in the signal regions: (top right): 3 jets, (bottom left): 4 jets, and (bottom right): ≥ 5 jets, before the fit procedure.

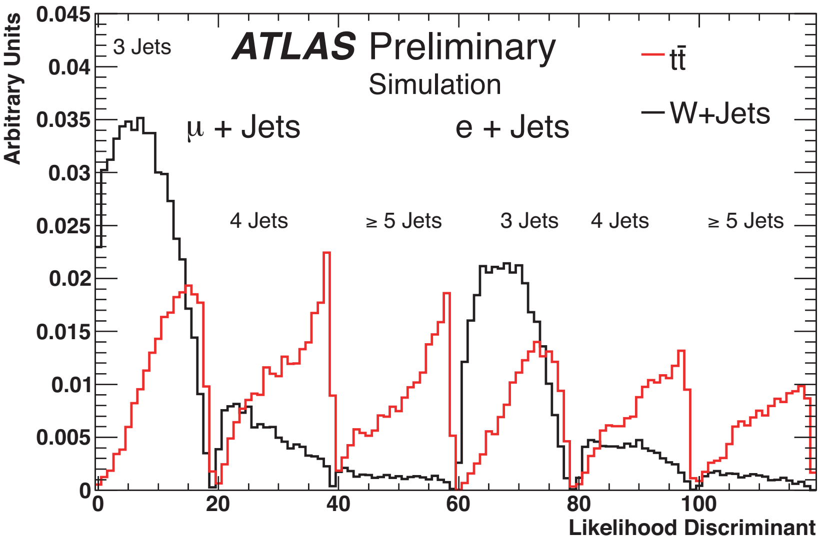

Figure 10.5.: Likelihood discriminant in the $\mu+$jets (3, 4, ≥ 5 jets) and $e+$jets (3, 4, ≥ 5 jets) channels, showing the separation between the $t\bar{t}$ and the W+jets processes.

10.6. The Fit and Results

The $t\bar{t}$ production cross section is extracted by performing a *binned profile likelihood fit* to the discriminant distribution observed in data, using templates with 120 bins for the signal and the background processes. The definition of the likelihood is similar to the one used for the $t\bar{t}V$ cross section measurement (see Equation 8.3), except for the treatment of:

- **Background normalisation parameters:** are described by parameters $\beta_j = \sigma/\sigma_{SM}$ ($j = 1, ..., N_{process}$), constrained by Gaussian distributions with width Δ_j, corresponding to the a priori uncertainty on these parameters. Therefore, their nominal values are centred at 1, whereas in the $t\bar{t}V$ measurement, the normalisation of the background processes was controlled by nuisance parameters related to the uncertainty on the cross section of each process.

- **Template Statistics:** is evaluated outside the fit using pseudo-experiments (PEs), whereas in the $t\bar{t}V$ measurement, the MC statistical uncertainty on each summed-template bin [3] is included in the likelihood as nuisance parameters.

10.6.1. Systematic Uncertainties

In contrast to the treatment in the $t\bar{t}V$ measurement, not all systematic uncertainties are included as nuisance parameters in the fit. Table 10.4 shows a summary of the different systematic uncertainty categories, indicating which are included in the fit as nuisance parameters (NP), or evaluated outside the fit with pseudo-experiments (PE).

The systematic uncertainties related to physics objects are treated as nuisance parameters inside the fit. For leptons, the uncertainties on the electron SFs, energy scale, and energy resolution are considered, as well as the uncertainties on the muon SFs, momentum scale, and resolution in the ID and the MS, treated uncorrelated. The jet energy scale (JES) is also split into several components, coming from the calorimeter response, the η-intercalibration, the noise term, the parton shower model, the underlying event model, the b-jet energy scale, and the pile-up effect. The latter is split into four subcomponents, for the low and high p_T jets, in the central and forward detector region. The uncertainty on the jet energy resolution and the jet reconstruction efficiency are each treated as one NP. The uncertainty on the missing transverse energy is split into two components. One parameter accounts for the uncertainty on the combined soft-jet, cell-out, and pile-up terms. The other accounts for a “missing region” in the LAr calorimeter, due to a full front-end board of the LAr calorimeter which was not useable for analysis during the early 2011 data taking period.

Based on the argument that the treatment of systematic uncertainties as nuisance parameters in the fit assumes their continuous nature, most of the uncertainties related to the modelling of the background and signal processes are evaluated outside the fit by performing pseudo-experiments. These uncertainties include, for the background modelling:

- The variation of the ALPGEN parameters associated with the parton matching threshold (*ptjmin10*: 10 GeV parton p_T threshold, alternative to the default of 15 GeV) and the choice of the factorisation scale (*iqopt2* with a factorisation scale choice of the form m_W^2, alternative to the default $m_W^2 + \sum p_T(\text{jet})$), for the W+jets background process.

---

[3] Sum of the templates of all physics processes.

	Systematic uncertainty	Treatment	Components
Physics Objects	Electron	NP	3
	Muon	NP	4
	Jet energy scale	NP	10
	Jet energy resolution	NP	1
	Jet reconstruction efficiency	NP	1
	E_T^{miss} systematics	NP	2
Sig and Bkg	W+jets modelling: Alpgen scale	PE	1
	QCD multijet modelling	PE	2
	$t\bar{t}$ modelling: generator	PE	1
	$t\bar{t}$ modelling: parton shower	PE	1
	$t\bar{t}$ modelling: ISR and FSR	NP	2
	$t\bar{t}$ PDF	PE	1

Table 10.4.: List of systematic uncertainties considered. "NP" denotes that the uncertainty is included in the likelihood fit as a nuisance parameter, whereas "PE" indicates that the effect of the uncertainty is evaluated outside the fit, with pseudo-experiments. Some of the systematic uncertainties are split into several different components for a more accurate treatment, indicated by the number under the column labeled as "Components".

- The comparison of the default QCD multijet background matrix method model with an alternative model in the e+jets channel based on an inverted electron identification cut [214], and with the same model but using the fake rate from a different control region in the $\mu +$ jets channel.

The signal modelling uncertainties include one related to the generator choice, using Powheg+Herwig as the alternative generator, one related to the parton shower choice, derived by comparing Powheg+Herwig with Powheg+Pythia [4], and one related to the PDF choice, evaluated from the effect of independent error sets of CTEQ66 PDFs on the acceptance and shape of the discriminant. The only systematic uncertainties related to the modelling of physics processes which are included in the fit as nuisance parameters, are those related to the initial and final state radiation modelling in $t\bar{t}$. The ISR and FSR are controlled by the corresponding parameters in Pythia, and the variation of these parameters ensures a continuous increase or decrease of radiation activity in the event.

The justification of including such modelling uncertainties in the fit as nuisance parameters has been extensively discussed. There are two main arguments in favour of profiling such binary systematic uncertainties:

- A priori, it is unknown whether one model or the other, or a model in between, is the one that reproduces data. The only reason why an alternative model "B" is compared to the nominal model "A" in order to asses the corresponding modelling uncertainty, is because those models have been generated as MC samples. But each model has its free parameters, which can be modified internally and yield different discriminant distributions.

---

[4] MC@NLO can not be interfaced with Pythia.

Therefore, if the corresponding nuisance parameter is fitted between these two model values, that is, $0 < |\theta| < 1$, it means that data prefers a model (some specific combination of model parameters) leading to an effect on the fitted discriminant distribution, which lies in between the effect of the nominal and the alternative model.

- Typically models are different in three aspects: the normalisation per jet multiplicity bin, the discriminant shape in each fit region, and the flavour composition of additional jets. As shown for the $t\bar{t}V$ measurement in Section 8.2, those modelling-related systematic uncertainties with a significant effect on the shape and/or the normalisation per jet bin are split into different components, and treated as uncorrelated in the fit. In this way, profiling one model with respect to the other is split into the different effects, so that data has enough freedom to disentangle them and prefer one model over the other for each effect separately.

As mentioned before, the a priori uncertainty on the normalisation of the background processes is included as the standard deviation, Δ_j, in the Gaussian constraint of the β_j parameters. Given that each of the six fit regions correspond to a different jet multiplicity, and that the W+jets MC is not expected to perfectly describe their relative normalisations, six different normalisation parameters are assigned to each of the six W+jets templates in the fit. The corresponding Δ_j Gaussian constraints are motivated by the Berends scaling, with a magnitude of 42% in the e/μ+3 jets fit region, 48% in the e/μ+4 jets fit region, and 54% in the e/μ $\geq$5 jets fit region. The Berends scaling states that the ratio of the number of $W + n$ jets events to the number of $W + (n + 1)$ jets events is expected to be approximately constant as a function of n [215, 216]. Therefore, the number of W events in the n-jet sample, $N_W^{n-\text{jets}}$, can be estimated as:

$$N_W^{n-\text{jets}} = N_W^{2-\text{jets}} \cdot \sum_{i=2}^{n} \left(\frac{N_W^{2-\text{jets}}}{N_W^{1-\text{jet}}} \right)^i . \tag{10.5}$$

The uncertainty on this assumption is found to be 24%. Extrapolating this uncertainty to higher jet multiplicities results in the aforementioned uncertainties in each fit region. The Berends scaling and the uncertainty of modelling the relative normalisation across jet multiplicities also applies to Z+jets. This was the first approach used in the $t\bar{t}V$ analysis, to assign an uncertainty on the extrapolation of the initial 4% theory uncertainty to higher jet multiplicities in Z+jets. Nevertheless, it was replaced by a better physics-motivated uncertainty, based on the variation of the parameter controlling the renormalisation scale in ALPGEN, *ktfac*, and resulting in a similar uncertainty per jet multiplicity. In the context of the $t\bar{t}$ cross section measurement, the Z+jets background contribution is much smaller than the W+jets one, and its normalisation is therefore described with one fit parameter, with a theoretical uncertainty of 30%, with a Gaussian constraint. Single top and diboson templates are treated as correlated across the different fit regions, and each one has an assigned fit parameter with the theoretical uncertainty of 10% and 5%, respectively. Finally, the QCD multijet templates are treated uncorrelated across fit regions, assigning six different fit parameters, β_j, with a 50% uncertainty on each, from the matrix method estimate.

10.6.2. Expected Fit Performance

The Asimov dataset used in the $t\bar{t}V$ measurement to estimate the expected fit performance has been only recently proved to be formally mathematically justified [196]. Therefore, in the early $t\bar{t}$ cross section measurement, pseudo-experiments are used to test the performance and stability of the fit. The pseudo-data of a fit distribution is created from the sum of predicted events for each physics process in each bin of the distribution. In order to take into account the statistical and systematic uncertainties, the following steps are performed:

- The prediction per process and bin is drawn from a random Poisson distribution, with a mean equal to the original prediction.
- Random shifts of the background normalisation parameters, β_j $(j > 0)$, and the nuisance parameters, θ_i, are applied, following a Gaussian distribution with the corresponding $\pm 1\sigma$ (or Δ_j for the β_j parameters) pre-fit uncertainty as standard deviation. The vertical template morphing is used to propagate the changes of the nuisance parameters into the template distribution (see Section 8.1). The Gaussian distribution is truncated at $\pm 1.25\sigma$, since the knowledge on the behaviour of the parameters beyond that value is limited.

The expected uncertainty is estimated from an ensemble test with 1000 pseudo-experiments, by fitting the same templates that are later fitted to data in each PE. The parameter of interest, β_0, representing the $t\bar{t}$ cross section normalised to the SM prediction, is extracted from the fit to each PE, and the average spread of this parameter corresponds to the total expected uncertainty of the measurement. The total expected uncertainty is measured to be 3.6%. The expected statistical uncertainty is measured in a similar way, but without including the nuisance parameters in the PEs, nor in the fit, resulting in a statistical uncertainty of 2.2%. An estimate of the expected systematic uncertainty is extracted from the quadratic subtraction of the total expected uncertainty minus the expected statistical uncertainty. No significant bias is seen in the fitted β_0.

10.6.3. Fit to Data

The combined profile likelihood fit of the six analysis regions to the likelihood discriminant distribution in data is performed, including the systematic uncertainties treated as nuisance parameters shown in Table 10.4, and yields a $t\bar{t}$ production cross section of:

$$\sigma_{t\bar{t}} = 179.0^{+7.0}_{-6.9}\,(\mathrm{stat}+\mathrm{syst}) \pm 6.6\,(\mathrm{lumi})\,\mathrm{pb}\,. \tag{10.6}$$

An uncertainty on the luminosity of 3.7% is added in quadrature to the post-fit uncertainty. The result of the fit is shown in Fig. 10.6 and indicates an excellent agreement between data and the fitted background, as well as the $t\bar{t}$ signal model.

Figure 10.7 shows the profile likelihood curve as a function of β_0, for the combined fit and for separate fits in the $e+\mathrm{jets}$ and $\mu+\mathrm{jets}$ channels. It can be seen that the fitted $t\bar{t}$ cross section in the $\mu+\mathrm{jets}$ channel is slightly higher than in the combined fit, but both are consistent within uncertainties.

The fitted central values and errors of the nuisance parameters are shown in Figure 10.8. The post-fit central values of the nuisance parameters are, on average, centred around the nominal value, $\theta = 0$. Slight differences in the pulls of the jet-related nuisance parameters are seen across the different fits, which are explained by internal correlations or the need to improve the agreement between data and simulation in certain regions. As expected from the usage of the leading jet p_T as an input variable for building the discriminant, most of the uncertainties related to the jet energy scale are constrained after the fit procedure. Also, since the fit regions are split into jet multiplicity bins, the fit is also sensitive to uncertainties affecting the migration of events across regions, such as ISR and FSR, and has therefore the power to constrain the corresponding nuisance parameters.

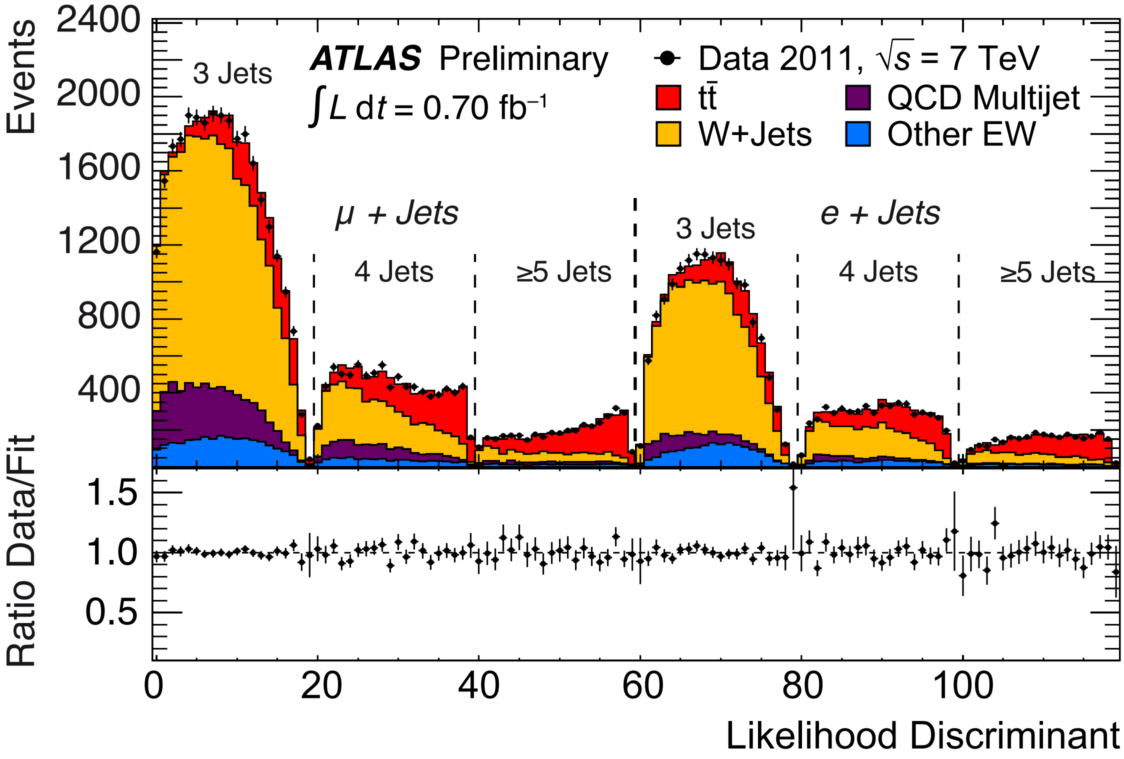

Figure 10.6.: Result of the combined fit to data in the exclusive three-jet bin, the exclusive four-jet bin, and the inclusive five-jet bin of the $e+$jets and $\mu+$jets channels. The lower plot shows the ratio of data to the sum of the fitted signal and background contributions. Uncertainties on the ratio include data and MC statistical uncertainties.

The contribution from the remaining systematic uncertainties, which are not included in the fit, are estimated from pseudo-experiments. In this case, the PEs are drawn as described in Section 10.6.2, but shifting the template of the corresponding systematic uncertainty according to the $\pm 1\sigma$ variation, that is, replacing the nominal template with the alternative model. Each systematic uncertainty on the $t\bar{t}$ cross section is extracted by taking the difference between the average fit result of β_0 in the corresponding modified setup, and the one in the nominal setup. Finally, these systematic uncertainties are added in quadrature to the uncertainties obtained in the fit to data.

After including the *out-of-fit* uncertainties, $\sigma_{t\bar{t}}$ is measured to be:

$$\sigma_{t\bar{t}} = 179.0 \pm 3.9\,(\mathrm{stat}) \pm 9.0\,(\mathrm{syst}) \pm 6.6\,(\mathrm{lumi})\,\mathrm{pb} = 179.0 \pm 11.8\,\mathrm{pb}.$$

Table 10.5 displays the effects of various sources of uncertainties on the measurement. To quantify the effect of individual systematic uncertainties included via nuisance parameters in the fit on the total $\sigma_{t\bar{t}}$ uncertainty, the nuisance parameter corresponding to the systematic uncertainty under study is fixed to its fitted value. The quadratic difference in relative uncertainty between the two fits is taken as a measure of the individual contribution to the total uncertainty. This approach is, in principle, different to the one used in the $t\bar{t}V$ measurement, where

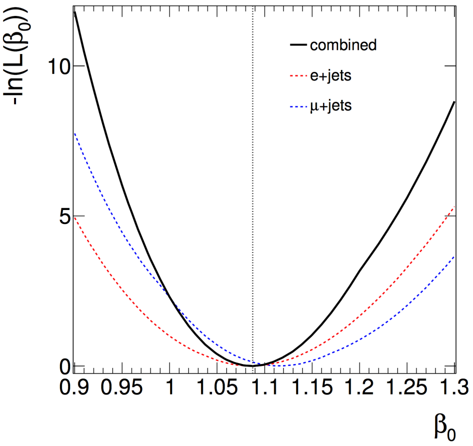

Figure 10.7.: Profile likelihood curve, $-\ln\lambda(\beta_0)$, as a function of the parameter of interest, β_0, for the six-region-combined fit (black solid line), as well as for the fit in the $e+$jets channel (red dashed line), and $\mu+$jets channel (blue dashed line) only. The vertical line indicates the fit result for the combined fit [217].

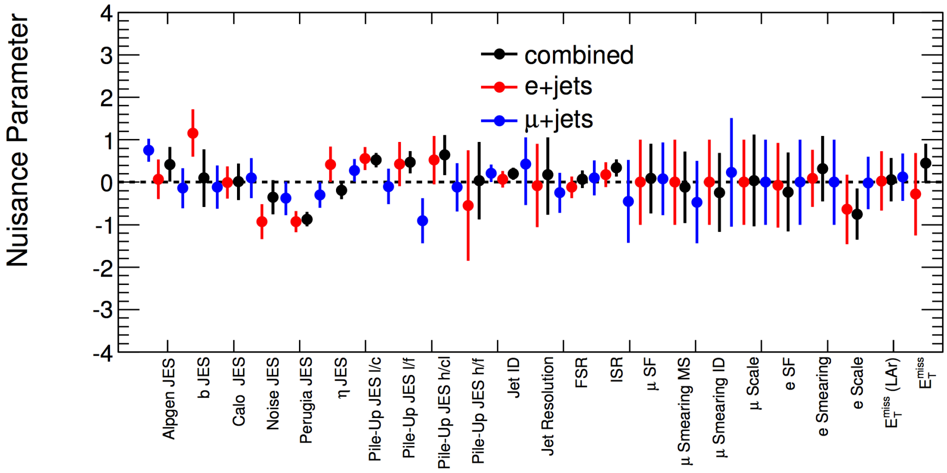

Figure 10.8.: Post-fit central values and errors of each nuisance parameter, with respect to the pre-fit values, $\theta_i = 0 \pm 1$, shown in the $y - axis$ for comparison. The fit results are shown for the combined fit (black), for the individual fit in the $e+$jets channel (red), and for the individual fit in the $\mu+$jets channel (blue). There is, in general, a good agreement between the individual results and the combined one [217].

the nuisance parameters are fixed to the post-fit $\pm 1\sigma$ and the maximum difference between the fitted signal strength is taken as the post-fit effect of that systematic uncertainty. However, both methods give similar results in practice. A fit to data performed without nuisance parameters is used to estimate the statistical uncertainty.

The largest contribution to the systematic uncertainty on the measured $\sigma_{t\bar{t}}$ comes from the choice of the signal MC generator, followed by the uncertainties on the jet energy scale calibration, the muon identification efficiency, and the modelling of initial and final state radiation. Similar to the $t\bar{t}V$ measurement, the uncertainty on the modelling of the $t\bar{t}$ process is one the

Uncertainty	up (pb)	down (pb)	up (%)	down (%)
Statistical	3.9	−3.9	2.2	−2.2
Detector simulation				
Jets	3.2	−4.3	1.8	−2.4
Muon	4.1	−4.1	2.3	−2.3
Electron	2.7	−3.0	1.5	−1.7
E_T^{miss}	2.0	−1.6	1.1	−0.9
Signal model				
Generator$^{*)}$	5.4	−5.4	3.0	−3.0
Parton Shower$^{*)}$	0.9	−0.9	0.5	−0.5
ISR/FSR	3.0	−2.3	1.7	−1.3
PDF$^{*)}$	1.8	−1.8	1.0	−1.0
Background model				
QCD shape$^{*)}$	0.7	−0.7	0.4	−0.4
W shape$^{*)}$	0.9	−0.9	0.5	−0.5
MC statistics$^{*)}$	3.2	−3.2	1.8	−1.8
Systematic	9.0	−9.0	5.0	−5.0
Stat. & Syst.	9.8	−9.8	5.4	−5.4
Luminosity	6.6	−6.6	3.7	−3.7
Total	11.8	−11.8	6.6	−6.6

Table 10.5.: Table of estimated statistical and systematic uncertainties on the $t\bar{t}$ cross section. Uncertainties marked with $^{*)}$ are evaluated outside the fit.

dominant components of the total systematic uncertainty, especially if the corresponding systematics are not allowed to be constrained by data in the fit, as in the presented $t\bar{t}$ cross section measurement. In contrast to the JES and ISR/FSR uncertainty contributions, to which the discriminant is sensitive, and which are constrained in the fit, the muon identification efficiency uncertainty affects mostly the rate, and cannot be constrained by the data. Since its pre-fit effect is quite large, due to the large uncertainty on the modelling of the muon trigger, it is one of the largest contributions in the breakdown of post-fit effects of the systematic uncertainties.

Similar to the $t\bar{t}V$ measurement, the result of the fit is also tested by modifying the MC samples according to the fitted values of the systematic uncertainties and the event yields, θ_i and β_j, respectively, and comparing this new model, corresponding to the output of the fit, to data. Figures 10.9 to 10.14 show examples of post-fit distributions in each of the six fit regions. A significant improvement in the agreement between data and the model is observed, not only for the input variables distributions, used to built the discriminant, but also for other distributions, such as E_T^{miss} and $m_T(W)$. The yellow error band in the ratio of the figures shows the uncertainty from MC statistics. Uncertainties on the ratio points include data and MC statistical uncertainties.

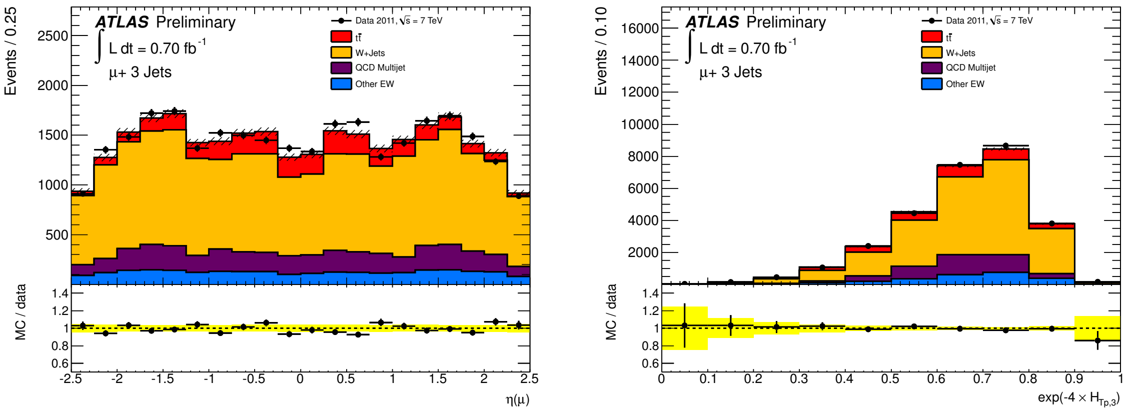

Figure 10.9.: Data-MC comparison of (left): the muon η and (right): $\exp[-4 \times H_{\mathrm{T,3p}}]$ after the fit procedure for the exclusive μ+3 jets channel.

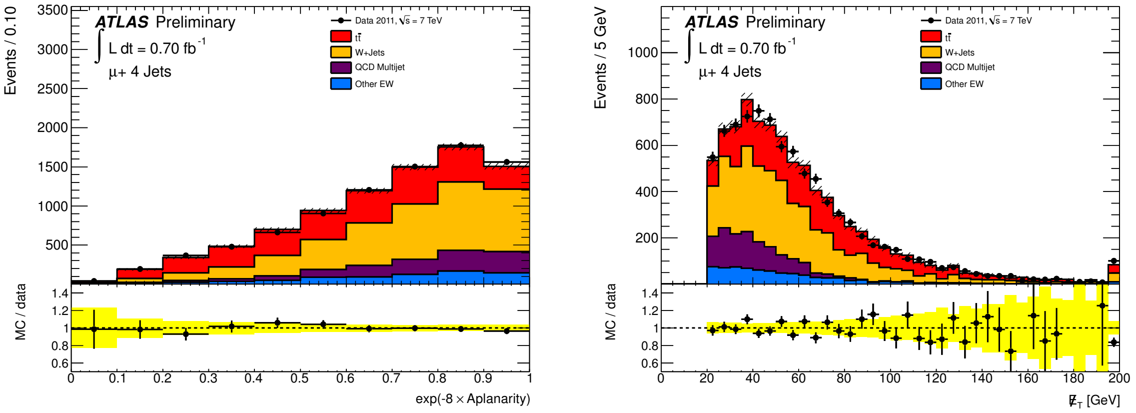

Figure 10.10.: Data-MC comparison of (left): $\exp[-8 \times \mathcal{A}]$ and (right): E_T^{miss} after the fit procedure for the exclusive μ+4 jets channel. The last bin of the right plot includes overflow.

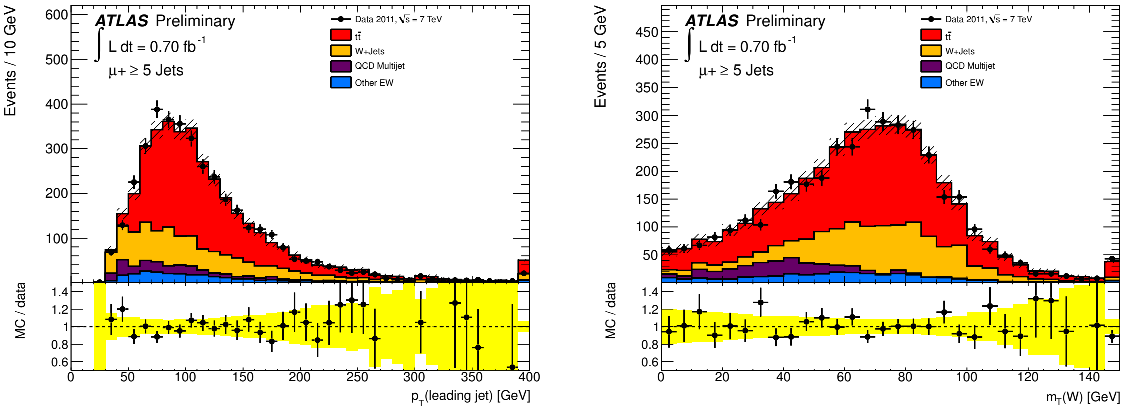

Figure 10.11.: Data-MC comparison of (left): the leading jet p_T and (right): W-boson transverse mass after the fit procedure for the inclusive μ+5 jets channel. The last bin includes overflow.

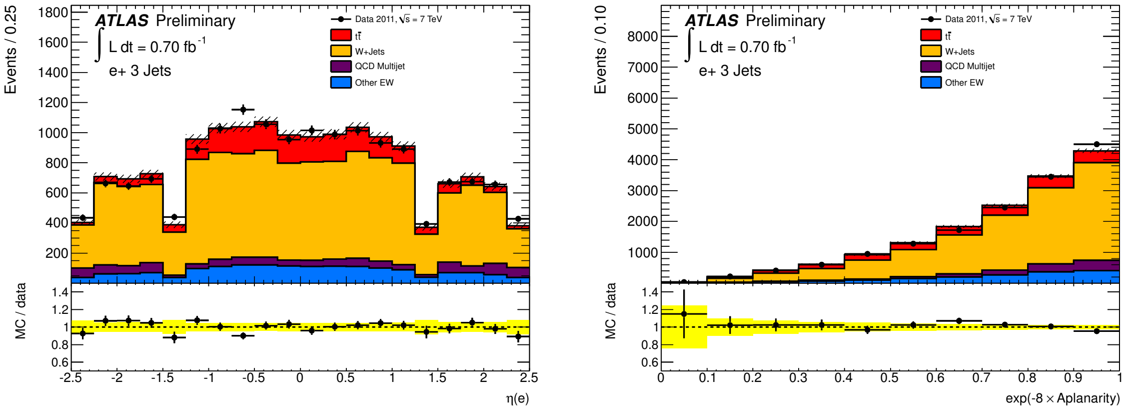

Figure 10.12.: Data-MC comparison of (left): the electron η and (right): $\exp[-8 \times \mathcal{A}]$ after the fit procedure for the exclusive e+3 jets channel.

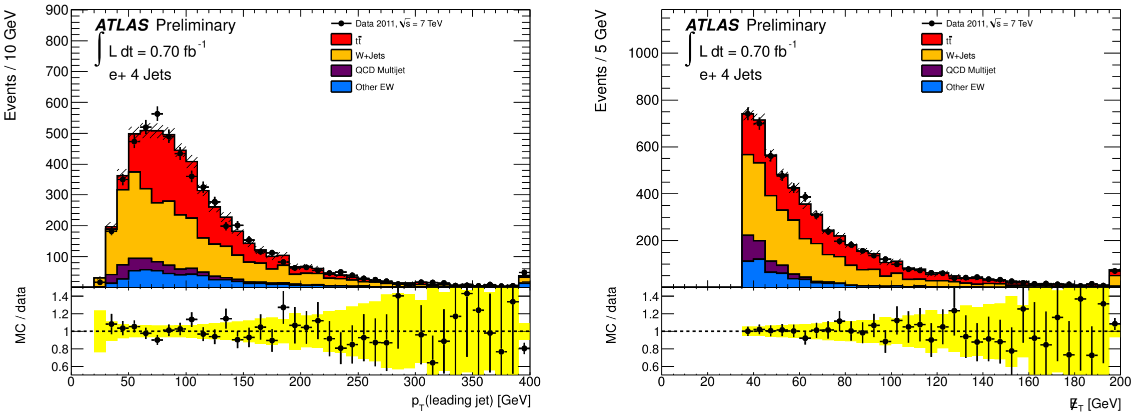

Figure 10.13.: Data-MC comparison of (left): the leading jet p_T and (right): E_T^{miss} after the fit procedure for the exclusive e+4 jets channel. The last bin includes overflow.

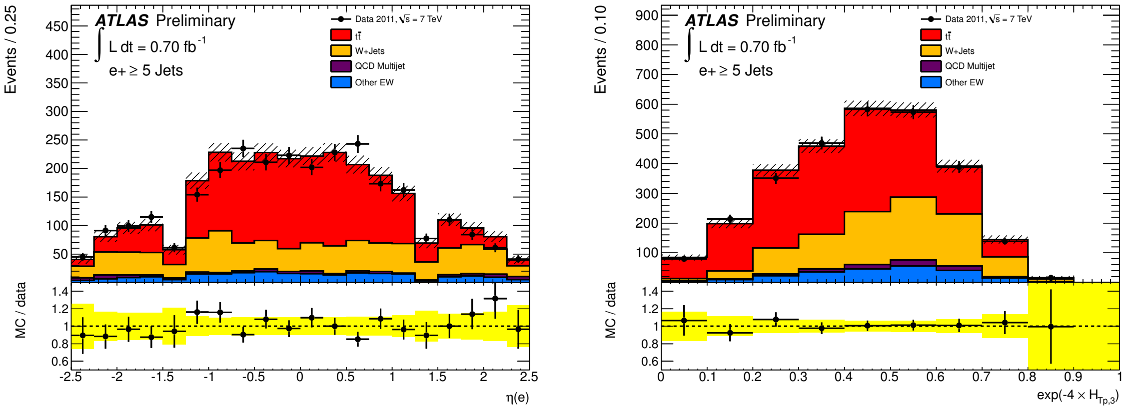

Figure 10.14.: Data-MC comparison of (left): the electron η and (right): $\exp[-4 \times H_{\mathrm{T,3p}}]$ after the fit procedure for the inclusive e+5 jets channel.

Since the $t\bar{t}$ acceptance depends on the assumed m_{top}, the dependence of the measured cross section on the assumed top quark mass in the MC samples is studied, by replacing the default $t\bar{t}$ and single top samples generated with a top quark mass of $m_t = 172.5$ GeV, with the corresponding samples generated at different masses. In the range of masses between 160 GeV and 190 GeV, the dependence of the cross section on the MC mass is well-described by a linear function, as shown in Figure 10.15: $\sigma_{t\bar{t}} = 411.9 - 1.35 \times m_{top}(\text{GeV})$ pb.

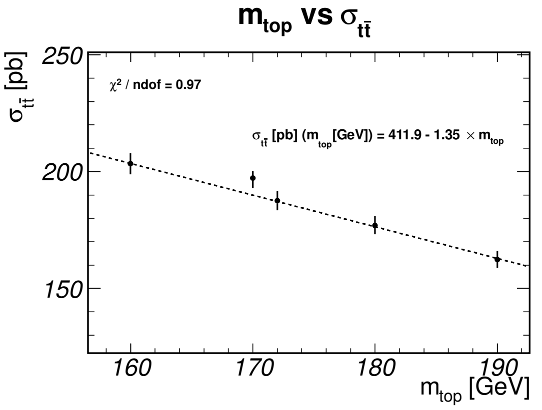

Figure 10.15.: The $t\bar{t}$ cross section ($y-axis$) as a function of input top quark mass in MC ($x-axis$) in the narrow range around the world average top quark mass (160 GeV - 190 GeV).

10.7. Conclusions

The $t\bar{t}$ production cross section was measured in the ℓ+jets channel at $\sqrt{s} = 7$ TeV from a binned profile likelihood fit, exploiting kinematic event information to separate signal from background. The measured $t\bar{t}$ cross section, $\sigma_{t\bar{t}} = 179.0 \pm 11.8\,\text{pb}$, is in agreement with the approximate [5] NNLO QCD theoretical prediction available at the time, $\sigma_{t\bar{t}}^{\text{theory}} = 165^{+11}_{-16}\,\text{pb}$ [218, 219, 220]. The experimental precision of 6.6% exceeds the theoretical calculation precision of 10%. The accuracy of the prediction is denoted as "approximate" NNLO, since at the time, only the exact NLO matrix element calculation existed, adding to it several additional terms, such as NNLL enhancements at the threshold, corrections from Coulomb terms in two loops, and scale dependent terms at NNLO. A top quark mass of $m_t = 172.5$ GeV is used in the calculation, as well as the CTEQ66 PDF set.

High-precision $t\bar{t}$ cross section measurements from the Tevatron and LHC, such as the one presented in this chapter, motivated the increasing need of more precise $t\bar{t}$ cross section theoretical predictions. A new era of full NNLO calculations allowed to decrease the theoretical uncertainty to the level of the experimental precision. An illustrative summary of the evolution of the theoretical $t\bar{t}$ cross section predictions at $\sqrt{s} = 8$ TeV at fixed orders in QCD, complemented with additional logarithmic soft-gluon resummation terms, is shown in Figure 10.16. The $x-axis$ corresponds to the year when a calculation became available. The last entry corresponds to the NNLO+NNLL QCD calculation, equivalent to the one used in the $t\bar{t}V$ measurement [6]. The

---

[5] By the time of the $t\bar{t}V$ measurement, the full NNLO prediction was available, as described in Section 2.3.1.

[6] The calculations shown in Figure 10.16 use a $m_t = 173.3$ GeV, whereas the calculation used in the presented $t\bar{t}V$ and $t\bar{t}$ analysis uses a $m_t = 172.5$ GeV

equivalent calculation at $\sqrt{s} = 7$ TeV of the third red entry from the left, NLO+NNLL, corresponds to the approximate NNLO calculation. It can also be seen that the convergence of the perturbative expansion is preserved after including the soft-gluon resummation terms. The figure shows the long-term effort of the theoretical community to provide high precision $t\bar{t}$ cross section calculations.

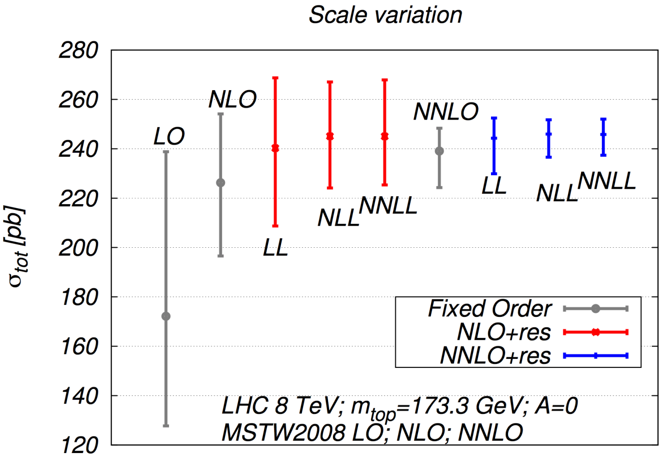

Figure 10.16.: Evolution of the $t\bar{t}$ cross section theoretical predictions with the corresponding scale uncertainty, shown in the $y - axis$, at different orders in perturbative QCD and with different soft-gluon resummation logarithm accuracy. A top quark mass of $m_t = 173.3$ GeV is used for the calculations, and the accuracy of the PDF set used matches the accuracy of the fixed order result in each case [221].

Using the same settings and methods presented in Section 2.3.1 for the full NNLO+NNLL $t\bar{t}$ cross section calculation at $\sqrt{s} = 8$ TeV, the predicted full NNLO+NNLL $t\bar{t}$ cross section at $\sqrt{s} = 7$ TeV is:

$$\sigma_{t\bar{t}} = 177^{+10}_{-11} \text{ pb}. \tag{10.7}$$

This value is much closer to the measured $t\bar{t}$ cross section presented in this thesis, than the one provided by the approximate NNLO QCD prediction. The full NNLO+NNLL theoretical uncertainty is reduced to approximately 6%. A summary of all $t\bar{t}$ cross section measurements performed by the ATLAS and CMS Collaborations at $\sqrt{s} = 7$ TeV up to July 2014, is presented in Figure 10.17, and compared to the aforementioned described full NNLO+NNLL QCD calculation. The first entry from the top corresponds to the presented $t\bar{t}$ cross section measurement. This measurement was combined with the $t\bar{t}$ cross section measured in the dilepton and all-hadronic (all-jets) channels, using an integrated luminosity of 0.7 fb^{-1} and 1.02 fb^{-1}, respectively [222]. The combined result is shown in the fourth entry from the top in the figure. Although later $t\bar{t}$ cross section measurements using more data at $\sqrt{s} = 7$ TeV in the dilepton channel achieved a higher precision, the presented $t\bar{t}$ cross section measurement remains the most precise cross section measurement in the ℓ+jets channel at $\sqrt{s} = 7$ TeV.

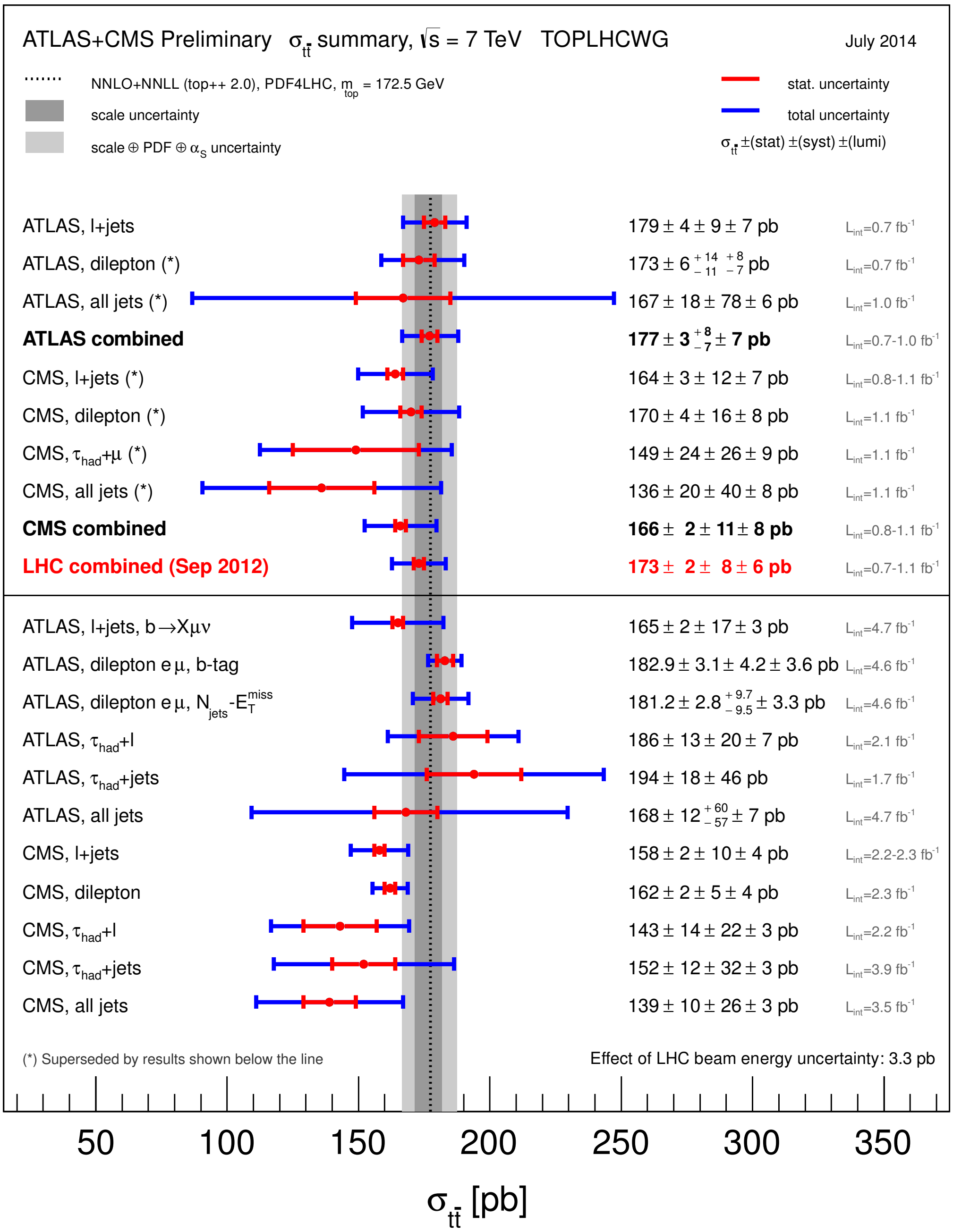

Figure 10.17.: Summary of the $t\bar{t}$ cross section measurements at the LHC at $\sqrt{s} = 7$ TeV until July 2014. The vertical grey dashed line shows the central value of the full NNLO+NNLL QCD prediction, and the dark and light grey bands correspond to the scale and to the total (renormalisation and factorisation scale, parton density functions and the strong coupling) uncertainty on the theoretical calculation, respectively. The measurements and the theory calculation are quoted at $m_t = 172.5$ GeV. The upper part shows early LHC measurements and their combination, where the first entry from the top corresponds to the $t\bar{t}$ cross section measurement presented in this thesis. The lower part summarises measurements performed after the LHC cross section combination [223].

The measurement of the inclusive $t\bar{t}$ cross section is useful for several reasons. From the dependence of the measured cross section on the MC top quark mass, and the comparison to the theoretical predictions, the top quark mass defined in the minimal subtraction ($\overline{\text{MS}}$) scheme, $m_t^{\overline{\text{MS}}}$, can be extracted. The $\overline{\text{MS}}$ top quark mass, contrary to the ambiguously-defined MC top quark mass, m_t, measured typically directly from fits to MC templates, is a *running* mass, defined at a hard scale of the process, μ, in analogy to the running coupling, $\alpha_S(\mu)$. From the extracted $m_t^{\overline{\text{MS}}}(m_t)$ from the $t\bar{t}$ cross section measurement [7], the *pole* or "on-shell" top quark mass, m_t^{pole}, can be calculated. With the latter, the electroweak vacuum stability constraint can be calculated, as done in Ref. [224]. The combined ATLAS $t\bar{t}$ cross section result at $\sqrt{s} = 7$ TeV [222] is also used in that study to extract the $m_t^{\overline{\text{MS}}}(m_t)$ for different PDF sets. Other theoretical studies used the combined ATLAS $\sigma_{t\bar{t}}$ result at $\sqrt{s} = 7$ TeV, together with complementary Tevatron and CMS top pair data, to directly constrain the gluon PDF, observing a significant reduction in the uncertainty at large x [225]. Figure 10.18 shows the improvement in the gluon PDF uncertainties from the NNPDF2.3 global fit after including the top quark data from the Tevatron and LHC (left), and from the NNPDF2.1 HERA-only fit after including the top quark data from the LHC (right). Since the NNPDF2.3 global fit already includes data from gauge boson production and inclusive jet cross sections, the reduction in uncertainties on the gluon PDF is more pronounced in the case of NNPDF2.1 HERA-only, where only deep-inelastic scattering data was included.

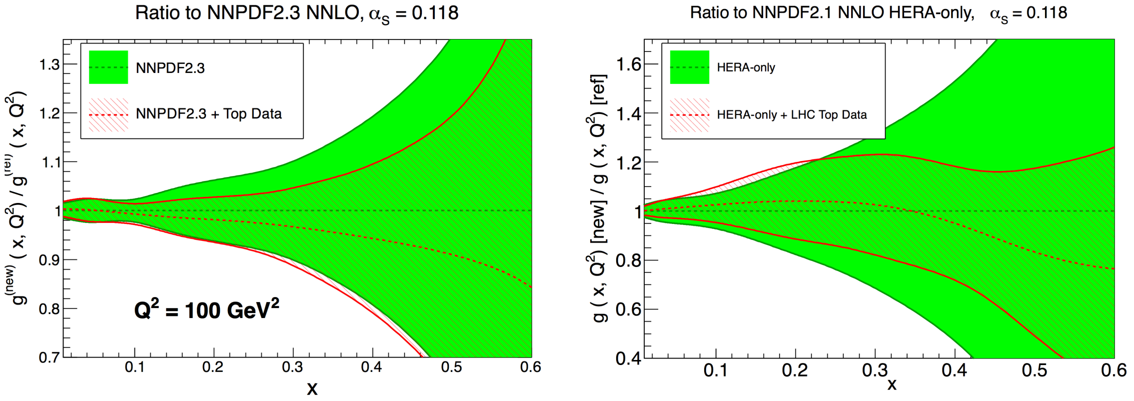

Figure 10.18.: (Left): the ratio of the NNPDF2.3 NNLO gluon PDF at $q^2 = 100$ GeV^2 between the default fit and after including the Tevatron and LHC top quark cross section data. (Right): the ratio of the NNPDF2.1 HERA-only gluon PDF between the default fit and after including the LHC top quark data [225].

Although many efforts have been dedicated to increasing the experimental precision of the inclusive $t\bar{t}$ cross section, there is an increasing interest from both the experimental and theoretical community to perform *differential* $t\bar{t}$ cross section measurements, which are feasible with the large amount of top pairs produced at the LHC. The measurement of the differential $t\bar{t}$ cross section as a function of event kinematics or the jet multiplicity, unfolded to the parton level after QCD radiation, allows the comparison with MC generator predictions and NLO QCD calculations. Two $t\bar{t}$ differential cross section measurements at $\sqrt{s} = 7$ TeV in ATLAS have been already introduced in the previous sections: the $t\bar{t}$ differential cross section as a function of top

---

[7] The $m_t^{\overline{\text{MS}}}(m_t)$ can be determined from the mass dependence of any observable measured precisely enough, and theoretically predicted beyond LO in QCD.

and $t\bar{t}$ kinematics [170], and the $t\bar{t}$ differential cross section as a function of the jet multiplicity and the jet p_T [212]. The former was used to derive the top and $t\bar{t}$ p_T corrections applied to the $t\bar{t}$ background in the $t\bar{t}V$ analysis. The latter showed the poor modelling from MC@NLO at high jet multiplicity, motivating the usage of Powheg+Pythia as the default $t\bar{t}$ MC generator. Differential $t\bar{t}$ cross section measurements provide a better understanding of the performance of each $t\bar{t}$ MC generator in different kinematic regions, and allow theorists to revisit and improve the settings of the MC generators.

CHAPTER 11

Conclusions

The work in this thesis was developed during approximately the same period of time as the first very successful run of the LHC. This gave the unique advantage of witnessing the evolution of the physics programme at the LHC as the results were being announced: living the fantastic flexible nature of knowledge, updating itself as more data was analysed.

Just after the rediscovery of the top quark at the LHC, a precision measurement of the top quark pair production cross section was performed with the first 0.7 fb^{-1} of data collected with the ATLAS experiment at $\sqrt{s} = 7$ TeV. The measured $t\bar{t}$ cross section of $\sigma_{t\bar{t}} = 179.0 \pm 11.8\,\text{pb}$ in the ℓ+jets channel, exceeded, with an experimental precision of 6.6%, the precision of the theoretical calculation at the time. In this way, the highly precise measurements of the top quark pair production cross section and top quark properties motivated an improvement of the theoretical calculations. This highlights the necessity of a very open and close communication between both experiment and theory, leading to the progress in the understanding of the physics with an increase of experimental knowledge.

The breakthrough of the Higgs discovery in the combination of several search channels, announced by both ATLAS and CMS experiments on the 4th of July 2012, shook the ground of particle physics: it redefined the research priorities, and opened new promising directions of research in High Energy Particle Physics. The $t\bar{t}Z$ and $t\bar{t}W$ processes were not measured at the time by ATLAS, and they constitute an important and irreducible background of one of the still missing channels to observe the Higgs boson, $t\bar{t}H$. Furthermore, the $t\bar{t}Z$ process offers the unique opportunity to measure directly the neutral current top quark coupling, and thus provides access to the measurement of the third component of the weak isospin of the top quark. A challenging channel for the $t\bar{t}V$ search was chosen, the opposite-sign dilepton channel, with a very small signal contribution compared to the overwhelming background. The implementation of advanced multivariate techniques, such as a NN, together with a careful design of the fit regions and the usage of a profile likelihood fit to extract the signal cross section and reduce the uncertainties, allowed to extract a competitive and complementary result from this channel, which improved the combination. Since this channel is, by design, sensitive to both $t\bar{t}Z$ and $t\bar{t}W$ processes, it motivated the simultaneous measurement of both processes, without any assumptions made about the other production. The combined simultaneous measurement, performed at $\sqrt{s} = 8$ TeV with the full dataset of 20.3 fb^{-1}, shown in Figure 11.1, corresponds to an observed 3.1 standard deviations excess over the null hypothesis for each $t\bar{t}Z$ and $t\bar{t}W$

processes individually. This measurement gave ATLAS evidence, for the first time, of both $t\bar{t}Z$ and $t\bar{t}W$ processes.

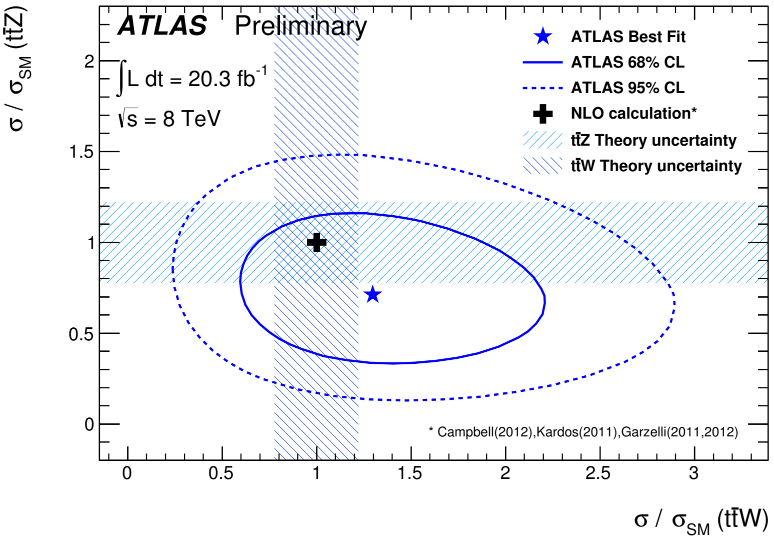

Figure 11.1.: The result of the combined simultaneous fit of the $t\bar{t}Z$ and $t\bar{t}W$ signal strengths along with the 68% CL and 95% CL uncertainty contours. The dashed area corresponds to the 22% uncertainty on the NLO QCD theoretical calculations of $\sigma(t\bar{t}Z)$ and $\sigma(t\bar{t}W)$.

Despite the impressive developments in the accuracy of the theoretical description of the physics processes, the modelling of the $t\bar{t}$ production is still a limiting factor in many top quark related measurements. There are also deficiencies in modelling of the well-known Z+jets process. Provisional corrections are being applied, but only a thorough understanding of the physics behind the mismodelling effects will allow for a reliable simulation of the process.

No deviations from the SM predictions have been observed so far. However, this is just the beginning of the study of the top quark coupling to vector bosons, in particular to the Z-boson, and more precise results are expected at higher luminosity and higher centre-of-mass energy. The second run of the LHC, starting in 2015, will bring particle physics to the next stage of high energy collisions, will provide more top quark pair data, will allow for more precise measurements, and will challenge physicists with more extreme kinematics. And possibly, with some luck, the second run of the LHC may have some unexpected and yet unknown physics prepared for the particle physics community, that continue to attempt to answer the most fundamental questions about the origin of matter. The playground is ready.

APPENDIX A

Validation of NN variables

The input variables used in the multivariate discriminant (NN) are checked to be well modelled by the MC simulation in the regions of interest.

- Figures A.1-A.4 show the distribution in data and MC of the input variables used in the two signal regions in the 2ℓOSZveto region, $(4\text{j}, 1\text{b}+2\text{b})$ and $(\geq 5\text{j}, 1\text{b}+2\text{b})$, evaluated in events with exactly 4 jets or at least 5 jets, and 1 or 2 b-tagged jets.
  The distributions from top to bottom are:
  (Left column): Cent_{jet}, $M_{\text{jj}}^{\text{MindR}}$, $N_{\text{jets}}^{|M_{jj}-M(V)|<30}$, $p_T{}^{\text{jet4}}$.
  (Right column): H1 Fox-Wolfram moment, max $M_{\ell\text{b}}^{\text{MindR}}$, $p_T{}^{\text{jet3}}$, $M_{\text{uu}}^{\text{Pt}_{\text{ord}}}$.
  (Bottom): $\Delta R_{\text{ave}}^{\text{jj}}$.

- Figures A.5 and A.6 show the distribution in data and MC of the input variables used in the signal region in the 2ℓOSZ region, $(\geq 5\text{j}, 2\text{b})$, evaluated in events with exactly 4 jets or at least 5 jets, and 2 b-tagged jets.
  The distributions from top to bottom are:
  (Left column): Cent_{jet}, $\Delta R_{\ell\ell}$, $M_{\text{bj}}^{\text{MaxPt}}$.
  (Right column): H1_{jet} Fox-Wolfram moment, $N_{\text{jets}}^{|M_{jj}-M(V)|<30}$, $M_{\text{bb}}^{\text{MaxPt}}$.
  (Bottom): N_{40}^{jet}.

The distribution of the NN outputs are also validated in data and MC.

- Figure A.7 shows the NN discriminants built for the 2ℓOSZveto $(4\text{j}, 1\text{b}+2\text{b})$ and $(\geq 5\text{j}, 1\text{b}+2\text{b})$ signal regions, evaluated in events with exactly 4 jets or at least 5 jets, and 1 or 2 b-tagged jets.

- Figure A.8 shows the NN discriminant built for the 2ℓOSZ $(\geq 5\text{j}, 2\text{b})$ signal region, evaluated in events with exactly 3 jets or 4 jets, and 2 b-tagged jets.

All distributions are shown before the fit procedure and the uncertainty bands include the MC statistical uncertainty only.

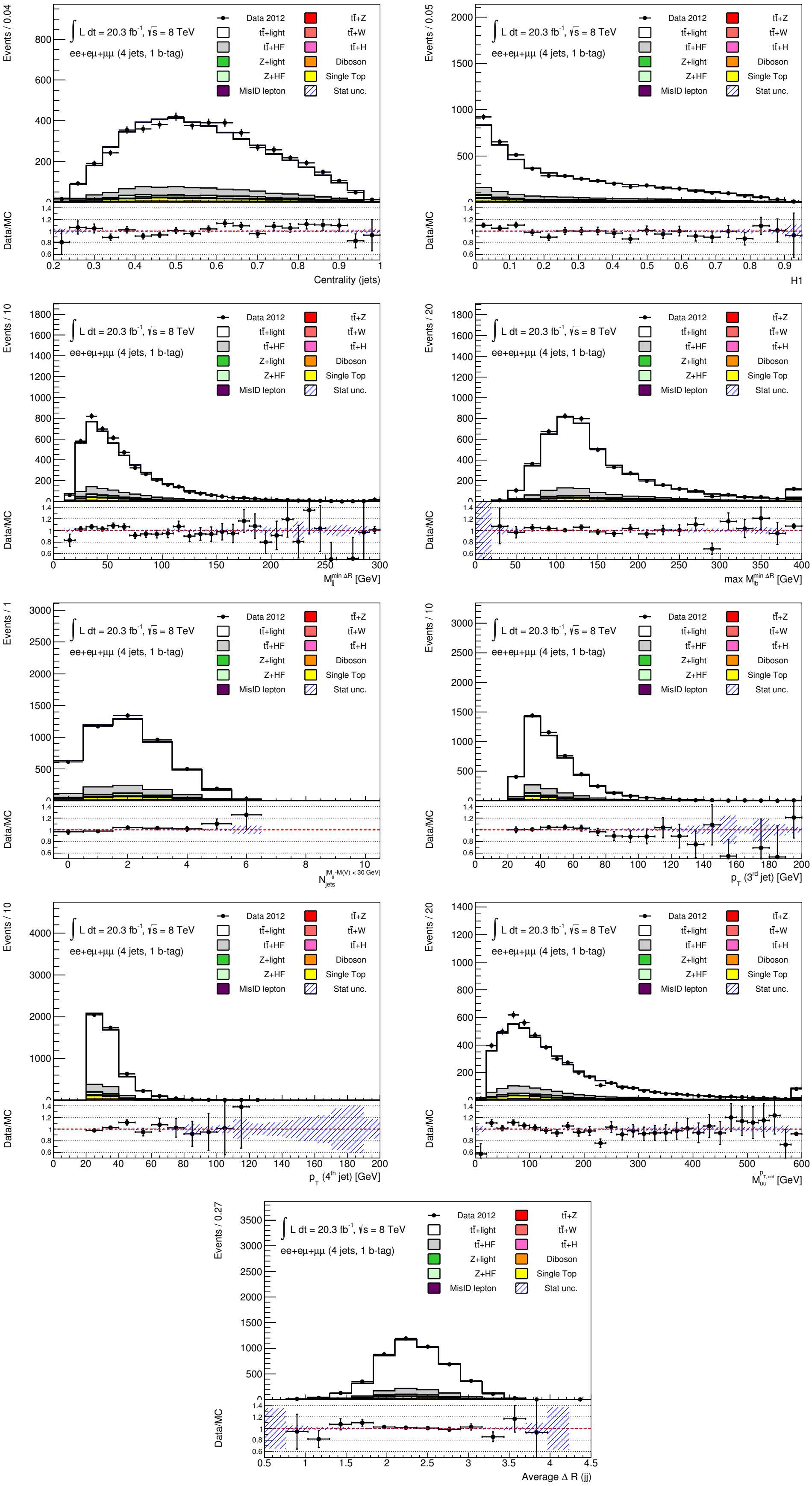

Figure A.1.: Data and MC distributions of the NN input variables in the 2ℓOSZveto (4j, 1b) region prior to the fit.

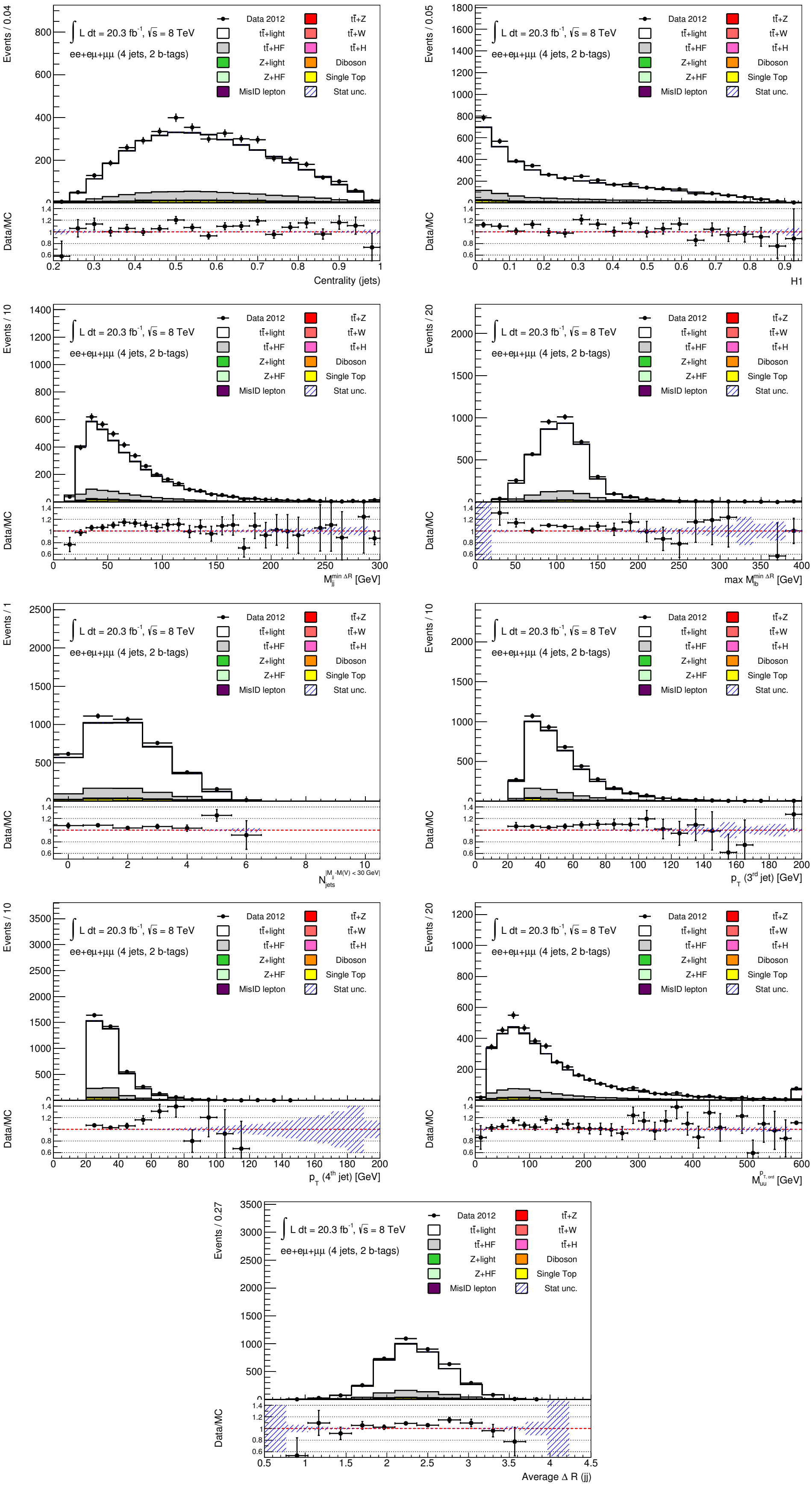

Figure A.2.: Data and MC distributions of the NN input variables in the 2ℓOSZveto (4j, 2b) region prior to the fit.

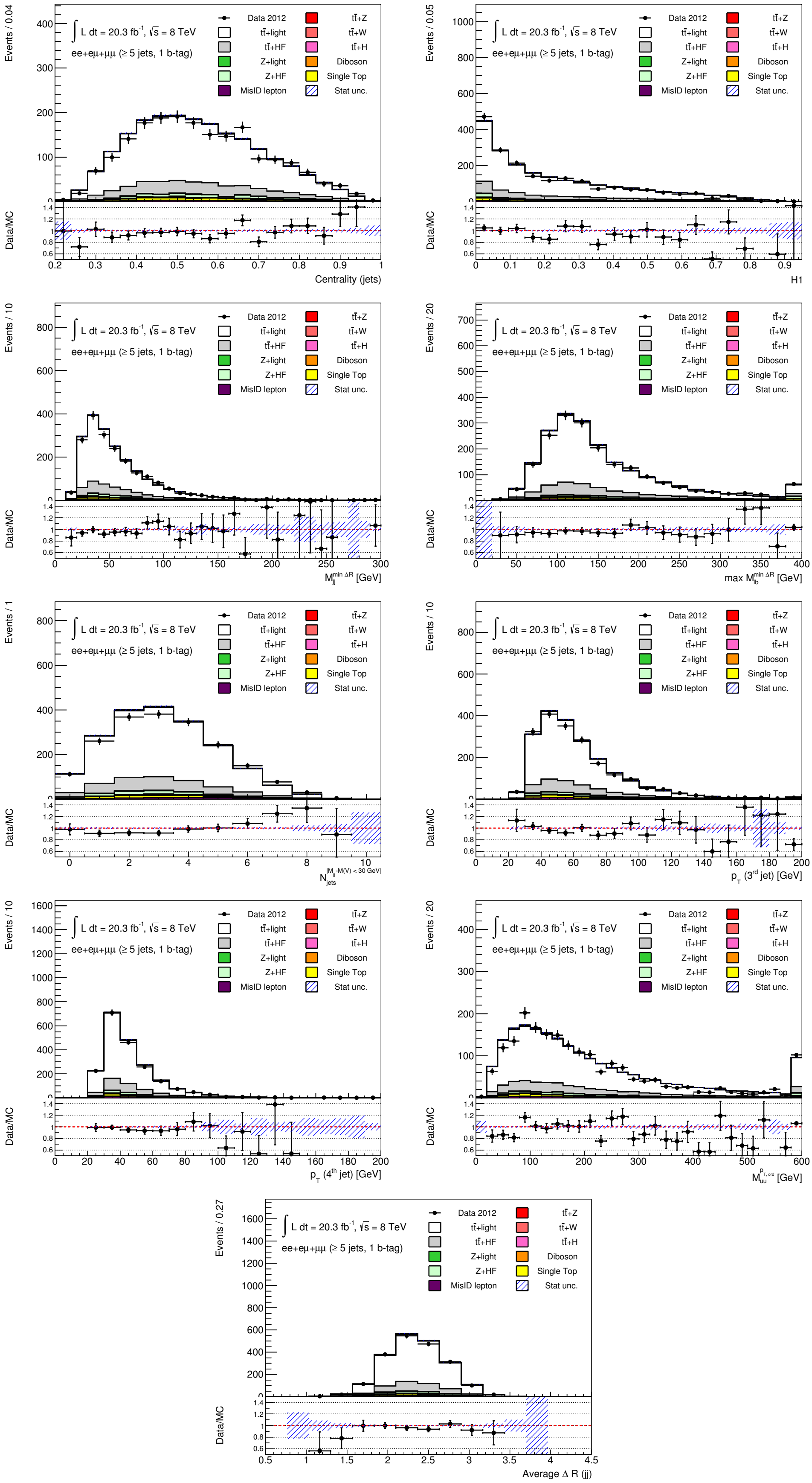

Figure A.3.: Data and MC distributions of the NN input variables in the 2ℓOSZveto ($\geq$ 5j, 1b) region prior to the fit.

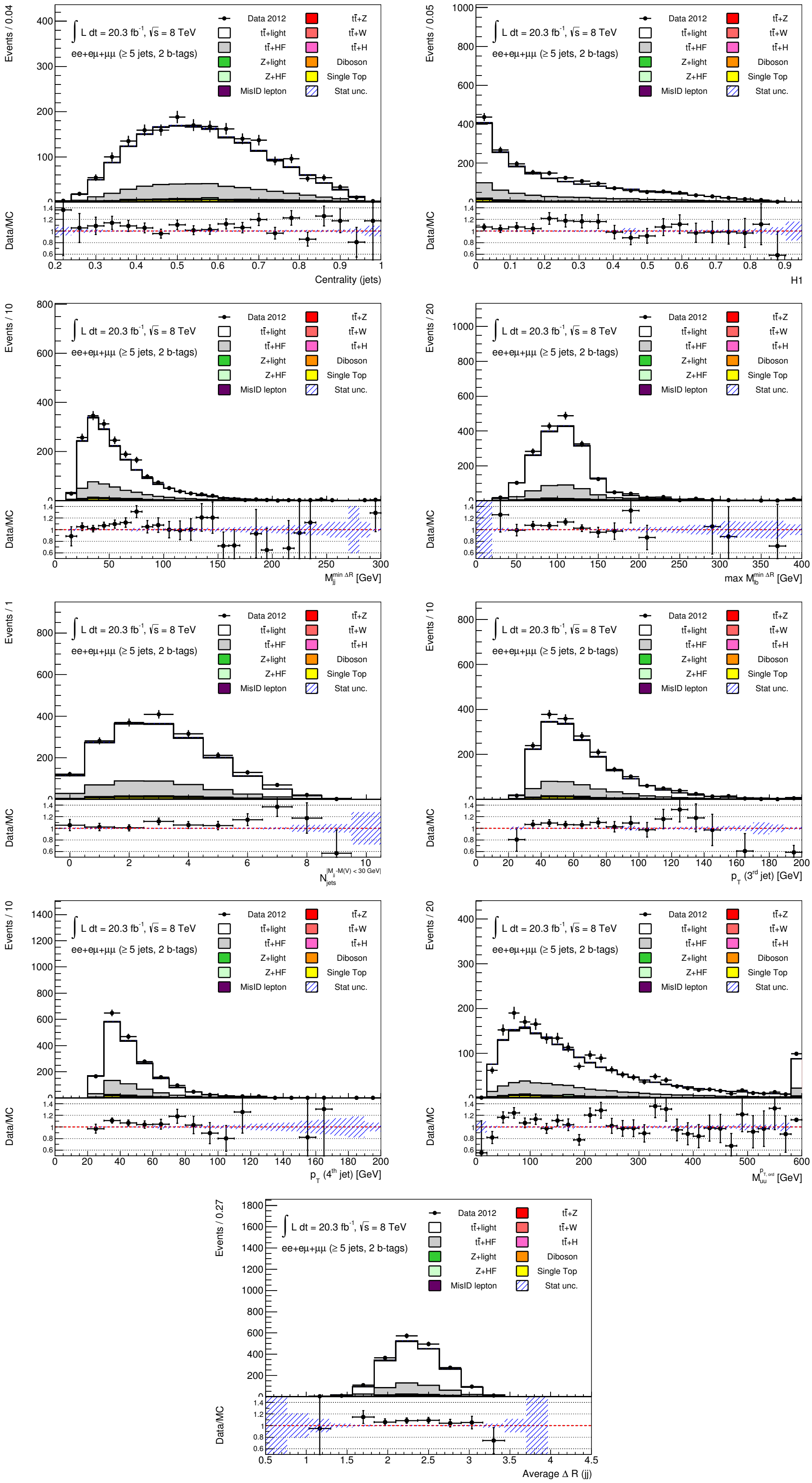

Figure A.4.: Data and MC distributions of the NN input variables in the 2ℓOSZveto ($\geq$ 5j, 2b) region prior to the fit.

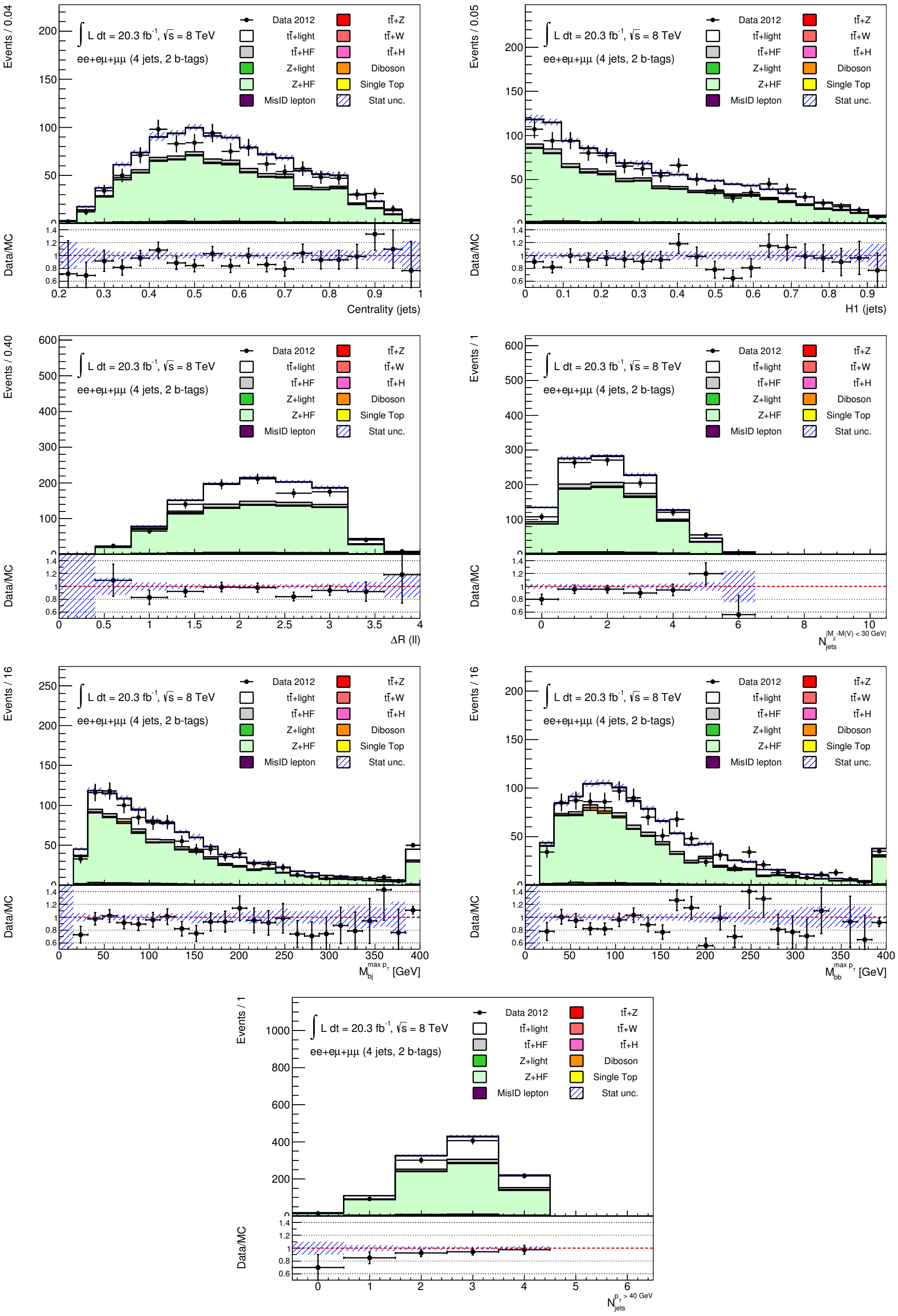

Figure A.5.: Data and MC distributions of the NN input variables in the 2ℓOSZ $(4\text{j}, 2\text{b})$ region prior to the fit.

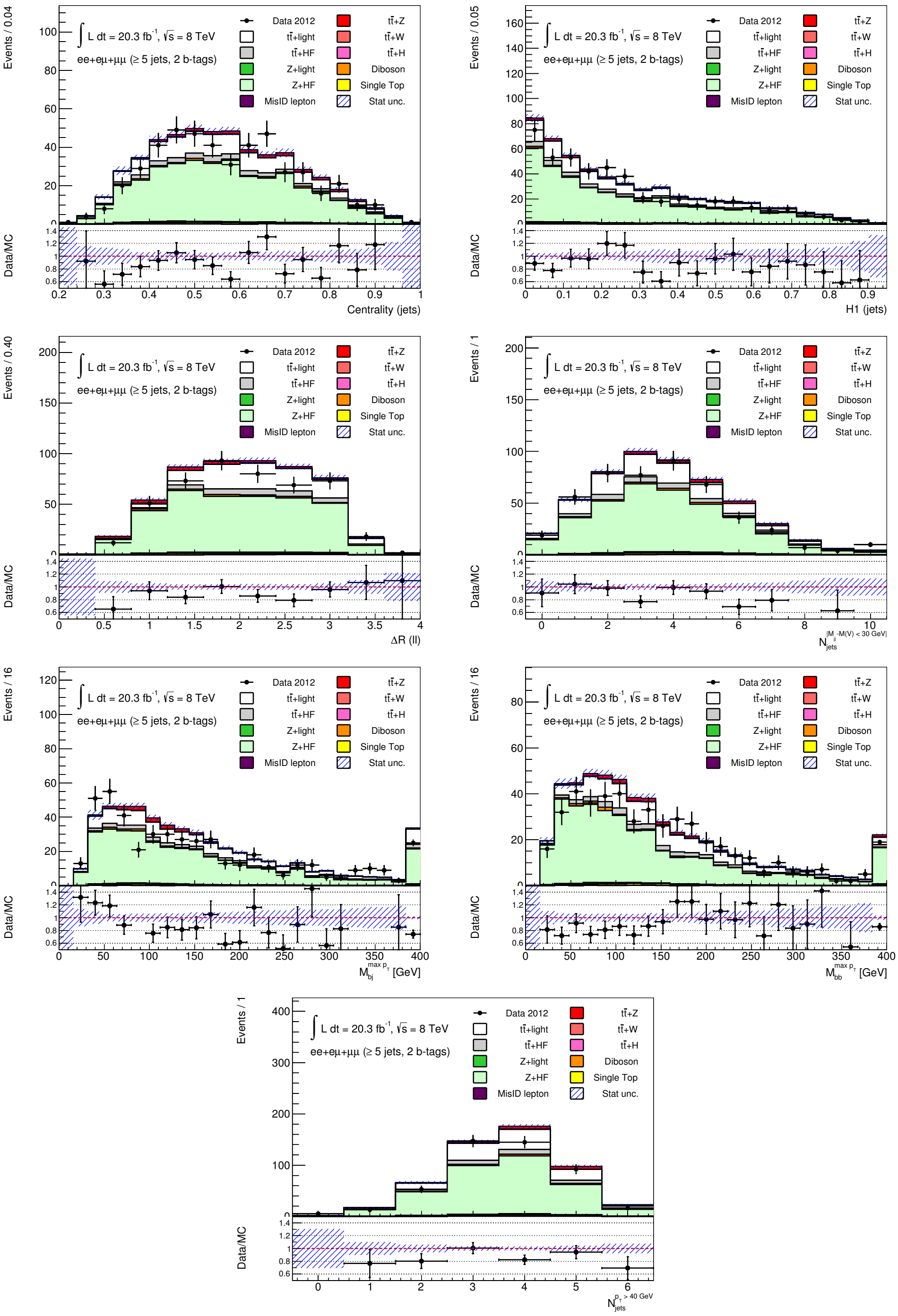

Figure A.6.: Data and MC distributions of the NN input variables in the 2ℓOSZ (≥ 5j, 2b) region prior to the fit.

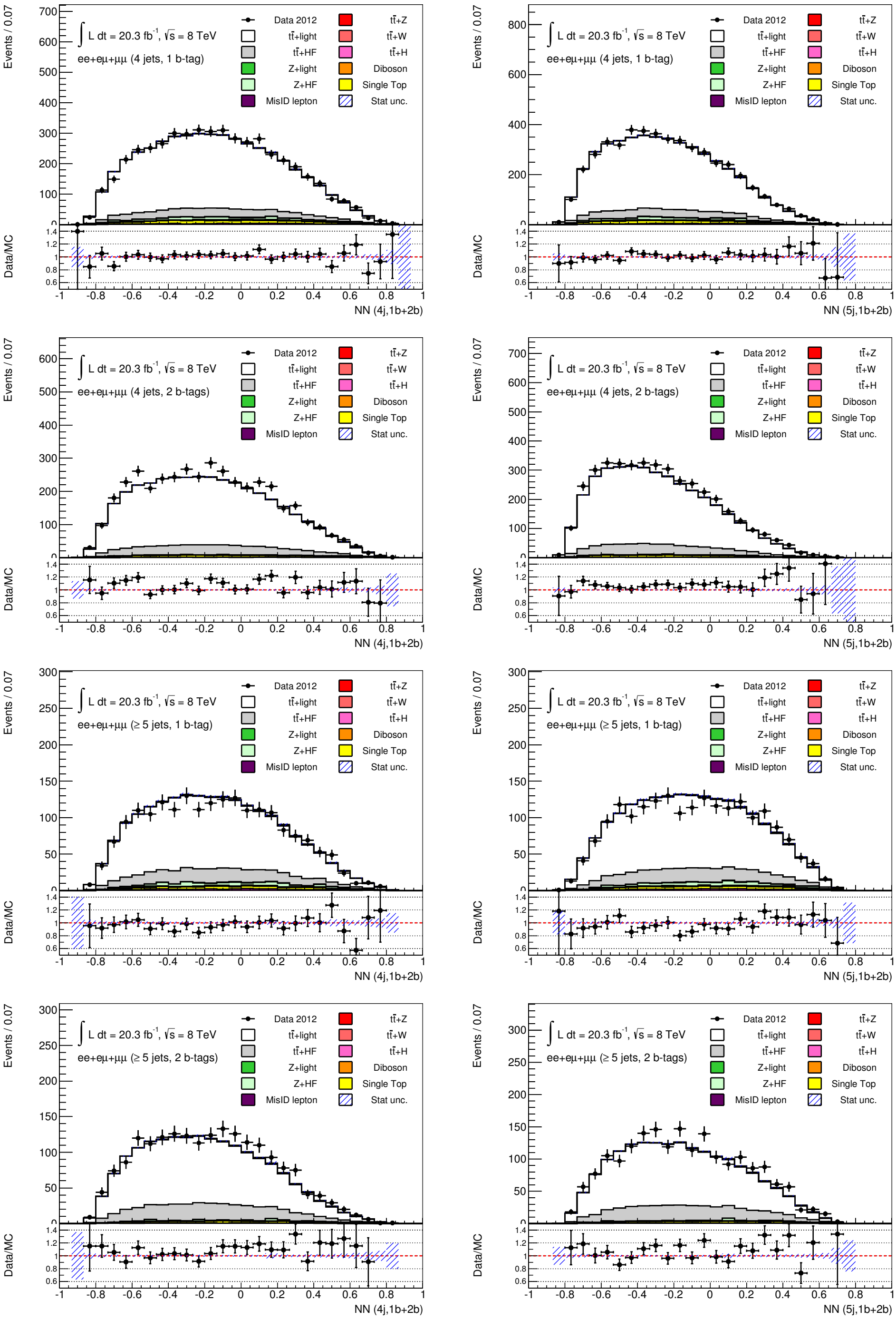

Figure A.7.: Data and MC distributions of the NN output distributions in the 2ℓOSZveto (4j, 1b), (4j, 2b), (≥ 5j, 1b) and (≥ 5j, 2b) regions prior to the fit.

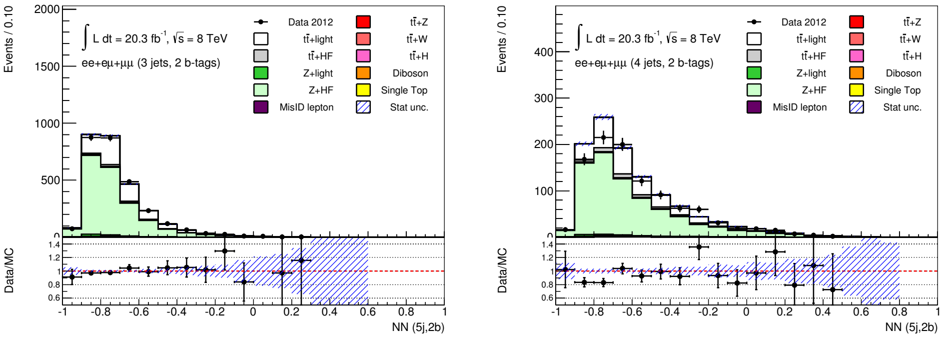

Figure A.8.: Data and MC distributions of the the NN output distribution in the 2ℓOSZ $(3\text{j}, 2\text{b})$ and $(4\text{j}, 2\text{b})$ regions prior to the fit.

APPENDIX B

Modelling Uncertainties on Z+jets and $t\bar{t}$ events

B.1. Alpgen Scales in Z+jets MC

Figure B.1 shows the effect of the renormalisation (*ktfac*) and factorisation (*qfac*) scale variations on the p_T(Z), H_T^{had}, and jet multiplicity distributions. The plots show that the *ktfac* variation is larger than the recommended uncertainty, based on the Berends scaling, explained in Section 10.6.1, and an early 2010 W+jets measurement of the uncertainty of this assumption, resulting in 42%, 48%, and 54% uncertainty due to the extrapolation to higher jet multiplicities in the ($3j$), ($4j$), and ($\geq 5j$) regions, respectively. The *ktfac* variation is also always larger than the *qfac* variation per jet multiplicity, and there is no significant effect of *qfac* on the H_T^{had} distribution used in the fit. For these reasons, only the *ktfac* systematic uncertainty is included in the fit to represent the Alpgen scale variations and any additional ad-hoc extrapolation uncertainty is ignored.

To allow shape variations in each jet multiplicity bin, the generator and parton shower systematic uncertainty is included by using the Z+jets Sherpa MC sample generated with massive b and c quarks, as an alternative model for the Z+jets background. Initially, it was represented by two parameters in the fit: one affecting normalisation and another the shape. The fit showed that the nuisance parameter representing Sherpa shape is significantly constrained. The effect was traced to the 2ℓOSZ $(3\mathrm{j}, 2\mathrm{b})$ region, where H_T^{had} Sherpa shape is significantly different from the default ALPGEN+PYTHIA, and is not supported by data. The shapes in the 2ℓOSZ $(4\mathrm{j}, 2\mathrm{b})$ and $(\geq 5\mathrm{j}, 2\mathrm{b})$ regions agree very well between the two generators. Thus, the Sherpa sample does not bring any additional shape information to the fit in these regions. For this reason, Sherpa modelling is treated as a normalisation uncertainty only.

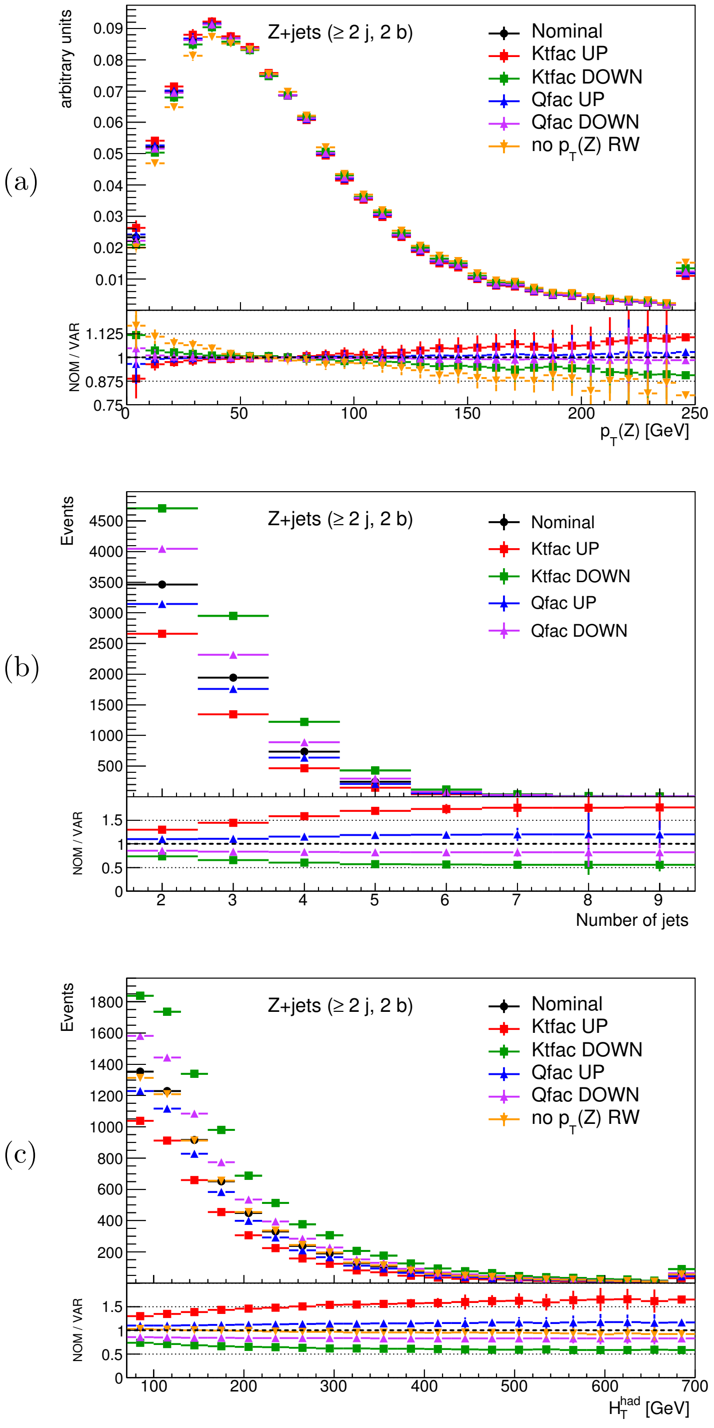

Figure B.1.: Effect of the Z+jets Alpgen MC scale variations compared to the effect of turning off the $p_T(\mathrm{Z})$ correction in the 2ℓOSZ ($\geq$ 2 j, 2 b) region on **(a)** the $p_T(\mathrm{Z})$ distribution, **(b)** the N_{jets} distribution, and **(c)** the H_T^{had} distribution.

B.2. Data/MC comparison for alternative MC models

Figure B.2 compares the agreement between data and MC simulation in the 2ℓOSZveto region for the default $t\bar{t}$ generator, Powheg+Pythia (right column), and for the alternative Madgraph+Pythia model (left column).

Figure B.3 compares the agreement between data and MC simulation in the 2ℓOSZ region for the default Z+jets generator, Alpgen+Pythia (right column), and for the alternative Sherpa model (left column).

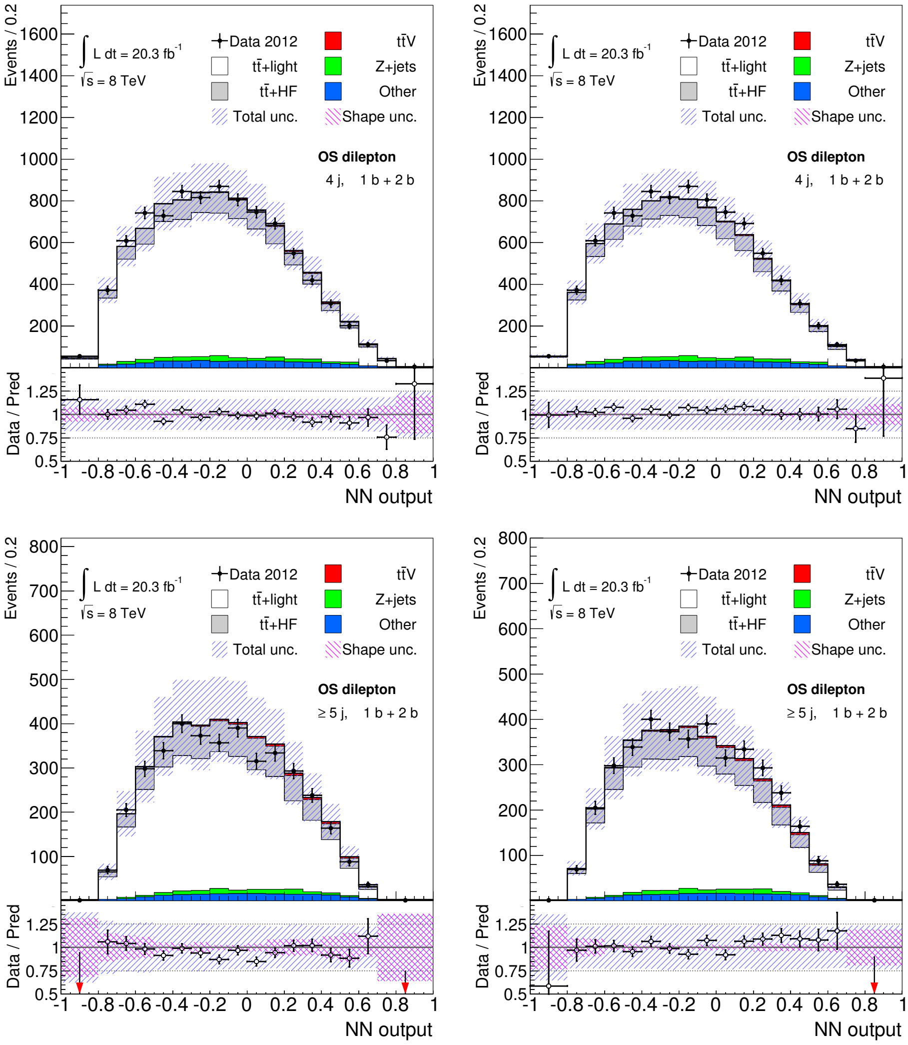

Figure B.2.: Data and MC distributions of the NN discriminants in the (top): 2ℓOSZveto $(4\text{j}, 1\text{b}+2\text{b})$ and (bottom): $(\geq 5\text{j}, 1\text{b}+2\text{b})$ fit regions, with (left column): Madgraph+Pythia, or (right column): Powheg+Pythia, as the $t\bar{t}$ generator. The hashed blue band shows the total uncertainty (statistical and systematic) and the hashed magenta band shows the statistical and systematic uncertainties affecting only the shape of the discriminants.

Figure B.4 shows the comparison of the event yields in data and MC simulation in the six regions used in the fit, using the nominal and alternative generators for each $t\bar{t}$ and Z+jets process. The yields in all fit regions for all considered generators agree with data within the total uncertainty bands before the fit.

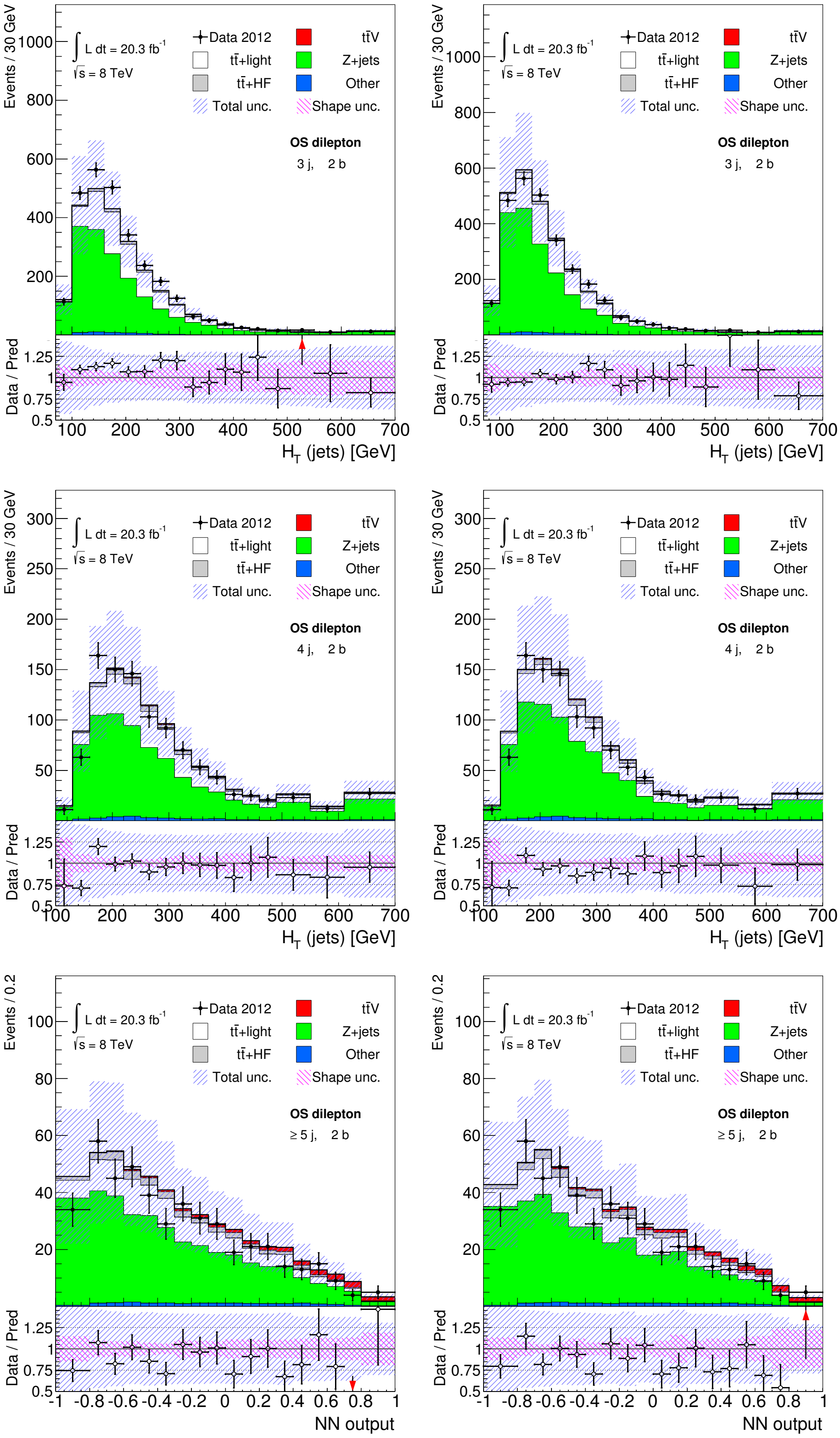

Figure B.3.: Data and MC distributions of the discriminants in the fit regions in the 2ℓOSZ region: H_T^{had} in (top): (3j, 2b) and (middle): (4j, 2b), and NN in (bottom): ($\geq$ 5j, 2b), with (left column): Sherpa, or (right column): Alpgen+Pythia, as the Z+jets generator. The hashed blue band shows the total uncertainty (statistical and systematic) and the hashed magenta band shows the statistical and systematic uncertainties affecting only the shape of the discriminants.

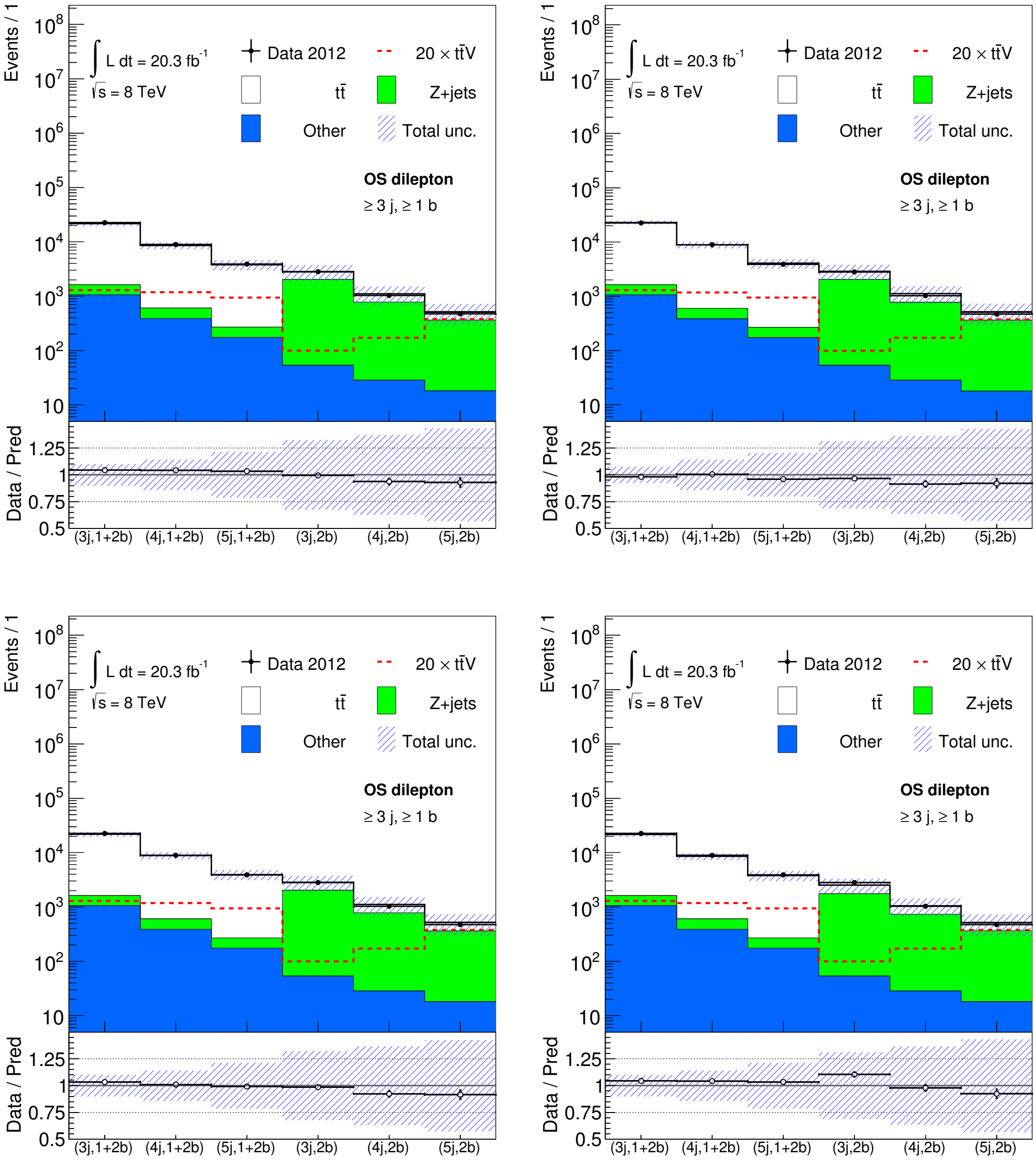

Figure B.4.: Rate per fit region before the fit for (top left): the nominal set of MC generators, (top right): for Madgraph+Pythia as the $t\bar{t}$ generator, (bottom left): for Powheg+Herwig as the $t\bar{t}$ generator, and (bottom right): for Sherpa as the Z+jets generator. The first three bins on the x-axis correspond to the three fit regions in the 2ℓOSZveto region, and the last three bins correspond to the three fit regions in the 2ℓOSZ region. The red dashed line shows the expected normalisation of $t\bar{t}V$ in each fit region, multiplied by a factor of 20.

APPENDIX C

Pruning

The result of the pruning is shown in Figures C.1 and C.2 for acceptance and shape effects, respectively. Systematic uncertainties which are ignored (accepted) for a given process in a given fit region are highlighted in green (red). The fit regions and processes of the fit are shown on the vertical axis, whereas the systematic sources are shown on the horizontal axis. As can be seen for all the samples in the 2ℓOSZveto $(3\mathrm{j}, 1\mathrm{b} + 2\mathrm{b})$ region, there is no shape effect from any systematic uncertainty because only event counting information from this region is included in the fit.

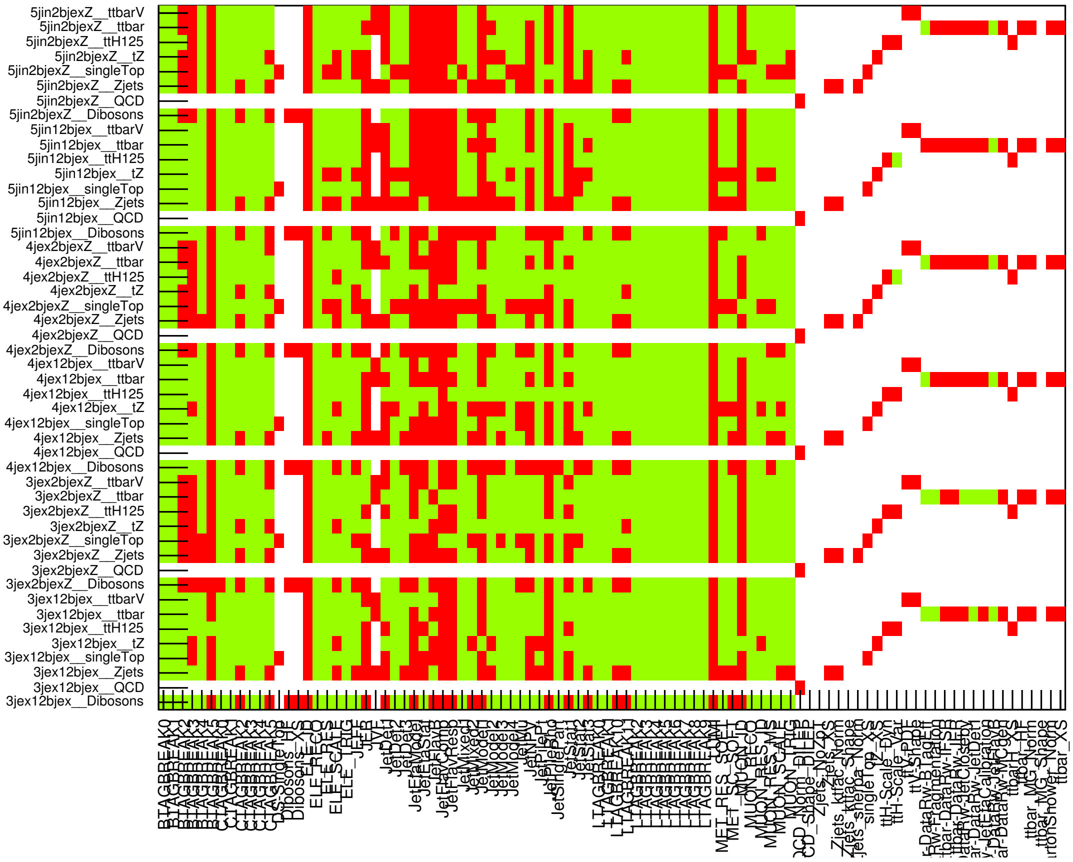

Figure C.1.: Pruning of the systematics based on the acceptance effect for each sample and region in the fit. Red regions highlight systematics for a given sample and region which are included in the fit. Green regions are pruned away by the algorithm.

]]>

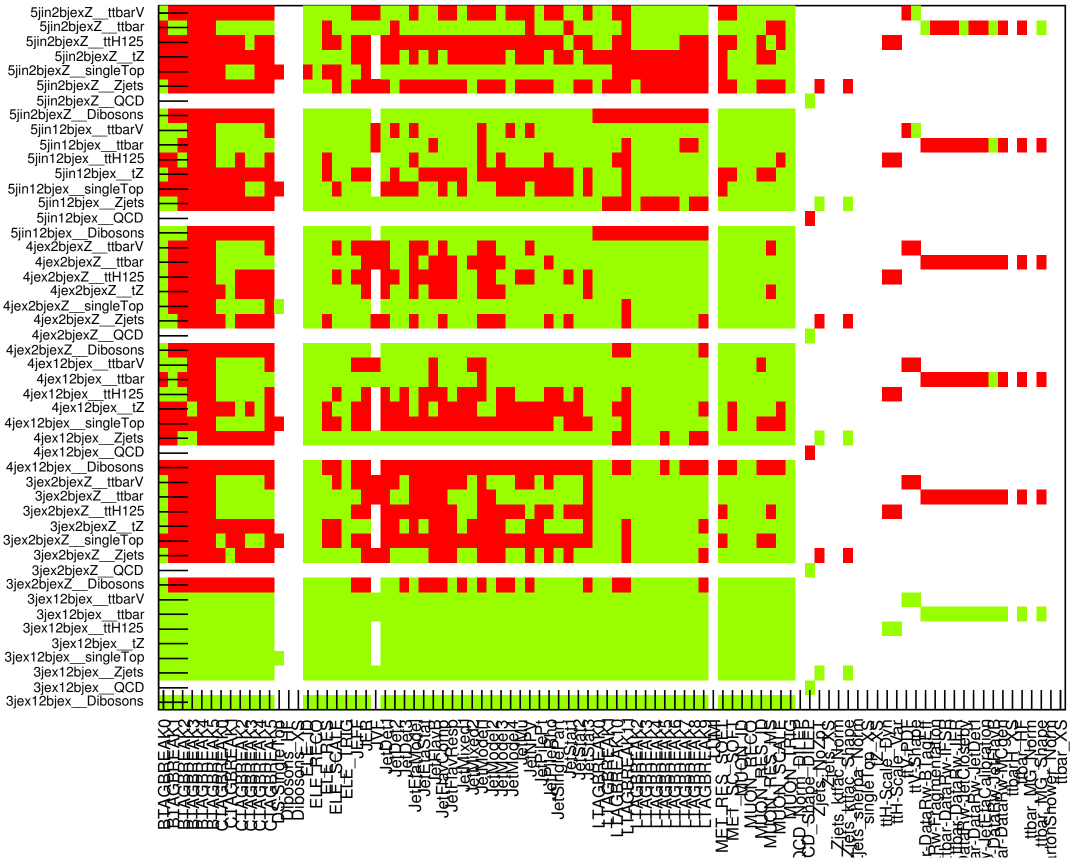

Figure C.2.: Pruning of the systematics based on their shape effect for each sample and region in the fit. Red regions highlight systematics for a given sample and region which are included in the fit. Green regions are pruned away by the algorithm.

Bibliography

[1] M. Thomson, *Modern Particle Physics*, Cambridge University Press, Cambridge (2013).

[2] D. Griffiths, *Introduction to Elementary Particles*, Wiley-VCH, Weinheim (2008).

[3] E. Noether, *Invariante Variationsprobleme*, Nachr. d. Koenig. Gesellsch. d. Wiss. zu Goettingen, Math-phys. Klasse (1918).

[4] K.A. Olive et al. (Particle Data Group), *The Review of Particle Physics*, Chin. Phys. C **38** (2014) 090001.

[5] The ATLAS Collaboration, CDF Collaboration, CMS Collaboration, D0 Collaboration, *First combination of Tevatron and LHC measurements of the top-quark mass*, `arXiv:1403.4427 [hep-ex]`.

[6] © Excellence Cluster Universe.

[7] S. L. Glashow, *Partial-symmetries of weak interactions*, Nucl. Phys. **22** (1961) 579–588.

[8] A. Salam et al., *Electromagnetic and weak interactions*, Phys. Lett. **13** (1964) 168–171.

[9] S. Weinberg, *A Model of Leptons*, Phys. Rev. Lett. **19** (1967) 1264–1266.

[10] N. Cabibbo, *Unitary Symmetry and Leptonic Decays*, Phys. Rev. Lett. **10** (1963) 531–533.

[11] M. Kobayashi and T. Maskawa, *CP-Violation in the Renormalizable Theory of Weak Interaction*, Prog. Theor. Phys. **49** (1973) 652–657.

[12] G. 't Hooft, *Renormalization of massless Yang-Mills fields*, Nucl. Phys. B **33** (1971) 173–199.

[13] G. 't Hooft, *Renormalizable Lagrangians for massive Yang-Mills fields*, Nucl. Phys. B **35** (1971) 167–188.

[14] G. 't Hooft and M. Veltman, *DIAGRAMMAR*, CERN report **73-9** (1973).

[15] P. Higgs, *Broken symmetries, massless particles and gauge fields*, Phys. Lett. **12** (1964) 132–133.

[16] P. Higgs, *Broken Symmetries and the Masses of Gauge Bosons*, Phys. Rev. Lett. **13** (1964) 508–509.

[17] G. Guralnik et al., *Global Conservation Laws and Massless Particles*, Phys. Rev. Lett. **13** (1964) 585–587.

[18] F. Englert and R. Brout, *Broken Symmetry and the Mass of Gauge Vector Mesons*, Phys. Rev. Lett. **13** (1964) 321–323.

[19] A. Djouadi, *The Anatomy of electro-weak symmetry breaking. I: The Higgs boson in the standard model*, Phys.Rept. **457** (2008) 1–216.

[20] D. J. Gross and F. Wilczek, *Ultraviolet Behaviour of Non-Abelian Gauge Theories*, Phys. Rev. Lett. **30** (1973) 1343–1346.

[21] D. J. Gross and F. Wilczek, *Asymptotically Free Gauge Theories. I*, Phys. Rev. D **8** (1973) 3633–3652.

[22] H. D. Politzer, *Reliable Perturbative Results for Strong Interactions?*, Phys. Rev. Lett. **30** (1973) 1346–1349.

[23] H. G. Savas Dimopoulos, *Softly broken supersymmetry and SU(5)*, Nucl. Phys. B **193** (1981) 150–162.

[24] N. Arkani-Hamed, S. Dimopoulos, and G. Dvali, *The Hierarchy problem and new dimensions at a millimeter*, Phys. Lett. **B429** (1998) 263–272.

[25] L. Randall and R. Sundrum, *A Large mass hierarchy from a small extra dimension*, Phys. Rev. Lett. **83** (1999) 3370–3373.

[26] G. L. Kane and M. Peskin, *A constraint from B decay on models with no t quark*, Nucl. Phys. B **195** (1982) 29–38.

[27] The CLEO Collaboration, *Improved Upper Limit on Flavor Changing Neutral Current Decays of the B Quark*, Phys. Rev. D **35** (1987) 3533.

[28] D. Roy and S. U. Sankar, *Upper limit on B_d^0 and $\bar{B}_d^0$ mixing as evidence for the existence of the top quark*, Phys. Lett. B **243** no. 3, (1990) 296 – 300.

[29] The ARGUS Collaboration, *Observation of B0 - anti-B0 Mixing*, Phys. Lett. B **192** (1987) 245.

[30] The ARGUS Collaboration, *A Study of anti-B0 → D*+ lepton- anti-neutrino and B0 anti-B0 mixing using partial D*+ reconstruction*, Phys. Lett. B **324** (1994) 249–254.

[31] The CLEO Collaboration, *Two measurements of B0 anti-B0 mixing*, Phys. Rev. Lett. **71** (1993) 1680–1684.

[32] The CDF Collaboration, *Observation of Top Quark Production in $\overline{p}p$ Collisions with the Collider Detector at Fermilab*, Phys. Rev. Lett. **74** (1995) 2626–2631.

[33] The D0 Collaboration, *Observation of the Top Quark*, Phys. Rev. Lett. **74** (1995) 2632–2637.

[34] The LEP Electroweak Working Group,. `http://lepewwg.web.cern.ch/LEPEWWG`.

[35] The ATLAS Collaboration, *Observation of a new particle in the search for the Standard Model Higgs boson with the ATLAS detector at the LHC*, Phys. Lett. B **716** (2012) 1 – 29.

[36] The CMS Collaboration, *Observation of a new boson at a mass of 125 GeV with the CMS experiment at the LHC*, Phys. Lett. B **716** (2012) 30 – 61.

[37] A. Quadt, *Top Quark Physics at Hadron Colliders*, Eur. Phys. J. C **C48** (2006) 835–1000.

[38] F.-P. Schilling, *Top Quark Physics at the LHC: A Review of the First Two Years*, Int. J. Mod. Phys. **A27** (2012) 1230016.

[39] R. Chierici, *Top quark physics at the LHC*, Riv.Nuovo Cim. **37** no. 02, (2014) 47–123.

[40] U. Langenfeld, S. Moch, and P. Uwer, *New results for t anti-t production at hadron colliders*, `arXiv:0907.2527 [hep-ph]`.

[41] H. L. Lai et al., *New parton distributions for collider physics*, Phys. Rev. D **82** (2010) 074024.

[42] J. Gao et al., *The CT10 NNLO Global Analysis of QCD*, `arXiv:1302.6246 [hep-ph]`.

[43] The Durham HepData Project,. `http://hepdata.cedar.ac.uk/pdf/pdf3.html`.

[44] M. Cacciari et al., *Top-pair production at hadron colliders with next-to-next-to-leading logarithmic soft-gluon resummation*, Phys. Lett. **B710** (2012) 612.

[45] P. Barnreuther et al., *Percent Level Precision Physics at the Tevatron: First Genuine NNLO QCD Corrections to* $q\bar{q} \to t\bar{t}$, Phys. Rev. Lett. **109** (2012) 132001.

[46] M. Czakon and A. Mitov, *NNLO corrections to top-pair production at hadron colliders: the all-fermionic scattering channels*, JHEP **1212** (2012) 054.

[47] M. Czakon and A. Mitov, *NNLO corrections to top-pair production at hadron colliders: the quark-gluon reaction*, JHEP **1301** (2013) 080.

[48] M. Czakon, P. Fiedler, and A. Mitov, *The total top quark pair production cross-section at hadron colliders through* $\mathcal{O}(\alpha_S^4)$, Phys. Rev. Lett. **110** (2013) 252004.

[49] M. Czakon and A. Mitov, *Top++: a program for the calculation of the top-pair cross-section at hadron colliders*, `arXiv:1112.5675 [hep-ph]`.

[50] M. Botje et al., *The PDF4LHC Working Group Interim Recommendations*, `arXiv:1101.0538 [hep-ph]`.

[51] A. D. Martin et al., *Parton distributions for the LHC*, Eur. Phys. J. C **63** (2009) 189.

[52] A. D. Martin et al., *Uncertainties on alpha*$_S$ *in global PDF analyses and implications for predicted hadronic cross sections*, Eur. Phys. J. C **64** (2009) 653.

[53] R. D. Ball et al., *Parton distributions with LHC data*, Nucl. Phys. **B867** (2013) 244.

[54] F. Maltoni, G. Ridolfi, and M. Ubiali, *b-initiated processes at the LHC: a reappraisal*, JHEP **1207** (2012) 022.

[55] J. Campbell, K. Ellis, and C. Williams, "Mcfm - monte carlo for femtobarn processes." `http://mcfm.fnal.gov`.

[56] J. Adelman, B. Alvarez Gonzalez, Y. Bai, M. Baumgart, R. K. Ellis, et al., *Top Couplings: pre-Snowmass Energy Frontier 2013 Overview*, `arXiv:1309.1947 [hep-ex]`.

[57] The D0 Collaboration. `http://www-d0.fnal.gov/Run2Physics/top/top_public_web_pages/top_feynman_diagrams.html`.

[58] U. Baur, A. Juste, L. H. Orr, and D. Rainwater, *Probing electroweak top quark couplings at hadron colliders*, Phys. Rev. D **71** (2005) 054013.

[59] A. Czarnecki, J. G. Körner, and J. H. Piclum, *Helicity fractions of W bosons from top quark decays at next-to-next-to-leading order in QCD*, Phys. Rev. D **81** (2010) 111503.

[60] The CDF Collaboration, *Measurement of W-boson polarization in top-quark decay using the full CDF Run II data set*, Phys. Rev. D **87** (2013) 031104.

[61] The D0 Collaboration, *Measurement of the W boson helicity in top quark decays using* 5.4 fb^{-1} *of $p\bar{p}$ collision data*, Phys. Rev. D **83** (2011) 032009.

[62] The CDF and D0 Collaboration, *Combination of CDF and D0 measurements of the W boson helicity in top quark decays*, Phys. Rev. D **85** (2012) 071106.

[63] The ATLAS Collaboration, *Measurement of the W boson polarization in top quark decays with the ATLAS detector*, JHEP **2012** no. 6, (2012).

[64] The CMS Collaboration, *Measurement of the W-boson helicity in top-quark decays from* 5.4$\mathrm{t\bar{t}}$ *production in lepton+jets events in pp collisions at $\sqrt{s} = 7$ TeV*, JHEP **2013** no. 10, (2013).

[65] The CMS Collaboration, *Measurement of the W-boson helicity in top decays from ttbar production in lepton+jets events at the LHC at $\sqrt{s} = 8$ TeV*, CMS-PAS-TOP-13-008.

[66] The ATLAS and CMS Collaboration, *Combination of the ATLAS and CMS measurements of the W-boson polarization in top-quark decays*, ATLAS-CONF-2013-033 / CMS-PAS-TOP-12-025.

[67] *Measurement of the ratio $B(t \to Wb)/B(t \to Wq)$ in pp collisions at $\sqrt{s} = 8$ TeV*, Phys. Lett. B **736** no. 0, (2014) 33 – 57.

[68] The CMS Collaboration, *Measurement of the t-channel single-top-quark production cross section and of the $|V_{tb}|$ CKM matrix element in pp collisions at $\sqrt{s} = 8$ TeV*, JHEP **2014** no. 6, (2014).

[69] The CDF Collaboration, *Evidence for $t\bar{t}\gamma$ production and measurement of $\sigma_{t\bar{t}\gamma}/\sigma_{t\bar{t}}$*, Phys. Rev. D **84** (2011) 031104.

[70] The ATLAS Collaboration, *Measurement of the inclusive $t\bar{t}\gamma$ cross section with the ATLAS detector*, ATLAS-CONF-2011-153.

[71] The CMS Collaboration, *Measurement of the inclusive top-quark pair + photon production cross section in the muon + jets channel in pp collisions at 8 TeV*, CMS-PAS-TOP-13-011.

[72] The ATLAS Collaboration, *Search for the Standard Model Higgs boson produced in association with top quarks and decaying to* $b\bar{b}$ *in pp collisions at* $\sqrt{s} = 8$ *TeV with the ATLAS detector at the LHC*, ATLAS-CONF-2014-011.

[73] The ATLAS Collaboration, *Search for* $H \to \gamma\gamma$ *produced in association with top quarks and constraints on the Yukawa coupling between the top quark and the Higgs boson using data taken at 7 TeV and 8 TeV with the ATLAS detector*, `arXiv:1409.3122 [hep-ex]`.

[74] The CMS Collaboration, *Search for the associated production of the Higgs boson with a top-quark pair*, JHEP **1409** (2014) 087.

[75] R. Roentsch and M. Schulze, *Constraining couplings of top quarks to the Z boson in* $t\bar{t} + Z$ *production at the LHC*, JHEP **1407** (2014) 091.

[76] P. Nason, *A new method for combining NLO QCD with shower Monte Carlo algorithms*, JHEP **11** (2004) 040.

[77] S. Frixione, P. Nason, and C. Oleari, *Matching NLO QCD computations with Parton Shower simulations: the POWHEG method*, JHEP **11** (2007) 070.

[78] S. Alioli, P. Nason, C. Oleari, and E. Re, *A general framework for implementing NLO calculations in shower Monte Carlo programs: the POWHEG BOX*, JHEP **06** (2010) 040.

[79] G. Bevilacqua, M. Czakon, M. Garzelli, A. van Hameren, A. Kardos, et al., *HELAC-NLO*, Comput. Phys. Commun. **184** (2013) 986–997.

[80] M. Garzelli, A. Kardos, C. Papadopoulos, and Z. Trocsanyi, $t\,\bar{t}\,W^{+-}$ *and* $t\,\bar{t}\,Z$ *Hadroproduction at NLO accuracy in QCD with Parton Shower and Hadronization effects*, JHEP **1211** (2012) 056.

[81] J. M. Campbell and R. K. Ellis, $t\bar{t}W^{+-}$ *production and decay at NLO*, JHEP **1207** (2012) 052.

[82] The ATLAS Collaboration, *Search for* $t\bar{t}Z$ *production in the three lepton final state with* 4.7 fb^{-1} *of* $\sqrt{s} = 7$ *TeV pp collision data collected by the ATLAS detector*, ATLAS-CONF-2012-126 (2012).

[83] The CMS Collaboration, *Measurement of associated production of vector bosons and top quark-antiquark pairs at sqrt(s) = 7 TeV*, Phys. Rev. Lett. **110** (2013) 172002.

[84] The CMS Collaboration, *Measurement of top quark-antiquark pair production in association with a W or Z boson in pp collisions at* $\sqrt{s} = 8$ *TeV*, Eur. Phys. J. C **74** (2014) 3060.

[85] The ALEPH Collaboration, DELPHI Collaboration, L3 Collaboration, OPAL Collaboration, SLD Collaboration, LEP Electroweak Working Group, SLD Electroweak Group, SLD Heavy Flavour Group Collaboration, *Precision electroweak measurements on the Z resonance*, Phys.Rept. **427** (2006) 257–454.

[86] The DELPHI Collaboration, *A Study of b anti-b Production in e+e- Collisions at s**(1/2) = 130-GeV - 207-GeV*, Eur. Phys. J. C **60** (2009) 1–15.

[87] G. Altarelli and R. Barbieri, *Vacuum polarization effects of new physics on electroweak processes*, Phys. Lett. B **253** no. 1-2, (1991) 161 – 167.

[88] G. Altarelli, R. Barbieri, and S. Jadach, *Toward a model-independent analysis of electroweak data*, Nucl. Phys. B **369** no. 1-2, (1992) 3 – 32.

[89] G. Altarelli, R. Barbieri, and F. Caravaglios, *Nonstandard analysis of electroweak precision data*, Nucl. Phys. B **405** (1993) 3–23.

[90] J. Aguilar-Saavedra, *A Minimal set of top anomalous couplings*, Nucl. Phys. B **812** (2009) 181–204.

[91] U. Baur, A. Juste, L. Orr, and D. Rainwater, *Probing Electroweak Top Quark Couplings at Hadron and Lepton Colliders*, Nucl. Phys. B **160** no. 0, (2006) 17 – 21.

[92] E. L. Berger, Q.-H. Cao, and I. Low, *Model Independent Constraints Among the Wtb, Zb anti-b, and Zt anti-t Couplings*, Phys. Rev. D **80** (2009) 074020.

[93] The CMS Collaboration, *Measurement of the properties of a Higgs boson in the four-lepton final state*, Phys. Rev. D **89** (2014) 092007.

[94] J. Campbell, R. K. Ellis, and R. Roetsch, *Single top production in association with a Z boson at the LHC*, Phys. Rev. D **87** no. 11, (2013) 114006.

[95] O. S. Bruening, P. Collier, P. Lebrun, S. Myers, R. Ostojic, J. Poole, and P. Proudlock, *LHC Design Report v.1 : the LHC Main Ring*, CERN-2004-003-V-1.

[96] O. S. Bruening, P. Collier, P. Lebrun, S. Myers, R. Ostojic, J. Poole, and P. Proudlock, *LHC Design Report v.2 : the LHC Infrastructure and General Services*, CERN-2004-003-V-2.

[97] M. Benedikt, P. Collier, V. Mertens, J. Poole, and K. Schindl, *LHC Design Report v.3 : the LHC Injector Chain*, CERN-2004-003-V-3.

[98] CERN, *LEP design report v.2 : The LEP main ring*, CERN-LEP-84-01.

[99] The ATLAS Collaboration, *The ATLAS Experiment at the CERN Large Hadron Collider*, JINST **3** (2008) S08003.

[100] The CMS Collaboration, *The CMS experiment at the CERN LHC*, JINST **3** (2008) S08004.

[101] The ALICE Collaboration, *The ALICE experiment at the CERN LHC*, JINST **3** (2008) S08002.

[102] The LHCb Collaboration, *The LHCb Detector at the LHC*, JINST **3** (2008) S08005.

[103] "LHC: the guide." `https://cds.cern.ch/record/1165534/files/CERN-Brochure-2009-003-Eng.pdf`, 2009.

[104] M. Lamont on behalf of the LHC team, "The LHC's first long run." `http://cerncourier.com/cws/article/cern/54381`, 2013.

[105] Courtesy of the ATLAS experiment.

[106] A. Miucci, *The ATLAS Insertable B-Layer project*, Journal of Instrumentation **9** no. 02, (2014) C02018.

[107] A. E. Phoboo, "A new subdetector for ATLAS." `http://home.web.cern.ch/about/updates/2014/05/new-subdetector-atlas`.

[108] A. Vogel, *ATLAS Transition Radiation Tracker (TRT): Straw tube gaseous detectors at high rates*, Nuclear Instruments and Methods in Physics Research Section A: Accelerators, Spectrometers, Detectors and Associated Equipment **732** no. 0, (2013) 277 – 280.

[109] O. Igonkina, *ATLAS trigger menu and performance in Run 1 and prospects for Run 2*, Proceedings for 2013 IEEE Nuclear Science Symposium and Medical Imaging Conference (NSS/MIC 2013) (2013).

[110] The ATLAS Collaboration, *ATLAS detector and physics performance: Technical Design Report*, ATLAS-TDR-14, CERN-LHCC-99-014 (1999).

[111] L. Fiorini, *ATLAS Results and Future Prospects*, Presentation at the conference IMFP14, Benasque (2014).

[112] The ATLAS Collaboration. `https://twiki.cern.ch/twiki/bin/view/AtlasPublic/LuminosityPublicResults`. September 2014.

[113] M. Lamont, *The First Years of LHC Operation for Luminosity Production*, Proceedings for IPAC2013, Shanghai, China (2013).

[114] The ATLAS Collaboration, *Electron reconstruction and identification efficiency measurements with the ATLAS detector using the 2011 LHC proton proton collision data*, Eur. Phys. J. C **74** (2014) 2941.

[115] The ATLAS Collaboration, *Electron efficiency measurements with the ATLAS detector using the 2012 LHC proton-proton collision data*, ATLAS-CONF-2014-032.

[116] The ATLAS Collaboration. `https://twiki.cern.ch/twiki/bin/view/AtlasPublic/EgammaTriggerPublicResults`. September 2014.

[117] The ATLAS Collaboration. `https://twiki.cern.ch/twiki/bin/view/AtlasPublic/ElectronGammaPublicCollisionResults`. September 2014.

[118] The ATLAS Collaboration, *Measurement of the muon reconstruction performance of the ATLAS detector using 2011 and 2012 LHC proton-proton collision data*, `arXiv:1407.3935`.

[119] K. Rehermann and B. Tweedie, *Efficient Identification of Boosted Semileptonic Top Quarks at the LHC*, JHEP **1103** (2011) 059.

[120] The ATLAS Collaboration. `https://twiki.cern.ch/twiki/bin/view/AtlasPublic/MuonTriggerPublicResults`. September 2014.

[121] The ATLAS Collaboration, *Preliminary results on the muon reconstruction efficiency, momentum resolution, and momentum scale in ATLAS 2012 pp collision data*, ATLAS-CONF-2013-088.

[122] The ATLAS Collaboration. `https://twiki.cern.ch/twiki/bin/view/AtlasPublic/MuonPerformancePublicPlotsOld`. November 2014.

[123] M. Cacciari and G. P. Salam, *Dispelling the N^3 myth for the k_t jet-finder*, Phys. Lett. B **641** (2006) 57.

[124] M. Cacciari, G. P. Salam, and G. Soyez, *The anti-k_t jet clustering algorithm*, JHEP **04** (2008) 063.

[125] M. Cacciari, G. P. Salam, and G. Soyez, *FastJet User Manual*, Eur. Phys. J. C **72** (2012) 1896.

[126] The ATLAS Collaboration, *Jet energy measurement and its systematic uncertainty in proton-proton collisions at $\sqrt{s} = 7$ TeV with the ATLAS detector*, `arXiv:1406.0076 [hep-ex]`.

[127] The ATLAS Collaboration, *Pile-up subtraction and suppression for jets in ATLAS*, ATLAS-CONF-2013-083.

[128] A. B. Galtieri, F. Margaroli, and I. Volobouev, *Precision measurements of the top quark mass from the Tevatron in the pre-LHC era*, Rept.Prog.Phys. **75** (2012) 056201.

[129] The ATLAS Collaboration, *Calibrating the b-Tag and Mistag Efficiencies of the SV0 b-Tagging Algorithm in 3 pb^{-1} of Data with the ATLAS Detector*, ATLAS-CONF-2010-099.

[130] The ATLAS Collaboration, *Commissioning of the ATLAS high-performance b-tagging algorithms in the 7 TeV collision data*, ATLAS-CONF-2011-102.

[131] The ATLAS Collaboration, *Performance of Impact Parameter-Based b-tagging Algorithms with the ATLAS Detector using Proton-Proton Collisions at $\sqrt{s} = 7$ TeV*, ATLAS-CONF-2010-091.

[132] G. Piacquadio and C. Weiser, *A new inclusive secondary vertex algorithm for b-jet tagging in ATLAS*, J.Phys.Conf.Ser. **119** (2008) 032032.

[133] The ATLAS Collaboration, *Measurement of the b-tag Efficiency in a Sample of Jets Containing Muons with 5 fb^{-1} of Data from the ATLAS Detector*,.

[134] The ATLAS Collaboration, *Soft Muon Tagging*, ATL-PHYS-PUB-2009-021.

[135] The ATLAS Collaboration, *Measurement of the Mistag Rate with 5 fb^{-1} of Data Collected by the ATLAS Detector*, ATLAS-CONF-2012-040.

[136] The ATLAS Collaboration, *b-jet tagging calibration on c-jets containing D^{*+} mesons*, ATLAS-CONF-2012-039.

[137] The ATLAS Collaboration, *Calibration of the b-tagging efficiency for c jets with the ATLAS detector using events with a W boson produced in association with a single c quark*, ATLAS-CONF-2013-109.

[138] The ATLAS Collaboration, *Calibration of b-tagging using dileptonic top pair events in a combinatorial likelihood approach with the ATLAS experiment*, ATLAS-CONF-2014-004.

[139] Courtesy of V. Dao.

[140] The ATLAS Collaboration, *Performance of Missing Transverse Momentum Reconstruction in ATLAS studied in Proton-Proton Collisions recorded in 2012 at 8 TeV*, ATLAS-CONF-2013-082.

[141] The ATLAS Collaboration, *Performance of Missing Transverse Momentum Reconstruction in Proton-Proton Collisions at 7 TeV with ATLAS*, Eur. Phys. J. C **72** (2012) 1844.

[142] T. Sjöstrand, S. Mrenna, and P. Skands, *Pythia 6.4 Physics and Manual*, JHEP **05** (2006) 026.

[143] G. Corcella et al., *HERWIG 6: an event generator for hadron emission reactions with interfering gluons (including supersymmetric processes)*, JHEP **01** (2001) 010.

[144] T. Gleisberg, S. Hoeche, F. Krauss, M. Schonherr, S. Schumann, et al., *Event generation with SHERPA 1.1*, JHEP **0902** (2009) 007.

[145] S. Catani, F. Krauss, R. Kuhn, and B. Webber, *QCD matrix elements + parton showers*, JHEP **0111** (2001) 063.

[146] F. Krauss, *Matrix elements and parton showers in hadronic interactions*, JHEP **0208** (2002) 015.

[147] A. Schalicke and F. Krauss, *Implementing the ME+PS merging algorithm*, JHEP **0507** (2005) 018.

[148] L. Lonnblad, *Correcting the color dipole cascade model with fixed order matrix elements*, JHEP **0205** (2002) 046.

[149] M. L. Mangano et al., *Multijet matrix elements and shower evolution in hadronic collisions:* $Wb\bar{b} + n$ *jets as a case study*, Nucl. Phys. **B 632** (2002) 343.

[150] M. Mangano, M. Moretti, F. Piccinini, R. Pittau, and A. Polosa, *ALPGEN, a generator for hard multiparton processes in hadronic collisions*, JHEP **0307** (2003) 1.

[151] J. Alwall et al., *MadGraph/MadEvent v4: the new web generation*, JHEP **09** (2007) 028.

[152] The ATLAS Collaboration, *The ATLAS Simulation Infrastructure*, Eur. Phys. J. C **70** (2010) 823.

[153] S. Agostinelli et al., *Geant4: a simulation toolkit*, Nucl. Instr. Meth. A **506** no. 3, (2003) 250.

[154] T. Yamanaka and the ATLAS Collaboration, *The ATLAS calorimeter simulation FastCaloSim*, Journal of Physics: Conference Series **331** no. 3, (2011) 032053.

[155] J. Pumplin et al., *New generation of parton distributions with uncertainties from global QCD analysis*, JHEP **07** (2002) 012.

[156] The ATLAS Collaboration, *ATLAS tunes of PYTHIA6 and Pythia8 for MC11*, ATL-PHYS-PUB-2011-009.

[157] F. Maltoni, M. Mangano, I. Tsinikos, and M. Zaro, *Top-quark charge asymmetry and polarization in $t\bar{t}W^{\pm}$ production at the LHC*, Phys. Lett. B **736** (2014) 252–260.

[158] J. Alwall, R. Frederix, S. Frixione, V. Hirschi, F. Maltoni, et al., *The automated computation of tree-level and next-to-leading order differential cross sections, and their matching to parton shower simulations*, JHEP **1407** (2014) 079.

[159] Private Communication with J. McFayden.

[160] K. Melnikov and F. Petriello, *Electroweak gauge boson production at hadron colliders through $\mathcal{O}(\alpha_s^2)$*, Phys. Rev. D **74** (2006) 114017.

[161] P. Z. Skands, *Tuning Monte Carlo Generators: The Perugia Tunes*, Phys. Rev. **D82** (2010) 074018.

[162] J. Campbell and R. Ellis, *An update on vector boson pair production at hadron colliders*, Phys. Rev. D **60** (1999) 113006.

[163] S. Frixione, E. Laenen, P. Motylinski, and B. R. Webber, *Single-top production in MC@NLO*, JHEP **03** (2006) 092.

[164] N. Kidonakis, *Next-to-next-to-leading-order collinear and soft gluon corrections for t-channel single top quark production*, Phys. Rev. D **83** (2011) 091503.

[165] N. Kidonakis, *Next-to-next-to-leading logarithm resummation for s-channel single top quark production*, Phys. Rev. D **81** (2010) 054028.

[166] N. Kidonakis, *Two-loop soft anomalous dimensions for single top quark associated production with a W- or H-*, Phys. Rev. D **82** (2010) 054018.

[167] P. Golonka and Z. Was, *PHOTOS Monte Carlo: a precision tool for QED corrections in Z and W decays*, Eur. Phys. J. C **45** (2006) 97.

[168] S. Jadach, J. H. Kühn, and Z. Wa̧s, *TAUOLA - a library of Monte Carlo programs to simulate decays of polarized τ leptons*, Comput. Phys. Commun. **64** (1991) 275.

[169] The LHC Higgs Cross Section Working Group Collaboration, S. Heinemeyer et al., *Handbook of LHC Higgs Cross Sections: 3. Higgs Properties*, `arXiv:1307.1347 [hep-ph]`.

[170] The ATLAS Collaboration, *Measurements of normalized differential cross-sections for $t\bar{t}$ production in pp collisions at $\sqrt{s}$=7 TeV using the ATLAS detector*, `arXiv:1407.0371 [hep-ex]`.

[171] The ATLAS Collaboration, *Measurement of the Production Cross section of jets in Association with a Z Boson in pp Collisions at 7 TeV Using the ATLAS Detector*, JHEP **07** (2013) 32.

[172] The D0 Collaboration, *Measurement of the top quark mass using dilepton events*, Phys. Rev. Lett. **80** (1998) 2063–2068.

[173] The D0 Collaboration, *Measurement of the top quark mass in the dilepton channel*, Phys. Rev. D **60** (1999) 052001.

[174] J. Meyer, *Measurement of the Top Quark Mass using Dilepton Events and a Neutrino Weighting Algorithm with the DØExperiment at the Tevatron (Run II)*, FERMILAB-THESIS-2007-65 (2007).

[175] J. Erdmann, S. Guindon, K. Kroeninger, B. Lemmer, O. Nackenhorst, et al., *A likelihood-based reconstruction algorithm for top-quark pairs and the KLFitter framework*, Nucl. Instr. Meth. A **A748** (2014) 18–25.

[176] A. Caldwell, D. Kollar, and K. Kroeninger, *BAT - The Bayesian analysis toolkit*, Computer Physics Communications **180** no. 11, (2009) 2197 – 2209.

[177] S. Guindon, *A Top Quark Mass Measurement Using the Stabilized R_{32} Variable with the ATLAS Detector*, CERN-THESIS-2012-140 (2012).

[178] B. Lemmer, *Measurement of Spin Correlations in $t\bar{t}$ Events from pp Collisions at $\sqrt{s} = 7$ TeV in the Lepton + Jets Final State with the ATLAS Detector*, `arXiv:1410.1791 [hep-ex]`.

[179] N. Metropolis, A. W. Rosenbluth, M. N. Rosenbluth, A. H. Teller, and E. Teller, *Equation of State Calculations by Fast Computing Machines*, The Journal of Chemical Physics **21** no. 6, (1953) 1087–1092.

[180] A. Gelman and D. B. Rubin, *Inference from Iterative Simulation Using Multiple Sequences*, Statist. Sci. **7** no. 4, (1992) 457–472.

[181] S. Kirkpatrick, C. D. Gelatt, and M. P. Vecchi, *Optimization by Simulated Annealing*, Science **220** no. 4598, (1983) 671–680.

[182] S. Frixione and B. R. Webber, *Matching NLO QCD computations and parton shower simulations*, JHEP **0206** (2002) 029.

[183] J. Butterworth, J. Forshaw, and M. Seymour, *Multiparton interactions in photoproduction at HERA*, Z. Phys. C **72** (1996) 637.

[184] The ATLAS Collaboration, *First tuning of HERWIG/JIMMY to ATLAS data*, ATL-PHYS-PUB-2010-014.

[185] The ATLAS Collaboration, *Evidence for the associated production of a vector boson (W, Z) and top quark pair in the dilepton and trilepton channels in pp collision data at $\sqrt{s} = 8$ TeV collected by the ATLAS detector at the LHC*, ATLAS-CONF-2014-038 (2014).

[186] Phi-T GmbH, "NeuroBayes package." `http://neurobayes.phi-t.de/`.

[187] M. Feindt and U. Kerzel, *The NeuroBayes neural network package*, Nucl. Instr. Meth. A **A559** (2006) 190–194.

[188] J. Neyman and E. Pearson, *On the problem of the most efficient tests of statistical hypotheses*, Philos. Trans. Roy. Soc. London Ser. A. **231** (1933) 289–337.

[189] P. Speckmayer, "Multivariate Data Analysis with TMVA." `https://indico.cern.ch/event/90840/material/slides/1.pdf`, 2010.

[190] M. Leshno, V. Y. Lin, A. Pinkus, and S. Schocken, *Multilayer Feedforward Networks With a Nonpolynomial Activation Function Can Approximate Any Function*, Neural networks **6** (1993) 861–867.

[191] R. H. Byrd, P. Lu, J. Nocedal, and C. Zhu, *A Limited Memory Algorithm for Bound Constrained Optimization*, SIAM J. Sci. Comput. **16** no. 5, (1995) 1190–1208.

[192] G. C. Fox and S. Wolfram, *Event shapes in e^+e^-annihilation*, Phys. Rev. Lett. **41** (1978) 1581.

[193] C. Bernaciak, M. S. A. Buschmann, A. Butter, and T. Plehn, *Fox-Wolfram Moments in Higgs Physics*, Phys. Rev. D **87** (2013) 073014.

[194] M. Baak, G. Besjes, D. Cote, A. Koutsman, J. Lorenz, et al., *HistFitter software framework for statistical data analysis*, `arXiv:1410.1280 [hep-ex]`.

[195] The ROOT Collaboration, K. Cranmer, G. Lewis, L. Moneta, A. Shibata, and W. Verkerke, *HistFactory: A tool for creating statistical models for use with RooFit and RooStats*, CERN-OPEN-2012-016.

[196] G. Cowan, K. Cranmer, E. Gross, and O. Vitells, *Asymptotic formulae for likelihood-based tests of new physics*, Eur. Phys. J. C **71** no. 2, (2011).

[197] S. S. Wilks, *The large-sample distribution of the likelihood ratio for testing composite hypotheses*, Ann. Math. Statist. **9** (1938) 60–2.

[198] L. Moneta, K. Cranmer, G. Schott, and W. Verkerke, *The RooStats project*, `arXiv:1009.1003 [physics.data-an]`.

[199] The ATLAS Collaboration, *Luminosity determination in pp collisions at $\sqrt{s} = 7$ TeV using the ATLAS detector at the LHC*, Eur. Phys. J. C **71** (2011) 1630.

[200] The ATLAS Collaboration, *Improved luminosity determination in pp collisions at $\sqrt{s} = 7$ TeV using the ATLAS detector at the LHC*, Eur. Phys. J. C **73** (2013) 2518.

[201] The ATLAS Collaboration, *Jet energy measurement with the ATLAS detector in proton-proton collisions at $\sqrt{s} = 7$ TeV*, Eur. Phys. J. C **73** (2013) 2304.

[202] The ATLAS Collaboration. `https://twiki.cern.ch/twiki/bin/view/AtlasPublic/JetEtmissApproved2013JESUncertainty`. October 2014.

[203] The ATLAS Collaboration, *Jet energy resolution in proton-proton collisions at $\sqrt{s} = 7$ TeV recorded in 2010 with the ATLAS detector*, Eur. Phys. J. C **73** (2013) 2306.

[204] The ATLAS Collaboration. `https://twiki.cern.ch/twiki/bin/view/AtlasPublic/JetEtmissApproved2013Jer2011`. October 2014.

[205] S. Frixione, E. Laenen, P. Motylinski, C. White, and B. R. Webber, *Single-top hadroproduction in association with a W boson*, JHEP **07** (2008) 029.

[206] B. Cooper et al., *Importance of a consistent choice of alpha(s) in the matching of AlpGen and Pythia*, Eur. Phys. J. C **72** (2012) 2078.

[207] The ATLAS Collaboration. `https://atlas.web.cern.ch/Atlas/GROUPS/PHYSICS/CombinedSummaryPlots/SM`. November 2014.

[208] The ATLAS Collaboration, *Measurement of the ttbar production cross-section in pp collisions at sqrts = 7 TeV using kinematic information of lepton+jets events*, ATLAS-CONF-2011-121.

[209] The ATLAS Collaboration, *Measurement of the top quark pair production cross-section with ATLAS in the single lepton channel*, Phys. Lett. B **711** (2012) 244–263.

[210] The ATLAS Collaboration, *Measurement of the top quark pair production charge asymmetry in proton-proton collisions at $\sqrt{s} = 7$ TeV using the ATLAS detector*, JHEP **1402** (2014) 107.

[211] The D0 Collaboration, *Measurement of the $t\bar{t}$ production cross section in $p\bar{p}$ collisions at $\sqrt{s} = 1.96$ TeV using kinematic characteristics of lepton + jets events*, Phys. Rev. D **76** (2007) 092007.

[212] The ATLAS Collaboration, *Measurement of the $t\bar{t}$ production cross-section as a function of jet multiplicity and jet transverse momentum in 7 TeV proton-proton collisions with the ATLAS detector*, `arXiv:1407.0891 [hep-ex]`.

[213] A. Hoecker, P. Speckmayer, J. T. J. Stelzer, E. von Toerne, and H. Voss, *TMVA - Toolkit for Multivariate Data Analysis*, PoS ACAT **040** (2007).

[214] The ATLAS Collaboration, *Top Quark Pair Production Cross-section Measurements in ATLAS in the Single Lepton+Jets Channel without b-tagging*, ATLAS-CONF-2011-023 (2011).

[215] F. A. Berends, W. Giele, H. Kuijf, R. Kleiss, and W. J. Stirling, *Multi - Jet Production in W, Z Events at $p\bar{p}$ Colliders*, Phys. Lett. B **224** (1989) 237.

[216] S. Ellis, R. Kleiss, and W. Stirling, *W's, Z's and jets*, Phys. Lett. B **154** no. 5-6, (1985) 435–440.

[217] A. Henrichs, A. Quadt, and E. Shabalina, *Precision Measurements of the Top Quark Pair Production Cross Section in the Single Lepton Channel with the ATLAS Experiment*, CERN-THESIS-2012-043 (2012).

[218] S. Moch and P. Uwer, *Theoretical status and prospects for top-quark pair production at hadron colliders*, Phys. Rev. D **78** (2008) 034003.

[219] U. Langenfeld, S. Moch, and P. Uwer, *New results for t anti-t production at hadron colliders*, `arXiv:0907.2527 [hep-ph]`.

[220] M. Beneke, M. Czakon, P. Falgari, A. Mitov, and C. Schwinn, *Threshold expansion of the $gg(q\bar{q}) \to Q\bar{Q} + X$ cross section at $\mathcal{O}(\alpha_s^4)$*, Phys. Lett. B **690** (2010) 483–490.

[221] M. Czakon, P. Fiedler, A. Mitov, and J. Rojo, *Further exploration of top pair hadroproduction at NNLO*, `arXiv:1305.3892 [hep-ph]`.

[222] The ATLAS Collaboration, *Statistical combination of top quark pair production cross-section measurements using dilepton, single-lepton, and all-hadronic final states at* $\sqrt{s} = 7$ *TeV with the ATLAS detector*, ATLAS-CONF-2012-024 (2012).

[223] The ATLAS Collaboration. `https://atlas.web.cern.ch/Atlas/GROUPS/PHYSICS/CombinedSummaryPlots/TOP`. November 2014.

[224] S. Alekhin, A. Djouadi, and S. Moch, *The top quark and Higgs boson masses and the stability of the electroweak vacuum*, Phys. Lett. B **716** (2012) 214–219.

[225] M. Czakon, M. L. Mangano, A. Mitov, and J. Rojo, *Constraints on the gluon PDF from top quark pair production at hadron colliders*, JHEP **1307** (2013) 167.

Acknowledgements

"Gracias a la vida, que me ha dado tanto..."

- Violeta Parra -

The last page of the thesis, but the first page I started writing in my mind since I first entered through the doors of the II. Institute of Physics in Göttingen. A first page that has grown so much over the past years that now I need to summarise, so I already apologise to those I may have forgotten! Thank you to all of you that filled this long way with strength and joy!

A first and big thank you to my thesis supervisor, Arnulf Quadt, for inviting me to join the particle physics world, who, "Schritt für Schritt", taught me and challenged me, and made me understand the priceless joy of research. Thank you for believing in me, and reminding me every time about the courage of those women in the poster on the back of the door. I would also like to thank Ariane Frey for agreeing to be the co-referee of this thesis, especially with such short notice!

There are no words to express how thankful I am to Lisa Shabalina. If there is someone that knows what I went through, from start to finish, that is you. Thanks for sharing your infinite wisdom, in physics and non-physics matters, for being sincere with me, and for standing up for me in the hardest moments. Thanks for coming up with the $t\bar{t}V$ challenge, and believing I could do it. You showed me with actions the virtues of a good scientist and an amazing supervisor.

I want to thank all the people in the II. Institute for making feel "die Spanier" like at home right from the start. Thanks to Boris Lemmer, my first office mate who still has not given up speaking in German with me, despite my countless errors, and made me laugh involuntarily, even in the hard moments; to Matze George and Jens Weingarten for having always their doors opened; to Jörn Grosse-Knetter, for supervising my first incursion in particle physics hardware during my Pixel Qualification task, for his patience and support. Thanks to the happy theorists, Steffen Schumann and Erik Gerwick, who arrived to the Institute with all the positive vibrations. Big thanks to the big "Kebin" Kröninger, for letting me ask him the physics questions I did not dare to ask anyone else, and for being such an amazing teacher. Arriving late to the Top Meeting is not that much fun anymore without you in the Institute. Thanks to all of you with whom

I shared nice moments along the way: Leonid, Despoina, Olaf, Johannes, Andrea, Katharina, Oleg, Nina, Jörg, Eric, Ulla, Chris, Julia.

Anna Henrichs and Adam Roe, who arrived from CERN in full-research mode, and shared your knowledge with me in record-time. You showed me how much satisfaction comes after lots of work and struggle. Thanks for the patience to, still in stressful times, explain obvious things to that unexperienced apprentice.

Thanks to the Mediterranean team! Zinonas Zinonos, Jordi Nadal and Maria Moreno Llacer, I am so happy to have shared with you over the past year breaks, lunches and office visits. I don't feel the only louder person in the Institute anymore. Special thanks to Maria, my last office mate, a hurricane of energy and love, amazing support in the hardest and most stressful moments of my whole PhD. "We can do it!", Maria, and this is my modest testimony of it.

Big thanks to Lisa, Stefan, Kevin, and Erik for proof-reading this work in such a short timescale, and reminding me that three-lines-long sentences only exist in Spanish. Thanks to John Amador-Bedford for providing the perfect translation of the starting quote of this thesis, and helped me satisfy my personal need of including Julio Cortázar somehow in a physics thesis.

All the persons that made my one-year stay at CERN unforgettable, thanks! The list of all the amazing, and inspiring people is hard to summarise: thanks to my 2010 CERN Summer Student friends, especially to Christina Williamson and Laura Franconi for the amazing women and friends they are, thanks to Dani Cámpora for giving me shelter in such a short notice. A big thank you to all the $t\bar{t}H$ people that made the "background" $t\bar{t}V$ feel part of the family; I wouldn't have survived this long journey, the approval processes and the countless requests without your wisdom, support, and positiveness. Thanks Eve, Jahred, Julian, Quake, Mark, Michele!

The three $t\bar{t}H$ musketeers: Javier Montejo, Valerio Dao, and Stefan Guindon. You have made the most stressful time of my life, the most enjoyable one. You showed me the real definition of team-work, and it is probably one of the reasons that makes me still believe in collaborative physics, and more importantly, in physics&fun. Thanks to you, and Nani and Lilly, for reminding me about the important things in life. And special thanks to Vale, who every time he entered in my office at CERN, left me with a big idea, a full page with encrypted notes, and a big smile.

The $t\bar{t}V$ experience allowed me to work and discuss intensively with great physicists. I want to thank the Top Properties convenors, James Ferrando, Frederic Deliot and Nuno Castro, and the Top Group convenors, Tancredi Carli and Alison Lister, for giving me the chance to show that the initial least sensitive $t\bar{t}V$ channel can, with some effort, win a place in the combination. Thanks Alison for the many advices and encouragement! Also to the "trilepton" team, Kerim Suruliz, Josh McFayden, Jörgen Sjölin, and Hovhannes Khandanyan, for showing me what the challenges of a low statistics channel are, and struggling together in the last steps before the approval.

A special thanks to my *mentees*, Natalia Revelo, Dominika Lyzwa, and Andreea Scacioc, who were always there, sharing their passion for science and life with me. You helped me to keep focused, to keep fighting, and don't give up the woman I believed in. Thanks to amazing women and scientists like you, I have no doubts the new female role model will soon be real. And of course, how can I forget my mentor, Sharmishtha Dattagupta, who opened her heart and listened, and listened, and made me realise that I had the answer already, just needed some help to find it. Your office was for me my spiritual retreat; your courage, my inspiration.

I want to thank the Dorothea Schlözer Programme, which not only supported financially this project, but also provided me the possibility to join the Mentoring Programme, and feel part of the joint efforts of many women to achieve a real gender equality in science.

Continuing the nomadic tendence in my life, I had so many homes during these past years, and in each of them I shared my everyday with such amazing souls, who helped me to recover from the monopoly that physics sometimes has over me. I have to start therefore thanking the three amazons from Göttingen, my Schillerstrasse mothers, Trudi Heinrich, Karin El Eid, and Lucie Hamdi; you were there when I just arrived, naive and unexperienced, and also now that I am finishing; so many things happened in between, so many things changed, except you and your solid beliefs and your huge warm hearts. Thanks to Lea and Simone for the recovering chats in the kitchen, for trying to understand my crazy working hours, for feeding me with your vegetarian deliciousnesses!

My biggest thanks goes to my family, Marina Schröder, Guillermo Vázquez, and my sister and best friend Katya Vázquez Schröder; ustedes son la razón por la que hoy estoy acá, feliz, positiva, libre y amando lo que hago. Gracias por darme la libertad de elegir mi camino, por creer firmemente en mí y en mis decisiones, por ayudarme incluso cuando no sabía que estaba perdida, por sentirlos tan cerca incluso cuando se fueron de vuelta al otro lado del océano. Gracias por ser mi norte y mi patria.

Finally, my biggest THANK YOU to Stefan Guindon, who lived my excitement of my first grid job submission, and lives now my excitement of the last lines of my PhD thesis. There are no words to thank you for all the happiness and the support you gave me, for the true belief that I could manage this in an impossible timescale. Thanks for reminding me that there are no major problems that cannot be solved with scissors and string, and lots of willingness. You were my source of power during this past amazing year. For that, and so much more, thanks.
So I've started out for God knows where / I guess I'll know when I get there.